行政院國家科學委員會補助專題研究計畫 ☑ 成 果 報 告 □期中進度報告

（計畫名稱）

垂直圓柱容器中向下強制氣流流過一水平加熱晶圓之渦旋流結構與相關熱傳特性研究

計畫類別：☑ 個別型計畫　　□ 整合型計畫
計畫編號：NSC 92－2212－E－009－009
執行期間：2001 年 08 月 01 日至 2004 年 07 月 31 日

計畫主持人：林清發
計畫參與人員： 謝瑞青、陳尚緯、謝汎鈞、鄭詔文、吳佳鴻、羅文賢

成果報告類型(依經費核定清單規定繳交)：□精簡報告　☑完整報告

本成果報告包括以下應繳交之附件：
□赴國外出差或研習心得報告一份
□赴大陸地區出差或研習心得報告一份
□出席國際學術會議心得報告及發表之論文各一份
□國際合作研究計畫國外研究報告書一份

處理方式：除產學合作研究計畫、提升產業技術及人才培育研究計畫、列管計畫及下列情形者外，得立即公開查詢
□涉及專利或其他智慧財產權，□一年□二年後可公開查詢

執行單位：國立交通大學

中　華　民　國 九十三 年　十　月 二十七 日

ABSTRACT

In this three-year research project (August 2001 to July 2004) we investigate the flow and thermal characteristics in a model experimental vertical CVD processor for processing 8-inch silicon wafer. In the CVD processor, the flow field is an important factor for growing a uniform thin film and it depends on the flowrate, jet-to-disk separation distance, injection pipe diameter and disk rotation. To obtain uniform temperature on disk surface we use copper disk to replace silicon wafer and heated by three heating resistance coils. Each coil is independently heated by A.C. power.

The experimental results clearly reveal a new vortex roll. More specifically, in the upper range of the jet Reynolds number tested here a small tertiary inertia-driven circular vortex roll appears near the upper wall of the chamber, in addition to the previously known primary and secondary inertia-driven rolls. Besides, we also note that a reduction in the jet-to-disk separation distance causes a delayed onset of the inertia-driven rolls except for $H \geqq 20.0$ mm and in the meantime causes a substantial decrease in the Rayleigh number since $Ra \propto H^3$, which in turn significantly reduces the size and strength of the buoyancy-driven roll. Moreover, at the smallest H of 10 mm the flow filed becomes steady state. Our data also suggest that the onset of the buoyancy roll takes place when the local buoyancy-to-inertia ratio at the edge of the disk $Gr/Re_{we}^2 \approx 33.0$ within the experimental uncertainty. The buoyancy-driven roll can be eliminated by rotation disk due to action of the strong centrifugal force at a certain high disk rotation speed. Finally, the temperature data indicate that the steady radial air temperature distributions are nonmonotonic which mainly reflects the counter-rotating vortex flow structure of the primary inertia-driven and buoyancy-driven rolls.

摘要

在此三年期研究計畫裡(2001 年 8 月至 2004 年 7 月)，我們探討在一垂直式 8 吋晶圓之 CVD 氣流場之實驗系統的熱流特性。在 CVD 成長薄膜單晶製程中，爲了成長均勻的薄膜，氣流場的特性變得相當重要且主要和氣流流速、氣流出口至加熱圓盤的高度、氣流出口管徑以及加熱圓盤是否旋轉有關。另外，爲了獲得均勻的溫度分佈，在加熱圓盤的表面，我們使用銅板來取代晶圓，且由 3 段電阻式加熱線圈來加熱，每段線圈是由交流電源獨立控制。

實驗結果顯示爐體存在新的渦流。另外，除了我們已知的 Primary 與 Secondary inertia-driven roll，在比較高的雷諾數時，有三次渦流在頂板且靠近衝擊流附近產生。除此之外，我們也發現如果降低頂板到底板距離，除了距離大於或等於 20.0mm 以外，會使得 Inertia-driven roll 出現的臨界雷諾數延遲，高度降低後同時也降低了雷利數，所以 Buoyancy-driven roll 的尺寸與強度都減小。再者，在 10mm 比較低的頂板到底板距離時，流場趨向於穩定。同時我們也發現 Buoyancy-driven roll 開始出現時的局部浮慣比約爲 33.0。浮力趨動的渦流，可以藉由旋轉加熱圓盤在某一高轉速下造成的離心力作用而消除。量測穩定或是統計學上穩定的流場在徑向方向的溫度發現有一最大值，這是因爲 Primary inertia-driven roll 與 Buoyancy-driven roll 同時存在的關係。

CONTENTS

ABSTRACT I

摘要 II

CONTENTS III

LIST OF TABLES V

LIST OF FIGURES VI

NOMENCLATURE XIV

CHAPTER 1 Introduction 1

1.1 Motivation of the study 1

1.2 Literature review—heat transfer and flow characteristics of impinging jets 2

1.3 Literature review—unsteady transitional impinging jets 5

1.4 Literature review—confined jet flow associated with CVD reactors and RTP processors 6

1.5 Objective of the research project 7

CHAPTER 2 Experimental Apparatus and Procedures 8

2.1 Experimental apparatus 8

2.2 Analysis of time-average and instantaneous air temperature 11

2.3 Experimental procedures 11

2.4 Uncertainty analysis 12

2.5 Verification of the experiment 12

CHAPTER 3 Characteristics of Vortex Flow at Long Time 19

3.1 Typical steady flow pattern 20

3.2 Onset of vortex flow 22

3.3 Effects of jet Reynolds number 25

3.4 Effects of Rayleigh number 28

3.5 Effects of processing chamber geometry 29

3.6 Size and location of the vortex rolls 30

3.7 Steady temperature distribution in vortex flow 32

3.8 Effects of disk rotation 32

CHAPTER 4 Characteristics of Time Dependent Vortex Flow 96

4.1 Time periodic vortex flows 96

4.2 Vortex flow suppression 99

4.3 Flow regime map 100

4.4 Formation of vortex flow 101

CHAPTER 5 Concluding Remarks and Recommendations for future work 115

5.1 Concluding remarks 115

5.2 成果自評 119

REFERENCES 120

LIST OF TABLES

Table 2.1 Summary of the uncertainty analysis. ----------13
Table 3.1 Critical condition for appearance of the secondary inertia-driven roll.----------34
Table 3.2 Critical condition for onset of time-dependent flow for unheated disk and D_j=10.0 mm. ----------35
Table 3.3 Critical condition for the onset of buoyancy-driven vortex roll. ----------36

LIST OF FIGURES

Fig. 2.1 Schematic diagram of the experimental system. ----------14

Fig. 2.2 Schematic of the test section from the top view (a) and 3-zone concentric heater (b). ----------15

Fig. 2.3 Schematic diagram of the test section with (a) horizontal and (b) inclined chamber tops. For clear illustration the diagrams are not plotted in proportion to the actual geometrical dimensions. ----------16

Fig. 2.4 The heater consists of three parts: resistances heating element, holder and insulator. ----------17

Fig. 2.5 The flow field for H/D_j=2 and Ra=0, left: the result from the present study at Re_j=406 for D_j=10.0 mm; right: contours of stream function from Law and Masliyah (1984) at Re=400.----------18

Fig. 3.1 Steady vortex flow pattern for D_j=10.0 mm and H=15.0 mm at Re_j=406 (Q_j=3.0 slpm) and Ra=3,170 (ΔT=10.0℃): (a) top view flow half of photo taken at the middle horizontal plane between the disk and chamber top, (b) side view flow photo taken at the vertical plane $\theta=0^\circ$ & 180° and (c) the corresponding schematically sketched cross plane vortex flow.----------37

Fig. 3.2 Steady side view flow photos taken at the cross plane $\theta=0°$ for various Re_j to illustrate the tertiary inertia-driven roll with Ra=0 & D_j=10.0 mm for (a) H=20.0 mm, (b) H=15.0 mm and (c) H=10.0 mm.----------38

Fig. 3.3 Steady side view flow photos at low Reynolds numbers for Ra=0 & H=20.0 mm: (a) Re_j=13.6 & D_j=10.0 mm, (b) Re_j=20.0 & D_j=10.0 mm, (c) Re_j=12.0 & D_j=22.1 mm and (d) Re_j=15.0 & D_j=22.1 mm.----------39

Fig. 3.4 Steady side view flow photos at low Reynolds numbers for Ra=0 & H=15.0 mm at Re_j = (a) 27 & D_j=10.0 mm, (b) 41 & D_j=10.0 mm, (c) 12 & D_j=22.1 mm and (d) 18 & D_j=22.1 mm. ----------40

Fig. 3.5 Steady side view flow photos at low jet Reynolds numbers for Ra=0 with H=10.0 mm at Re_j = (a) 13.5 & D_j=10.0 mm, (b) 27 & D_j=10.0 mm, (c) 37 & D_j=22.1 mm, (d) 43 & D_j=22.1 mm and (e) 49 & D_j=22.1

mm. ----------41

Fig. 3.6 Steady side view flow photos near the critical condition showing the flow near the onset of buoyancy-driven roll for Ra=1650 (ΔT=2.2℃) with (a) Re_j=612 & D_j=10.0 mm, (b) Re_j=680 & D_j=10.0 mm, (c) Re_j=748 & D_j=10.0 mm, (d) Re_j=275 & D_j=22.1 mm, (e) Re_j=305 & D_j=22.1 mm and (f) Re_j=336 & D_j=22.1 mm.. ----------42

Fig. 3.7 Steady side view flow photos taken at the cross plane θ=0° & 180° for various jet Reynolds numbers at Ra=0 (ΔT=0℃) for D_j= (a) 10.0 mm and (b) 22.1 mm.----------43

Fig. 3.8 Steady side view flow photos taken at the cross plane θ=0° & 180° for various jet Reynolds numbers at Ra=3,760 (ΔT=5.0℃) for D_j= (a) 10.0 mm and (b) 22.1 mm. ----------44

Fig. 3.9 Steady side view flow photos taken at the cross plane θ=0° & 180° for various jet Reynolds numbers at Ra=7,520 (ΔT=10.0℃) for D_j= (a) 10.0 mm and (b) 22.1 mm. ----------45

Fig. 3.10 Steady side view flow photos taken at the cross plane θ=0° & 180° for various jet Reynolds numbers at Ra=11,270 (ΔT=15.0℃) for D_j= (a) 10.0 mm and (b) 22.1 mm. ----------46

Fig. 3.11 Steady side view flow photos taken at the cross plane θ=0° & 180° for various jet Reynolds numbers at Ra=15,030 (ΔT=20.0℃) for D_j= (a) 10.0 mm and (b) 22.1 mm. ----------47

Fig. 3.12 Steady side view flow photos taken at the cross plane θ=0° & 180° for various jet Reynolds numbers at Ra=18,790 (ΔT=25.0℃) for D_j= (a) 10.0 mm and (b) 22.1 mm. ----------48

Fig. 3.13 Steady side view flow photos taken at the cross plane θ=0° & 180° for various jet Reynolds numbers at H=15.0 mm & Ra=0 (ΔT=0℃) for D_j= (a) 10.0 mm and (b) 22.1 mm.----------49

Fig. 3.14 Steady side view flow photos taken at the cross plane θ=0° & 180° for various jet Reynolds numbers at H=15.0 mm & Ra=1,590 (ΔT=5.0 ℃) for D_j= (a) 10.0 mm and (b) 22.1 mm.----------50

Fig. 3.15 Steady side view flow photos taken at the cross plane θ=0° & 180° for various jet Reynolds numbers at H=15.0 mm & Ra=3,170 (ΔT=10.0

℃) for D_j= (a) 10.0 mm and (b) 22.1 mm.----------51

Fig. 3.16 Steady side view flow photos taken at the cross plane θ=0° & 180° for various jet Reynolds numbers at H=15.0 mm & Ra=6,340 (ΔT=20.0 ℃) for D_j= (a) 10.0 mm and (b) 22.1 mm.----------52

Fig. 3.17 Steady side view flow photos taken at the cross plane θ=0° & 180° for various jet Reynolds numbers at H=15.0 mm & Ra=7,930 (ΔT=25.0 ℃) for D_j= (a) 10.0 mm and (b) 22.1 mm.----------53

Fig. 3.18 Steady top view flow photos taken at the middle horizontal plane between the disk and chamber top with Ra=0 (ΔT=0℃) & D_j=10.0 mm at H=15.0 mm for Re_j= (a) 135, (b) 270, (c) 406, (d) 541 and (e) 676.----------54

Fig. 3.19 Steady top view flow photos taken at the middle horizontal plane between the disk and chamber top with Ra=6,340 (ΔT=20.0℃) & D_j=10.0 mm at H=15.0 mm for Re_j= (a) 135, (b) 270, (c) 406, (d) 541 and (e) 676. ----------55

Fig. 3.20 Steady top view flow photos taken at the middle horizontal plane between the disk and chamber top with Ra=0 (ΔT=0℃) & D_j=22.1 mm at H=15.0 mm for Re_j= (a) 61, (b) 122, (c) 183, (d) 245 and (e) 306. ----------56

Fig. 3.21 Steady top view flow photos taken at the middle horizontal plane between the disk and chamber top with Ra=6,340 (ΔT=20.0℃) & D_j=22.1 mm at H=15.0 mm for Re_j= (a) 61, (b) 122, (c) 183, (d) 245 and (e) 306. ----------57

Fig. 3.22 Steady side view flow photos taken at the cross plane θ=0° & 180° for various jet Reynolds numbers at H=10.0 mm and Ra=0 (ΔT=0℃) for D_j= (a) 10.0 mm and (b) 22.1 mm.----------58

Fig. 3.23 Steady side view flow photos taken at the cross plane θ=0° & 180° for various jet Reynolds numbers at H=10.0 mm and Ra=470 (ΔT=5.0 ℃) for D_j= (a) 10.0 mm and (b) 22.1 mm.----------59

Fig. 3.24 Steady side view flow photos taken at the cross plane θ=0° & 180° for various jet Reynolds numbers at H=10.0 mm and Ra=940 (ΔT=10.0 ℃) for D_j= (a) 10.0 mm and (b) 22.1 mm.----------60

Fig. 3.25 Steady side view flow photos taken at the cross plane θ=0° & 180° for various jet Reynolds numbers at H=10.0 mm and Ra=1,410

(ΔT=15.0℃) for D_j= (a) 10.0 mm and (b) 22.1 mm. ----------61

Fig. 3.26 Steady side view flow photos taken at the cross plane θ=0° & 180° for various jet Reynolds numbers at H=10.0 mm and Ra=1,880 (ΔT=20.0℃) for D_j= (a) 10.0 mm and (b) 22.1 mm. ----------62

Fig. 3.27 Steady side view flow photos taken at the cross plane θ=0° & 180° for various jet Reynolds numbers at H=10.0 mm and Ra=2,350 (ΔT=25.0℃) for D_j= (a) 10.0 mm and (b) 22.1 mm. ----------63

Fig. 3.28 Top view flow photos taken at the middle horizontal plane between the disk and chamber top with Ra =940 (ΔT=10.0℃) and D_j=10.0 mm at H=10.0 mm for Re_j= (a) 135, (b) 270, (c) 406, (d) 541 and (e) 676.----------64

Fig. 3.29 Top view flow photos taken at the middle horizontal plane between the disk and chamber top with Ra=1,880 (ΔT=20.0℃) and D_j=22.1mm at H=10.0 mm for Re_j= (a) 61, (b) 122, (c) 184, (d) 245 and (e) 306. ----------65

Fig. 3.30 Top view flow photos taken at the middle horizontal plane between the disk and chamber top with Ra =2,350 (ΔT=25.0℃) and D_j=10.0 mm at H=10.0 mm for Re_j= (a) 135, (b) 270, (c) 406, (d) 541 and (e) 676.. ----------66

Fig. 3.31 Steady side view flow photos taken at the cross plane θ=0° & 180° for various Rayleigh numbers at Q_j=3.0 slpm for D_j= (a) 10.0 mm & Re_j=406 and (b) 22.1 mm & Re_j=184.----------67

Fig. 3.32 Steady side view flow photos taken at the cross plane θ=0° & 180° for various Rayleigh numbers at Q_j=5.0 slpm for D_j= (a) 10.0 mm & Re_j=676 and (b) 22.1 mm & Re_j=306.----------68

Fig. 3.33 Half of side view flow photos taken at θ=0° (left) and quarter of top view flow photos (right) taken at the middle horizontal plane between the disk and chamber top with Q_j=3.0 slpm, H=20.0 mm and D_j=10.0 mm at steady state for Ra= (a) 0, (b) 7,520 and (c) 15,030. ----------69

Fig. 3.34 Half side view flow photos taken at θ=0° (left) and quarter of top view flow photos (right) taken at the middle horizontal plane between the disk and chamber top with Q_j=3.0 slpm, H=20.0 mm and D_j=22.1 mm at steady state for Ra=(a) 0, (b) 7,520 and (c) 15,030. ----------70

Fig. 3.35 Steady side view flow photos taken at the cross plane θ=0° & 180° for various Rayleigh numbers at H=15.0 mm with Q_j=2.0 slpm for D_j=

(a) 10.0 mm and (b) 22.1 mm. ----------71

Fig. 3.36 Steady side view flow photos taken at the cross plane θ=0° & 180° for various Rayleigh numbers at H=15.0 mm with Q_j=4.0 slpm for D_j= (a) 10.0 mm and (b) 22.1 mm. ----------72

Fig. 3.37 Steady side view flow photos taken at the cross plane θ=0° & 180° for various Rayleigh numbers at H=15.0 mm with Q_j=5.0 slpm for D_j=(a) 10.0 mm and (b) 22.1 mm.----------73

Fig. 3.38 Half side view flow photos taken at θ=0° (left) and quarter of top view flow photos (right) taken at the middle horizontal plane between the disk and chamber top with Re_j=406, H=15.0 mm and D_j=10.0 mm at steady state for Ra= (a) 0, (b) 3,170 and (c) 6,340. ----------74

Fig. 3.39 Half side view flow photos taken at θ=0° (left) and quarter of top view flow photos (right) taken at the middle horizontal plane between the disk and chamber top with Re_j=184, H=15.0 mm and D_j=22.1 mm at steady state for Ra=(a) 0, (b) 3,170 and (c) 6,340.----------75

Fig. 3.40 Steady side view flow photos taken at the cross plane θ=0° & 180° for various Rayleigh numbers at H=10.0 mm & Q_j=1.0 slpm for D_j= (a) 10.0 mm and (b) 22.1 mm. ----------76

Fig. 3.41 Steady side view flow photos taken at the cross plane θ=0° & 180° for various Rayleigh numbers at H=10.0 mm & Q_j=3.0 slpm for D_j= (a) 10.0 mm and (b) 22.1 mm. ----------77

Fig. 3.42 Steady side view flow photos taken at the cross plane θ=0° & 180° for various Rayleigh numbers at H=10.0 mm & Q_j=5.0 slpm for D_j= (a) 10.0 mm and (b) 22.1 mm. ----------78

Fig. 3.43 Steady side view flow photos taken at the cross plane θ=0° & 180° at Q_j=3.0 slpm & H=20.0 mm with Ra=0. ----------79

Fig. 3.44 Steady side view flow photos taken at the cross plane θ=0° & 180° at H=20.0 mm. ----------80

Fig. 3.45 Steady side view flow photos taken at the cross plane θ=0° & 180° at H=15.0 mm with Ra=0.----------81

Fig. 3.46 Steady side view flow photos taken at the cross plane θ=0° & 180° at

H=15.0 mm. ----------82

Fig. 3.47 Steady side view flow photos taken at the cross plane θ=0° & 180° at H=10.0 mm. ----------83

Fig. 3.48 Steady side view flow photos taken at the cross plane θ=0° & 180° for D_j=10.0 mm at given ΔT=0℃ for various H. ----------84

Fig. 3.49 Steady side view flow photos taken at the cross plane θ=0° & 180° for D_j=10.0 mm at given ΔT=20.0℃ for various H. ----------85

Fig. 3.50 Steady side view flow photos taken at the cross plane θ=0° & 180° for D_j=22.1 mm at given ΔT=0℃ for various H. ----------86

Fig. 3.51 Steady side view flow photos taken at the cross plane θ=0° & 180° for D_j=22.1 mm at given ΔT=25.0℃ for various H. ----------87

Fig. 3.52 Radial extent of the primary inertia-driven roll with D_j=22.1 mm for H= (a) 10.0 mm, (b) 15.0 mm and (c) 20.0 mm. ----------88

Fig. 3.53 Radial location of the secondary inertia-driven roll with D_j=10 mm for H= (a) 10.0 mm, (b) 15.0 mm and (c) 20.0 mm. ----------89

Fig. 3.54 Radial variation in non-dimensional steady air temperature with various Re_j for H=15.0 mm & D_j=10.0 mm at Z=0.5 for Ra= (a) 3,170, (b) 6,340 and (c) 7,930. ----------90

Fig. 3.55 Radial variation in non-dimensional steady air temperature with various Re_j for H=15.0 mm & D_j=22.1 mm at Z=0.5 for Ra= (a) 3,170, (b) 6,340 and (c) 7,930. ----------91

Fig. 3.56 Radial variation in non-dimensional steady air temperature with various Re_j for H=10.0 mm & D_j=10.0 mm at Z=0.5 for Ra= (a) 1,410, (b) 1,880 and (c) 2,350. ----------92

Fig. 3.57 Radial variation in non-dimensional steady air temperature with various Re_j for H=10.0 mm & D_j=22.1 mm at Z=0.5 for Ra= (a) 1,410, (b) 1,880 and (c) 2,350. ----------93

Fig. 3.58 Steady side view flow photos taken at the cross plane θ=0° & 180° for various jet Reynolds numbers at Ra=0 (ΔT=0℃) and D_j=10.0 mm for (a)ω=0 and (b) ω=30 rpm (Re_ω=2,335). ----------94

Fig. 3.59 Steady side view flow photos taken at the cross plane θ=0° & 180° for various jet Reynolds numbers at Ra=15,030 (ΔT=20.0℃) and D_j=10.0 mm for (a) ω=0 and (b) ω=30 rpm (Re_ω=2,335).----------95

Fig. 4.1 Side view flow photos at the cross plane θ=0° & 180° at certain time instant in a typical periodic cycle and time records of air temperature at selected locations in the middle horizontal plane Z=0.5 with H=20.0 mm for (a) Re_j=136, Ra=11,270 & D_j=10.0 mm (t_p=21.1 sec) and (b) Re_j=61, Ra=15,030 & D_j=22.1 mm (t_p=13.8 sec). ----------103

Fig. 4.2 The time records of non-dimensional air temperature and the corresponding power spectrum densities for Ra=15,030 and D_j=22.1 mm at location (R, Z) =(0.52, 0.5) for θ=0º with H=20.0 mm for various Reynolds numbers Re_j= (a)49, (b)61, (c)73, (d)85 and (e)98. ----------104

Fig. 4.3 The time records of non-dimensional air temperature and corresponding power spectrum densities for Re_j=61 and D_j=22.1 mm at location (R, Z) =(0.52, 0.5) for θ=0º with H=20.0 mm for various Rayleigh numbers Ra= (a) 11,270, (b) 15,030 and (c) 18,790. ----------105

Fig. 4.4 Side view flow photos taken at the cross plane θ=0° for Re_j=61, Ra=11,270 and D_j=22.1 mm with H=20.0 mm at selected time instants (right) and the corresponding schematically sketched cross plane flow (left) in a typical periodic cycle (t_p=13.3sec). ----------106

Fig. 4.5 Half side view flow photos taken at θ=0° (left) and quarter of top view flow photos (right) taken at the middle horizontal plane between the disk and chamber top with Re_j= 61, Ra=11,270 and D_j=22.1 mm for H=20.0 mm at selected time instants in statistical state for (a) t=0 sec, (b) t=5 sec, (c) t=9 sec and (d) t=13 sec.----------107

Fig. 4.6 Side view flow photos at long time taken from the chambers at the cross plane θ=0º & 180? for △T=20.0℃ (Ra_o=15,030) for various jet flow rates with (a) D_j=10.0 mm & horizontal top, (b) D_j=10.0 mm & inclined top, (c) D_j=22.1 mm & horizontal top and (d) D_j=22.1 mm & inclined top. ----------108

Fig. 4.7 Time records of non-dimensional air temperature in the chambers with the inclined and horizontal tops for D_j=22.1 mm and Re_j=61 at location (R, Z) = (0.52, 0.5) for horizontal top and (0.52, 0.25) for inclined top for θ=0º for various Rayleigh numbers: (a) Ra_o=18,790, (b) Ra_o=22,550

and (c) Ra_o=26,300. ----------109

Fig. 4.8 Flow region map delineating the temporal state of the vortex flow for H=20.0 mm. ----------110

Fig. 4.9 The side view flow photos at selected time instants during flow formation at the cross plane θ =0° & 180° for Ra=0 at H=20.0 mm & D_j=10.0 mm for Re_j= (a) 136 and (b) 676. ----------111

Fig. 4.10 The side view flow photos at selected time instants during flow formation at the cross plane θ =0° & 180° for Ra=0 at H=20.0 mm & D_j=22.1 mm for Re_j= (a) 61 and (b) 306. ----------112

Fig. 4.11 Time variation of the size of the primary inertia-driven roll for various Re_j at Ra=0. ----------113

Fig. 4.12 Time variation of the location of the secondary inertia-driven roll for various Re_j at Ra=0. ----------114

NOMENCLATURE

D_j	Jet diameter at the injection pipe exit (mm)
f	Oscillation frequency of time periodic flow (Hz)
F	Non-dimensional oscillation frequency, $f/(\alpha/H^2)$
g	Gravitational acceleration (mm/s^2)
Gr	Grashof number, $g\beta\Delta TH^3/\nu^2$
Gr/Re_j^2	Critical buoyancy-to-inertia ratio for the onset of buoyancy induced roll
H	Distance between the exit of injection pipe and heated plate (mm)
Q_j	Jet flow rate (Standard Liter per Minute, slpm)
r_s	The center of the location of secondary inertia-driven roll (mm)
r, θ, z	Dimensional cylindrical coordinates
R, Θ, Z	Dimensionless cylindrical coordinates, $r/R_c, \theta, z/H$
Ra	Rayleigh number, $g\beta\Delta TH^3/\alpha\nu$
R_c	Radius of processing chamber (mm)
R_w	Radius of disk (mm)
Re_j	Jet Reynolds number, $\overline{V_j}D_j/\nu$
Re_w	Local Reynolds number in the wall-jet region, $\bar{u}H/\nu$
Re_{we}	Local Reynolds number in the wall-jet region at the edge of heated disk
Re_ω	Reynolds number of rotation, $\omega R_w^2/\nu$
S_I	Size of primary inertia-driven roll (mm)
S_O	Size of buoyancy-driven roll (mm)
T_f	Temperature of the heated disk (℃)
T_j	Temperature of jet at the injection pipe exit (℃)
t	Time (sec)

$\bar{u}$	Average velocity of the flow at wall-jet region (mm/s), $(Re_j D_j \nu)/(8rH)$
$\bar{V}_j$	Average velocity of the air jet at the injection pipe exit (mm/s)

Greek symbols

α	Thermal diffusivity (mm^2/s)
β	Thermal expansion coefficient (1/K)
ω	Rotation speed (rpm)
ΔT	Temperature difference between the heated disk and the injected air (℃)
ν	Kinematic viscosity (mm^2/s)
Φ	Non-dimensional temperature, $(T - T_j)/(\bar{T}_f - T_j)$

Superscript

—	Average

Subscripts

c	Processing chamber
e	Edge of heated disk
f	Fluid, Air
j	Jet impinging
I	Primary inertia-driven roll
O	Buoyancy-driven roll
s	Secondary inertia-driven roll
w	Wall-jet region

Chapter 1

Introduction

1.1 Motivation of the study

Over the past decades, the flow and heat transfer associated with a jet impinging onto a heated flat plate of various shapes have been the subject of many investigations because of its superior heat transfer capability. The results have been applied to improve the drying of textiles and paper, annealing of glass, cooling of gas turbine components and electronic equipments, freezing of tissue in cryosurgery, and many others. For some industrial applications, however, such as electronic cooling [1] and chemical vapor deposition [2], both high values and radial uniformity of heat and mass transfer rate are important. Besides, the flow needs to be stable and contain no vortices. The interest in the impinging gas jet confined in a chamber has accelerated recently because of the quick technological progresses in the growth of semiconductor thin crystal films on silicon wafers through rapid thermal processing (RTP) [3] and chemical vapor deposition (CVD) processes.

In order to obtain good thin film properties, the temperature uniformity of the wafer, appropriate geometry of vertical RTP and CVD chambers, suitable operating conditions and flow configuration are very important factors in designing the processors for the thin film growth [4]. Particularly, the flow recirculation in the processing chamber is detrimental to the film properties. Apparently, the structure of the vortex flow in the processing chamber is mainly affected by the jet inertia and the buoyancy force due to the heated wafer, along with the geometry of the chamber including the nozzle diameter, nozzle-to-wafer distance, wafer and chamber diameters. In the processing chambers three distinct flow regimes have been identified: (a) plug flow, where the gas flows smoothly over the substrate without any recirculation in the

chamber, (b) buoyancy-induced flow, where the buoyancy force associated with the heat substrate induces upward flow and recirculation of the gas, and (c) mixed flow, where the flow driven simultaneously by inertia and buoyancy forces. But, the details on how these parameters affect the vortex flow characteristics remain largely unexplored. In an initial attempt to examine the flow recirculation associated with the RTP processes Lin and his colleagues recently visualized the vortex flow of gas in a model vertical RTP processor [5] and found that the flow was dominated by the two axisymmetric vortex rolls. How the jet flow rate, jet-to-wafer temperature difference, and chamber pressure affected the vortex flow pattern was investigated in detail. In the present study a new experimental system with more precise flow and temperature control of the jet flow and heated wafer is established to explore the roles of the inertia and buoyancy forces in influencing various aspects of the vortex rolls. The detailed characteristics of the rolls driven simultaneously by the combined action of the inertia and buoyancy are to be delineated. In particular, the onset condition and the characteristics of the steady and time-dependent mixed convective vortex flow will be explored in detail. Besides, the detailed processes through which the vortex rolls are formed will be examined.

1.2 Literature review—heat transfer and flow characteristics of impinging Jets

Considerable amount of work from a number of research groups has been carried out in the past to study the fluid flow and heat transfer in the round or slot (two-dimensional) jet impinging onto a large horizontal plate. Most of the studies focus on quantifying the highly efficient heat transfer associated with the high speed impinging jets and the jets considered possess a much higher inertia force than the buoyancy force generated by the temperature nonuniformify in the flow. Therefore the

jet impinging flow is dominated by the jet inertia and some geometric parameters of the system. For instances, heat or mass transfer in the laminar and turbulent impinging jets was experimentally investigated by Gardon and Akfirat [6 & 7], Scholtz and Trass [8], Sparrow and Wang [9], Masliyah and Nguyen [10], and Hrycak [11]. Recently, the flow and thermal structures of the turbulent round jets were examined by Özdermir and Whitelaw [12] and Liu and Sullivan [13]. Moreover, the flow and heat transfer in the laminar impinging jets with the presence of an upper plate confinement were numerically predicted by Heiningen et al. [14], Saad et al. [15], and Law and Masliyah [16]. Besides, the results from the computation for the turbulent impinging jets were reported by Hosseinalipour and Mujumdar [17] and Morris and Garimella [18]. The corresponding heat transfer coefficient for the confined impinging jets was measured by Lin et al. [19]. A combined experimental and numerical study was recently conducted by Incropera and his colleagues [20 & 21] to explore the impinging liquid jets confined in a cylindrical container. The detailed flow characteristics in the impinging jets recently received considerable attention. The presence of a confinement plate above the target plate was noted to induce a big flow recirculation around the jet axis (Behnia et al. [22], Chua et al. [23], Voke and Gao [24]). The size and location of the recirculation center can be influenced by the jet Reynolds number and nozzle-to-plate spacing (Fitzgerald and Garimella [25], and Marple et al. [26]). The center of the flow recirculation was noted to move away from the jet axis when the nozzle-to-plate spacing was increased. This is in qualitative agreement with the experimental observation from Garimella and Rice [27]. The presence of the confinement plate is also known to restrict the jet flow entrainment from the surrounding, which reduces the jet spreading rate and leads to an increase in the potential core length (Ashforth-Frost et al. [28], and Ashforth-Frost and Jambunathan [29]). Additionally, a low pressure region is induced near the impinging

plate for single and double jets as the nozzle-to-plate spacing H/D is less than 2 (Baydar [30]). The pressure defect in the flow becomes more severe for a higher jet Reynolds number and a smaller nozzle-to-plate spacing. A round jet impinging onto a flat plate often results in double peaks in the Nusselt number distribution along the plate. The inner peak was considered to result from a local thinning of the boundary layer flow along the plate (Lee and Lee [31]) and it disappears for a large nozzle-to-plate spacing (Pamadi and Belov [32]). Lytle and Webb [33] and Li and Garimella [34] showed that the outer peak was more pronounced for a smaller nozzle-to-plate spacing and it moves radially outward for a higher jet Reynolds number. Schafer et al. [36] indicated that the outer heat transfer peak was due to the heat transfer enhancement associated with the secondary recirculation cell on the plate. Moreover, the flow in a confined jet was found to be dominated by a large recirculation vortex around the jet axis and a comparatively smaller adjacent secondary vortex right above the impinging plate (Law and Masliyah [16 & 35]). The location of the outer peak moves further away from the stagnation point at increasing jet Reynolds number but the location of the inner peak is independent of the Reynolds number (Colucci and Viskanta [37]).

The influences of the nozzle exit velocity profile on the impinging jet flow have been examined by Deshpande and Vaishnav [38]. Their results reveal that the peak values of the wall shear stress are lower for the uniform (flat) velocity profile. The results are attributed to the smaller momentum and kinetic energy for the same mass flux as compared with the parabolic velocity profile (fully developed velocity). Moreover, the potential core of the jet resulting from a fully developed velocity profile is longer than that from a flat velocity profile (Ashforth-Frost et al. [28]). Recently, Huang and El-Genk [39] examined a swirling impinging jet and found that the swirl caused the flow to spread radially outward much more rapidly than without

swirl. Besides, the swirl impinging jet induced markedly higher local and surface average Nusselt numbers and improved the radial uniformity of heat transfer on the impinged surface.

1.3 Literature Review—unsteady transitional impinging jets

More recently, the steady-to-unsteady flow transition for a confined laminar impinging jet (Re_j<1000) was numerically investigated by Chiriac and Ortega [40]. They pointed out that the critical jet Reynolds number for the onset of unsteady flow was between 585 and 610. The unsteady jet was characterized by a dominant frequency corresponding to the formation of shear layer vortices at the jet exit. More complete information on various characteristics of the impinging jets can be found from the recent critical reviews by Viskanta [41] and Jambunathan et al. [42]. It should be pointed out that in the above studies [6 - 40] the buoyancy force exhibits negligible effects on the jet flow. Recently, the importance of the buoyancy effects in a confined water impinging jet was illustrated by Ichimiya et al. [43] and a number of somewhat deformed buoyancy induced vortices were noted. Santen et al. [44, 45] indicated that the thermal instability for a confined jet impinging onto a heated circular plate did exist and the onset was affected by the Reynolds, Rayleigh and Prandtl numbers. Elison and Webb [46] found that during the transition between the laminar regime ($\mathrm{Re}_j \le 1500$) and the turbulent regime ($\mathrm{Re}_j \ge 1500$) the Nusselt number decreases for an increase in the jet Reynolds number. Some studies characterize the state of impinging jets according to jet's centerline turbulence intensities. Lin et al. [19] measured the turbulence intensities in a confined slot jet and found that for $\mathrm{Re}_j < 1226$ the turbulent intensity is less than 5% at the stagnation point. The jet flow is considered to be laminar. As the jet Reynolds number gradually

increases to 1226, the turbulence intensities at stagnation point increase sharply. Additionally, McNaughton and Sinclair [47] reported four characteristic jet regimes for circular free jets: dissipated-laminar jets for $\mathrm{Re}_j < 300$, fully laminar jets for $300 < \mathrm{Re}_j < 1000$, semi-turbulent jets for $1000 < \mathrm{Re}_j < 3000$, and fully turbulent jets for $\mathrm{Re}_j > 3000$.

1.4 Literature review—confined jet flow associated with CVD reactors and RTP processors

In the impinging jet flow encountered in the CVD and RTP processes, the gases input to the CVD reactors and RTP processors are at relatively low flowrates and the silicon wafer upon which semiconductor thin crystal films are grown and processed is at an elevated temperature. Under such circumstance the buoyancy in the flow is no longer small compared with the jet inertia. Significant flow recirculation can be induced by the buoyancy and the impinging jet flow is driven by the combined effects of inertia and buoyancy. The importance of the buoyancy on the recirculating flow in a vertical CVD reactor was demonstrated by Wahl [48]. Similar investigations have been carried out for various types of CVD reactors including the metal organic CVD [49-53] and single-wafer RTP processors [54, 55]. In these studies for the processing of the microelectronic circuits [45-55] various vortex flow patterns were reported in the jet impinging flow. Buoyancy induced symmetry breaking of the jet flow was also noted [53]. The optimal geometry of a MOCVD reactor was numerically investigated by Kusumoto et al. [56]. They found that the optimal geometry for a larger flow rate should have a smaller inlet-to-pedestal spacing and a larger inlet pipe diameter. In addition, Santen et al. [57] reported nonuniform deposition rate caused by the nonuniformity of heat transfer resulting from a larger vortex roll near the cold side

wall. Their data also shows that the rotating wafer and geometrical adjustments can be used to improve the deposition rate.

1.5 Objective of the research project

The above literature review clearly reveals that the detailed vortex flow and thermal characteristics associated with a mixed convective low speed vertical gas jet impinging onto a heated horizontal circular plate in a confined vertical chamber, which is directly related to the gas recirculation in CVD and RTP processes, are still poorly understood. In this study an experimental system is established to delineate how the inertia and buoyancy forces affect the vortex flow patterns in this confined impinging jet flow through the detailed flow visualization and transient temperature measurement. Attention is focused on the effects of the jet flow rate, the temperature difference between the heated plate and jet, disk rotation speed, and the geometry of the processing chamber, which includes diameter of the injection pipe and jet-to-disk separation distance, on the steady and time-dependent vortex flow patterns and their onset. Moreover, the formation of the inertia-driven rolls will be explored in detail.

Chapter 2

Experimental Apparatus and Procedures

In order to conduct the experiment at reasonably low cost, we use air as the working fluid to replace the inert gases normally employed in real CVD and RTP processes. In view of the similar thermodynamic and thermophysical properties for various gases, the results obtained here are still applicable to the CVD and RTP systems. The schematics of the experimental system established in the present study to investigate the mixed convective vortex flow characteristics resulting from a round air jet impinging vertically downwards onto a horizontal circular heated disk confined in a cylindrical chamber and the test section are respectively shown in Figs. 2.1 and 2.2. The system consists of four major parts – the processing chamber, temperature measurement and data acquisition unit, heating unit, and gas injection unit. The gas is first brought into the processing chamber through an injector and then injected directly onto a circular heated disk. The major parts are briefly described in the following.

2.1 Experimental apparatus

The processing chamber, which is made of 6.0-mm thick quartz glass to allow for the observation of the vortex flow in it, is cylindrical and has a diameter of 291.0 mm. The vertical distance between the jet inlet and exhaust ports of the processing chamber is 200.0 mm. The chamber can be installed with a horizontal top or an inclined top. For the horizontal top the distance between the injection pipe and the circular disk are, respectively, 10.0, 15.0, 20.0 and 30.0 mm (Fig. 2.3(a)). For the case with the tapering top the top of the processing chamber is inclined linearly downwards in the radial direction. More specifically, the top-to-disk separation

distance is reduced from 20.0 mm at the exit of the injection pipe to 10.0 mm at the chamber side (Fig. 2.3(b)). To facilitate the flow visualization, the two chamber tops are both made of acrylic plates. Air is injected vertically downwards from a long straight circular pipe into the cylindrical chamber along the axis of the chamber and impinges directly onto the heated disk. The air flows first over the heated disk, then moves through the annular section of the chamber, and finally leaves the chamber via twenty circular outlets of 12.7 mm in diameter opened at the bottom of the chamber (Fig. 2.2(a)). The chamber is sealed to prevent any gas leakage. The top, bottom and side walls of the chamber are thermally well insulated to reduce the heat loss from the processing chamber to the ambient by covering the entire chamber with a superlon insulator of 100.0-mm thick. The insulator can be opened during the flow visualization.

The heating unit is designed to maintain the circular disk at the preset uniform temperature during the experiment. It is composed of a 10.0 mm thick high purity circular copper plate of eight-inch in diameter, acting as the disk, placed on 15-mm thick stationary copper disk. The 10.0 mm thick circular disk is rotated by A.C. motor driver. The heater attached onto the back side of the stationary copper plate is divided into 3 concentric zones. The heating unit consists of a resistance heating element, a holder and an insulator. The holder which is made of stainless steel can support the resistance heating element and copper disk at the high temperature. The heater attached onto the back side of the copper plate is divided into 3 concentric zones (Fig. 2.4). Each zone is independently heated by a power supply with the D.C. current passing through the nickel coil placed on the stainless steel holder. The entire heating unit is then placed on a Teflon plate. Additionally, to reduce the heat loss from the sidewall of the copper plate and Teflon plate, the lateral surface of the entire heating unit is wrapped with a 16.0 mm thick thermal insulation layer of superlon. A proper

control of the voltage from each power supply allows us to maintain the copper plate at a nearly uniform temperature. Moreover, the copper plate temperature is measured by several corrected and calibrated T-type thermocouples at selected detection points located at 1-mm below the upper surface of the copper plate, which are fixed the detection points through the small holes drilled from the backside of the plate.

The gas injection unit consists of a 2HP air compressor, a flow meter, a smoke generator, filters, pressure regulator, connection pipes and injector. In the experiment, air is drawn from the ambient by the compressor and sent into a 300-liter and 100-psi high-pressure air tank and is filtered to remove moisture and tiny particles. The installation of the high-pressure air tank is to suppress the fluctuation of the air flow and extends the life of the compressor. Then, the air is mixed with smoke tracers in the smoke generator, and regulated by the pressure regulator and is later injected into the processing chamber through the straight circular injection pipe which is coaxial with the processing chamber. The downward vertical air jet issuing from the pipe outlet impinges directly onto the heated plate. In the present study, two injection pipes with diameters, 10.0 and 22.1 mm, are tested and the straight portions of the pipes are both 600.0 mm long. The length of the injection pipes is selected to ensure that they are long enough to allow us to have a fully developed air flow at the exits of the injection pipes. The air temperature at 600.0 mm upstream of the exits of the injection pipes is measured by a corrected and calibrated T-type thermocouple. The measured value is considered as the temperature of the air injected into the processing chamber since the whole injection pipe is thermally well insulated by a superlon insulation layer of 16.0-mm thick.

A smoke-tracer flow visualization technique is employed to observe the flow patterns resulting from the jet impinging onto the heated disk in the cylindrical chamber. The air flow pattern in the chamber is illuminated by the vertical and

horizontal plane light sheets produced by passing parallel lights from an overhead projector through two adjustable knife edges. The experimental system is located in a darkroom to improve the contrast of the flow photos. The time variations of the flow pattern during the entire transient stage from the top and side views are recorded by the Sony digital video camera DCR-PC100. The recorded images are later examined carefully in a personal computer.

2.2 Analysis of time-average and instantaneous air temperature

To understand thermal characteristics of the steady and unsteady vortex flows, the temperature of the air flow in the processing chamber is measured by inserting a thermocouple probe into the chamber through twenty-four holes of 1-mm in diameter opened at the selected locations on the top of the chamber. In the experiment, the thermocouple tip is positioned at selected vertical distances from the upper surface of the disk. More specifically, the thermocouple probe is an OMEGA (model HYPO) mini hypodermic extremely small T-type thermocouple implanted in a 1 inch long stainless steel hypodermic needle.

2.3 Experimental procedures

For each case the experiment starts with the air at the room temperature T_a compressed first into the high pressure tank and the smoke generator through the connection pipe, and then injected into the processing chamber. The air moves over the disk and finally leaves the chamber through the twenty circular outlets at the bottom of the chamber. In the meantime the temperature of disk and the air flow rate are controlled at the preset levels. As the air flow in the processing chamber reaches steady or statistically stable state, we begin to visualize and record the vortex flow pattern in the chamber.

2.4 Uncertainty analysis

Uncertainties in the Rayleigh number, Reynolds number and other independent parameters are calculated according to the standard procedures established by Kline and McClintock [58]. The uncertainties of the thermophysical properties of the air are included in the uncertainty analysis. The properties of the working fluid (air) are α=0.22(cm^2/s), β=0.0034 (1/k), ν=0.16 (cm^2/s) and Pr=0.72 at 30℃ and 1.0 bar. In addition, the uncertainties of the control unsteadiness and temperature nonuniformity of the heated disk are accounted for in the evaluation of the data uncertainty. The uncertainties of the temperature, volume flowrate, dimensions, Reynolds number and Rayleigh number measurements from this analysis are summarized in Table 2.1.

2.5 Verification of the experiment

To validate our experimental setup, the flow observed in the processing chamber for the limiting case when the disk is unheated (Ra=0) is compared with the numerical results from Law and Masliyah [16] for the impinging jet flow with the top plate confinement but without the sidewall confinement. The comparison is illustrated in Fig. 2.5 by showing the steady side view flow photo for an axisymmetric flow with the jet Reynolds number around 400 at D_j=10.0 mm and H/D_j=2. Note that in the region surrounding the jet axis the resulting vortex flow from our flow visualization is qualitatively the same as their numerical prediction. In the side wall region we have another circular vortex roll which results from the deflection of the boundary layer flow along the disk by the chamber side. But this is not seen in their prediction obviously due to the absence of a sidewall in their study. Thus, the experimental system established here is considered to be suitable for the present study.

Table 2.1 Summary of the uncertainty analysis

Parameter and Estimate Uncertainty	
Parameters	Uncertainty
D_j, D_w, H (m)	± 0.00005 m
T (℃)	± 0.2℃
ΔT (℃)	0.3℃
Q_j (slpm)	± 2%
μ (Nm/s^2) ρ (kg/m^3) υ (m^2/s)	± 0.05% ± 0.05% ± 0.07%
Ra	8.6%
Re_j	2.3%

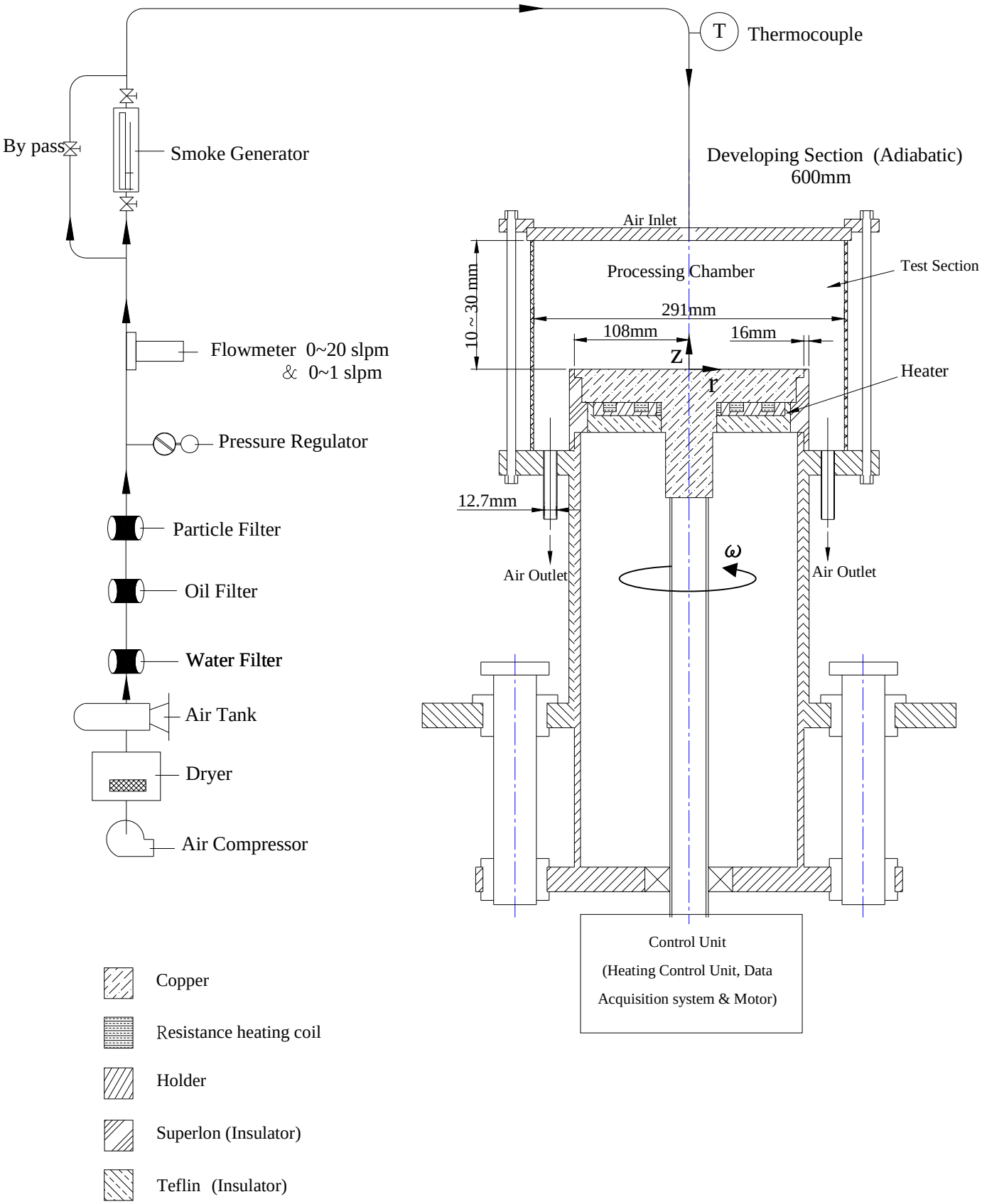

Fig. 2.1 Schematic diagram of the experimental system.

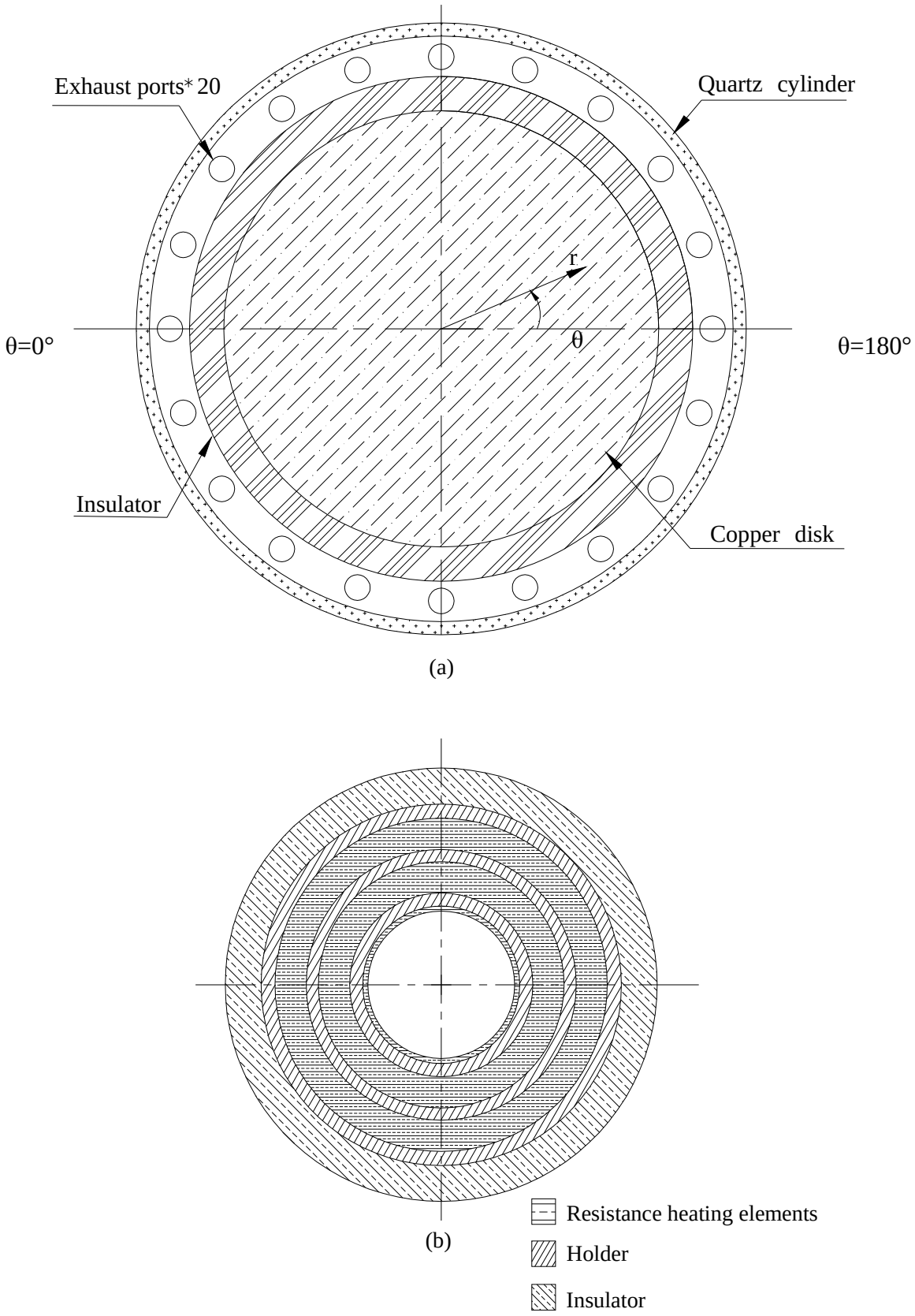

Fig. 2.2 Schematic of the test section from the top view (a) and 3-zone concentric heater (b).

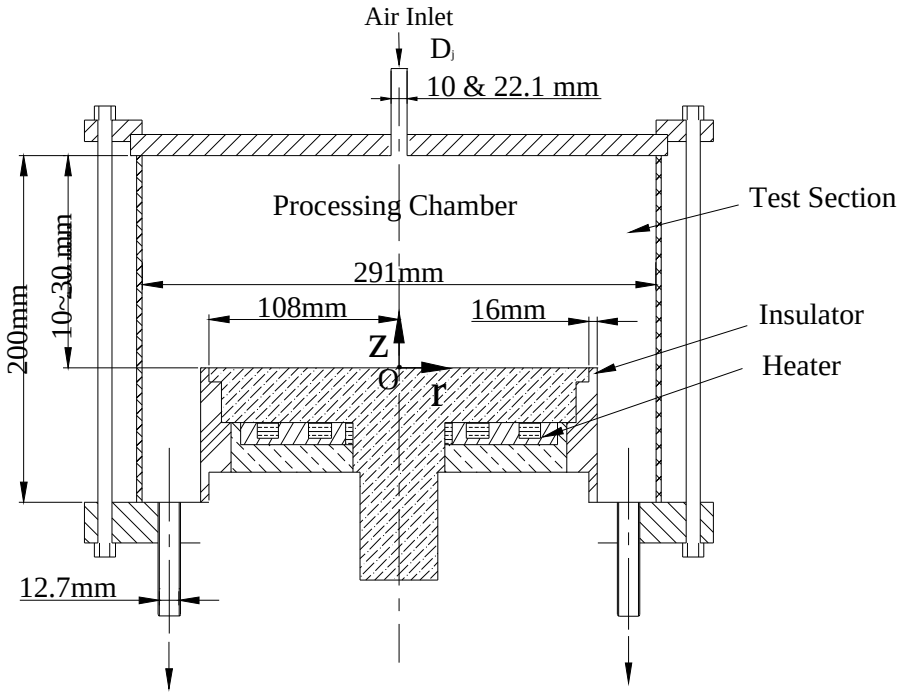

(a)

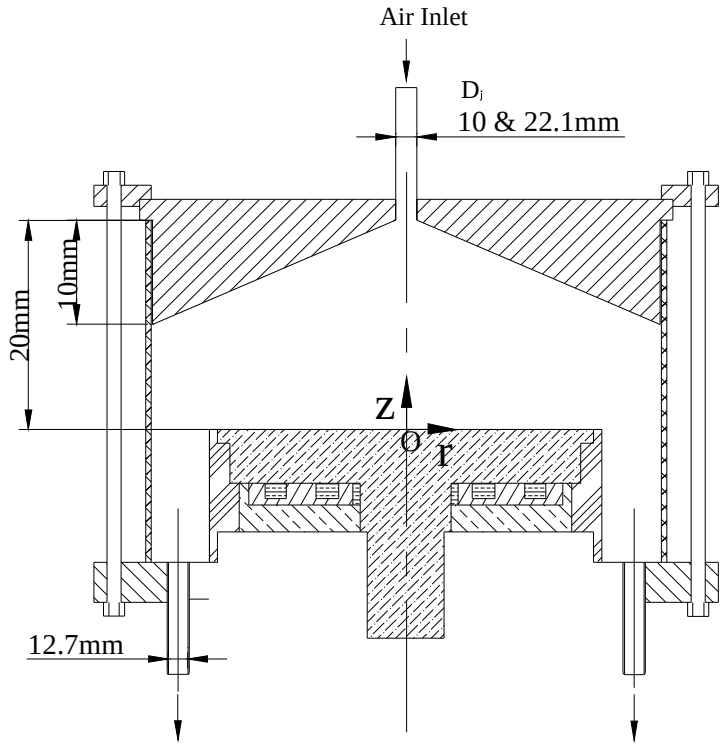

(b)

Fig. 2.3 Schematic diagram of the test section with (a) horizontal and (b) inclined chamber tops. For clear illustration the diagrams are not plotted in proportion to the actual geometrical dimensions.

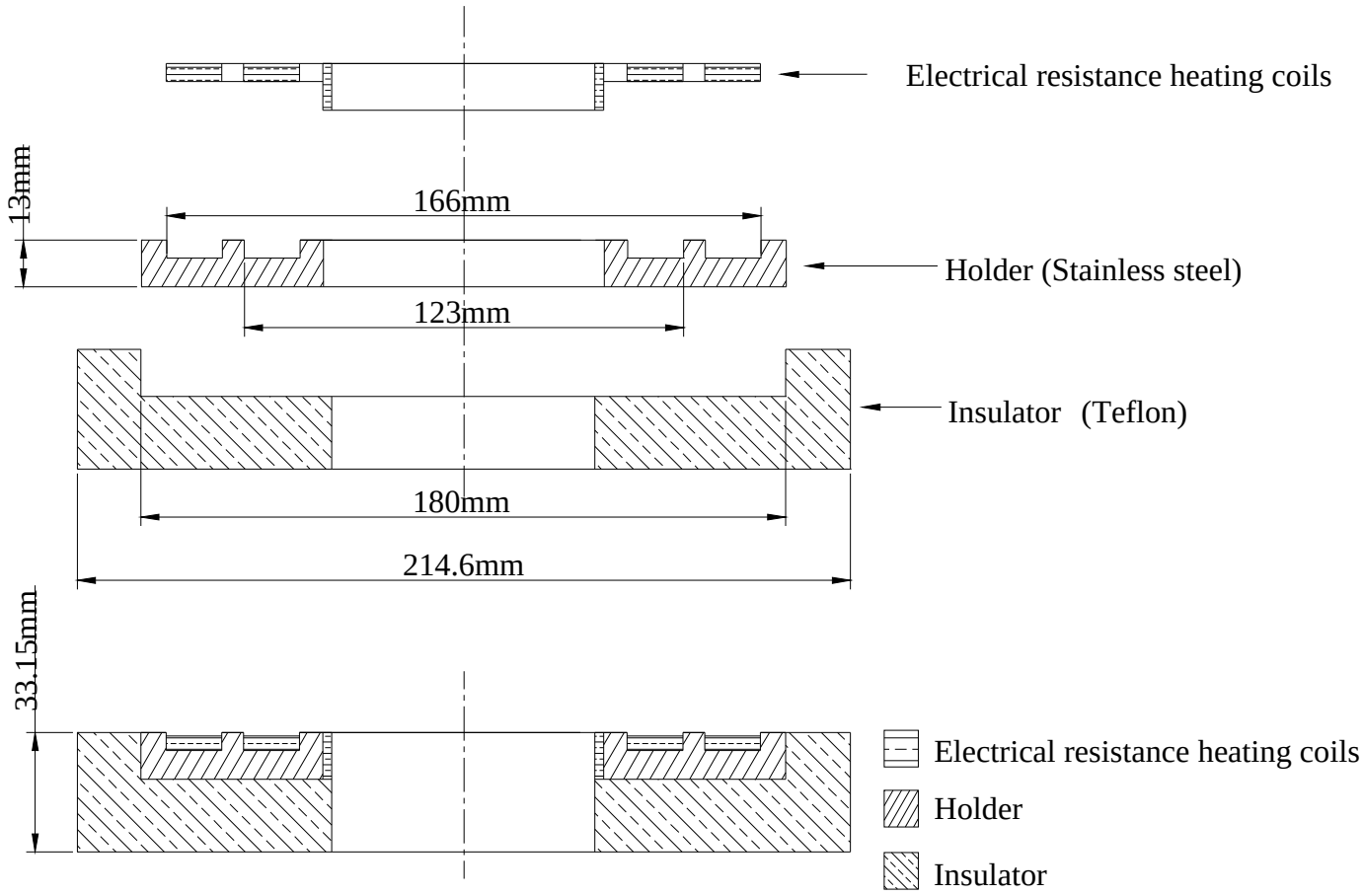

Fig. 2.4 The heater consists of three parts: resistance heating element, holder and insulator.

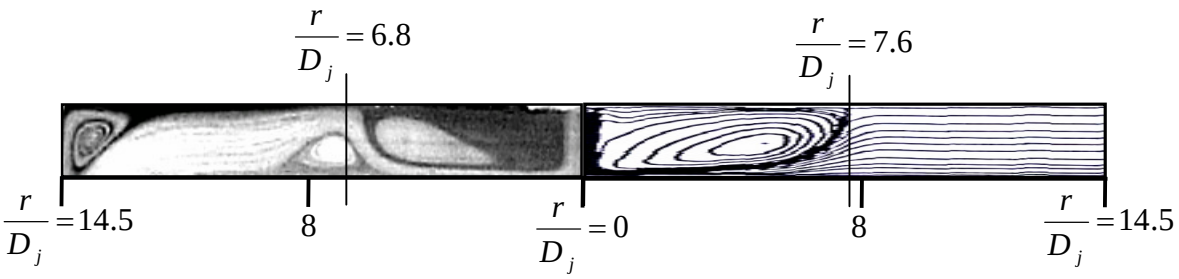

Fig. 2.5 The flow field for H/D_j=2 and Ra=0, left: the result from the present study at Re_j=406 for D_j=10.0 mm; right: contours of stream function from Law and Masliyah (1984) at Re_j=400.

Chapter 3

Characteristics of Vortex Flow at Long Time

As mentioned in Chapter 1, the flow characteristics associated with the air jet impinging onto the heated disk confined in the cylindrical space under investigation are affected by the jet inertia, buoyancy force due to the heated disk, and the geometry of the chamber including the injection pipe diameter and jet-to-disk separation distance. The present study intends to explore the effects of these parameters on the flow and thermal characteristics in the processing chamber. More specifically, in the present experiment the air flow rate Q_j is varied from 0.2 to 9.3 slpm (standard liter per minute) and the temperature difference between the heated plate and injected air ΔT is varied from 0 to 25.0℃ for two injection pipes with D_j=10.0 and 22.1 mm. Four jet-to-disk separation distances are considered with H=10.0, 15.0, 20.0, and 30.0 mm. The dimensionless groups governing the flow are the jet Reynolds number and the Rayleigh number. They are respectively defined as

$$Re_j = \overline{V}_j D_j / \nu = 4Q_j / \pi \nu D_j \qquad (3.1)$$

and

$$Ra = g\beta \Delta T H^3 / \alpha \nu \qquad (3.2)$$

In addition, the local Reynolds number and average radial velocity of the flow in the wall-jet region are respectively defined as

$$Re_w = \bar{u}H/\nu \qquad (3.3)$$

and

$$\bar{u} = Q_j / 2\pi rH = Re_j D_j \nu / (8rH) \qquad (3.4)$$

Hence Re_w can be rewritten as

$$Re_w = Re_j \cdot D_j / 8r \qquad (3.5)$$

Thus, in this part of the study the jet Reynolds number ranges from 12 to 1,258 and the Rayleigh number from 0 to 63,420. At this low Reynolds number the impinging

jet when unheated is laminar and steady, according to Chiriac and Ortega [40]. Only in examining the critical condition for the appearance of the inertia-driven and buoyancy-driven rolls, however, the maximum jet Reynolds number is increased to 1,258 (Q_j=9.3 slpm). The ranges of the parameters chosen above are in accordance with the values of the governing dimensionless groups for the flow often encountered in the CVD processes [4]. In what follows selected flow photos from the top and side views taken at steady or statistically stable state in the present study are examined closely to unravel how the jet Reynolds number, Rayleigh number, jet-to-disk separation distance and injection pipe diameter affect the recirculating gas flow patterns resulting from the impinging air jet in the processing chamber.

3.1 Typical steady vortex flow pattern

At first, the typical vortex flow pattern observed in the processing chamber with the jet issued from the small injection pipe (D_j=10.0 mm) at long time when the flow already reaches steady state for the case with a low buoyancy-to-inertia ratio Gr/Re_j^2 is illustrated in Fig. 3.1. Here Gr is the Grashof number and Gr=Ra/Pr. In the figure the steady flow photos from the top and side views taken respectively at the selected horizontal and vertical planes along with the schematic sketch of the flow based on the detailed flow visualization for a typical case with Q_j=3.0 slpm, ΔT=10.0℃ and H=15.0 mm (Re_j=406, Ra=3,170 and Gr/Re_j^2=0.019) are shown. Since the flow is axisymmetric at this low Gr/Re_j^2, only a half of the top view flow photo and the side view flow photo at the vertical plane $\theta=0^\circ$ & $\theta=180^\circ$ are given here. Examining the top and side view photos together reveals that the steady vortex flow consists of three circular vortex rolls in the processing chamber. The first (inner) circular roll directly surrounds the downward air jet and is much larger than the second vortex roll induced

in the middle zone of the chamber. The third (outer) roll is also large in size and dominates in the outer zone of the chamber. A close inspection of the successive top and side view flow photos in the video tapes taken during the transient stage of the flow formation indicates that immediately after the impinging, the jet is deflected by the circular disk to move obliquely upwards (Fig. 3.1(c)). Then the oblique flow is divided into two streams as it encounters the chamber top. One stream moves radially inwards towards the low pressure region created by the jet injection forming the inner toroidal vortex, which is considered as the primary inertia-driven vortex roll. This inner roll is also entrained by the jet and is normally stronger and larger at a higher jet Reynolds number. Another stream moves radially outwards, later turns to move downwards along the sidewall of chamber, and finally leaves the chamber through the outlets in the chamber bottom. Besides, the smaller second circular roll is found to be induced through the viscous shearing effects produced by the stronger and larger inner vortex roll, which is termed as the secondary inertia-driven roll. Moreover, the local maximum pressure occurs at the stagnation point and sharply decreases to minimum value after stagnation point. The local pressure after minimum value gradually increases since the available flow area increases as the air flows past the center of the primary inertia-driven roll. In the pressure recovering region, the positive pressure gradient enhances the occurrences of the flow separation. It should be mentioned that this secondary roll is induced only when the jet Reynolds number exceeds certain level around 180 for the small injection pipe (D_j=10.0 mm) when the disk is unheated with Ra=0. Moreover, the outer roll near the cold chamber side is driven by the buoyancy force associated with the heated disk and is regarded as the buoyancy-driven roll. For the large injection pipe (D_j=22.1 mm) at the same gas flow rate the secondary inertia-driven roll is weaker and smaller since the jet Reynolds number is much lower (Equ. (3.1)). In addition, for a further increase in the jet

Reynolds number a small circular roll appears near the top wall around the impinging jet at D_j=10.0 mm and it is considered as the tertiary inertia-driven roll. At this high Re_j for the small injection pipe the primary roll is strong enough to induce a tertiary roll through the viscous shearing of the stagnant flow around the primary roll. For D_j=22.1 mm the range of the jet Reynolds number covered in the present study is not high enough to induce a tertiary roll. The inertia-driven steady tertiary flow is illustrated in Fig. 3.2 by showing the steady side view flow photos taken at the cross plane θ=0? for slightly supercritical jet Reynolds numbers at various jet-to-disk separation distances for D_j=10.0 mm. Since the steady flow is still axisymmetric, only the results in the half plane are shown. The results in Fig. 3.2 manifest that the tertiary roll is small and appears in the region near the chamber top adjacent to the primary inertia-driven roll. The primary, secondary and tertiary inertia-driven rolls are smaller at the smaller jet-to-disk separation distance. This simply reflects the fact that at a smaller H the available space in the processing chamber for the rolls to develop is less. Note that at H=10.0 mm the tertiary roll is rather small. Besides, the tertiary roll grows slightly in size and in vortex intensity with the jet Reynolds number. At the larger jet-to-disk separation distance for H=20.0 mm the growth of the tertiary roll with Re_j is slightly larger, as evident from the results in Fig. 3.2(a). Moreover, the tertiary roll becomes smaller and weaker for an increase in Ra.

3.2 Onset of inertia- and buoyancy-driven vortex flow

The understanding of the critical condition for the appearance of the inertia- and buoyancy-driven vortex rolls in the chamber is of fundamental interest in the fluid flow study. Here we investigate the onset of the inertia-driven rolls by visualizating the flow in the processing chamber at various jet Reynolds numbers for an unheated disk (Ra=0). Note that the lowest jet flow rate which can be accurately resolved in the

present experimental apparatus is 0.1 slpm. Even at this small Q_j the primary inertia-driven roll is already seen in the chamber for all H with the jet issued from the small injection pipe (D_j=10.0 mm). For the large injection pipe (D_j=22.1 mm) the critical Re_j for the onset of the primary inertia-driven roll is somewhat higher and thus can be located here. The present data are summarized in Table 3.1 for the onset of the primary and secondary inertia-driven rolls at various jet-to-disk separation distances. The results suggest that as the jet Reynolds number exceeds certain low level the primary inertia-driven roll appears. The secondary inertia-driven roll is initiated at somewhat higher jet Reynolds numbers (Table 3.1). Some inertia-driven rolls at slightly supercritical Re_j are shown in Fig. 3.3 for the jet-to-disk separation distance fixed at 20.0 mm. The results manifest that the primary inertia-driven roll is much smaller and weaker for the large injection pipe (Figs. 3.3 (c) & (d)). More specifically, for D_j=10.0 and 22.1 mm the primary inertia-driven roll respectively appears at Re_j=13.6 and 15. Note that at the low Re_j near the critical level the roll is relatively small and appears near the exit of the injection pipe (Figs. 3.3 (a) & (d)). It should be mentioned that for an unheated disk an outer roll also appears in the duct (Figs. 3.3 (a) & (b)). This roll is formed by the deflection of the wall-jet flow along the disk by the chamber side. At a higher Re_j this outer roll is smaller and weaker (Fig. 3.3(b)) due to the radial thickening of the boundary layer flow along the disk and the deflection of the flow at the chamber side is milder. It has nothing to do with buoyancy effect since Ra=0. Besides, the onset conditions of the tertiary inertia-driven roll are also given in the table. It is of interest to note that at a smaller jet-to-disk separation distance the primary inertia-driven roll is induced at a slightly higher jet Reynolds number, as evident from comparing the results in Figs. 3.4 and 3.5.

The results summarized in Table 3.1 indicate that at given D_j the critical jet Reynolds numbers for the onset of the primary, secondary and tertiary inertia-driven

rolls increase when the jet-to-disk separation distance is reduced from 20.0 mm to 10.0 mm. However, it is of interest to note that the critical Re_j does not experience any change when H is reduced from 30.0 to 20.0 mm for the primary and tertiary rolls. The increase of the critical Re_j at decreasing H is conjectured to mainly result from the more significant retarding of the jet by the disk at a smaller H, which in turn yields a higher viscous damping effect on the impinging jet and a higher Re_j is needed to induce the flow recirculations.

As we continue to increase the jet Reynolds number slightly beyond the critical Re_j for the onset of the tertiary roll, the flow in the processing chamber does not reach any steady state at long time. Instead, the flow becomes time dependent and experiences a transition from steady to unsteady states. Obviously, this transition is driven by the jet inertia since $\Delta T=0$ and no buoyancy-driven rolls appear. The present data for the inertia driven steady-to-unsteady transition are summarized in Table 3.2 for D_j=10.0 mm. The results indicate that the critical Re_j for this flow transition increases when the jet-to-disk separation distance is shortened, similar to those for the onset of the inertia-driven rolls. It is of interest to note that the critical Re_j for this steady-unsteady transition increases with Ra at given H. The above results suggest that the time-dependent flow induced by the jet inertia can be stabilized by increasing the Rayleigh number Ra at $H \leqq 20.0$ mm. However, for H=30.0 mm an opposite trend is noted. This is due to the fact that at the longest H (=30.0 mm) tested here the radial extent of the buoyancy-driven roll is so large and it directly contacts with the primary inertia-driven roll. As Re_j gradually increases, both the primary inertia-driven and buoyancy-driven rolls squeeze each other resulting in time-dependent flow.

When the disk is heated, our flow visualization further shows that for given D_j, ΔT and H the buoyancy-driven roll begins to appear in the region near the heated disk edge as Re_j is below certain critical level for a given Ra. This critical condition is

considered to be reached as long as we can barely see the buoyancy-driven roll in the video films recording the images of the vortex rolls. This is exemplified in Fig. 3.6. Moreover, Table 3.3 summarizes the critical condition for the onset of the buoyancy-driven roll based on the present data. The data indicate that for given D_j and H the critical Re_j for the onset of the buoyancy driven roll is higher for a higher Gr. It should be mentioned that how the onset condition of the buoyancy roll is affected by the jet-to-disk separation distance is reflected in the Grashof number since Gr is proportional to H^3. Note that the critical buoyancy-to-inertia ratio Gr/Re_j^2 for the onset of the buoyancy roll is nearly constant for a given D_j, irrespective of the jet-to-disk separation distance. For D_j=10.0 and 22.1 mm the critical ratio Gr/Re_j^2 is nearly equal to 0.0045 and 0.021, respectively. It is also noted that the onset of the buoyancy-driven roll occurs when the wall-jet flow in the radial direction is reversed by the upward buoyancy associated with the heated disk and hence the onset should be mainly determined by the local flow condition characterized by the local Reynolds number of the wall-jet flow Re_w and the Grashof number Gr. Besides, the onset is most likely to take place near the outer edge of the disk. Therefore, the onset condition is expected to depend primarily on the local buoyancy-to-inertia ratio Gr/Re_w^2. The data given in Table 3.3 do show that the buoyancy roll begins to appear when the local buoyancy-to-inertia ratio at the edge of the disk Gr/Re_{we}^2 is around 33.0 with the deviations within the experimental uncertainty for all D_j and H considered.

3.3 Effects of jet Reynolds number

How the Reynolds number of the impinging jet affects the gas flow pattern at long time in the processing chamber is demonstrated in Figs. 3.7-3.12 by presenting the steady side view flow photos for the cross plane $\theta=0^\circ$ & 180° for selected Ra at

various jet Reynolds numbers for two injection pipes with the jet-to-disk separation distance H=20.0 mm. As the disk is unheated, apparently the primary and secondary inertia-driven rolls are dominated by the jet flowrate for a fixed H (Fig. 3.7). The secondary inertia-driven roll first appears in the processing chamber when Re_j approximately exceeds 180 for D_j=10.0 mm and 220 for D_j=22.1 mm. The inertia-driven rolls grow in size and intensity and its center moves radially outward at increasing Re_j. It should be mentioned that for an unheated disk an outer roll also appears in the chamber, as mentioned earlier (Fig. 3.7). This roll results from the deflection of the wall-jet flow along the disk by the chamber side. At a higher Re_j this outer roll is smaller due to the radial thickening of the boundary layer flow along the disk and the deflection of the flow at the chamber side is milder. It is nothing to do with the buoyancy effect since Ra=0. When the disk is heated with ΔT=5.0℃ (Ra=3,760), the results in Fig. 3.8(a) for the small injection pipe indicate that at this low buoyancy the gas flow in the chamber is still dominated by the three circular vortex rolls as the typical flow pattern shown in Fig. 3.1. We further note from Fig. 3.8(a) that at increasing Reynolds number the primary and secondary inertia-driven rolls grow in size and intensity with the accompanying decay of the buoyancy-driven roll. Similar trend is noted in Figs. 3.9-3.12 for the high buoyancies. In general, the stronger forced flow for a higher Re_j suppresses the buoyancy effects. Besides, the results clearly show that at higher Re_j($\geqq$406) the secondary inertia-driven roll can be large enough to merge with the buoyancy-driven roll for the small injection pipe (Figs. 3.9(a)-3.12(a)). The gas flow in the chamber then is dominated by two large circular vortex rolls. Additionally, it is important to note from the results in Figs. 3.7(b) and 3.8(b) that for the large injection pipe even at $Re_j \geqq 245$ the secondary inertia-driven roll disappears as Ra increases from 0 to 3,760 and higher, so we only have two circular vortex rolls in the chamber. Besides, the primary inertia-driven roll for the

large injection pipe is much weaker than that for the small injection pipe. It is also interesting to note that at the higher Ra the size of the primary inertia-driven roll changes insignificantly with the jet Reynolds number (Figs. 3.10-3.12).

It is of interest to investigate the effects of the jet Reynolds number on the vortex flow patterns in the processing chamber for a shorter jet-to-disk separation distance. This is shown in Figs. 3.13-3.17 for H=15.0 mm. These results, qualitatively similar to those for the larger H given in Figs. 3.7-3.12, indicate that for H=15.0 mm we still have three circular rolls in the chamber for the higher Re_j. The inertia-driven rolls also increase in size and intensity at increasing Re_j except at high Ra (Fig. 3.17). The secondary inertia-driven roll is seen in the processing chamber at $Re_j \geqq 270$ for D_j=10.0 mm and at $Re_j \geqq 306$ for D_j=22.1 mm (Fig. 3.13) when the disk is unheated. A close inspection of the results in Figs. 3.7-3.17 does reveal some differences in the vortex flow patterns for the change in the jet-to-disk separation distances. Besides, the inertia and buoyancy-driven rolls are much smaller for the smaller H and the merging of the secondary inertia-driven roll and buoyancy-driven roll does not occur even at the highest Ra considered here. The corresponding top view flow photos for several selected cases shown in Figs. 3.18-3.21 for H=15.0 mm clearly demonstrate the circular nature of the vortex rolls for the lower Ra.

For completeness, the long time vortex flow patterns in the processing chamber are presented in Figs. 3.22-3.30 for various Re_j for the smallest jet-to-disk separation distance considered here with H=10.0 mm. Similar trends are again noted. But at this smallest H no secondary inertia-driven roll is induced even for Re_j=306 for the large injection pipe. It is important to note that at this H (=10.0 mm) the buoyancy-driven vortex flow is somewhat different especially at low Re_j. More specifically, at the high buoyancy-to-inertia ratio for the small Re_j the steady buoyancy-driven vortex flow consists of two small circular rolls (Figs. 3.24-3.27).

3.4 Effects of Rayliegh number

The effects of the Rayleigh number on the recirculating flow patterns in the chamber are illustrated in Figs. 3.31 & 3.32 by showing the steady side view flow photos for various Ra at given Q_j for the fixed jet-to-disk separation distance H=20.0 mm. Some selected side view and top view photos are displayed together in Figs. 3.33 and 3.34. We first note from the results for the unheated disk (Ra=0) that the outer roll due to the flow deflection at the chamber side is rather small and weak for the large injection pipe (Figs. 3.31(b) & 3.32(b)). As the disk becomes heated, the buoyancy-driven roll grows significantly in size and intensity with the Rayleigh number. Note that in the chamber installed with the small injection pipe the buoyancy-driven roll at certain high Ra can be large enough to merge with the secondary inertia-driven roll (Figs. 3.31(a) and 3.32(a) at Ra=15,030). Thus, at certain high Ra ($\geqq$15,030) there are only two steady circular rolls in the chamber. The situation is somewhat different for the large injection pipe due to the absence of the secondary inertia-driven roll (Figs. 3.31(b) and 3.32(b)). More specifically, the radial size growth of the buoyancy-driven roll with Ra is milder for the large injection pipe. Additionally, for the both injection pipes significant size growth of the primary inertia-driven roll with Ra occurs except for H=10.0 mm.

For the smaller jet-to-disk separation distance of 10.0 mm and 15.0 mm, the effects of the Rayleigh number on the vortex flow in the chamber are similar to those for H=20.0 mm, as evident from the results in Figs. 3.35-3.42. Note that the Rayleigh number is proportional to H^3 according to Equation (3.2) and hence the buoyancy effects are much weaker for the smaller H for the range of ΔT examined here. The buoyancy-driven roll is smaller and it does not have a chance to merge with the secondary inertia-driven roll.

3.5 Effects of processing chamber geometry

In addition to the physical parameters—Reynolds and Rayleigh numbers, the geometry of the processing chamber including the injection pipe diameter and jet-to-disk separation distance is also expected to significantly affect the vortex flow in the processing chamber. This is the direct consequence of the simple fact that at given Q_j and ΔT the jet Reynolds number Re_j is inversely proportional to the injection pipe diameter D_j and the Rayleigh number Ra is proportional to the third power of the jet-to-disk separation distance H (Equs. (3.1) & (3.2)). In view of the dependence of Re_j and Ra on D_j and H, we examine the effects of the chamber geometry on the flow by comparing the results for different D_j and H at the same jet flowrate Q_j and disk-to-jet temperature difference ΔT.

First, the effects of the injection pipe diameter on the vortex flow pattern are illustrated in Figs. 3.43-3.47 by showing the steady side view flow photos at the same Q_j and ΔT for different jet-to-disk separation distances. The results in Fig. 3.43 indicate that the outer roll near the chamber side is larger for the small injection pipe with the disk unheated. The size of the corner roll increases slightly with the jet Reynolds number for both injection pipes. Besides, for the jet issuing from the large injection pipe the secondary inertia-driven roll appears at lower Re_j and it is weaker and smaller at the same Q_j than that for D_j=10.0 mm. As the disk is heated, the buoyancy-driven roll is substantially larger for the small injection pipe at certain high Q_j since it merges with the larger secondary inertia-driven roll (Figs. 3.44(b) and (d)). However, the radial extent of the primary inertia-driven roll is somewhat larger for the large injection pipe as the disk heated. At certain small jet-to-disk separation distance the size of the primary inertia-driven and the buoyancy-driven roll is less affected by the injection pipe diameter (Figs. 3.45-3.47).

The effects of the jet-to-disk separation distance on the flow pattern are shown

in Figs. 3.48-3.51 for both injection pipes at given temperature differences. We first note from Figs. 3.48 and 3.50 that the centers of the inertia-driven rolls in the chamber significantly move radially outward owing to the increase of the jet-to-disk separation distance from 10.0 to 30.0 mm for the unheated disk (Ra=0). Moreover, the size of the corner roll in the outer region of the chamber increases substantially with the jet-to-disk separation distance for D_j=10.0 mm (Fig. 3.48). Nevertheless, for the large injection pipe (D_j=22.1 mm) the corner roll is small and is insignificantly affected by the jet-to-disk separation distance (Fig. 3.50). As the disk is heated, the results in Figs. 3.49 and 3.51 clearly indicate that the buoyancy-driven roll which dominates in outer region of the processing chamber is much bigger for a larger H. This large increase in the size of the buoyancy-driven roll with the jet-to-disk separation distance is due to the large increase in Ra associated with a small increase in H since Ra is proportional to H^3. Moreover, the size of the inertia- and buoyancy-driven rolls for both injection pipes increases with the jet-to-disk separation distance. However, the results in Fig. 3.49(b) show that the radial extent of the buoyancy-driven roll for H=30.0 mm is not larger than that for H=20.0 mm because the secondary inertia-driven roll merging with the buoyancy-driven roll at a higher Re_j for the small injection pipe and for H=20.0 mm. It is of interest to note that at the longest H (=30.0 mm) tested here the radial extent of the primary inertia-driven roll is so large and it directly contacts with the buoyancy-driven roll as the disk heated. Thus, no space is available for the secondary inertia-driven roll to emerge. Only two circular vortex rolls appear in the chamber for H=30.0 mm.

3.6 Size and Location of the Vortex Rolls

To quantify the effects of the governing parameters on the vortex flow characteristics, the data for the maximum radial extent of the inner roll S_I, the

maximum height of the outer roll S_O, and the radial location of the center of the secondary roll r_s are measured from the steady side view flow photos for various cases tested in the present study. The results from this measurement are shown in Figs. 3.52-3.53, which indicate that S_I increases almost linearly with the jet Reynolds number for a given Ra. The increase is more significant for smaller H and Ra. A close inspection of the data reveals that at the small H of 10.0 mm the increase of S_I with Re_j is substantially larger. However, S_O decreases due to an increase in Re_j. We also note that the increase in the size of the inner and outer rolls with the Rayleigh number can be substantial at low Ra. To facilitate the flow design in the practical application, empirical equations are proposed to correlate the above data. They can be expressed as

(a) size of the primary inertia-driven roll

$$\frac{S_I}{H} = 1.852 + 7.287\times10^{-5}\,Ra + 0.00229\,Re_j \qquad (3.6)$$

for 0≤ Ra≤ 18,790, 61≤ Re_j≤ 6 76, 10.0 mm≤ D_j≤ 22.1 mm and 10.0 mm≤ H≤ 20.0 mm,

(b) size of the buoyancy-driven roll

$$\frac{S_O}{H} = 0.0433 + 0.00444Ra^{0.5} + 3.45\,Re_j^{-0.5} \qquad (3.7)$$

for 470≤ Ra≤ 18,790, 61≤ Re_j≤ 676, 10.0 mm≤ D_j≤ 22.1 mm and 10.0 mm≤ H≤ 20.0 mm,

(c) location of the secondary inertia-driven roll for D_j =10.0 mm

$$\frac{r_s}{D_j} = 3.283 + 0.000205Ra + 0.00316\,Re_j \qquad (3.8)$$

for 0≤ Ra≤ 7,930, 270≤ Re_j≤ 676 and 10.0 mm≤ H≤ 20.0 mm.

When compared with the present data, the standard deviations of Equs. (3.6)-(3.8) are respectively 12%, 13% and 12%.

3.7 Steady temperature distribution in vortex flow

In addition to the vortex flow characteristics presented above, selected results from the measured steady air temperature distributions in the vortex flow are shown in Figs. 3.54-3.57 along the horizontal line at the middle horizontal plane between the disk and chamber top Z=0.5 at θ=0°. The non-dimensional air temperature Φ is defined as $(T-T_j)/(T_f-T_j)$. Note that in the region dominated by the primary inertia-driven roll the air temperature increases with the radial distance measured from the jet axis. The air temperature reaches a maximum in the region when the wall-jet separates from the disk surface and moves obliquely upwards. Beyond that the air temperature starts to decline. Near the chamber side the temperature decline is relatively sharp due to the presence of the buoyancy-driven roll. Moreover, a sharper temperature decline at a lower Re_j for a given ΔT results from the stronger buoyancy roll. We also note that for a smaller jet-to-disk separation distance the air temperature in the middle horizontal plane is slightly lower. This is considered to result from the higher mean radial flow speed in the wall-jet region in the chamber with a smaller H for a given Q_j. Thus the above nonmonotonic radial air temperature distributions for a given H result directly from the presence of the counter-rotating primary inertia-driven and buoyancy-driven vortex rolls in the chamber and the deflection of the impinging jet flow by these rolls. A close examination of these data further reveals that at increasing jet Reynolds number the temperature peak moves away from the jet axis and the temperature decay in the region near the chamber side is smaller, reflecting from the fact that we have a larger primary inertia-driven roll and a weaker buoyancy-driven roll for a higher Re_j.

3.8 Effects of the disk rotation

How the rotation of the circular disk affects the flow pattern in the processing

chamber is illustrated in Figs. 3.58 and 3.59 by presenting the steady side flow photos for the cross plane $\theta=0^\circ$ & 180° for various Reynolds numbers for given Ra at the smaller injection pipe with the jet-to-disk separation distance H=20.0 mm. When the circular disk rotates, we begin to record the flow pattern with DV camera when the flow reaches steady state. As the disk is unheated, the flow pattern is dominated by inertia-driven roll (Fig. 3.58 (a)) at various Reynolds numbers with $\omega=0$ rpm. At the same time the corner roll near the circular disk edge appears in the processing chamber. After the air impinging the circular disk, it is pumped outward by the rotating disk and encountered the chamber sidewall to form a long recirculation cell. The results in Fig. 3.58 (b) show that the size of the inertia-driven roll is bigger due to the inertia force combined with the centrifugal force as the disk is rotated at ω=30.0 rpm. Additionally, the corner and the secondary inertia-driven rolls disappear at various Reynolds numbers with the rotation Reynolds number of 2,335.

Figure 3.59 (a) shows that the buoyancy-driven roll appears above the disk edge near the processing chamber sidewall. For $\omega=0$ rpm the buoyancy-driven roll is larger at increasing Re_j owing to the secondary inertia-driven roll merging with the buoyancy-driven roll. The results in Fig.3.59 (b) indicate that the buoyancy-driven roll is weaker and smaller with rising Re_j at Re_ω=2,335. This is due to the wall-jet Reynolds number increased by the rotational circular disk at a given Re_j. Meanwhile, the secondary inertia-driven roll disappears as the circular disk rotates. For higher Re_j larger than 406 the buoyancy-driven roll disappears at Re_ω=2,335 in the processing chamber due to action of the stronger centrifugal force combined with the inertia force. At higher Re_j the rotating disk can suppress the buoyancy-driven roll induced by natural convection. Specifically, for Ra=0 and 15,030 the processing chamber has nearly the same type of flow pattern at Re_ω=2,335 and Re_j>406 (Figs. 3.58(b) and 3.59(b)).

Table 3.1 Critical condition for appearance of the inertia-driven vortex roll ($\Delta T=0^{\circ}C$).

Vortex Roll	Separation distance (H, mm)	Jet diameter (D_j, mm)	Flowrate (Q_j, SLPM)	Re_j
Primary inertia-driven roll	30.0	22.1	0.25	15
	20.0	22.1	0.25	15
	15.0	22.1	0.3	18
	10.0	22.1	0.7	43
Secondary inertia-driven roll	30.0	10.0	0.8	108
		22.1	3.3	202
	20.0	10.0	1.3	180
		22.1	3.6	220
	15.0	10.0	1.7	230
		22.1	4.9	300
	10.0	10.0	1.8	245
		22.1	7.0	430
Tertiary inertia-driven roll	30.0	10.0	5.0	676
	20.0	10.0	5.0	676
	15.0	10.0	5.5	744
	10.0	10.0	7.0	947

Table 3.2 Critical condition for onset of time-dependent flow for D_j=10.0 mm.

H (mm)	ΔT (℃)	Gr	Q_j (slpm)	Re_j
10.0	0	0	7.7	1041
	5.0	652	8.6	1163
	10.0	1,304	8.6	1,163
	15.0	1,957	8.7	1,177
	20.0	2,609	9.0	1,217
	25.0	3,262	9.3	1,258
15.0	0	0	6.2	839
	5.0	2,202	6.5	879
	10.0	4,404	6.7	906
	15.0	6,606	6.9	933
	20.0	8,808	7.1	960
	25.0	11,010	7.2	974
20.0	0	0	5.9	798
	5.0	5,220	6.2	839
	10.0	10,439	6.5	879
	15.0	15,658	6.9	933
	20.0	20,878	7.2	974
	25.0	26,098	7.3	987
30.0	0	0	5.9	798
	5.0	18,120	5.7	771
	10.0	36,240	5.5	744
	15.0	54,360	5.0	676
	20.0	72,480	4.5	609
	25.0	90,600	3.5	473

Table 3.3 Critical condition for onset of the buoyancy-driven vortex roll.

Jet diameter (D_j, mm)	Separation distance (H, mm)	Gr	Re_j	Gr/Re_j^2	Gr/Re_{we}^2	Deviation (%)
10.0	20.0	3,340	879	0.0043	32.3	2.2
		4,200	947	0.0047	35.0	5.9
		5,220	1,082	0.0045	33.3	0.8
	15.0	1,321	541	0.0045	33.7	2.0
		2,202	676	0.0048	36.0	9.0
	10.0	1,304	541	0.0044	33.3	0.8
		1,957	676	0.0043	32.0	3.1
22.1	20.0	3,340	398	0.021	32.2	2.5
		4,200	459	0.020	30.5	7.7
		5,220	520	0.019	29.5	10.7
	15.0	1,321	245	0.022	33.7	2.0
		2,202	306	0.024	35.9	8.7
	10.0	1,304	245	0.022	33.2	0.5
		1,957	306	0.021	31.9	3.4

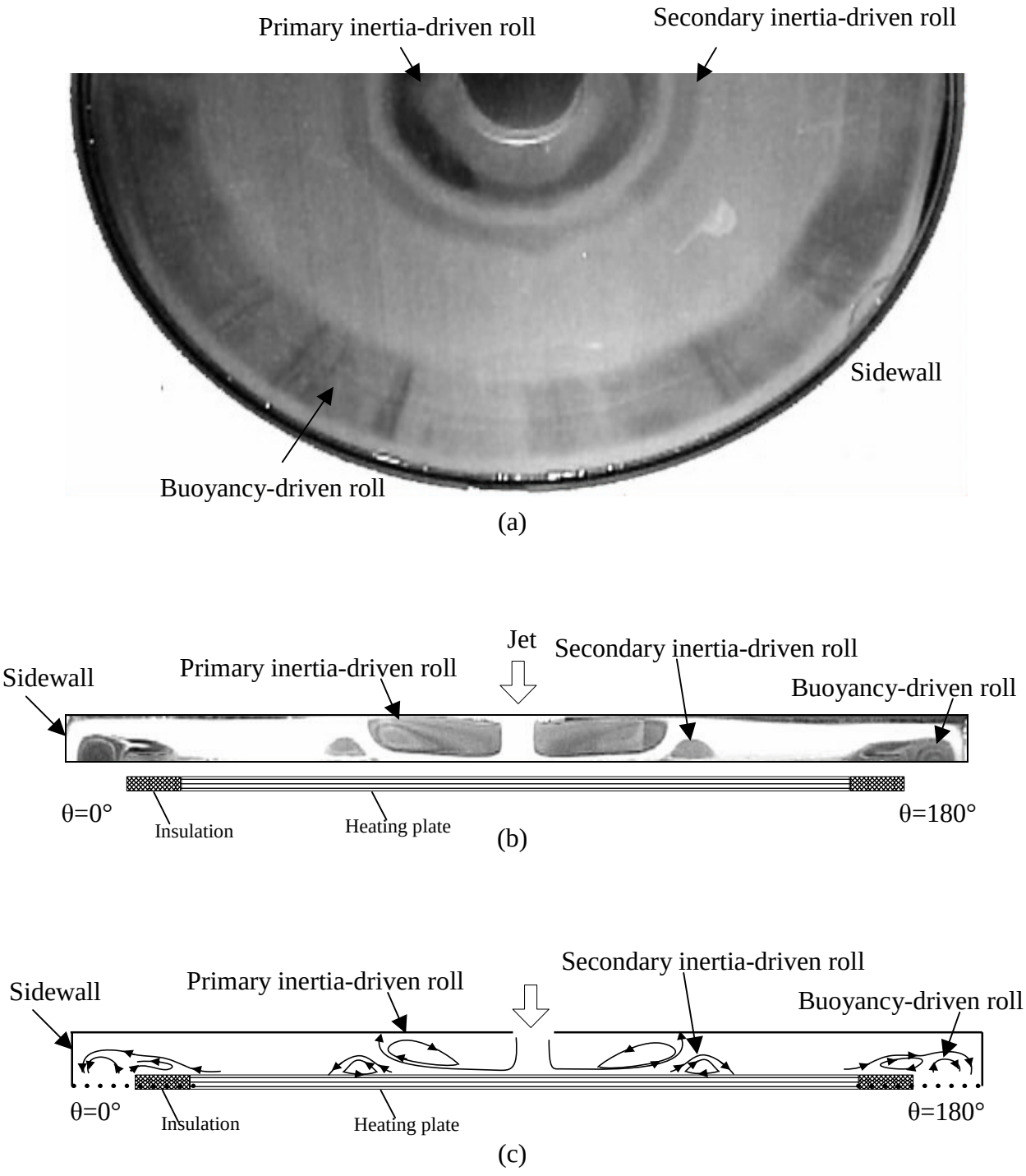

Fig. 3.1 Steady vortex flow pattern for D_j=10.0 mm and H=15.0 mm at Re_j=406 (Q_j=3.0 slpm) and Ra=3,170 (ΔT=10.0℃): (a) top view flow half of photo taken at the middle horizontal plane between the disk and chamber top, (b) side view flow photo taken at the vertical plane θ=0° & 180° and (c) the corresponding schematically sketched cross plane vortex flow.

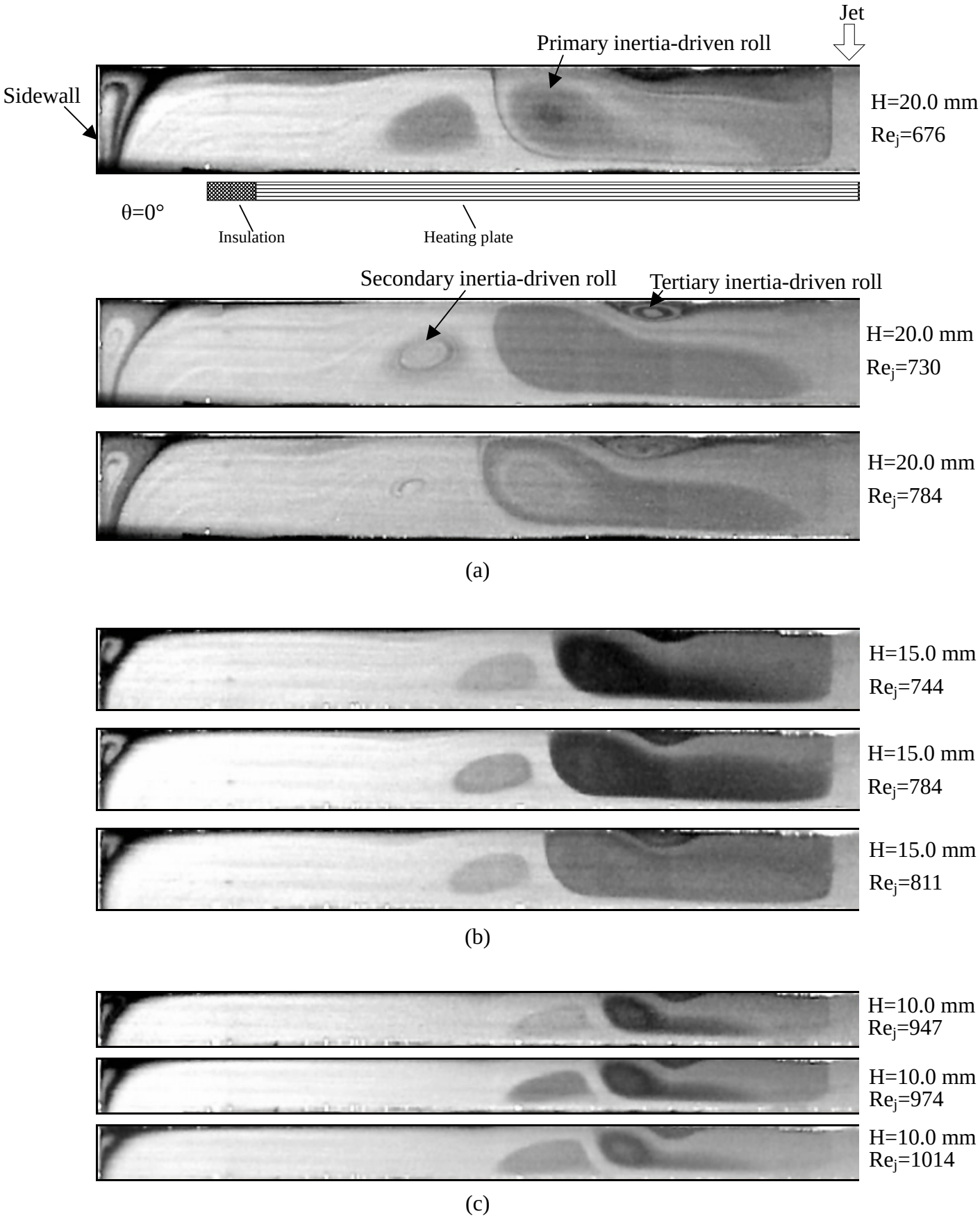

Fig. 3.2 Steady side view flow photos taken at the cross plane θ=0° for various Re_j to illustrate the tertiary inertia-driven roll with Ra=0 & D_j=10.0 mm for (a) H=20.0 mm, (b) H=15.0 mm, and (c) H=10.0 mm.

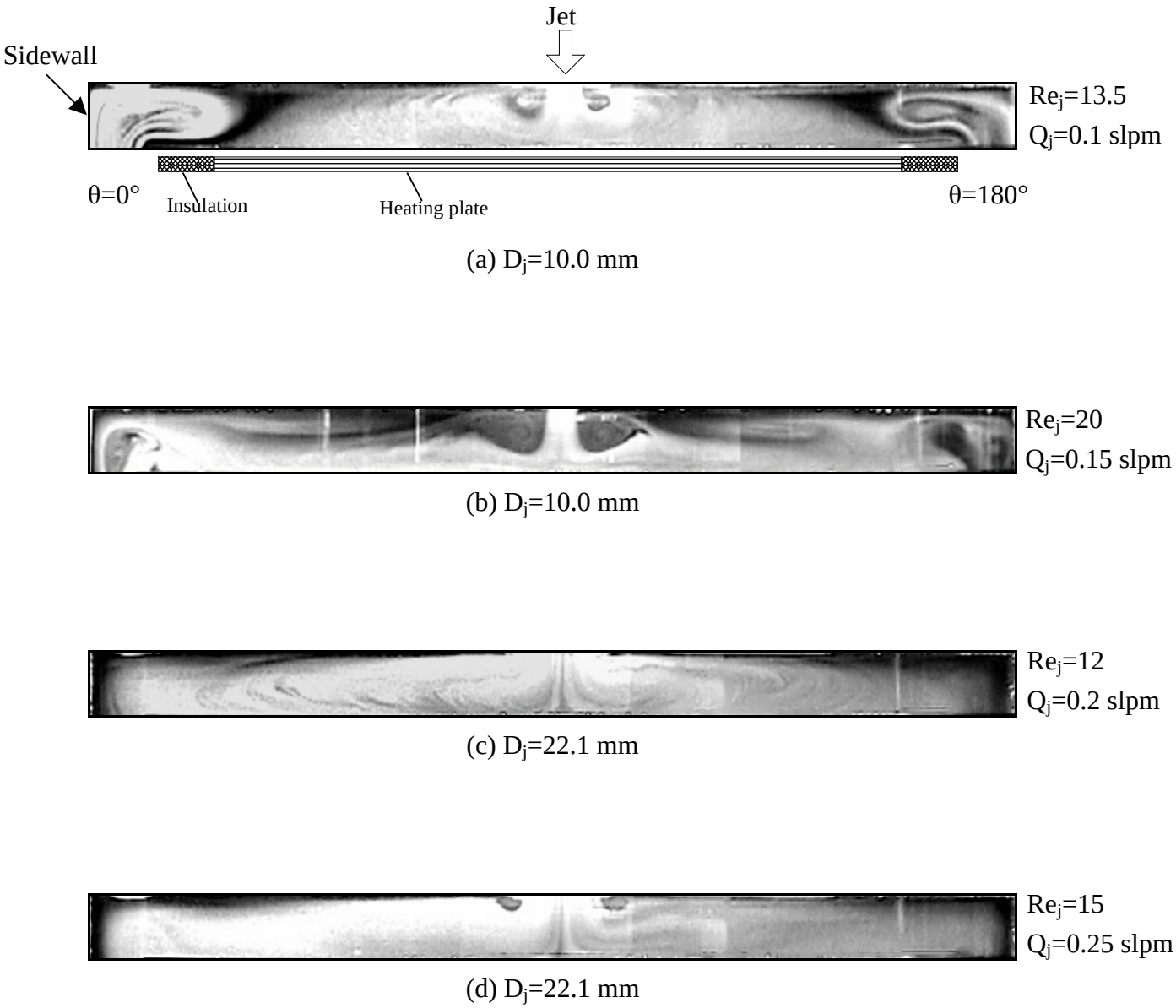

Fig. 3.3 Steady side view flow photos at low Reynolds numbers for Ra=0 & H=20.0 mm: (a) Re_j=13.6 & D_j=10.0 mm, (b) Re_j=20.0 & D_j=10.0 mm, (c) Re_j=12.0 & D_j=22.1 mm, and (d) Re_j=15.0 & D_j=22.1 mm.

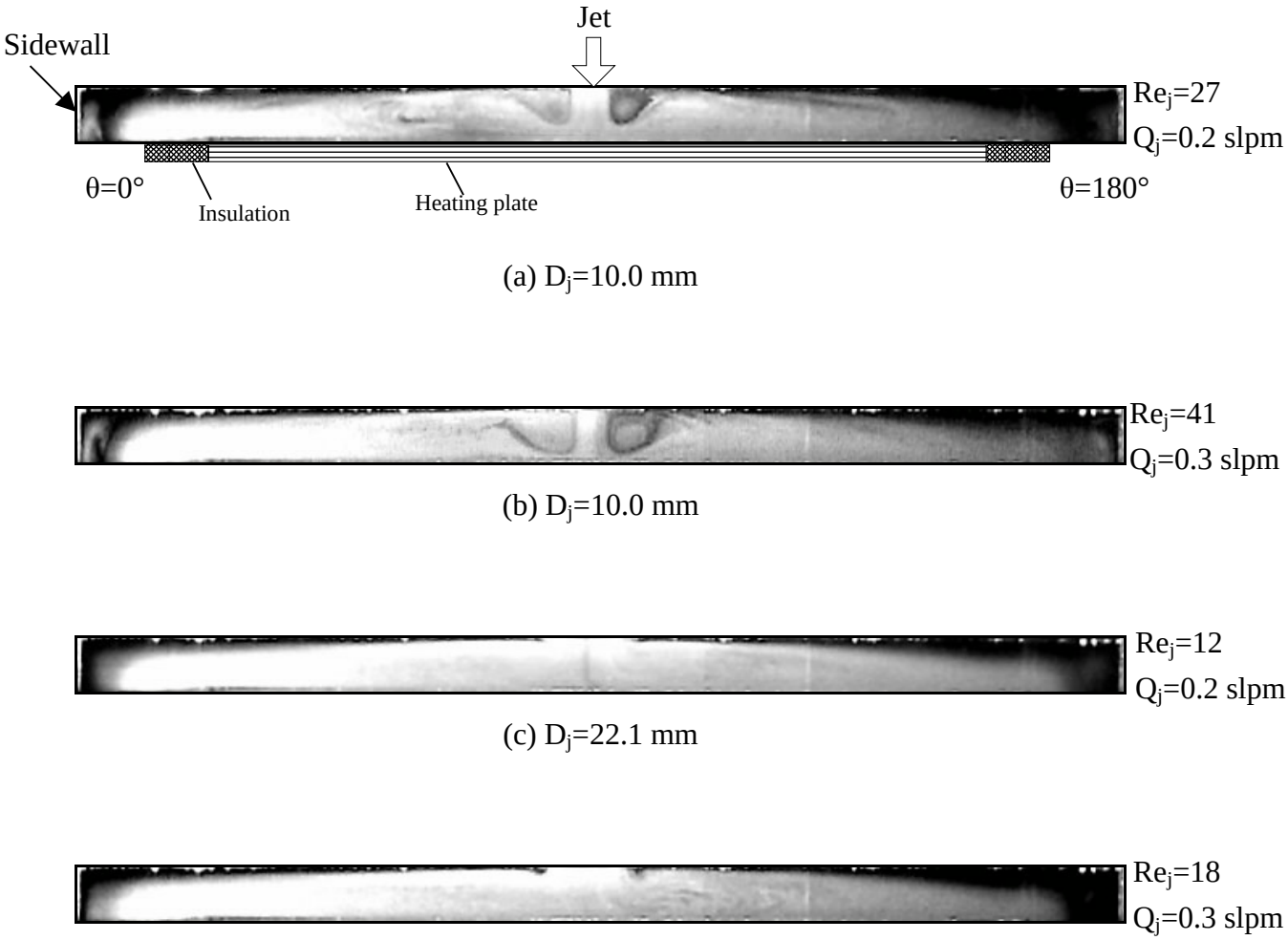

Fig. 3.4 Steady side view flow photos at low Reynolds numbers for Ra=0 & H=15.0 mm at Re_j = (a) 27 & D_j=10.0 mm, (b) 41 & D_j=10.0 mm, (c) 12 & D_j=22.1 mm, and (d) 18 & D_j=22.1 mm.

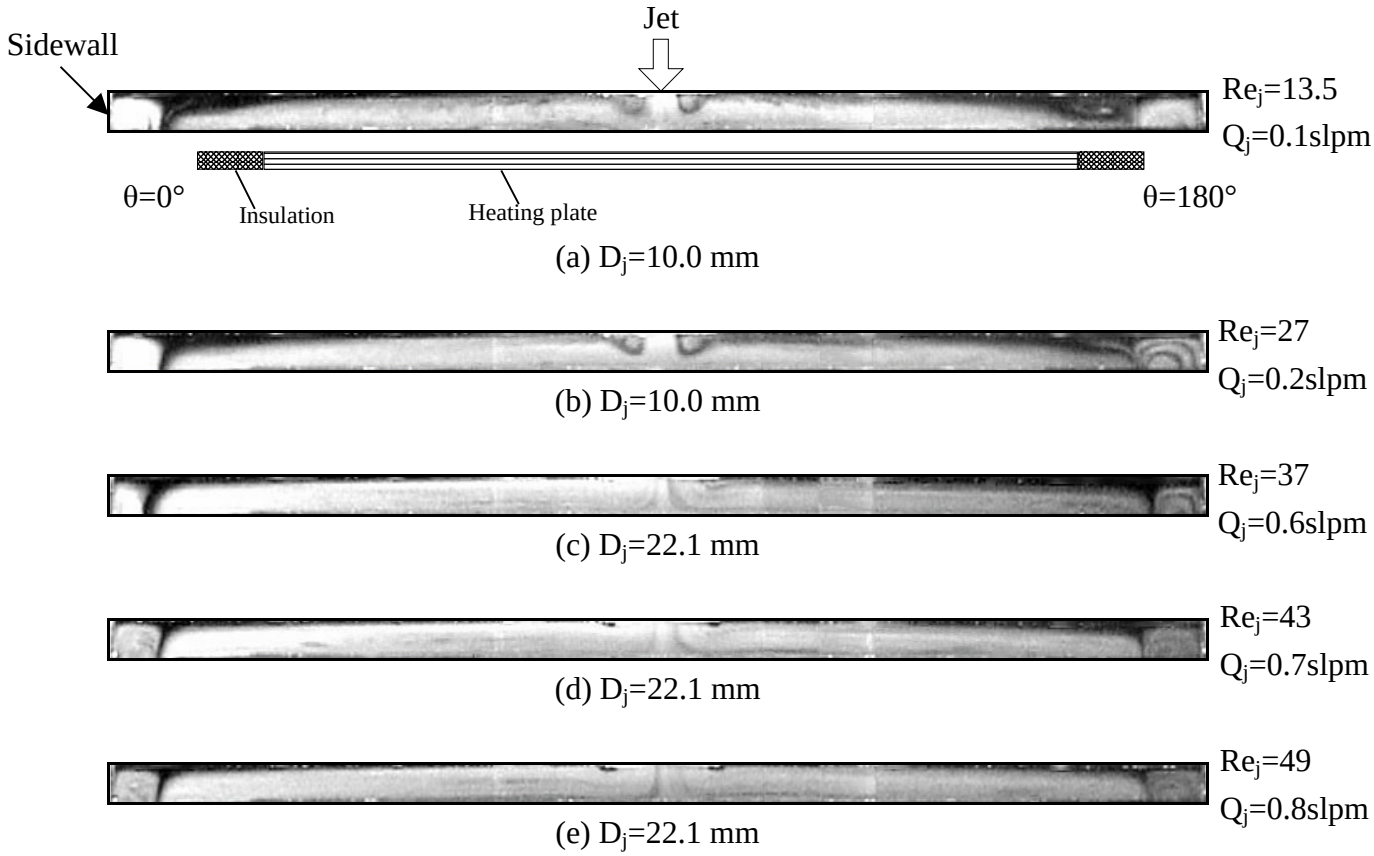

Fig. 3.5 Steady side view flow photos at low jet Reynolds numbers for Ra=0 with H=10.0 mm at Re_j = (a) 13.5 & D_j=10.0 mm, (b) 27 & D_j=10.0 mm, (c) 37 & D_j=22.1 mm, (d) 43 & D_j=22.1 mm, and (e) 49 & D_j=22.1 mm.

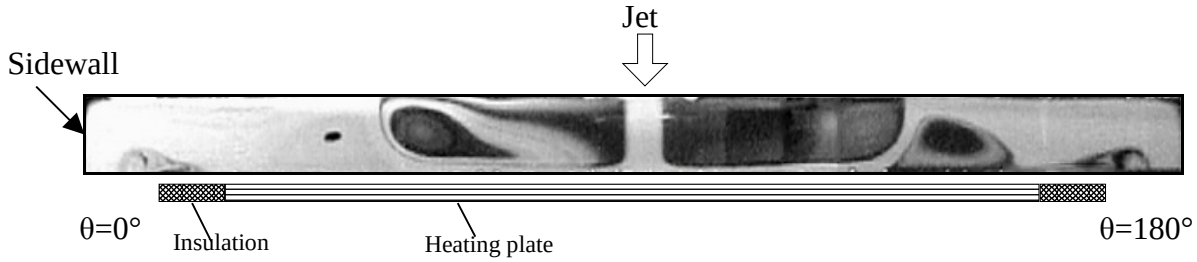

(a) Re_j=612 & D_j=10.0 mm

(b) Re_j=680 & D_j=10.0 mm

(c) Re_j=748 & D_j=10.0 mm

(d) Re_j=275 & D_j=22.1 mm

(e) Re_j=305 & D_j=22.1 mm

(f) Re_j=336 & D_j=22.1 mm

Fig. 3.6 Steady side view flow photos near the critical condition showing the flow near the onset of buoyancy-driven roll for Ra=1650 (ΔT=2.2℃) with (a) Re_j=612 & D_j=10.0 mm, (b) Re_j=680 & D_j=10.0 mm, (c) Re_j=748 & D_j=10.0 mm, (d) Re_j=275 & D_j=22.1 mm, (e) Re_j=305 & D_j=22.1 mm, and (f) Re_j=336 & D_j=22.1 mm.

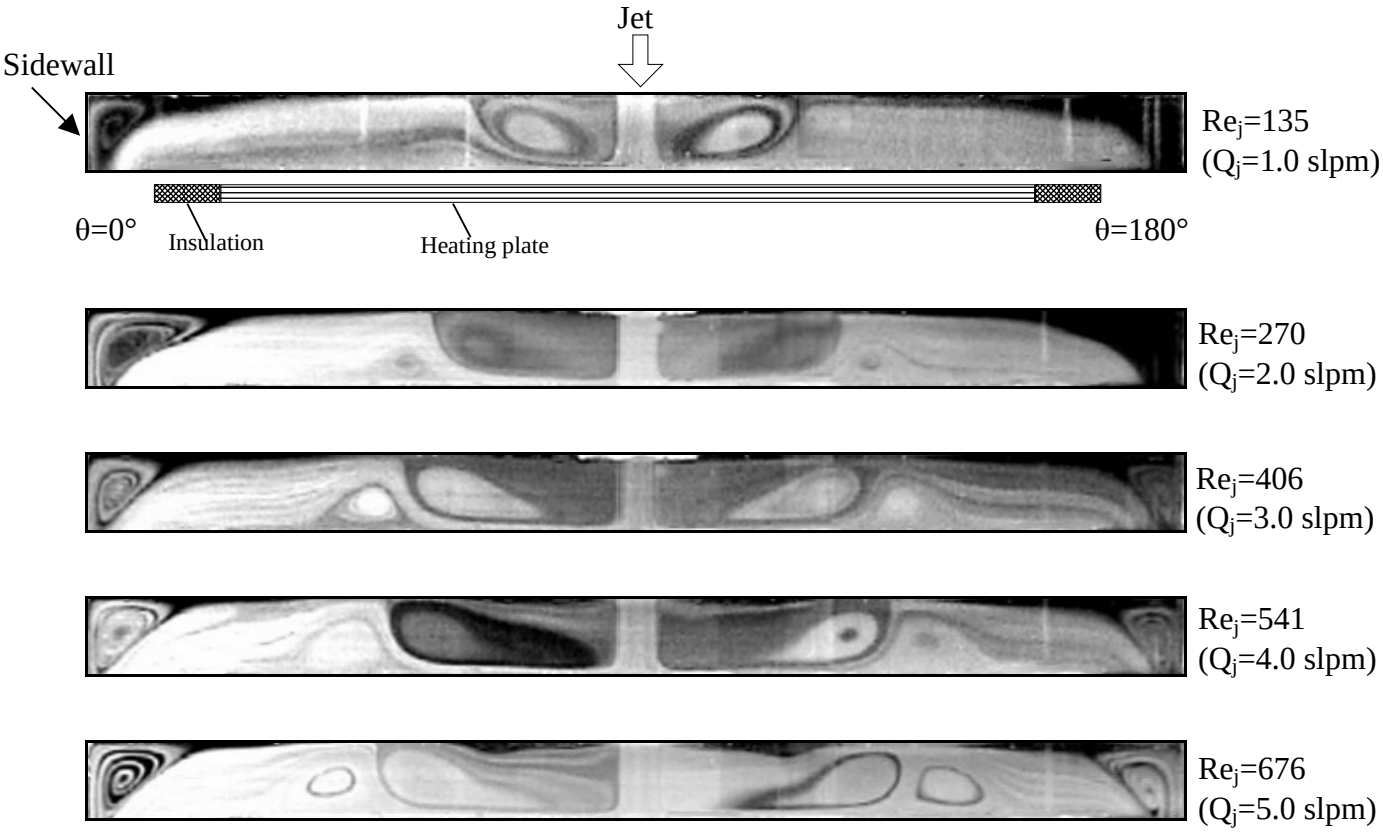

(a) D_j=10.0 mm

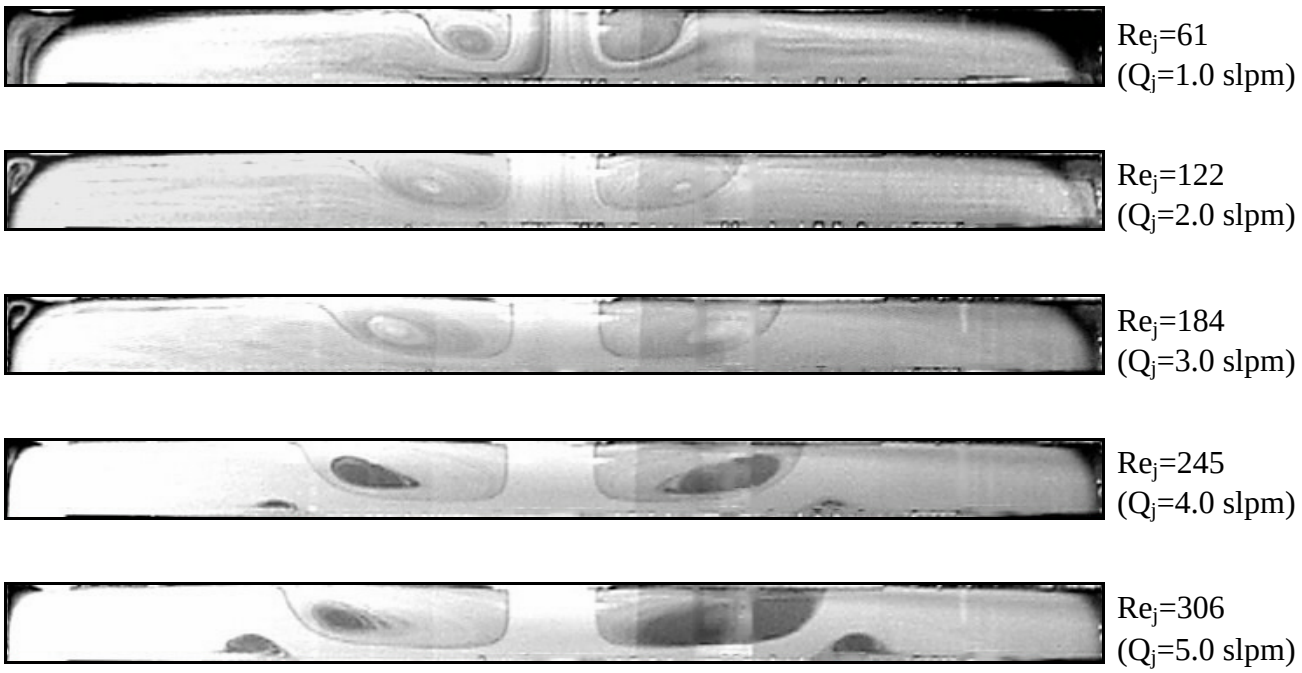

(b) D_j=22.1 mm

Fig. 3.7 Steady side view flow photos taken at the cross plane θ=0° & 180° for various jet Reynolds numbers at Ra=0 (ΔT=0℃) for D_j= (a) 10.0 mm and (b) 22.1 mm.

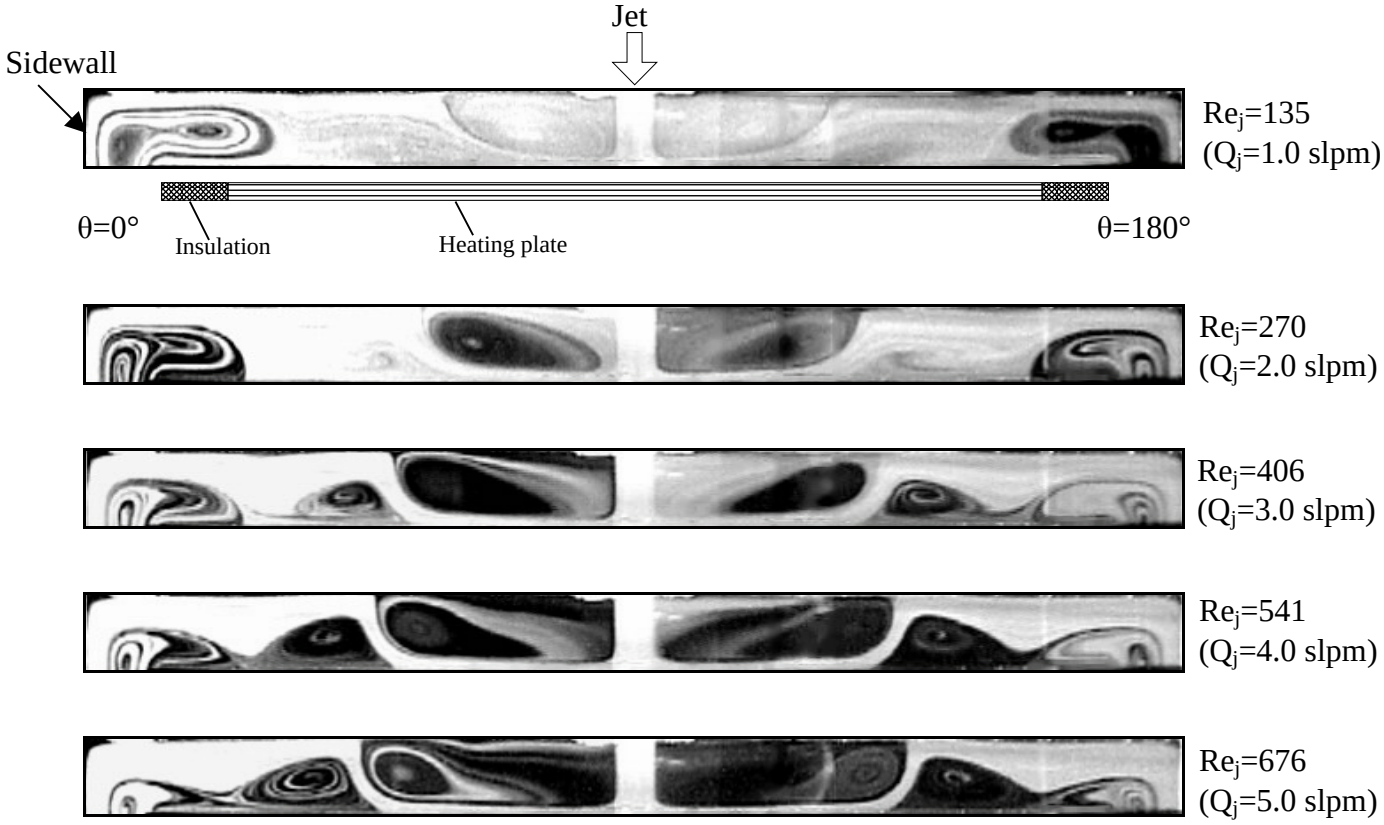

(a) D_j=10.0 mm

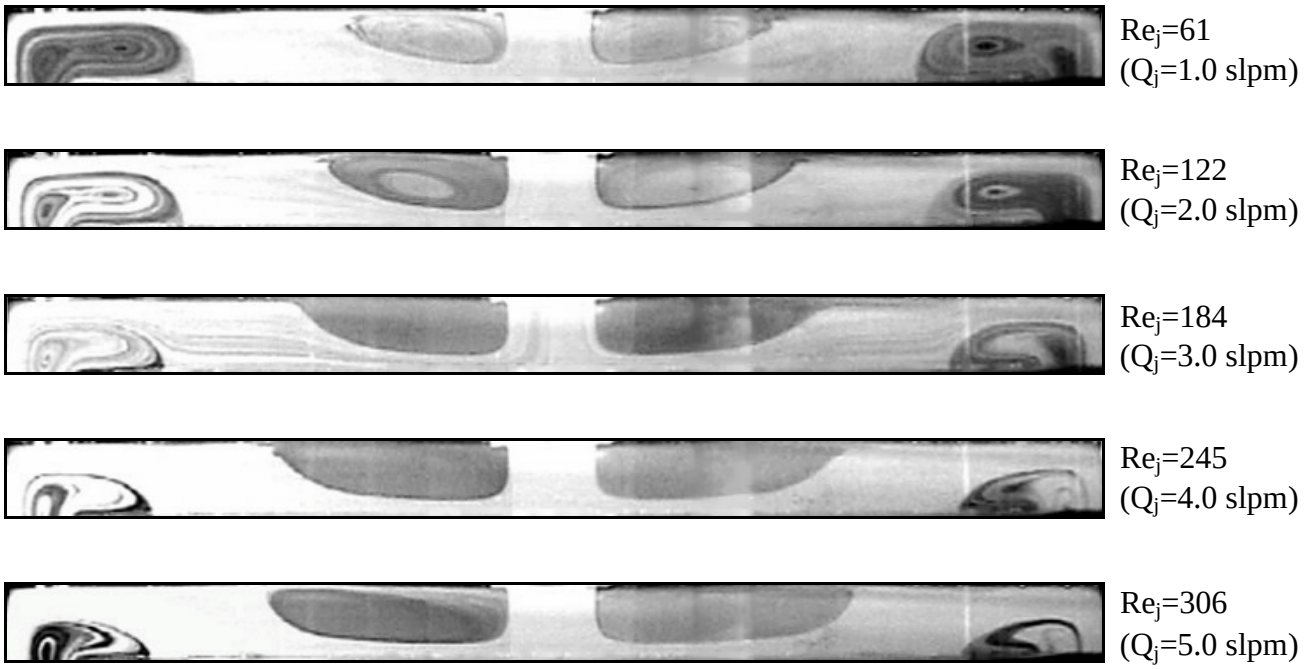

(b) D_j=22.1 mm

Fig. 3.8 Steady side view flow photos taken at the cross plane θ=0° & 180° for various jet Reynolds numbers at Ra=3,760 (ΔT=5.0℃) for D_j= (a) 10.0 mm and (b) 22.1 mm.

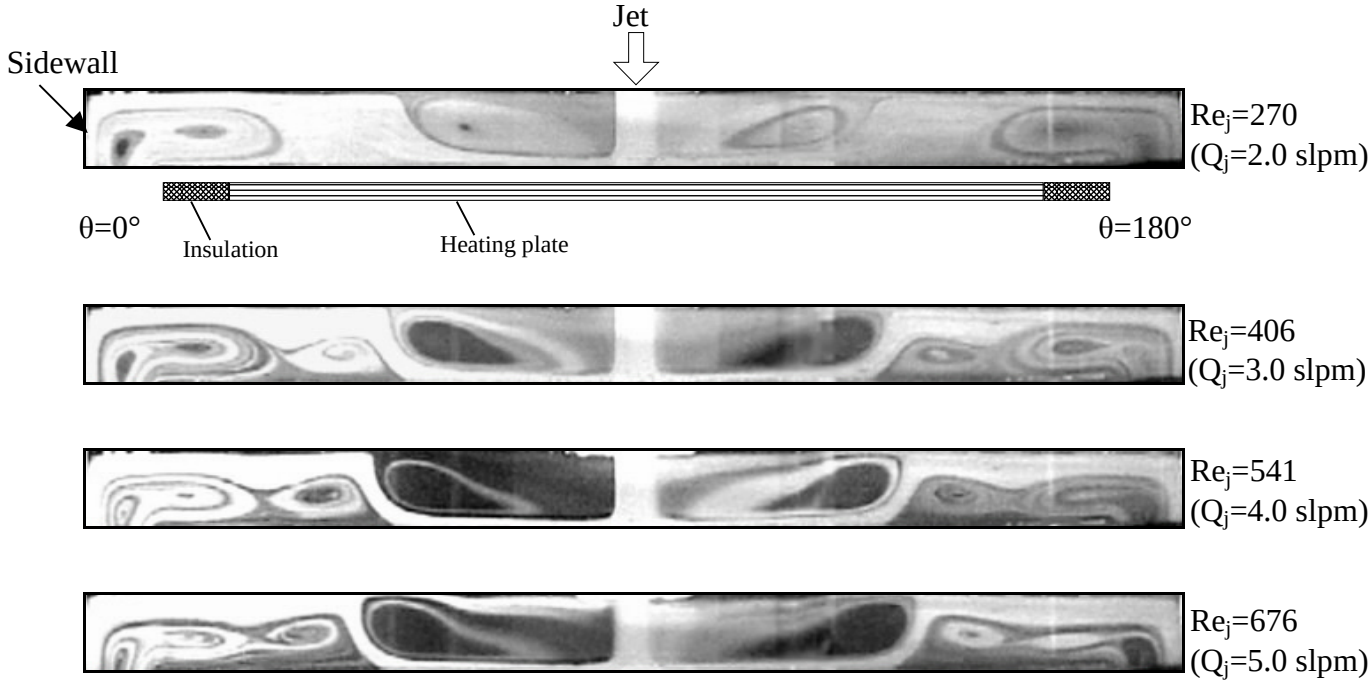

(a) D_j=10.0 mm

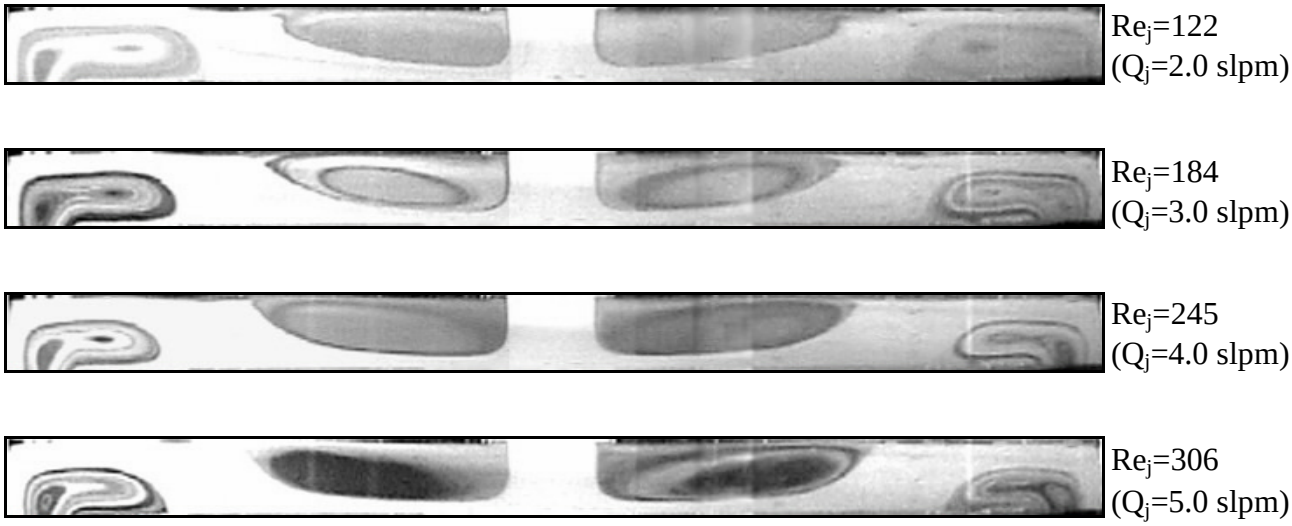

(b) D_j=22.1 mm

Fig. 3.9 Steady side view flow photos taken at the cross plane θ=0° & 180° for various jet Reynolds numbers at Ra=7,520 (ΔT=10.0℃) for D_j= (a) 10.0 mm and (b) 22.1 mm.

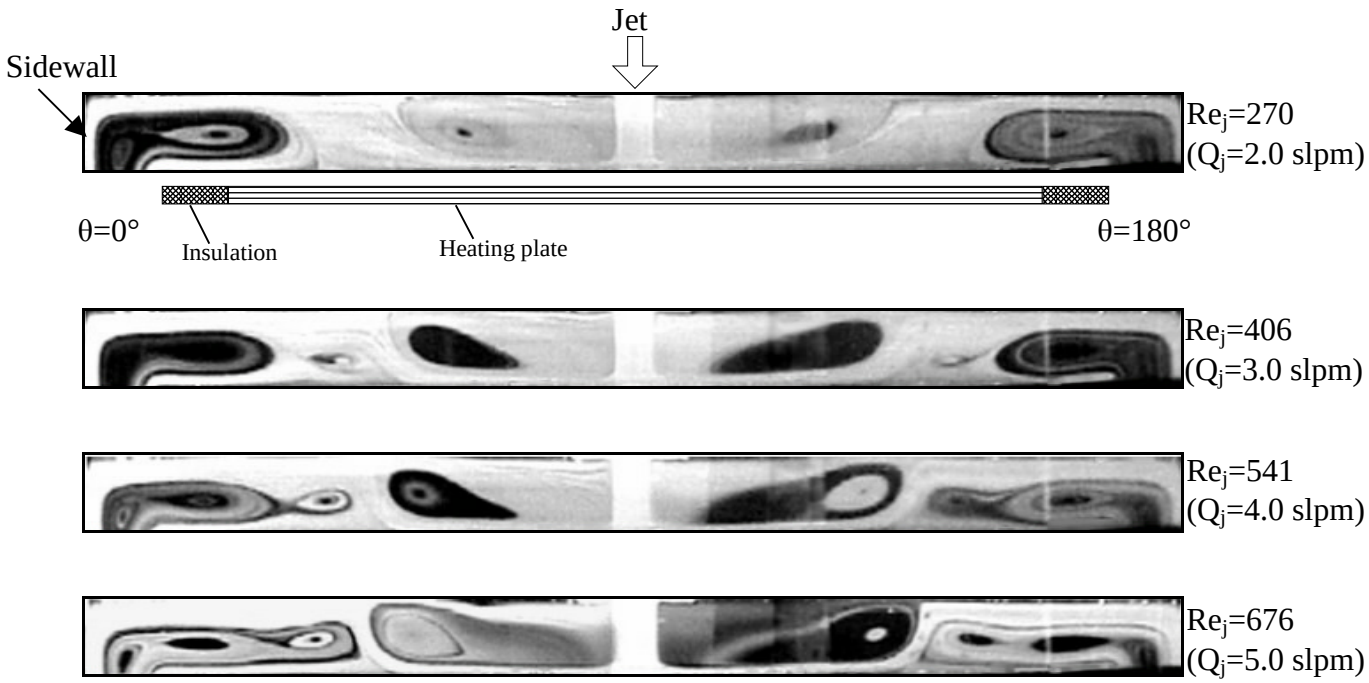

(a) D_j=10.0 mm

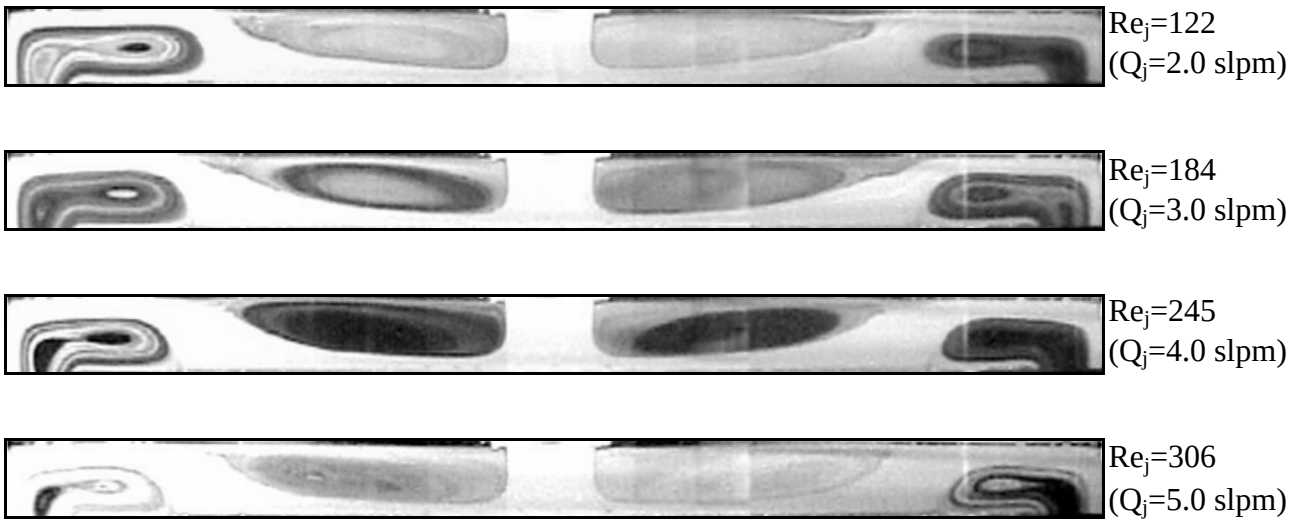

(b) D_j=22.1 mm

Fig. 3.10 Steady side view flow photos taken at the cross plane θ =0° & 180° for various jet Reynolds numbers at Ra=11,270 (ΔT=15.0℃) for D_j= (a) 10.0 mm and (b) 22.1 mm.

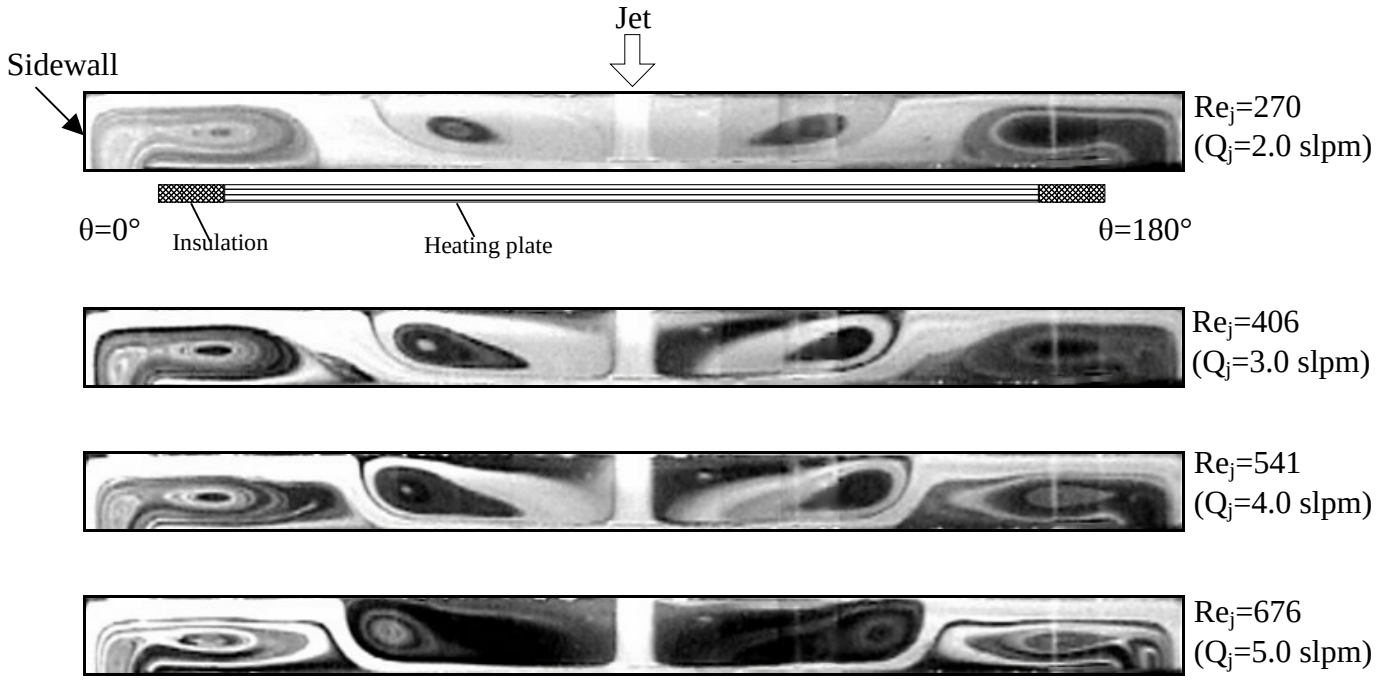

(a) D_j=10.0 mm

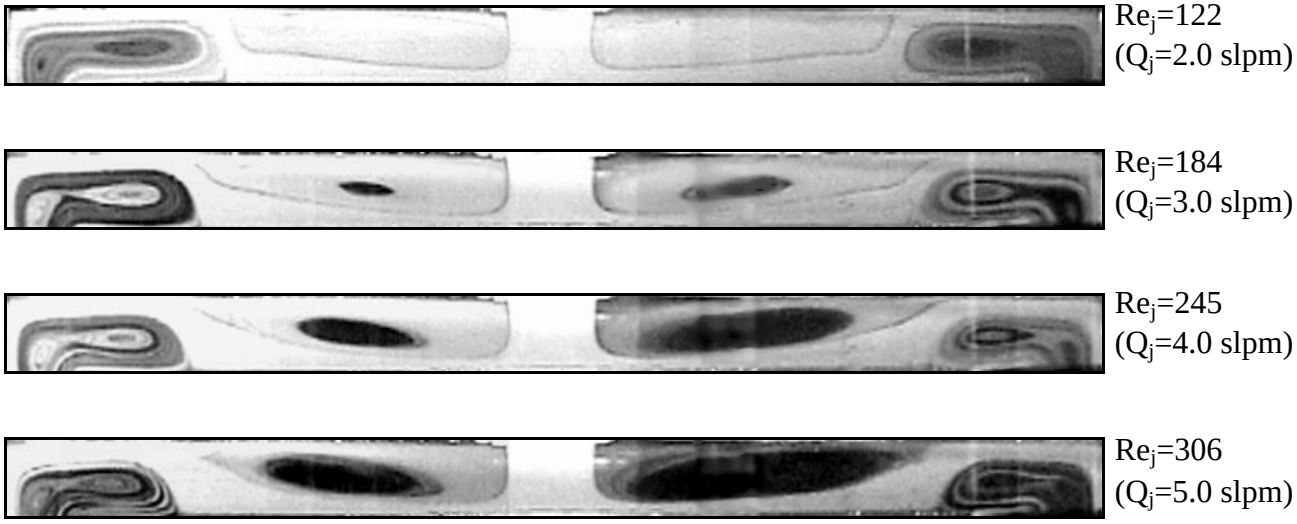

(b) D_j=22.1 mm

Fig. 3.11 Steady side view flow photos taken at the cross plane θ=0° & 180° for various jet Reynolds numbers at Ra=15,030 (ΔT=20.0℃) for D_j= (a) 10.0 mm and (b) 22.1 mm.

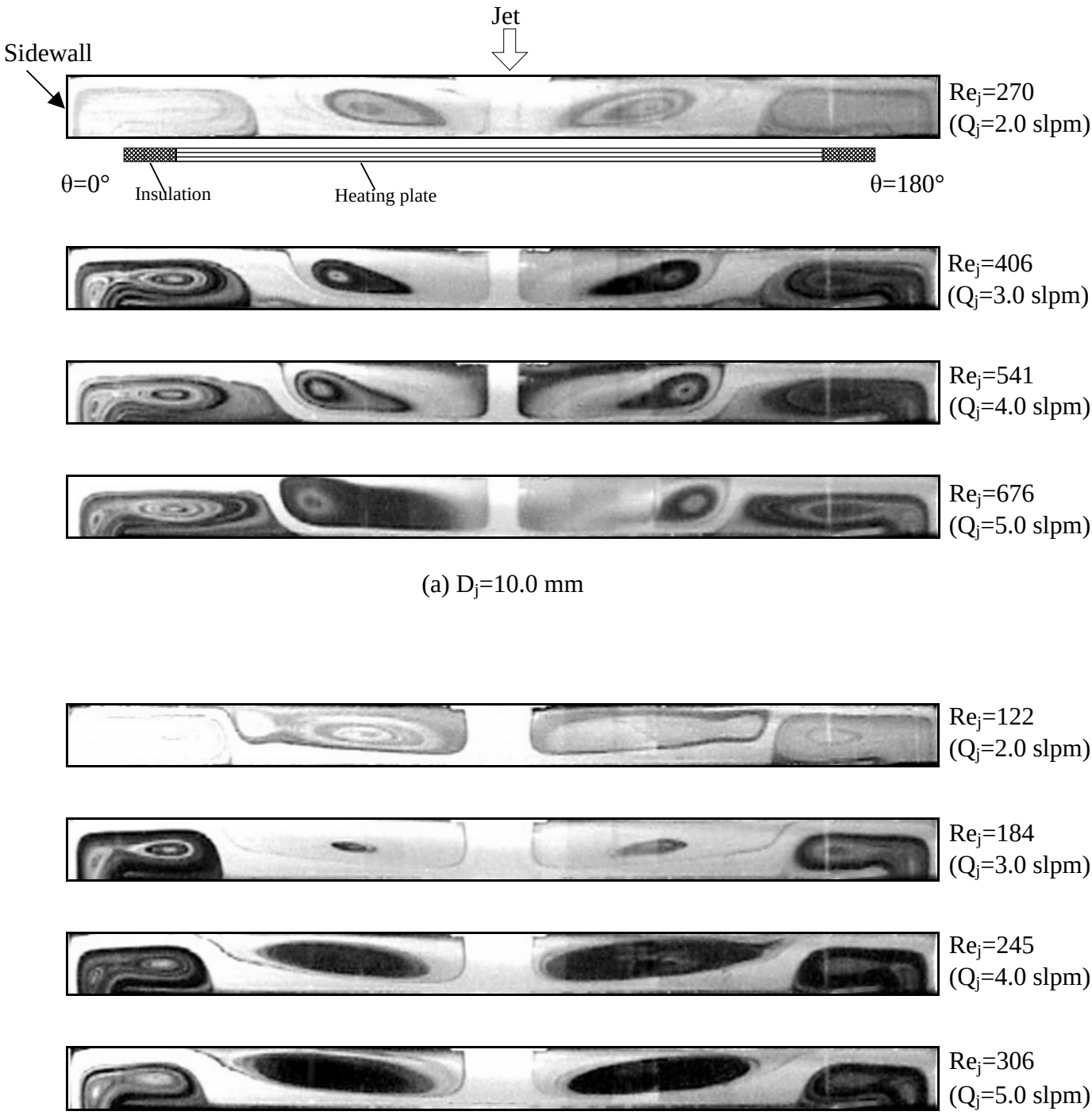

(a) D_j=10.0 mm

(b) D_j=22.1 mm

Fig. 3.12 Steady side view flow photos taken at the cross plane θ=0° & 180° for various jet Reynolds numbers at Ra=18,790 (ΔT=25.0℃) for D_j= (a) 10.0 mm and (b) 22.1 mm.

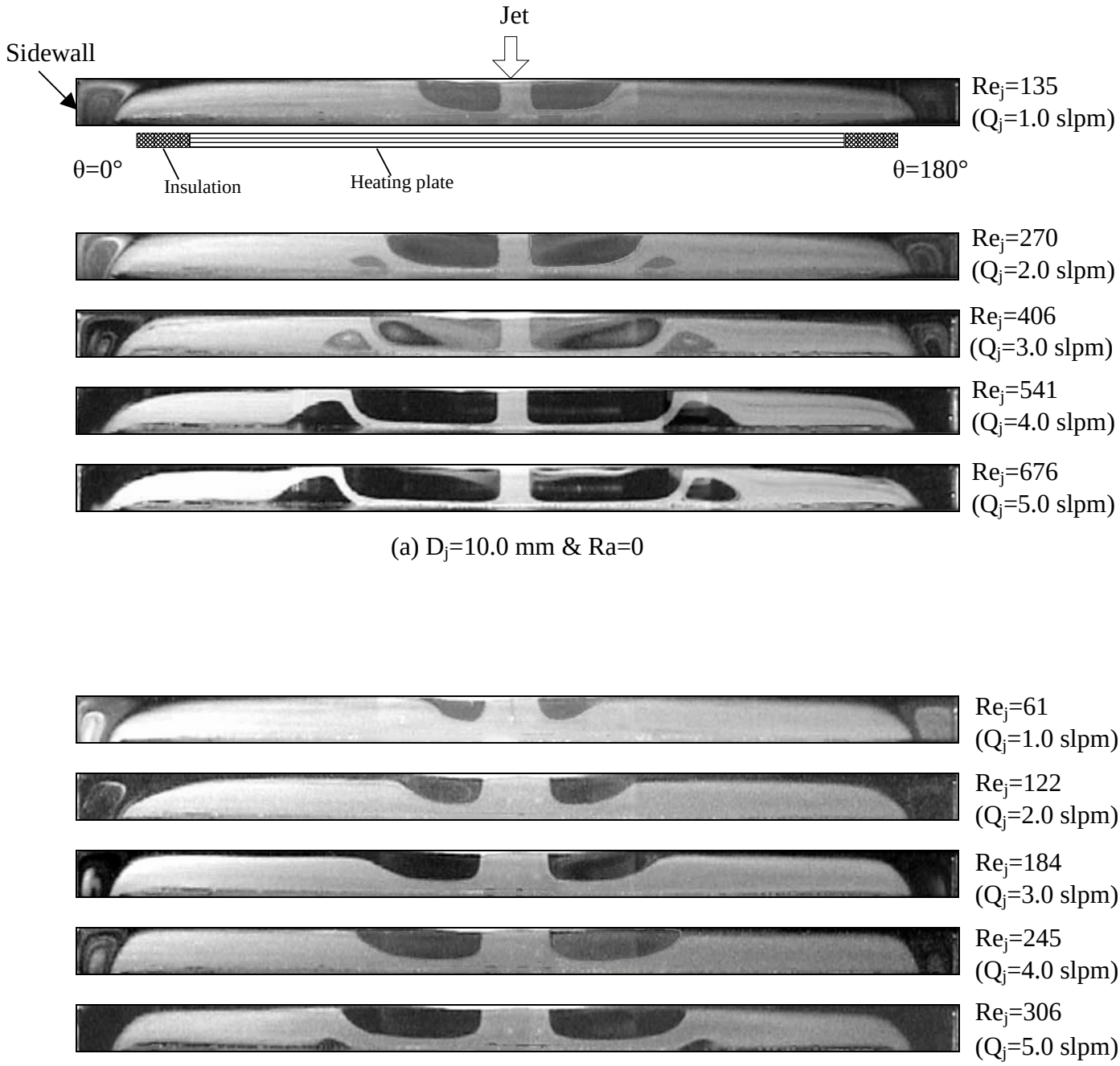

Fig. 3.13 Steady side view flow photos taken at the cross plane θ=0° & 180° for various jet Reynolds numbers at H=15.0 mm & Ra=0 (ΔT=0℃) for D$_j$= (a) 10.0 mm and (b) 22.1 mm.

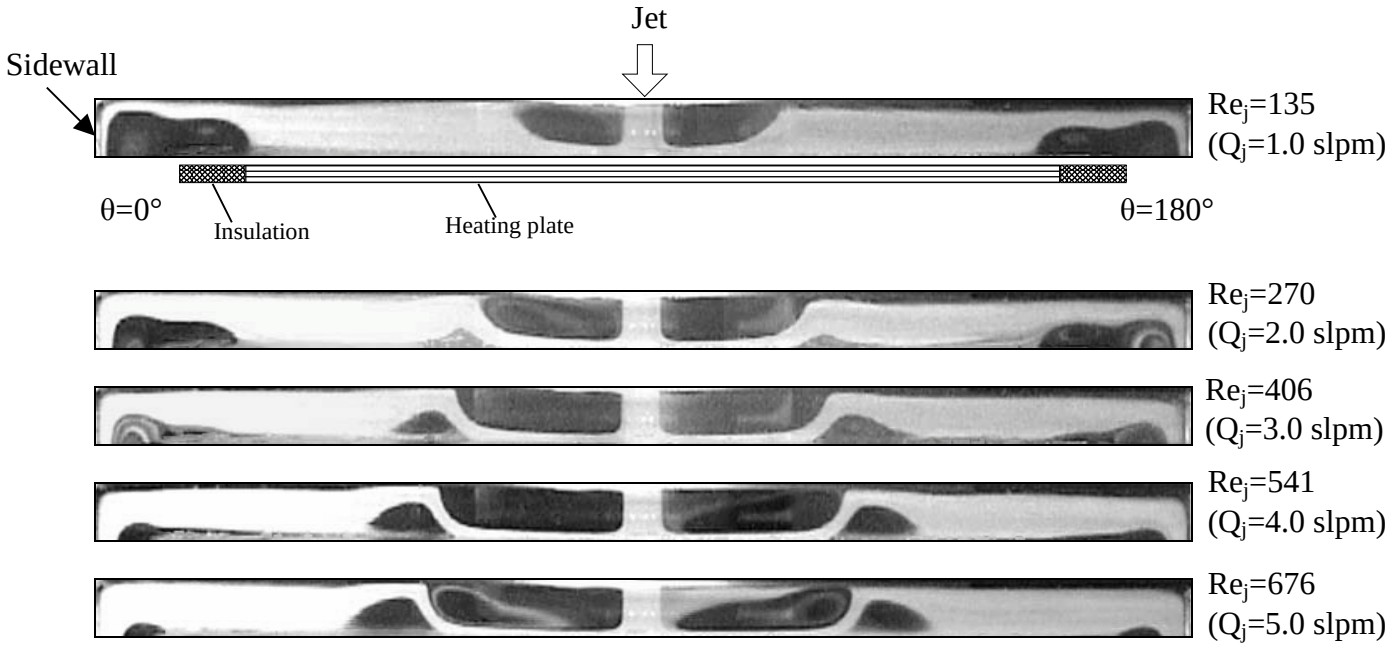

(a) D_j=10.0 mm & Ra=1,590

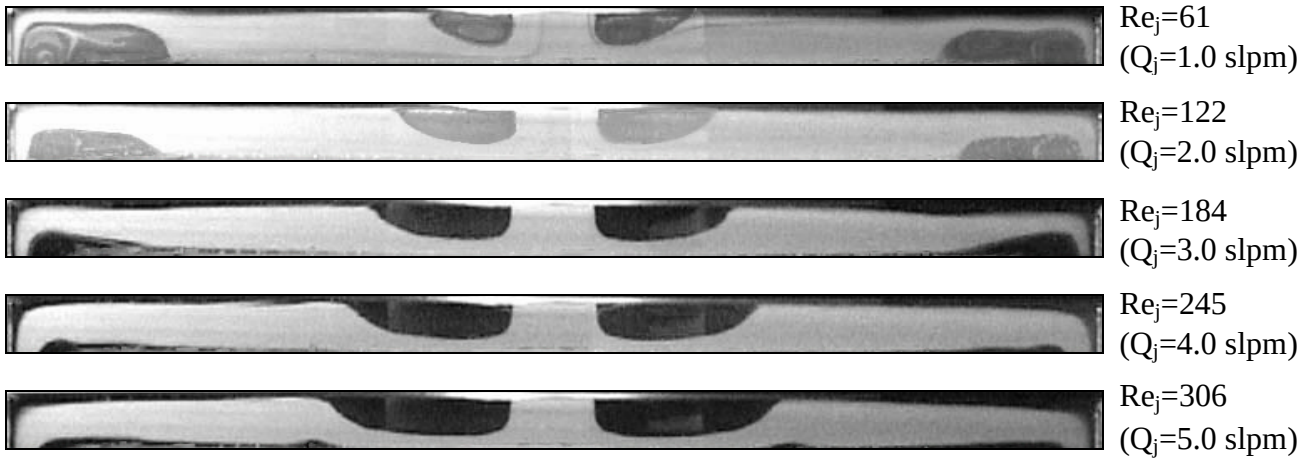

(b) D_j=22.1 mm & Ra=1,590

Fig. 3.14 Steady side view flow photos taken at the cross plane θ=0° & 180° for various jet Reynolds numbers at H=15.0 mm & Ra=1,590 (ΔT=5.0℃) for D_j= (a) 10.0 mm and (b) 22.1 mm.

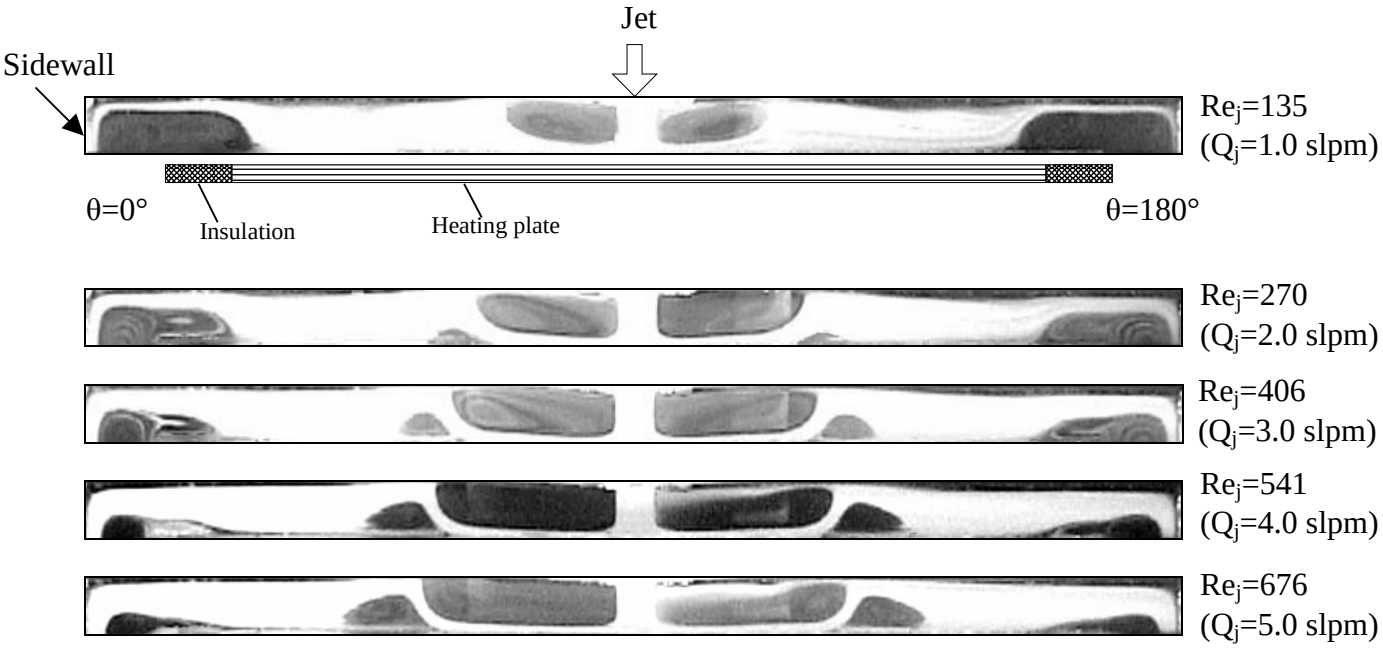

(a) D_j=10.0 mm & Ra=3,170

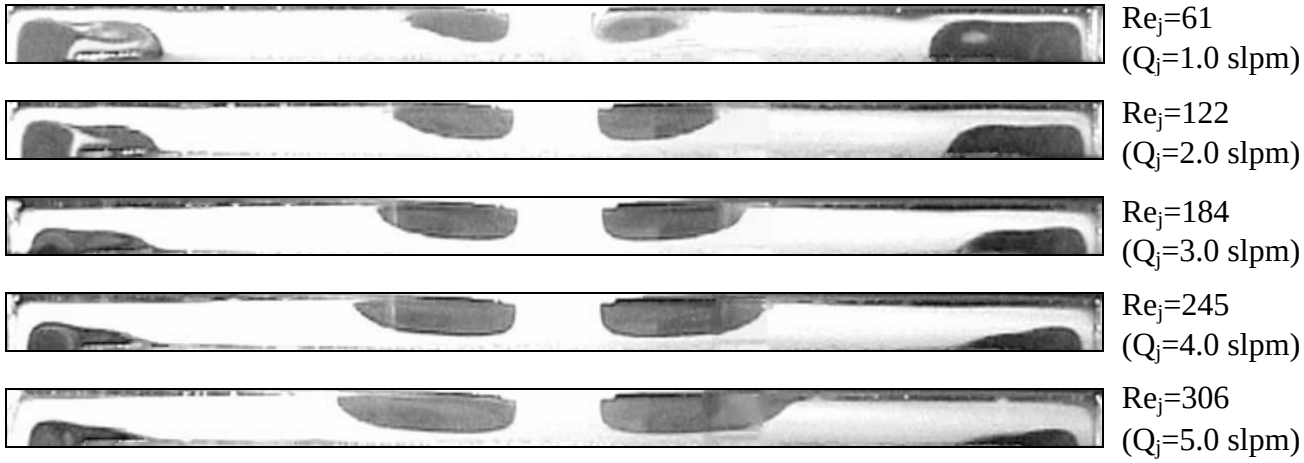

(b) D_j=22.1 mm & Ra=3,170

Fig. 3.15 Steady side view flow photos taken at the cross plane θ=0° & 180° for various jet Reynolds numbers at H=15.0 mm & Ra=3,170 (ΔT=10.0℃) for D_j= (a) 10.0 mm and (b) 22.1 mm.

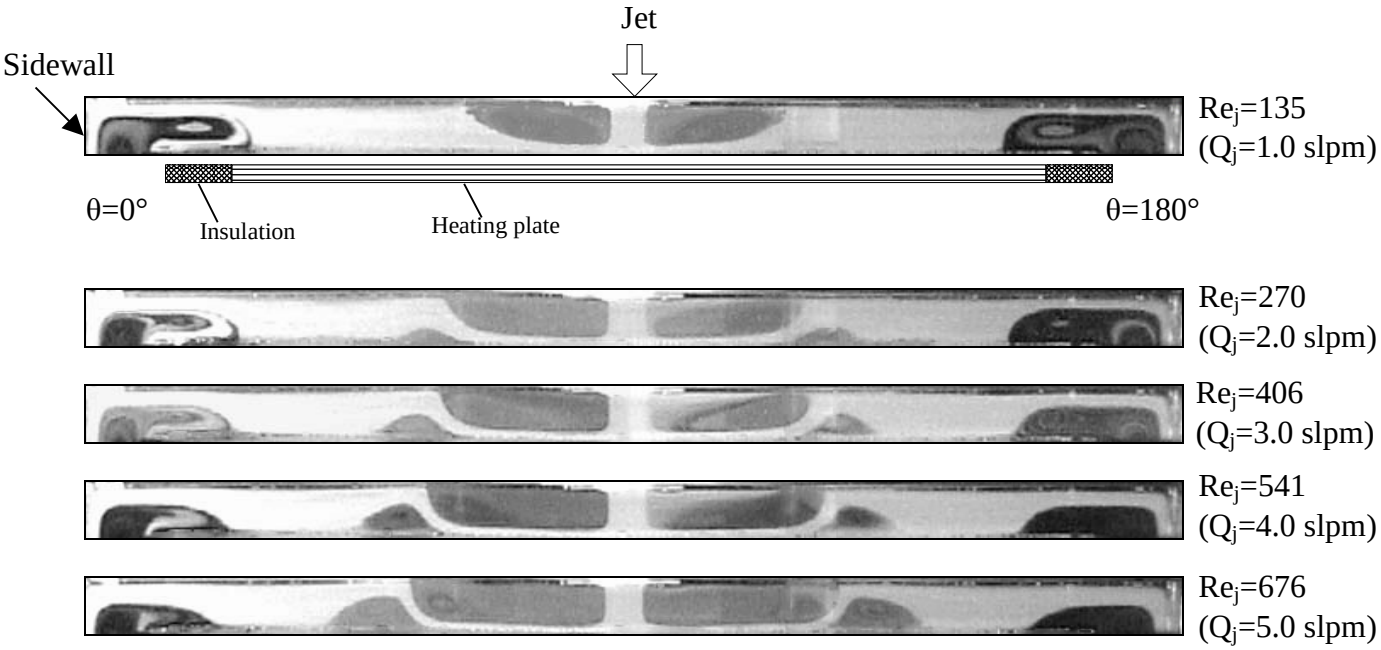

(a) D_j=10.0 mm & Ra=6,340

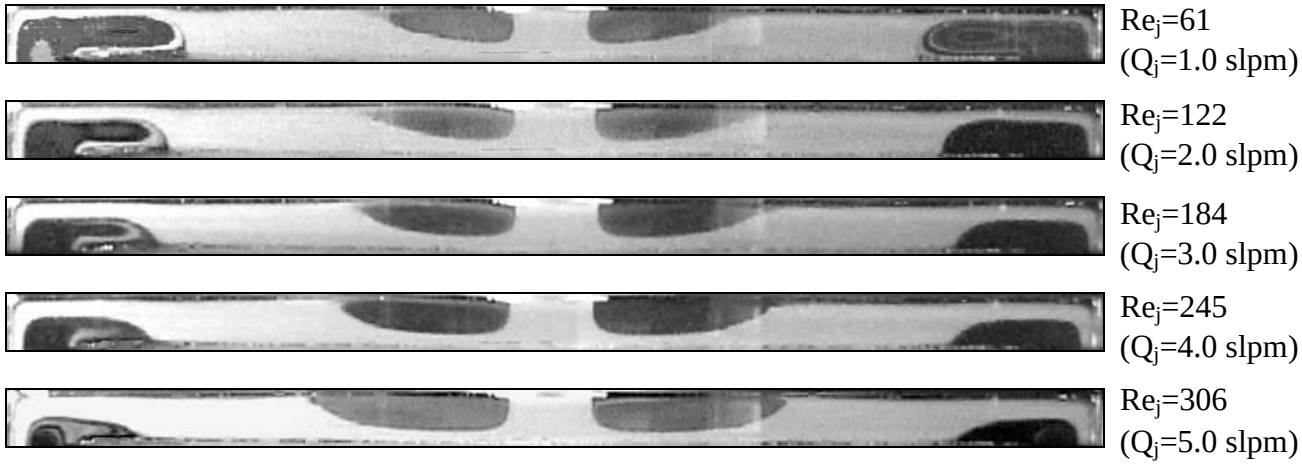

(b) D_j=22.1 mm & Ra=6,340

Fig. 3.16 Steady side view flow photos taken at the cross plane θ=0° & 180° for various jet Reynolds numbers at H=15.0 mm & Ra=6,340 (ΔT=20.0℃) for D_j= (a) 10.0 mm and (b) 22.1 mm.

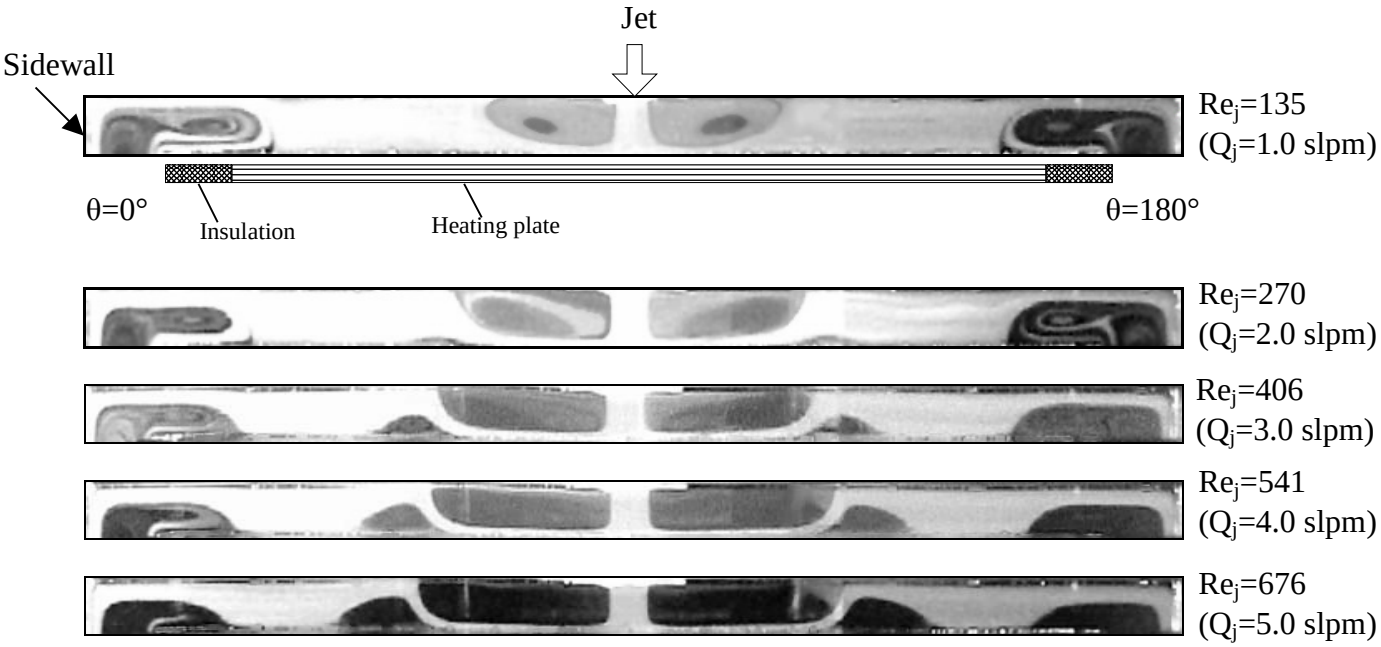

(a) D_j=10.0 mm & Ra=7,930

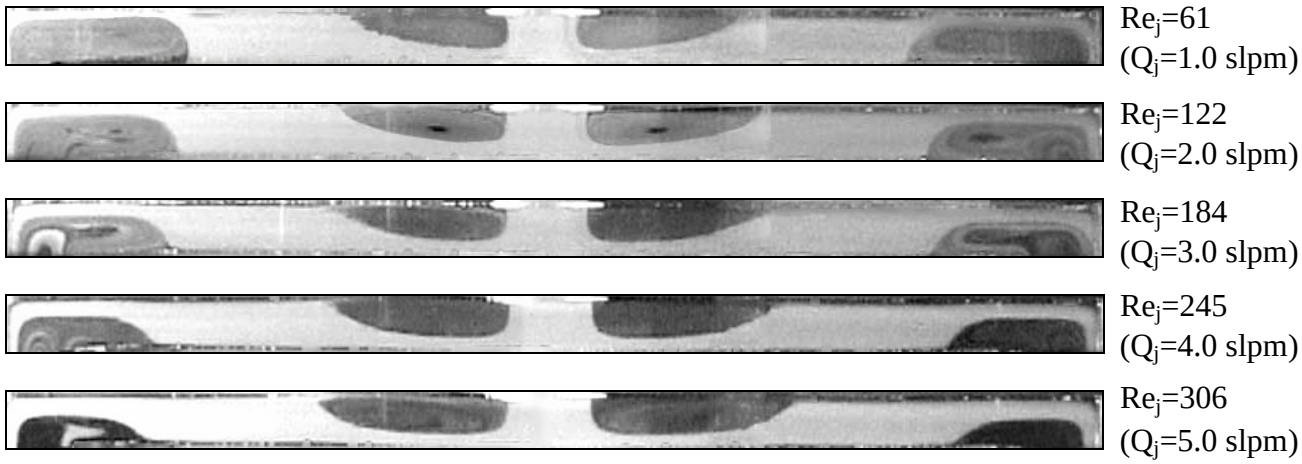

(b) D_j=22.1 mm & Ra=7,930

Fig. 3.17 Steady side view flow photos taken at the cross plane θ=0° & 180° for various jet Reynolds numbers at H=15.0 mm & Ra=7,930 (ΔT=25.0℃) for D_j= (a) 10.0 mm and (b) 22.1 mm.

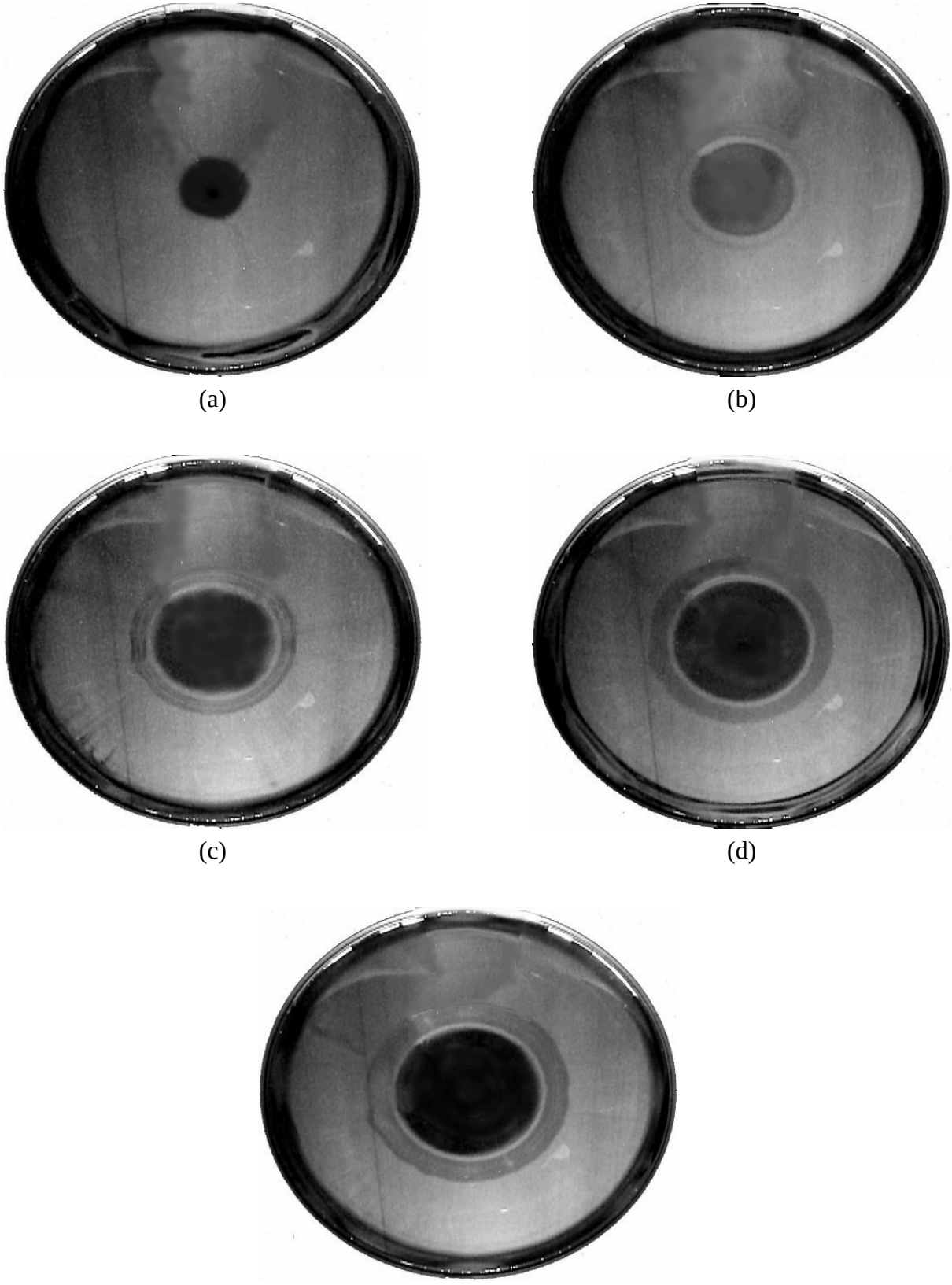

Fig. 3.18 Steady top view flow photos taken at the middle horizontal plane between the disk and chamber top with Ra=0 ($\Delta T=0$℃) & D_j=10.0 mm at H=15.0 mm for Re_j= (a) 135, (b) 270, (c) 406, (d) 541, and (e) 676.

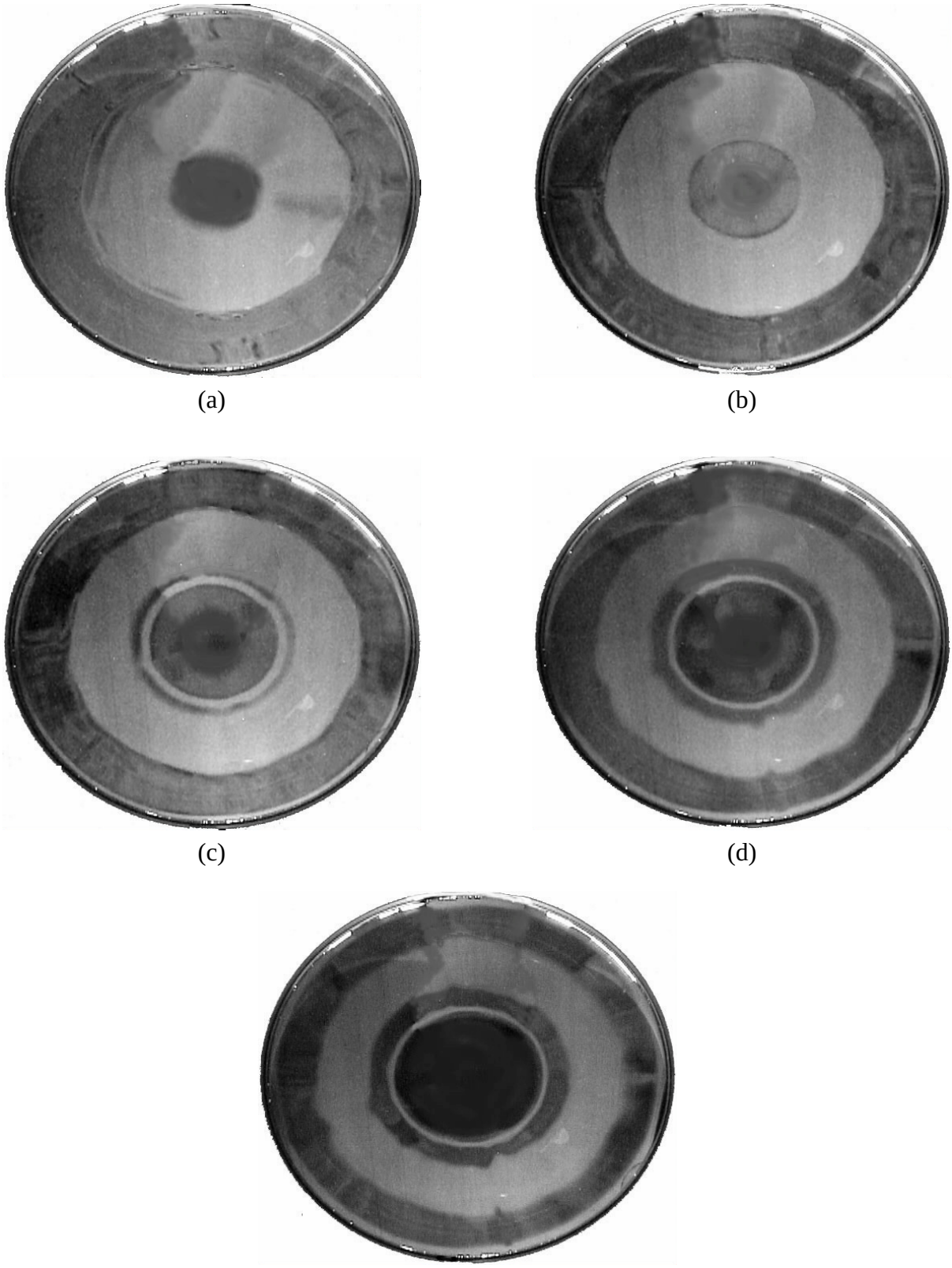

Fig. 3.19 Steady top view flow photos taken at the middle horizontal plane between the disk and chamber top with Ra=6,340 (ΔT=20.0℃) & D_j=10.0 mm at H=15.0 mm for Re_j= (a) 135, (b) 270, (c) 406, (d) 541, and (e) 676.

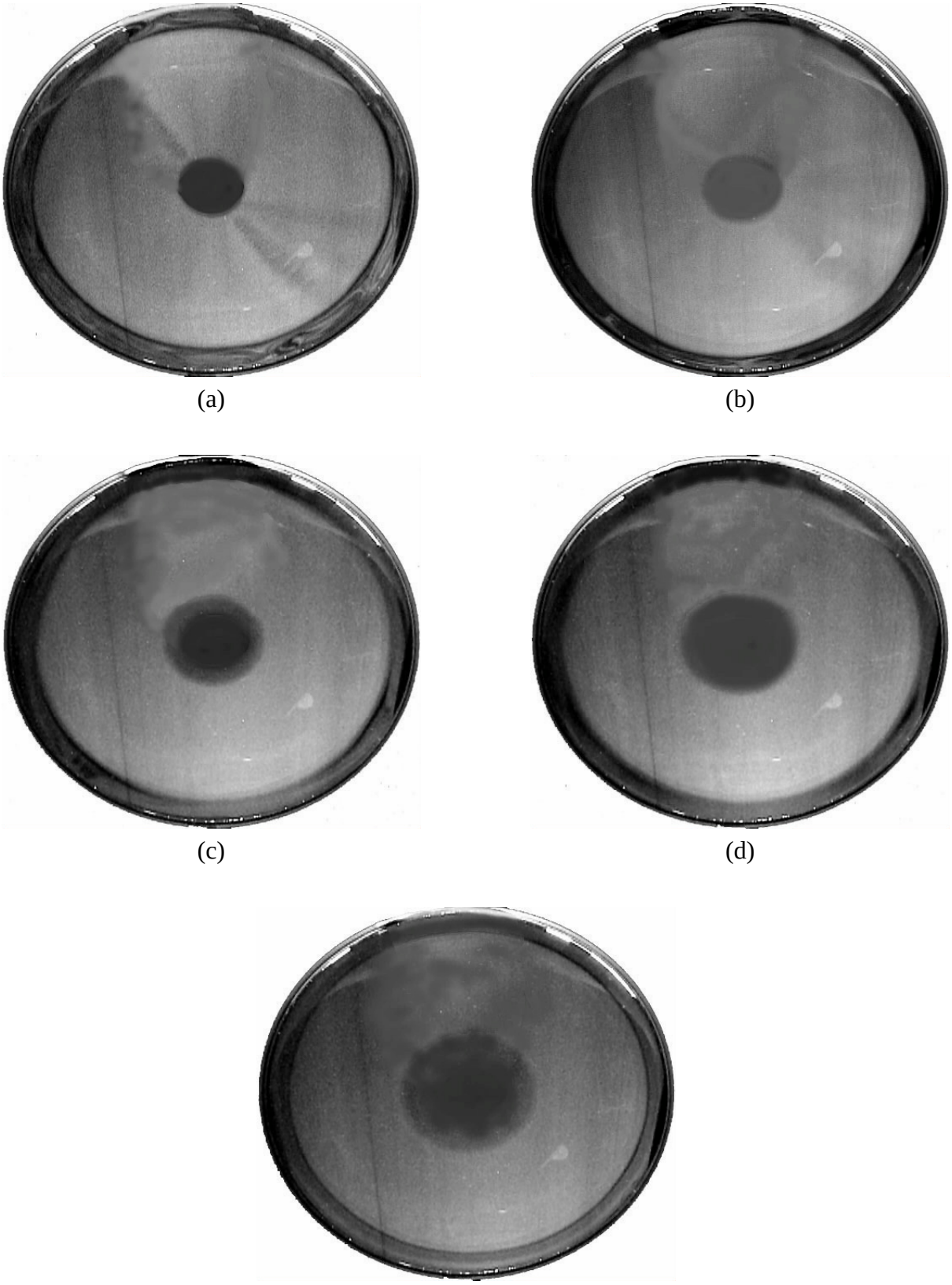

Fig. 3.20 Steady top view flow photos taken at the middle horizontal plane between the disk and chamber top with Ra=0 ($\Delta T=0$℃) & D_j=22.1 mm at H=15.0 mm for Re_j= (a) 61, (b) 122, (c) 183, (d) 245, and (e) 306.

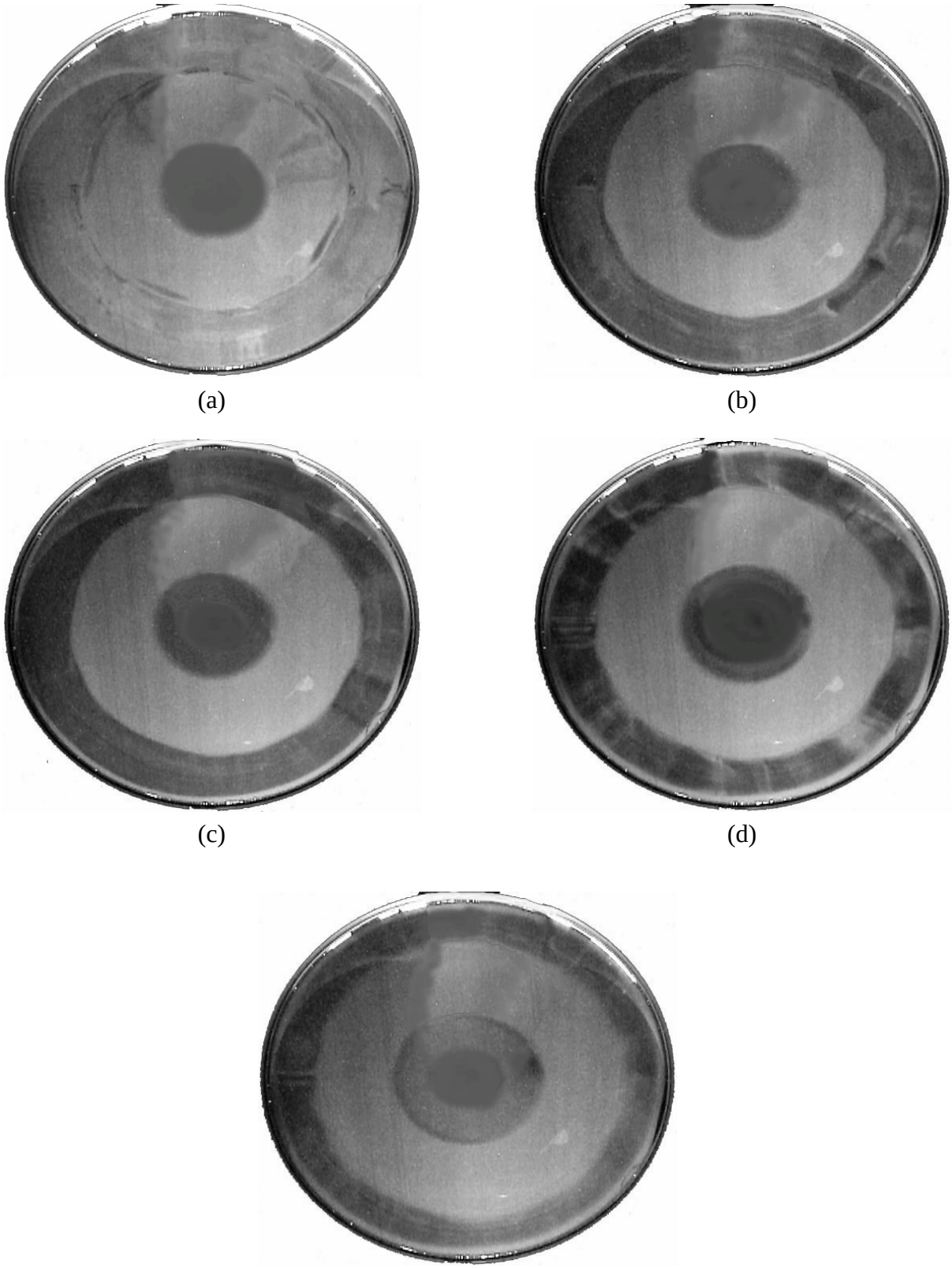

Fig. 3.21 Steady top view flow photos taken at the middle horizontal plane between the disk and chamber top with Ra=6,340 (ΔT=20.0℃) & D_j=22.1 mm at H=15.0 mm for Re_j= (a) 61, (b) 122, (c) 183, (d) 245, and (e) 306.

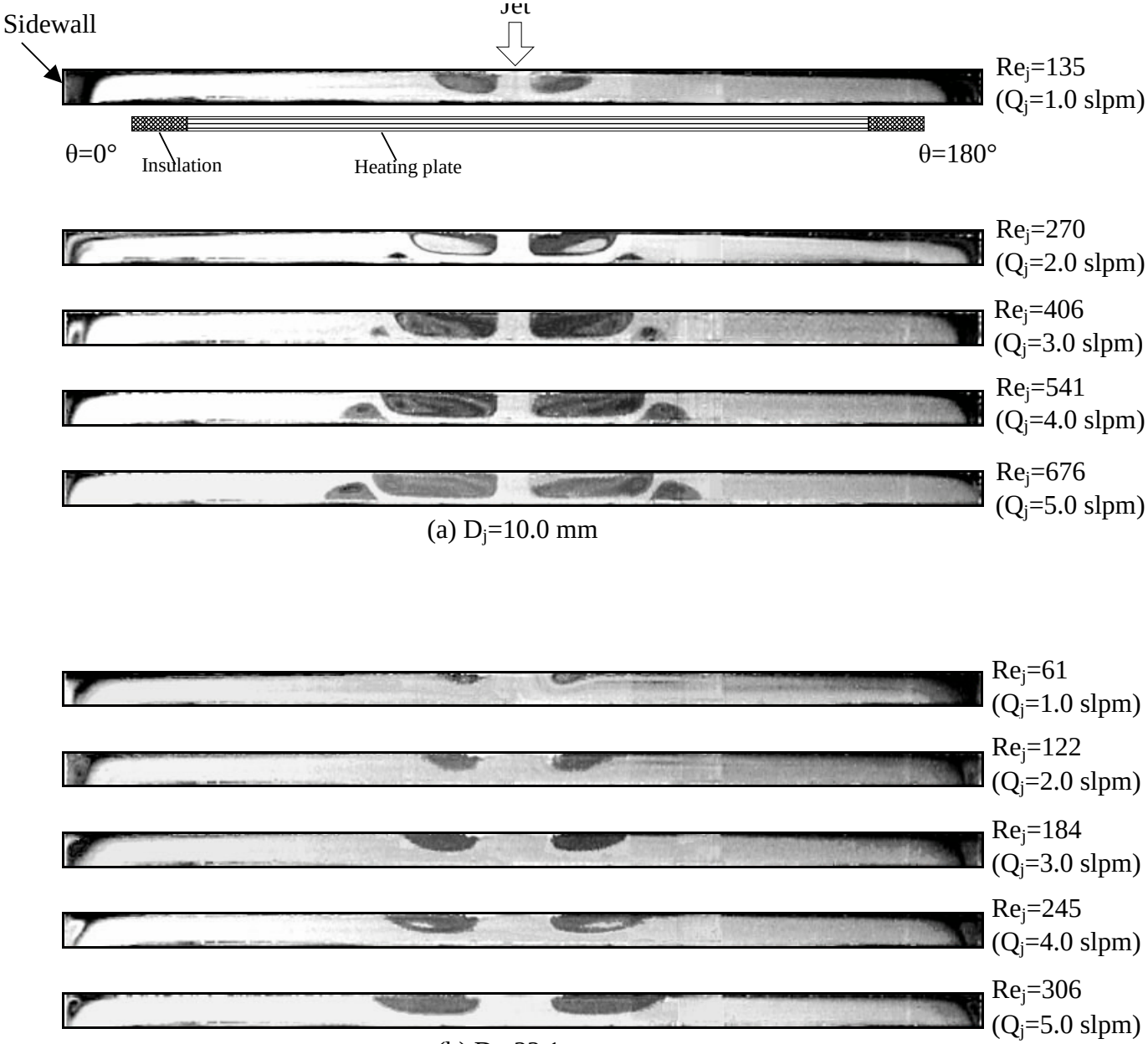

Fig. 3.22 Steady side view flow photos taken at the cross plane θ=0° & 180° for various jet Reynolds numbers at H=10.0 mm and Ra=0 (ΔT=0℃) for D$_j$= (a) 10.0 mm and (b) 22.1 mm.

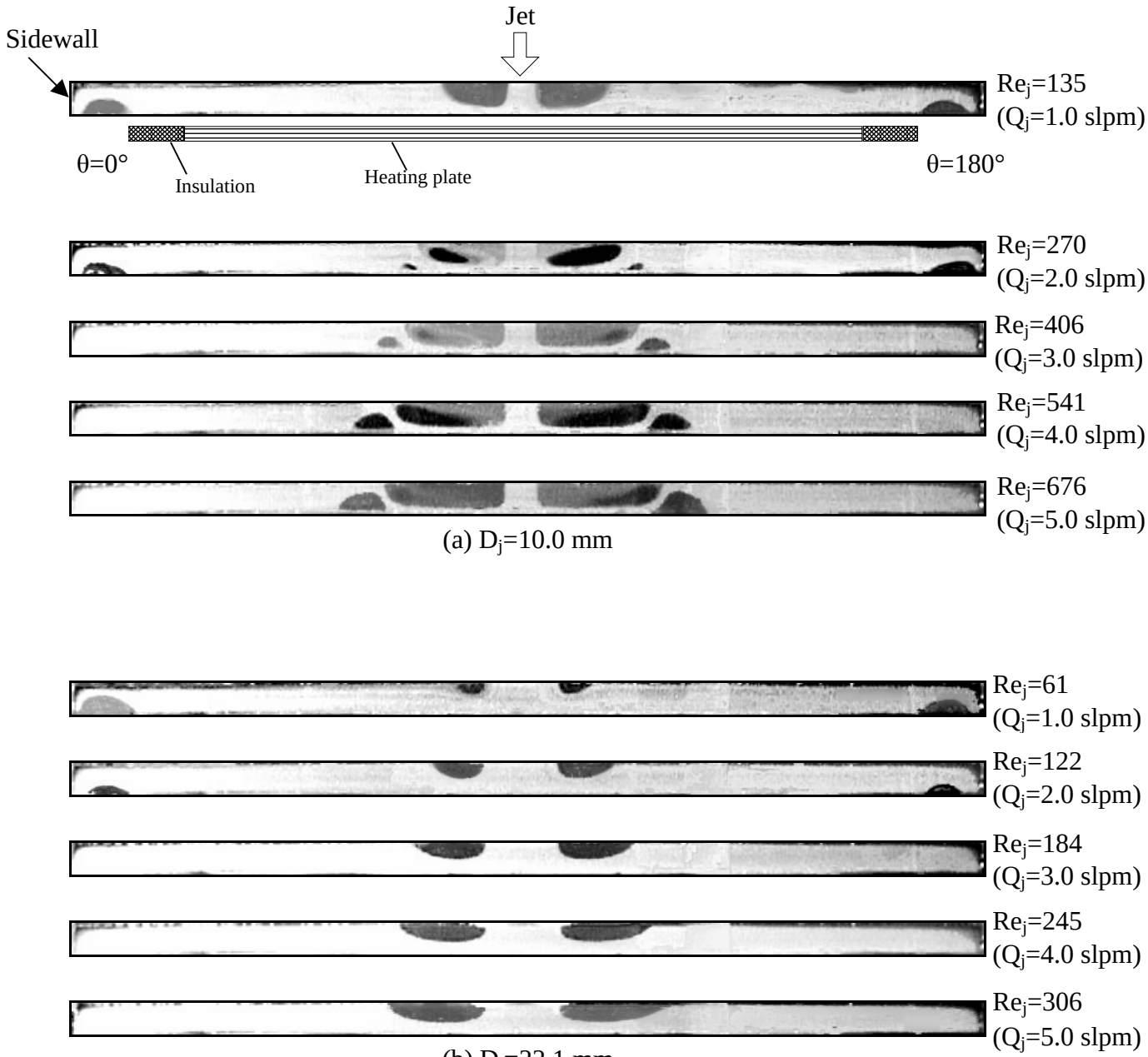

Fig. 3.23 Steady side view flow photos taken at the cross plane θ=0° & 180° for various jet Reynolds numbers at H=10.0 mm and Ra=470 (ΔT=5.0℃) for D$_j$= (a) 10.0 mm and (b) 22.1 mm.

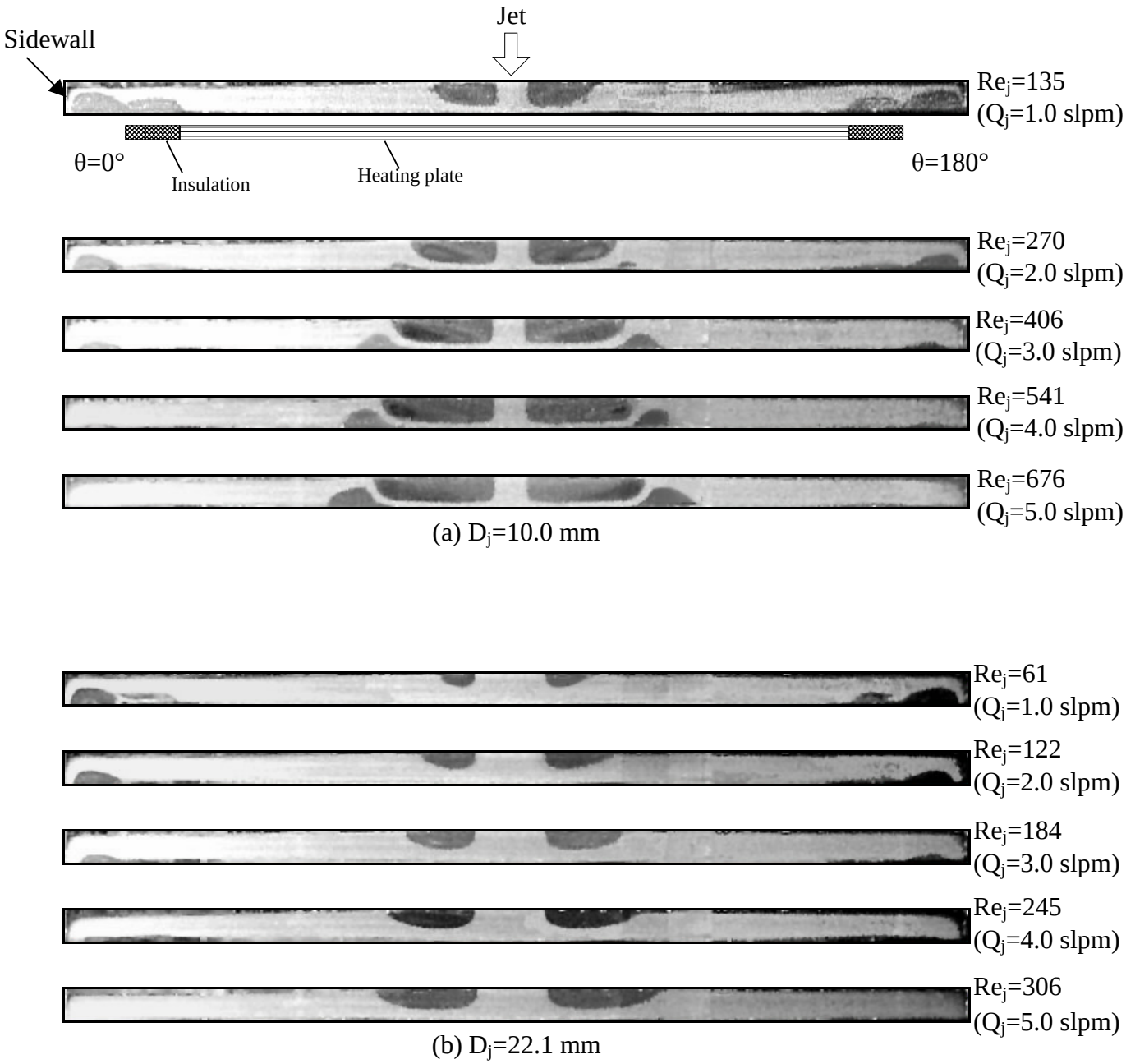

Fig. 3.24 Steady side view flow photos taken at the cross plane θ=0° & 180° for various jet Reynolds numbers at H=10.0 mm and Ra=940 (ΔT=10.0℃) for D$_j$= (a) 10.0 mm and (b) 22.1 mm.

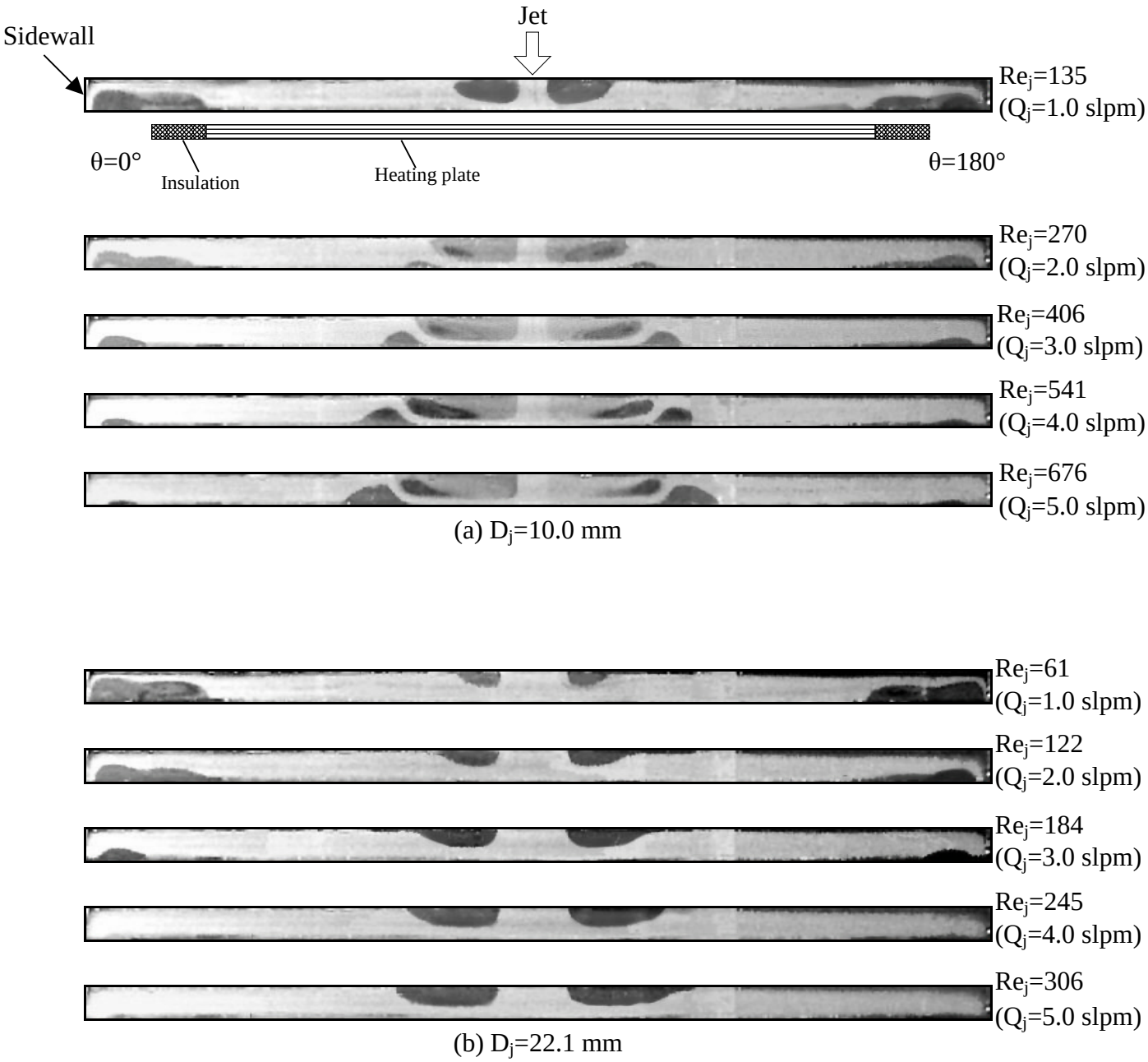

Fig. 3.25 Steady side view flow photos taken at the cross plane θ=0° & 180° for various jet Reynolds numbers at H=10.0 mm and Ra=1,410 (ΔT=15.0℃) for D$_j$= (a) 10.0 mm and (b) 22.1 mm.

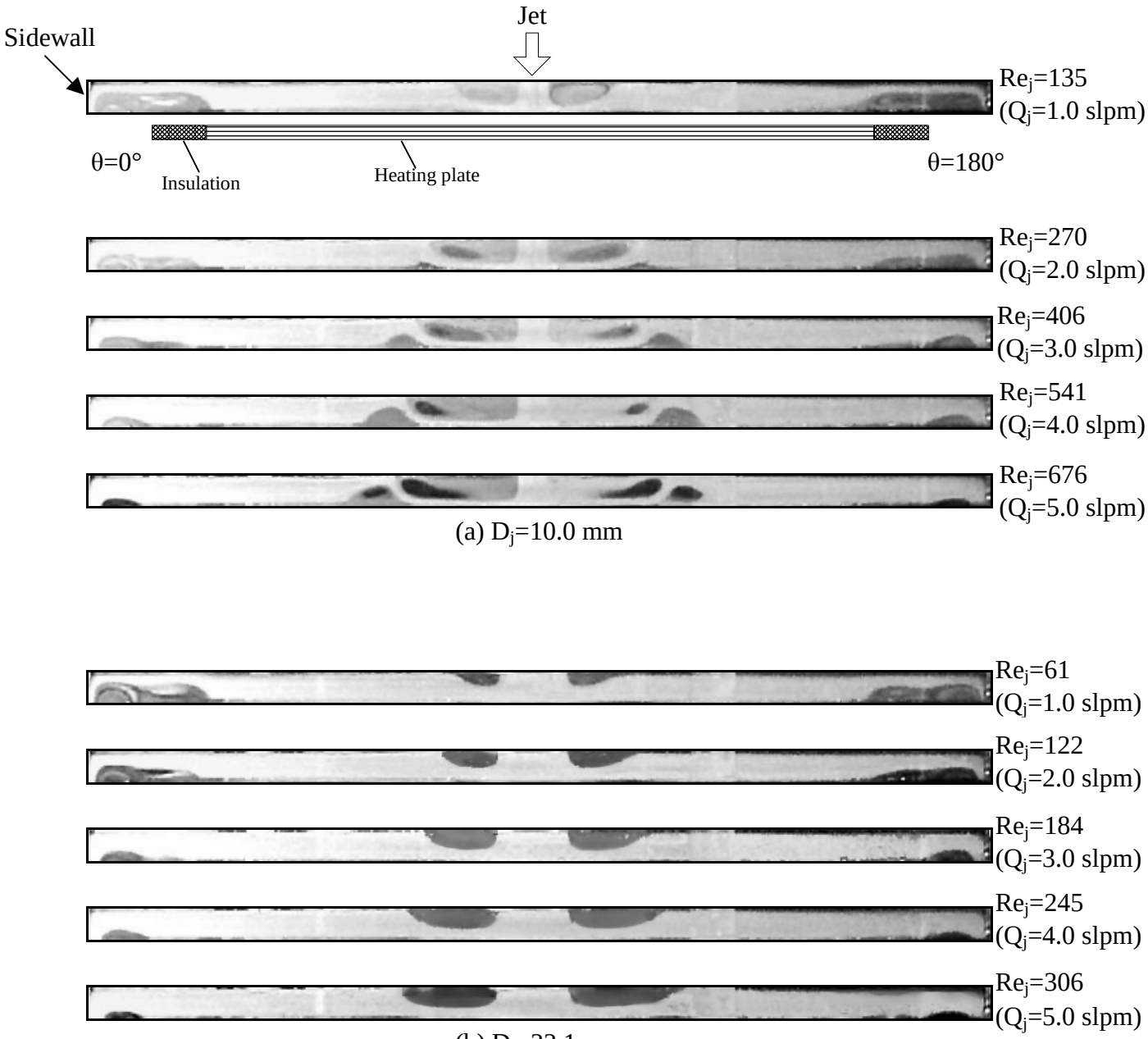

Fig. 3.26 Steady side view flow photos taken at the cross plane θ=0° & 180° for various jet Reynolds numbers at H=10.0 mm and Ra=1,880 (ΔT=20.0℃) for D$_j$= (a) 10.0 mm and (b) 22.1 mm.

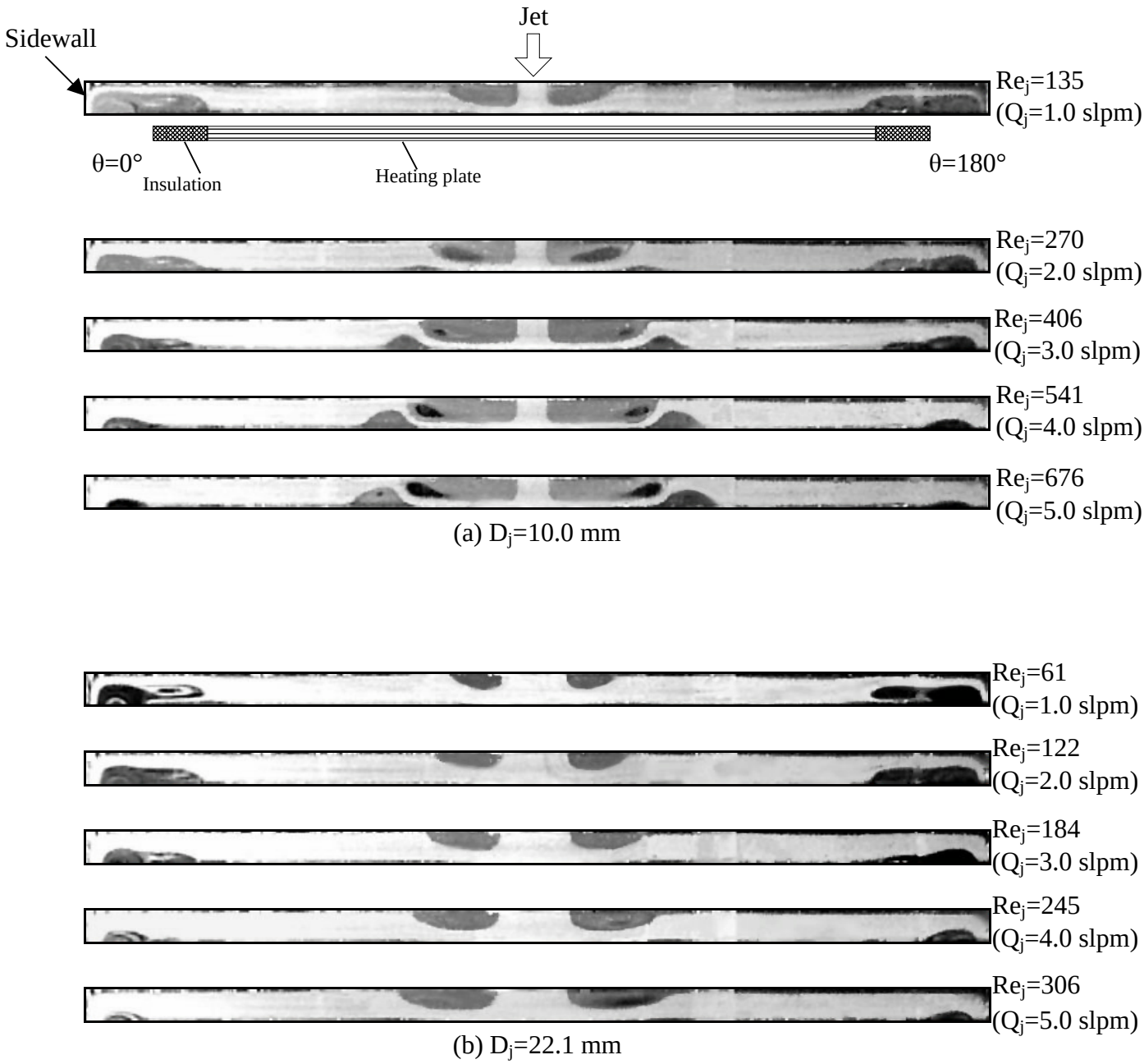

Fig. 3.27 Steady side view flow photos taken at the cross plane θ=0° & 180° for various jet Reynolds numbers at H=10.0 mm and Ra=2,350 (ΔT=25.0℃) for D$_j$= (a) 10.0 mm and (b) 22.1 mm.

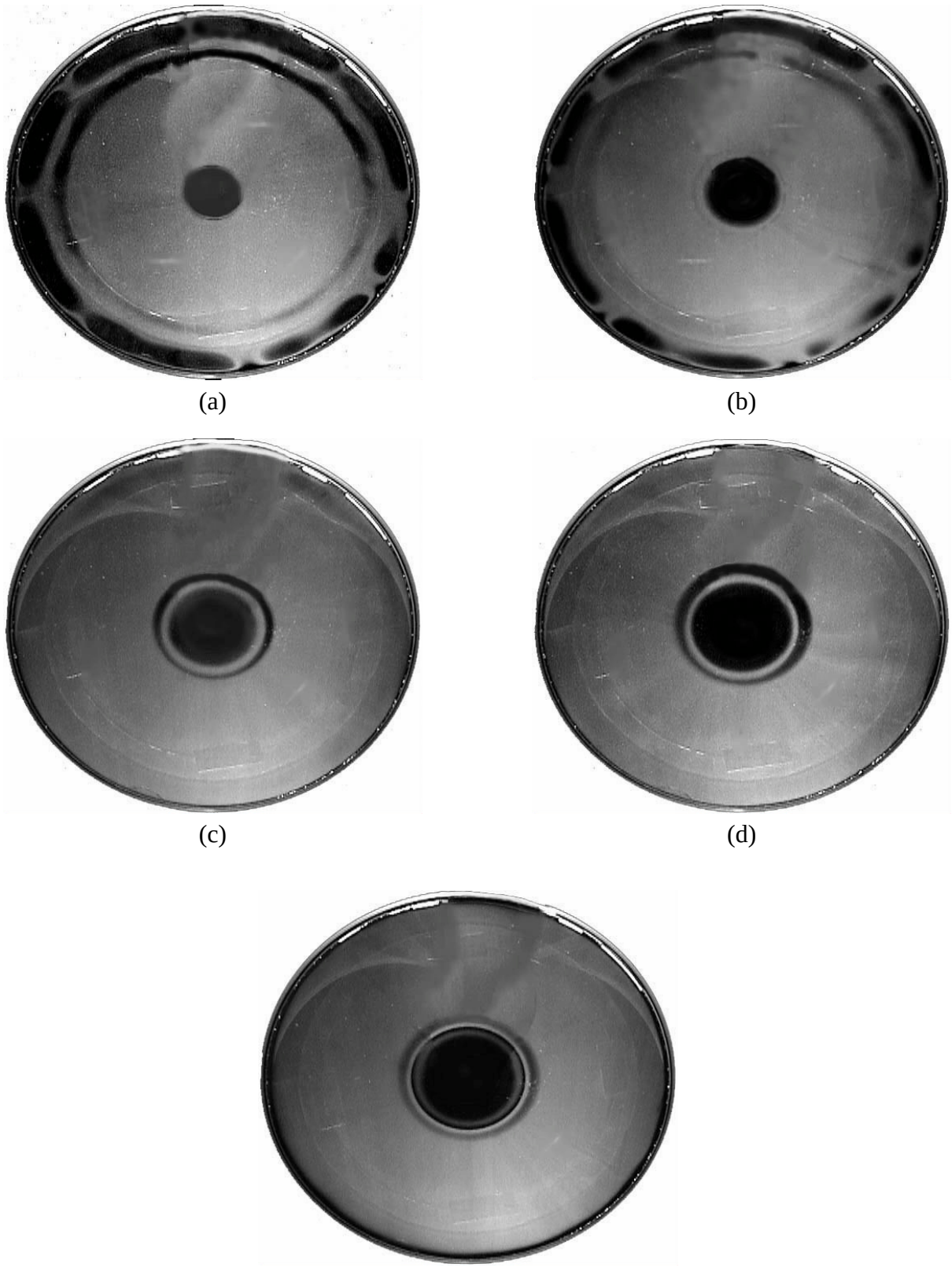

Fig. 3.28 Top view flow photos taken at the middle horizontal plane between the disk and chamber top with Ra =940 (ΔT=10.0℃) and D_j=10.0 mm at H=10.0 mm for Re_j= (a) 135, (b) 270, (c) 406, (d) 541, and (e) 676.

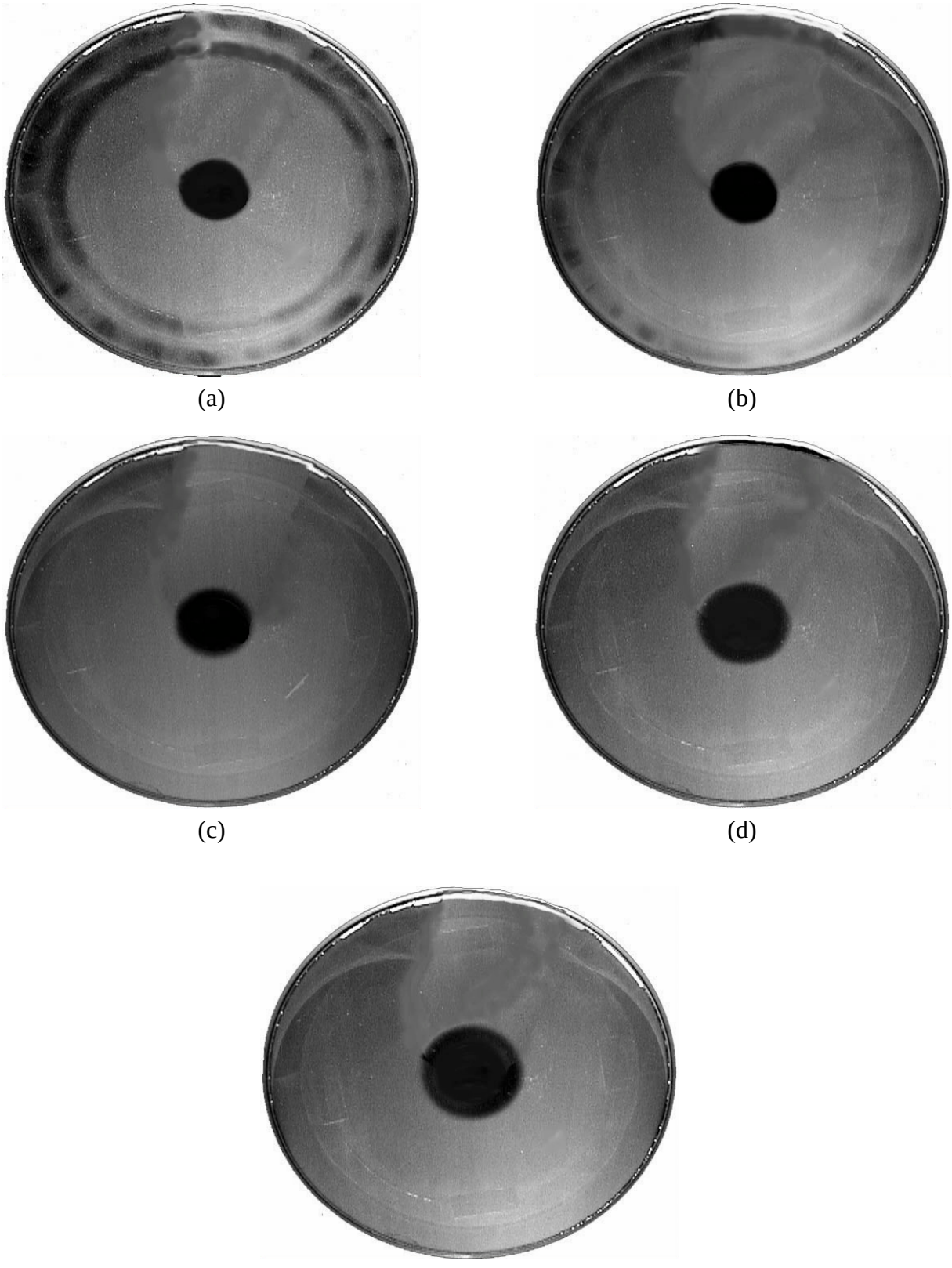

Fig. 3.29 Top view flow photos taken at the middle horizontal plane between the disk and chamber top with Ra=1,880 (ΔT=20.0℃) and D_j=22.1mm at H=10.0 mm for Re_j= (a) 61, (b) 122, (c) 184, (d) 245, and (e) 306.

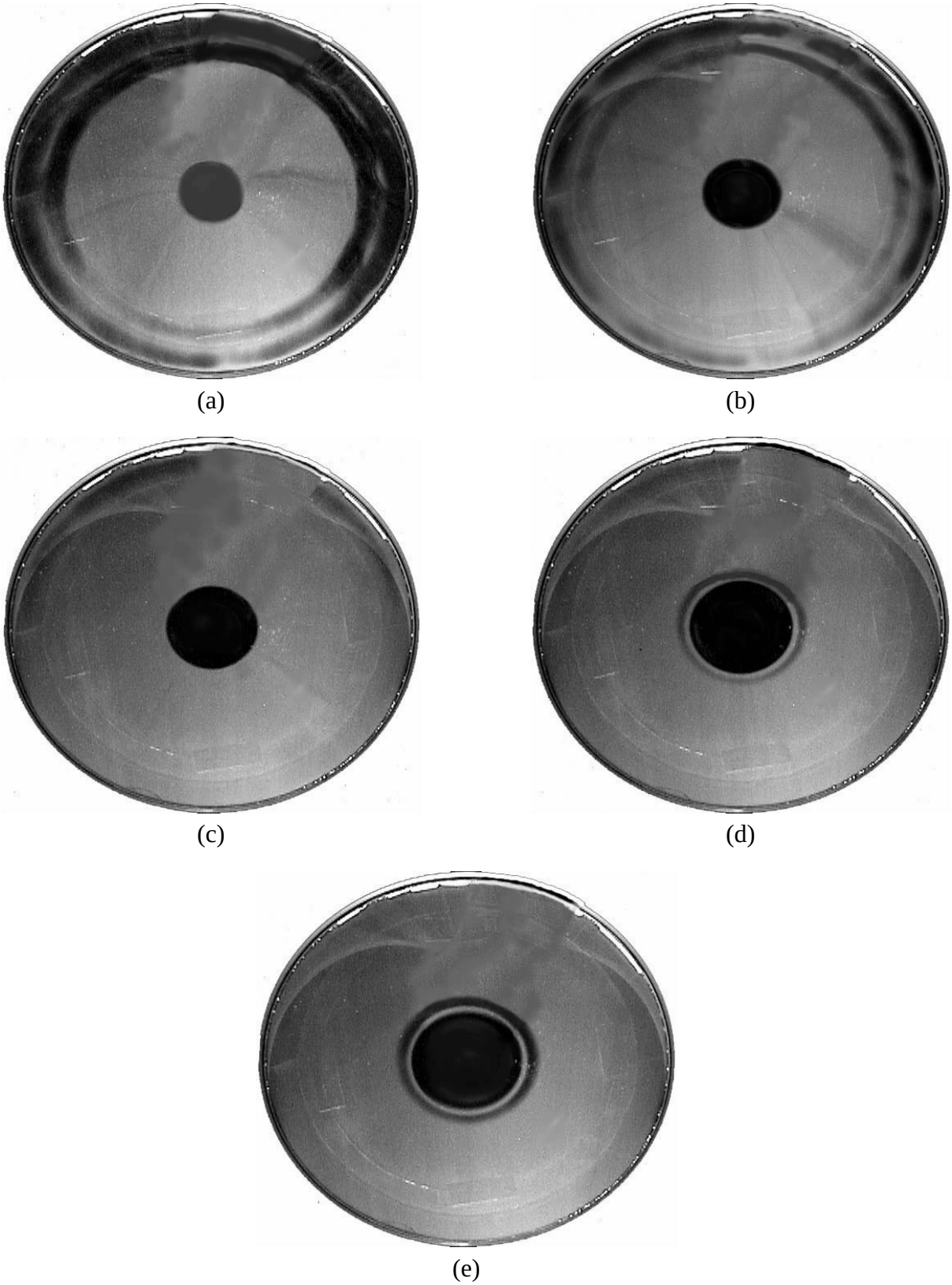

Fig. 3.30 Top view flow photos taken at the middle horizontal plane between the disk and chamber top with Ra =2,350 (ΔT=25.0℃) and D_j=10.0 mm at H=10.0 mm for Re_j= (a) 135, (b) 270, (c) 406, (d) 541, and (e) 676.

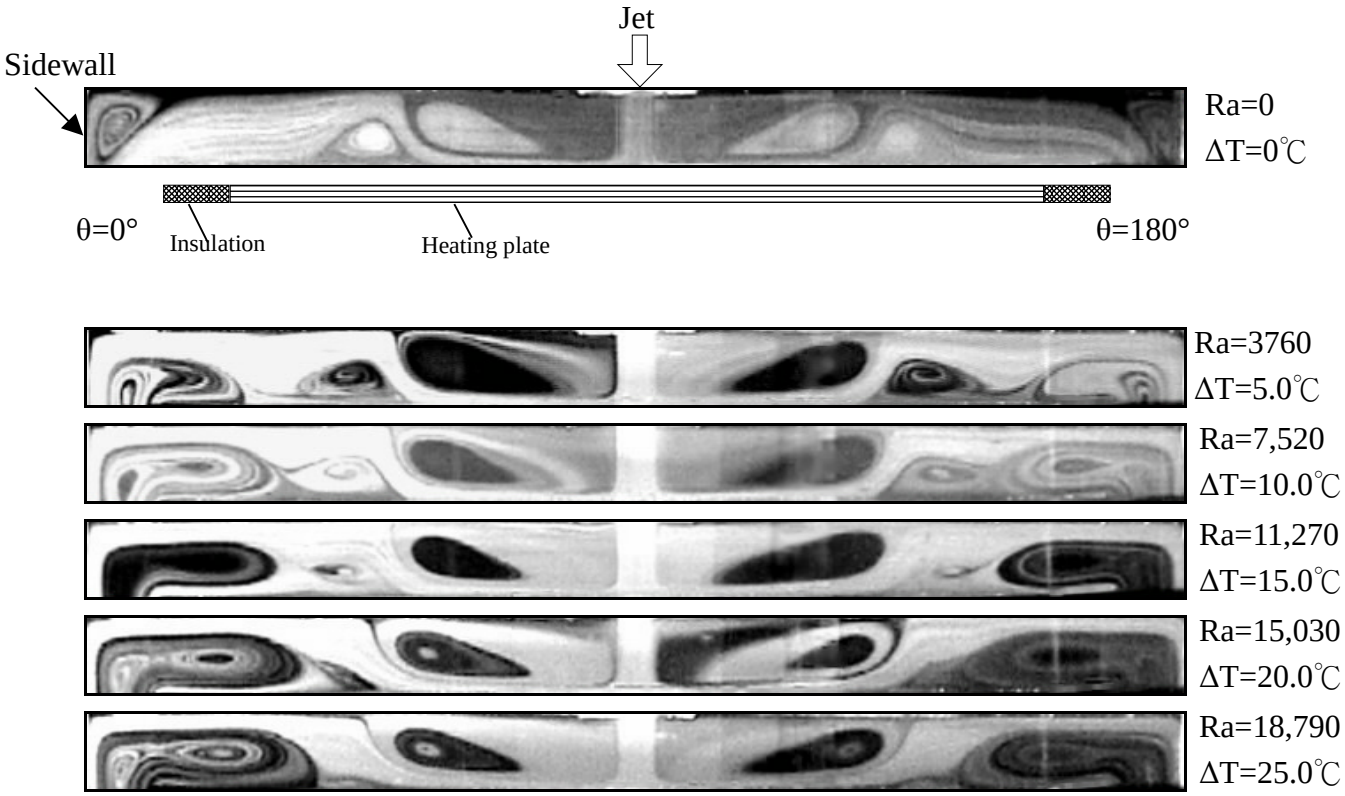

(a) D_j=10.0 mm & Re_j=406

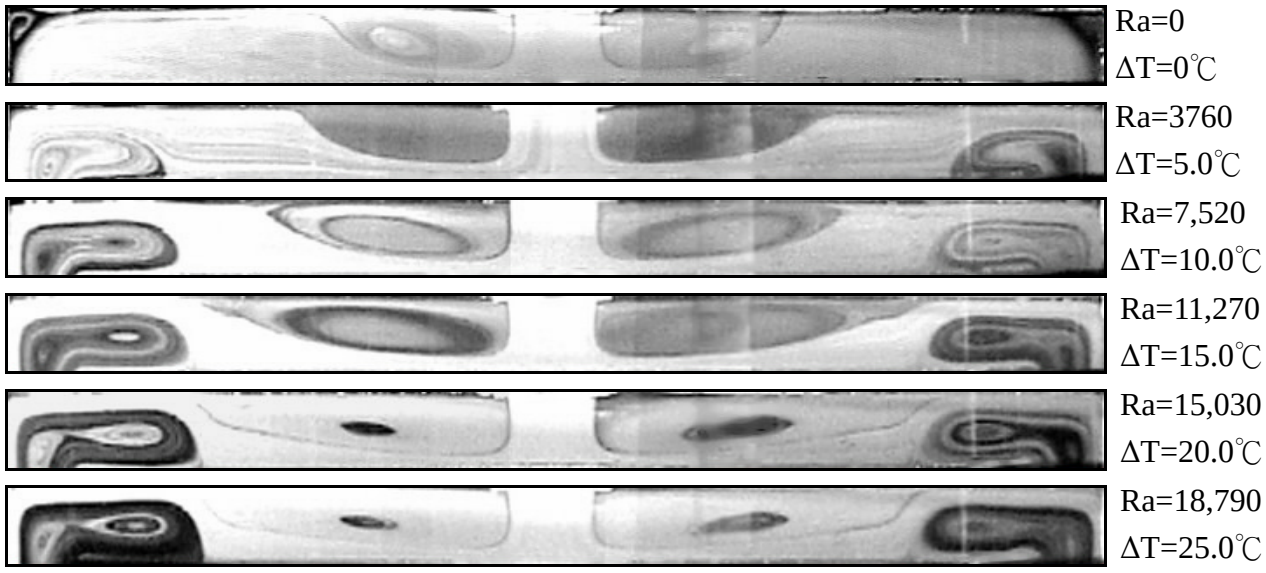

(b) D_j=22.1 mm & Re_j=184

Fig. 3.31 Steady side view flow photos taken at the cross plane θ=0° & 180° for various Rayleigh numbers at Q_j=3.0 slpm for D_j= (a) 10.0 mm & Re_j=406 and (b) 22.1 mm & Re_j=184.

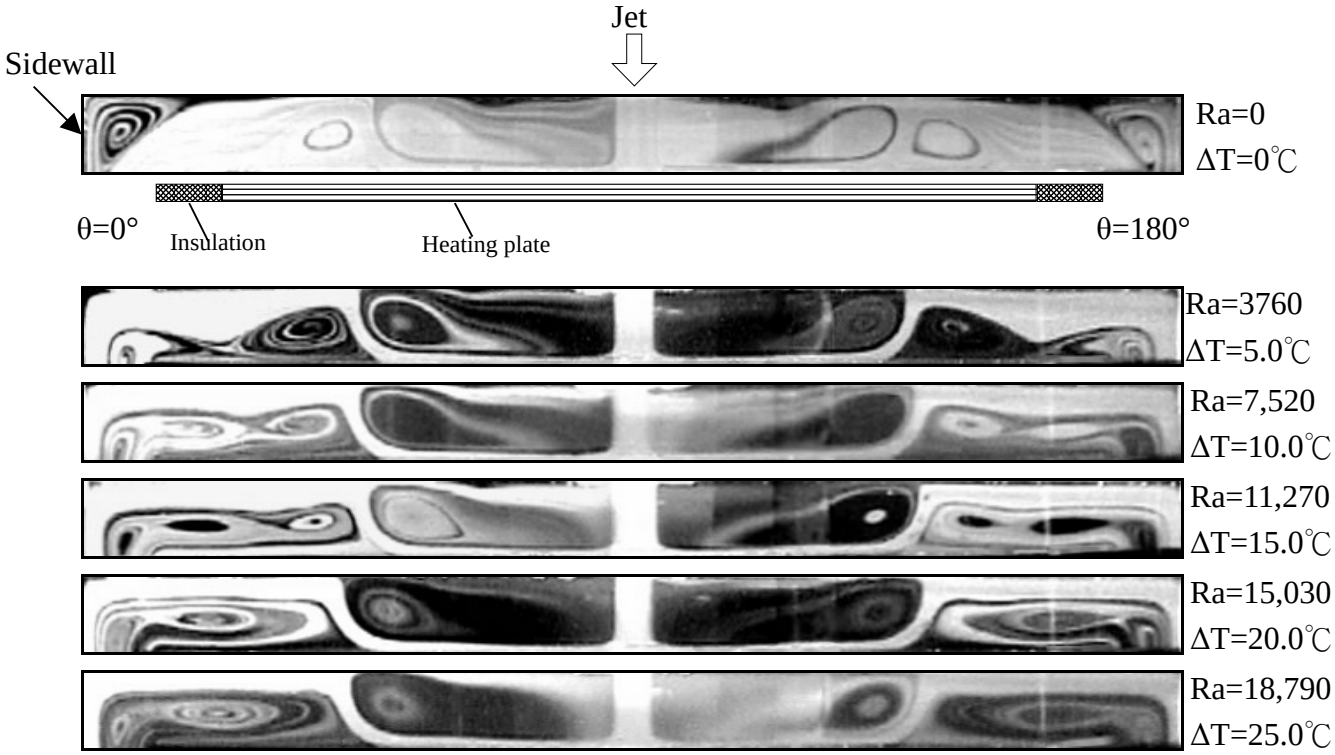

(a) D_j=10.0 mm & Re_j=676

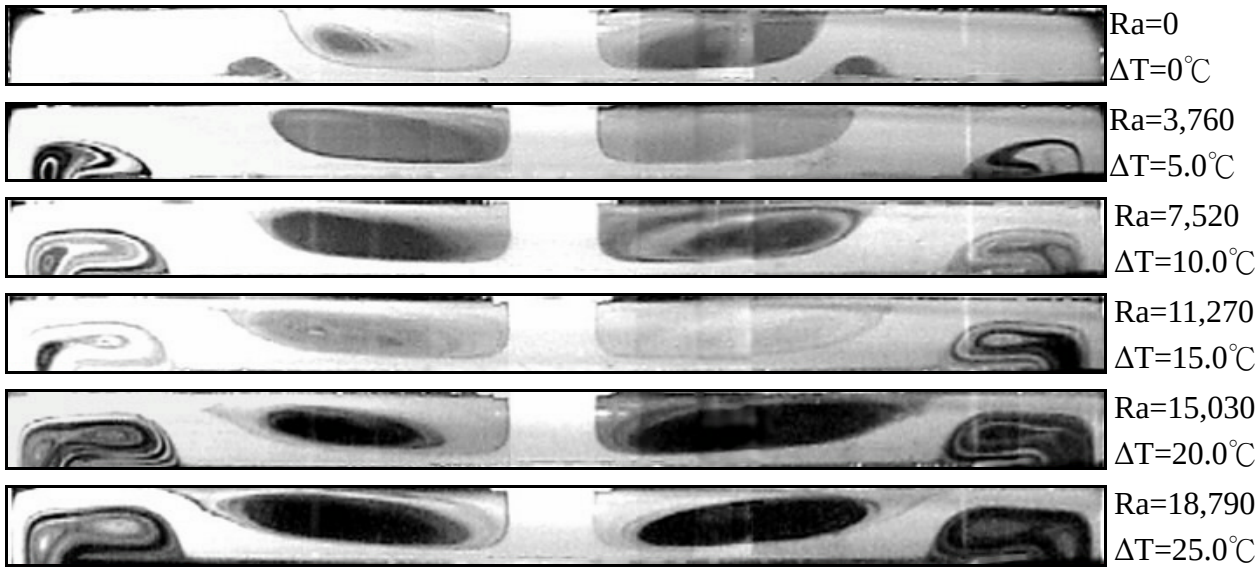

(b) D_j=22.1 mm & Re_j=306

Fig. 3.32 Steady side view flow photos taken at the cross plane θ=0° & 180° for various Rayleigh numbers at Q_j=5.0 slpm for D_j= (a) 10.0 mm & Re_j=676 and (b) 22.1 mm & Re_j=306.

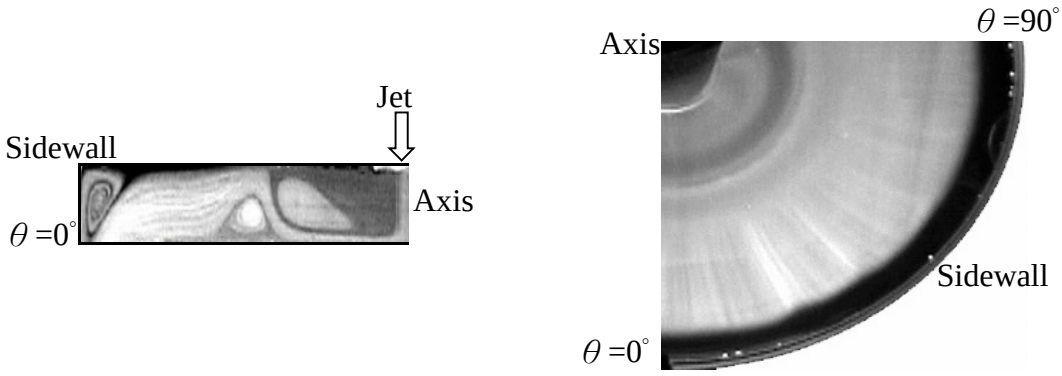

(a) Ra=0 & Re_j=406

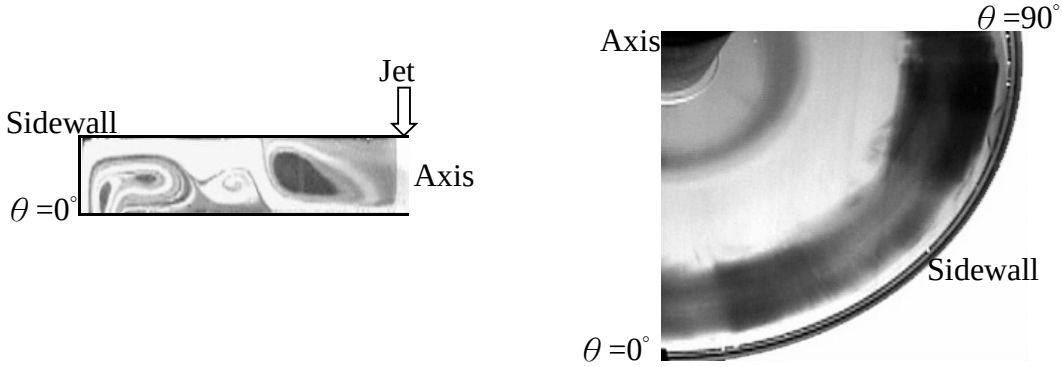

(b) Ra=7,520 & Re_j=406

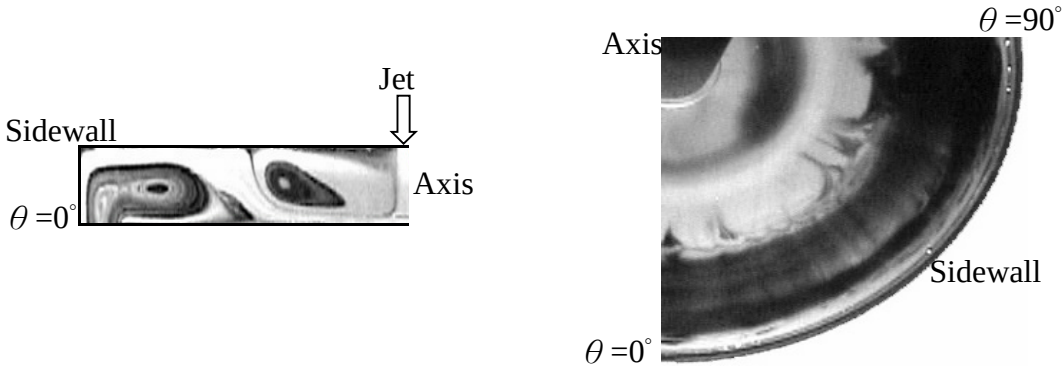

(c) Ra=15,030 & Re_j=406

Fig. 3.33 Half of side view flow photos taken at θ =0° (left) and quarter of top view flow photos (right) taken at midheight of the chamber with Q_j=3.0 slpm, H=20.0 mm and D_j=10.0 mm at steady state for Ra= (a) 0, (b) 7,520, and (c) 15,030.

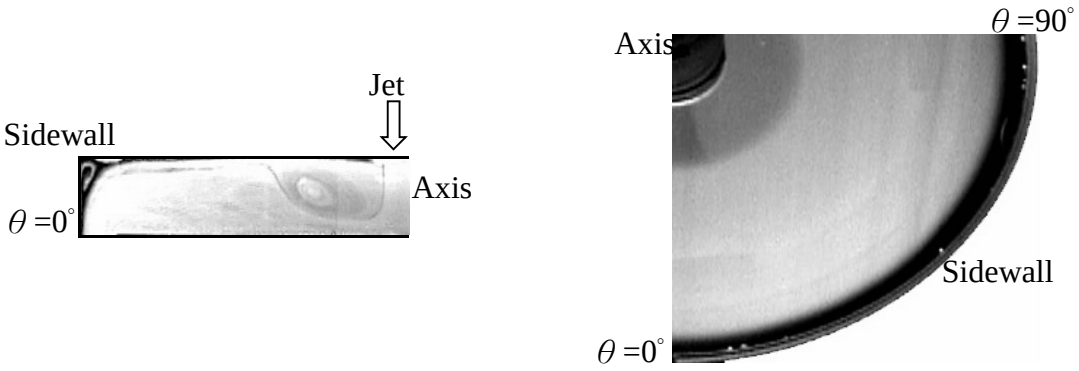

(a) Ra=0 & Re_j=184

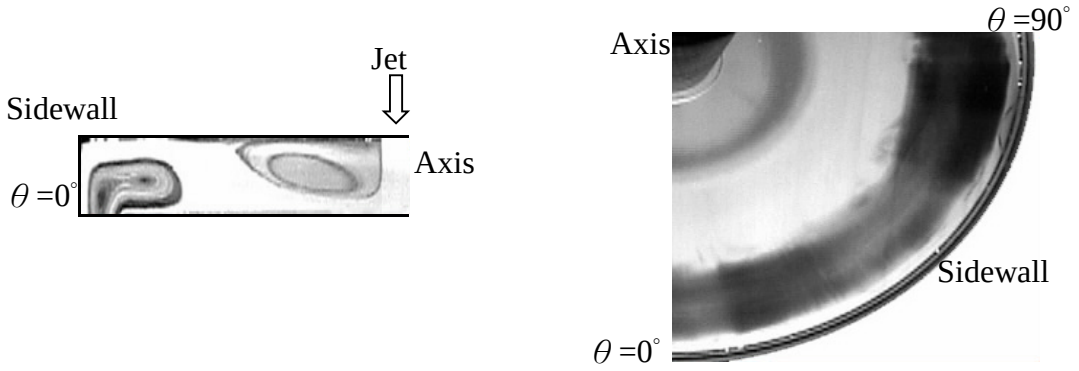

(b) Ra=7,520 & Re_j=184

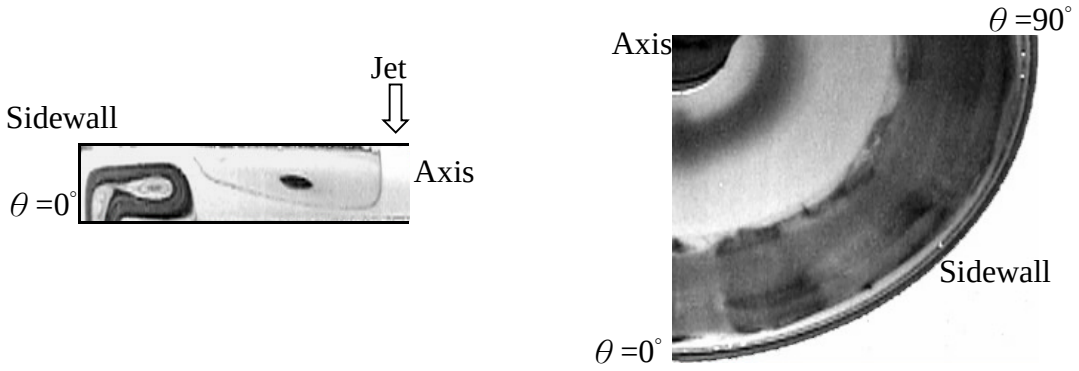

(c) Ra=15,030 & Re_j=184

Fig. 3.34 Half side view flow photos taken at θ =0° (left) and quarter of top view flow photos (right) taken at midheight of the chamber with Q_j=3.0 slpm, H=20.0 mm and D_j=22.1 mm at steady state for Ra=(a) 0, (b) 7,520, and (c) 15,030.

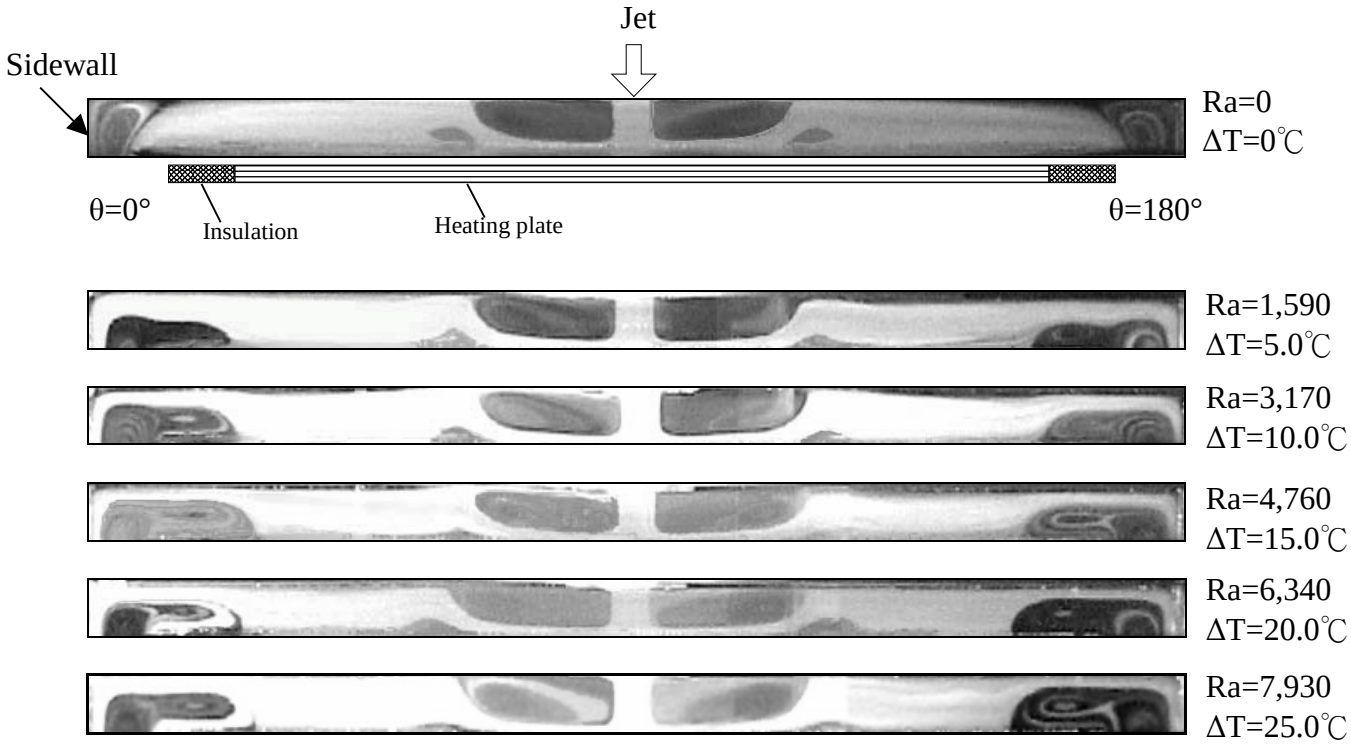

(a) D_j=10.0 mm & Re_j=270

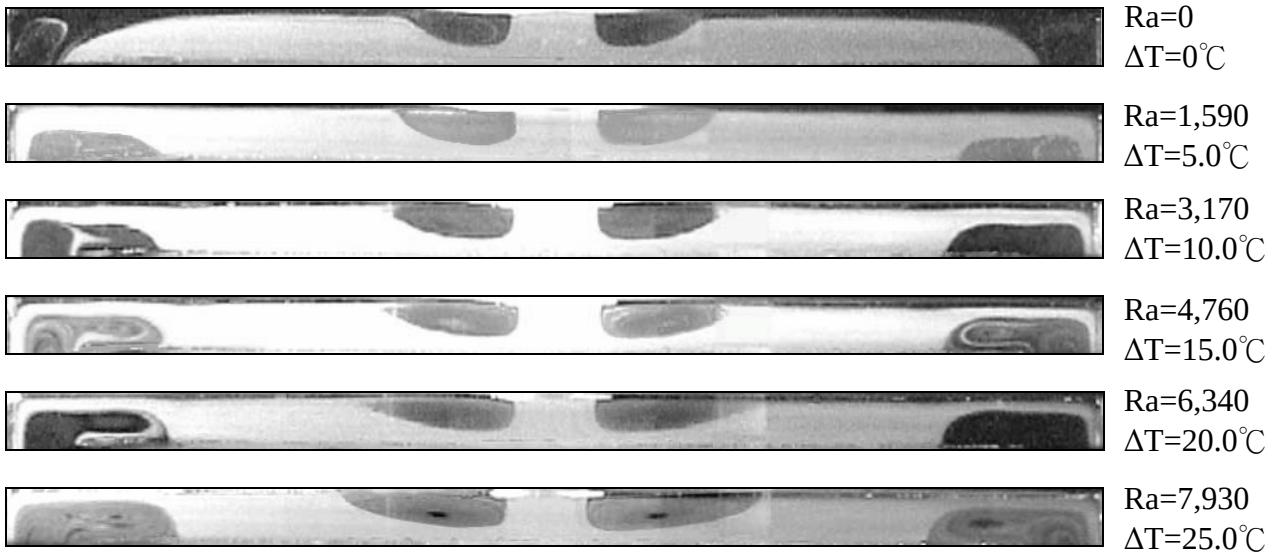

(b) D_j=22.1 mm & Re_j=122

Fig. 3.35 Steady side view flow photos taken at the cross plane θ=0° & 180° for various Rayleigh numbers at H=15.0 mm with Q_j=2.0 slpm for D_j= (a) 10.0 mm and (b) 22.1 mm.

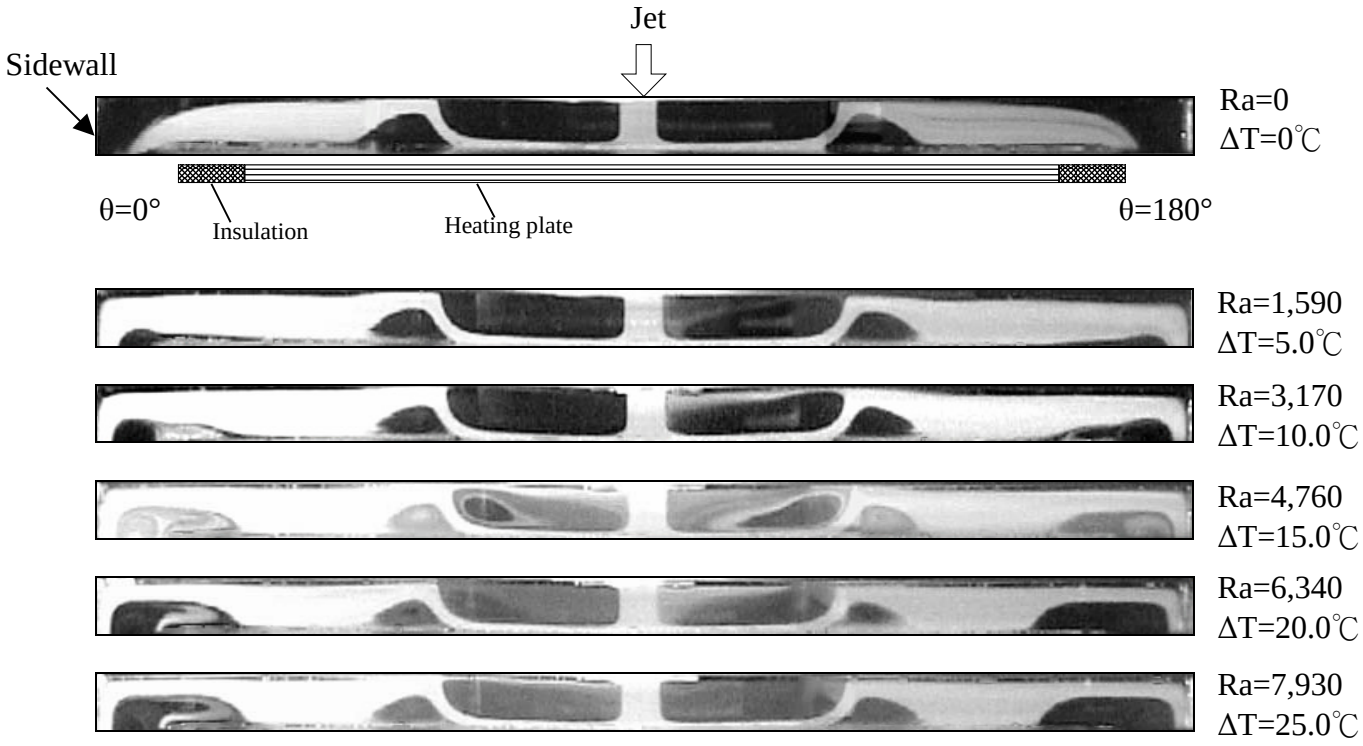

(a) D_j=10.0 mm & Re_j=541

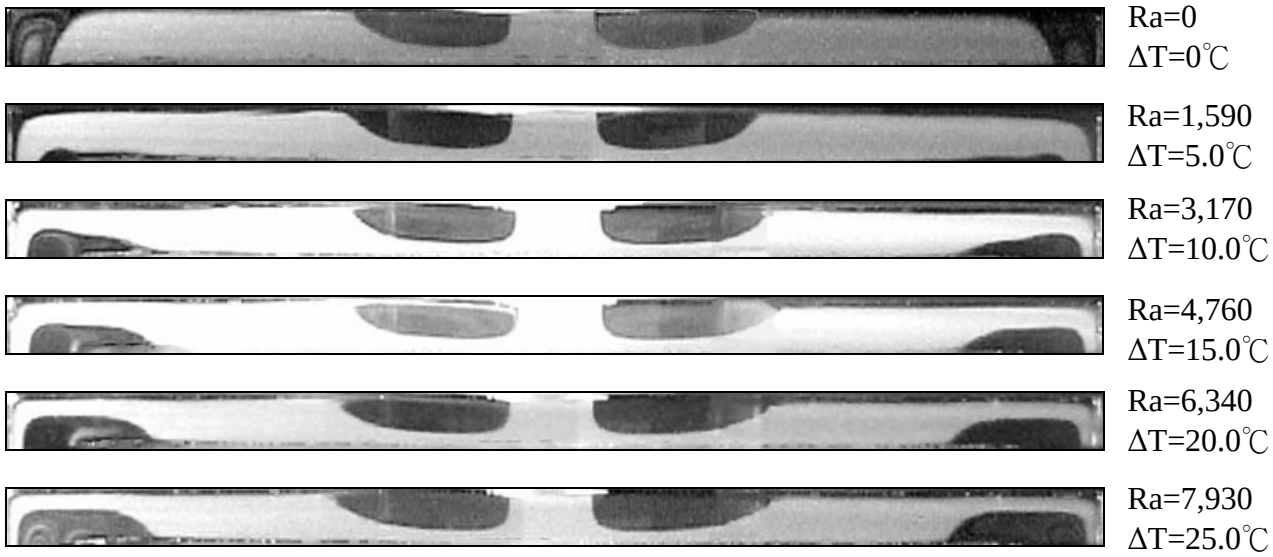

(b) D_j=22.1 mm & Re_j=240

Fig. 3.36 Steady side view flow photos taken at the cross plane θ=0° & 180° for various Rayleigh numbers at H=15.0 mm with Q_j=4.0 slpm for D_j= (a) 10.0 mm and (b) 22.1 mm.

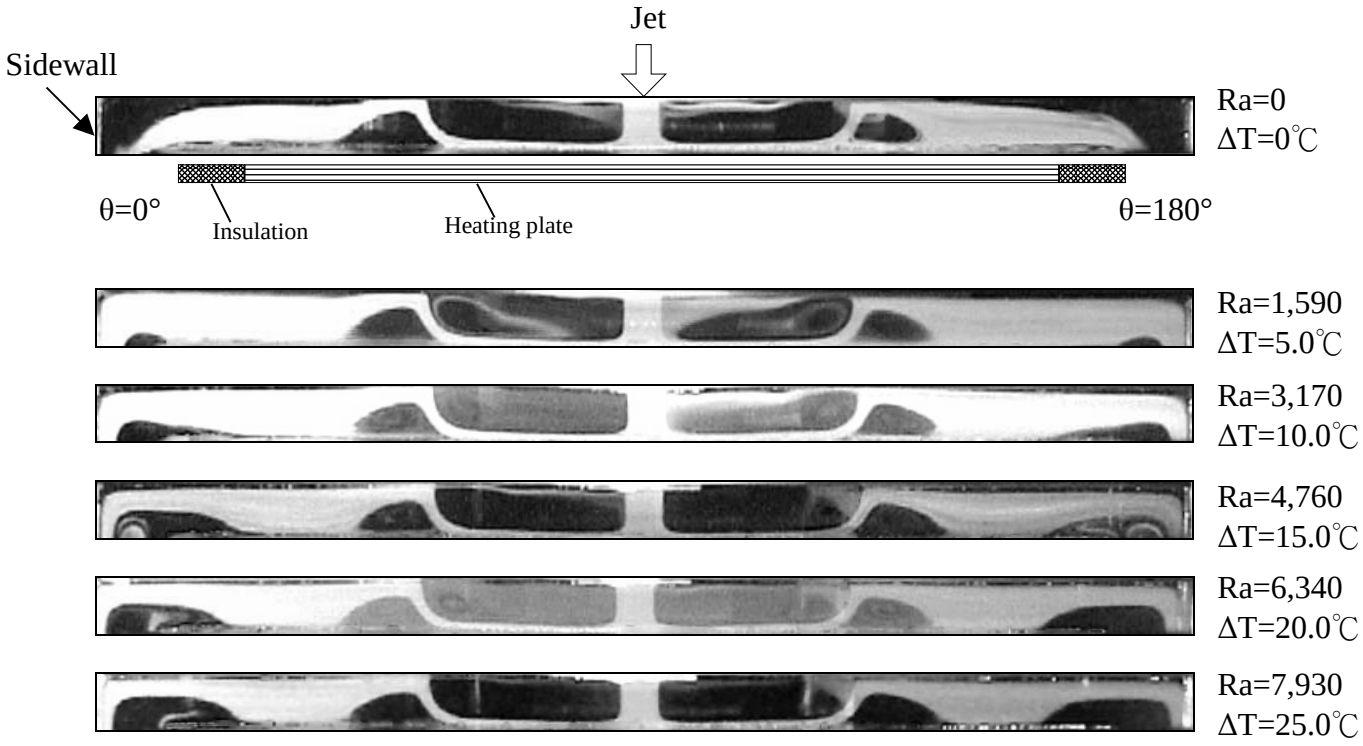

(a) D_j=10.0 mm & Re_j=676

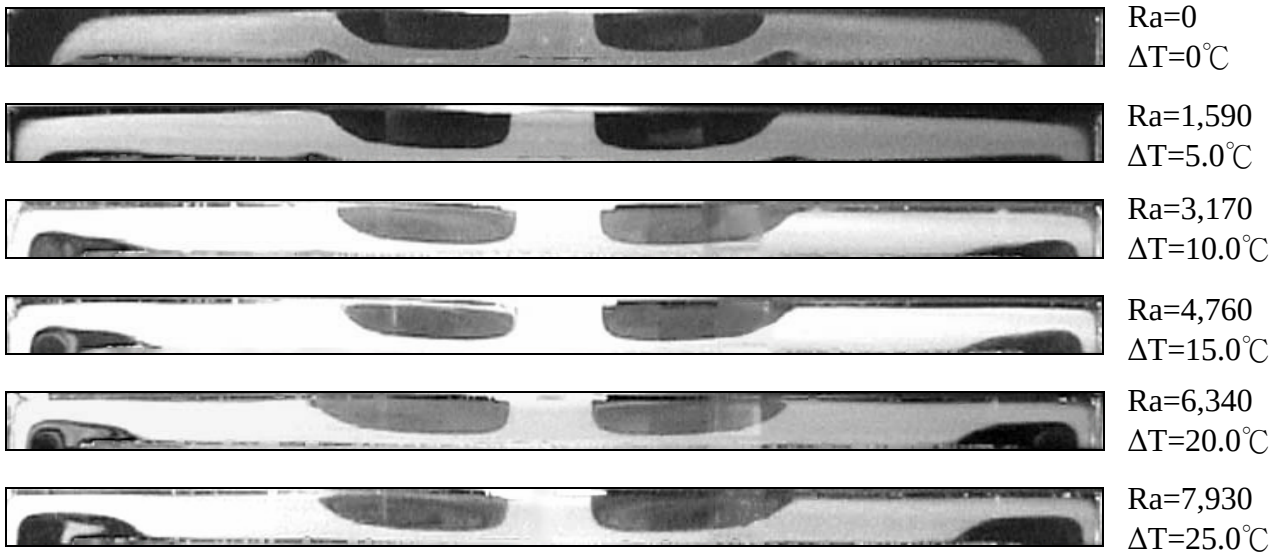

(b) D_j=22.1 mm & Re_j=306

Fig. 3.37 Steady side view flow photos taken at the cross plane θ=0° & 180° for various Rayleigh numbers at H=15.0 mm with Q_j=5.0 slpm for D_j=(a) 10.0 mm and (b) 22.1 mm.

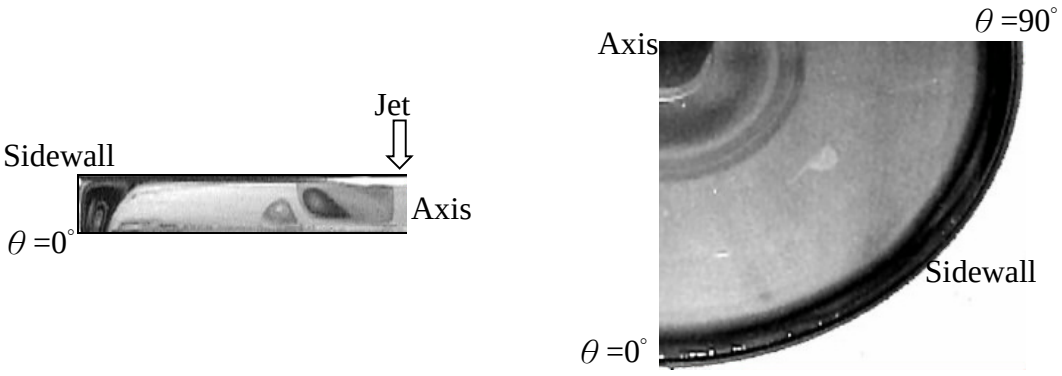

(a) Ra=0

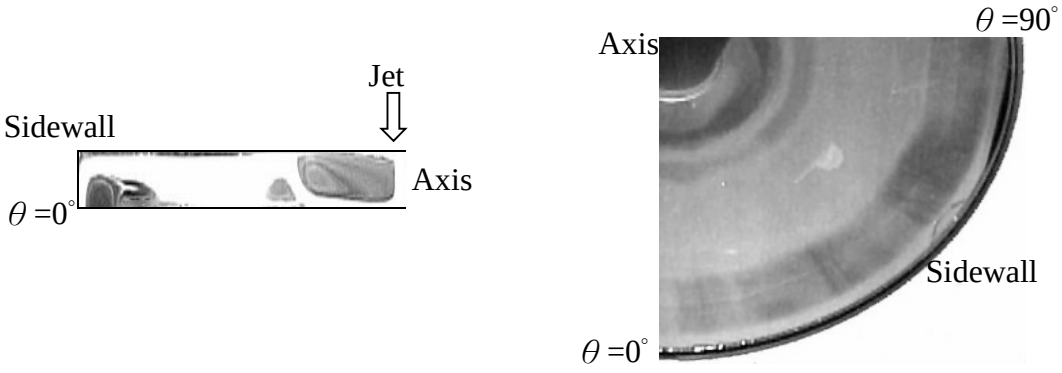

(b) Ra=3,170

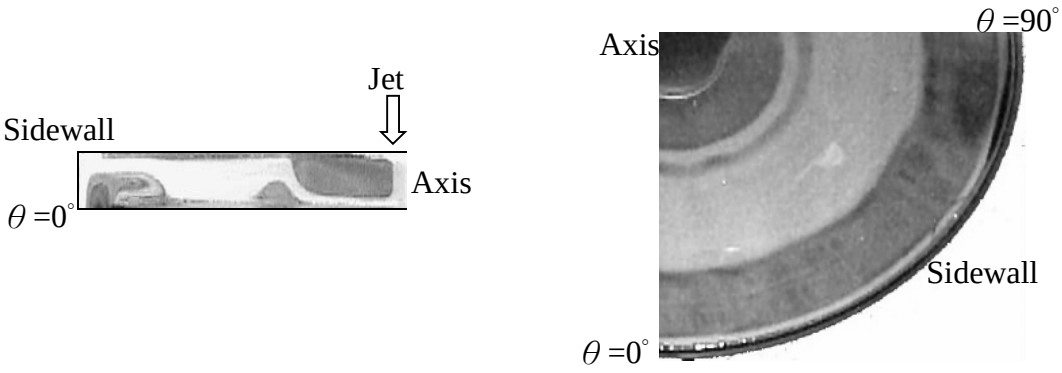

(c) Ra=6,340

Fig. 3.38 Half side view flow photos taken at θ =0° (left) and quarter of top view flow photos (right) taken at midheight of the chamber with Re_j=406, H=15.0 mm and D_j=10.0 mm at steady state for Ra= (a) 0, (b) 3,170, and (c) 6,340.

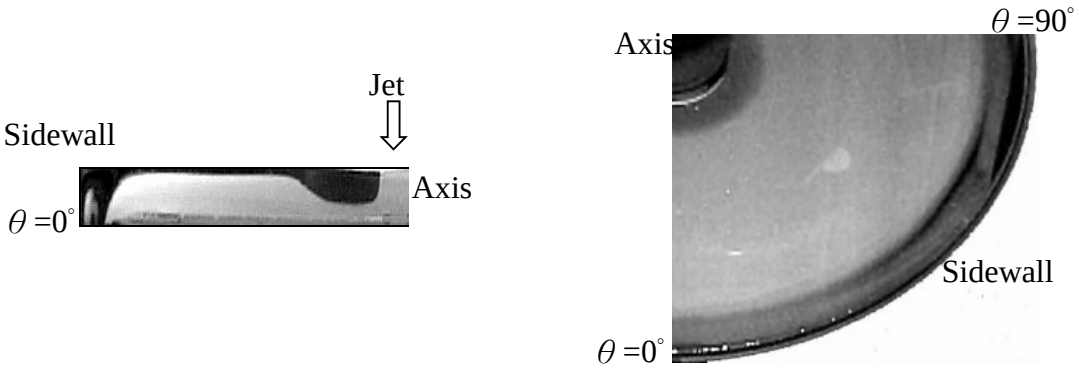

(a) Ra=0

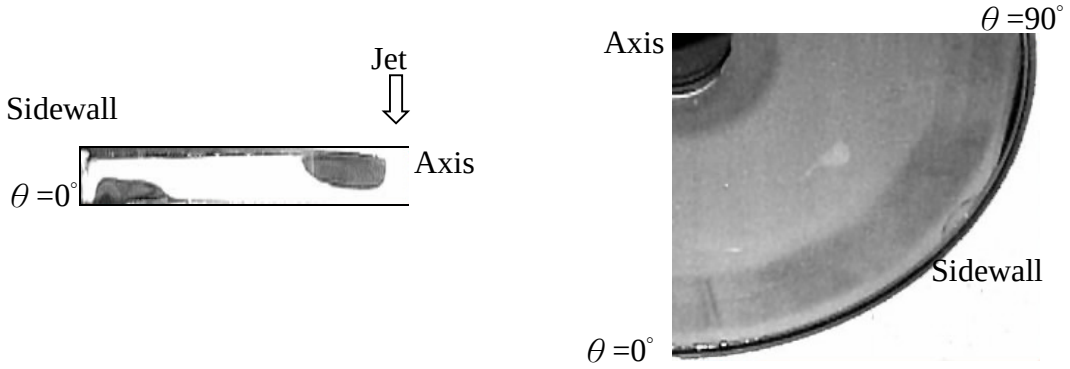

(b) Ra=3,170

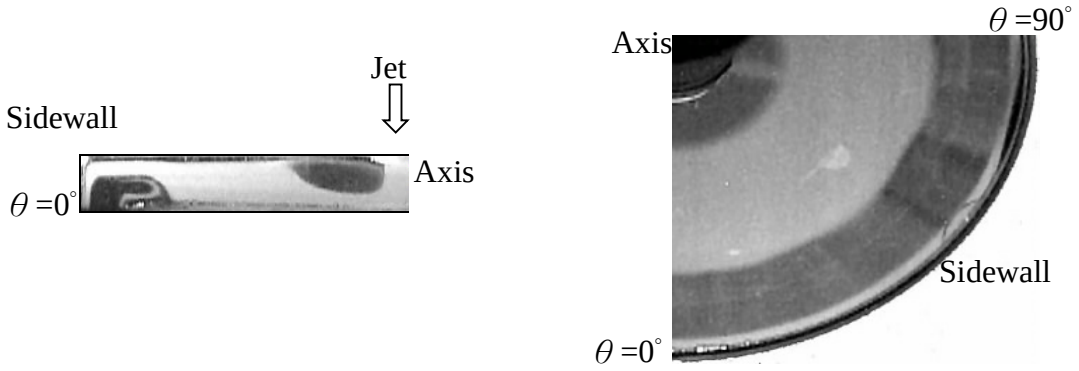

(c) Ra=6,340

Fig. 3.39 Half side view flow photos taken at θ =0° (left) and quarter of top view flow photos (right) taken at middle horizontal plane with Re_j=184, H=15.0 mm and D_j=22.1 mm at steady state for Ra=(a) 0, (b) 3,170, and (c) 6,340.

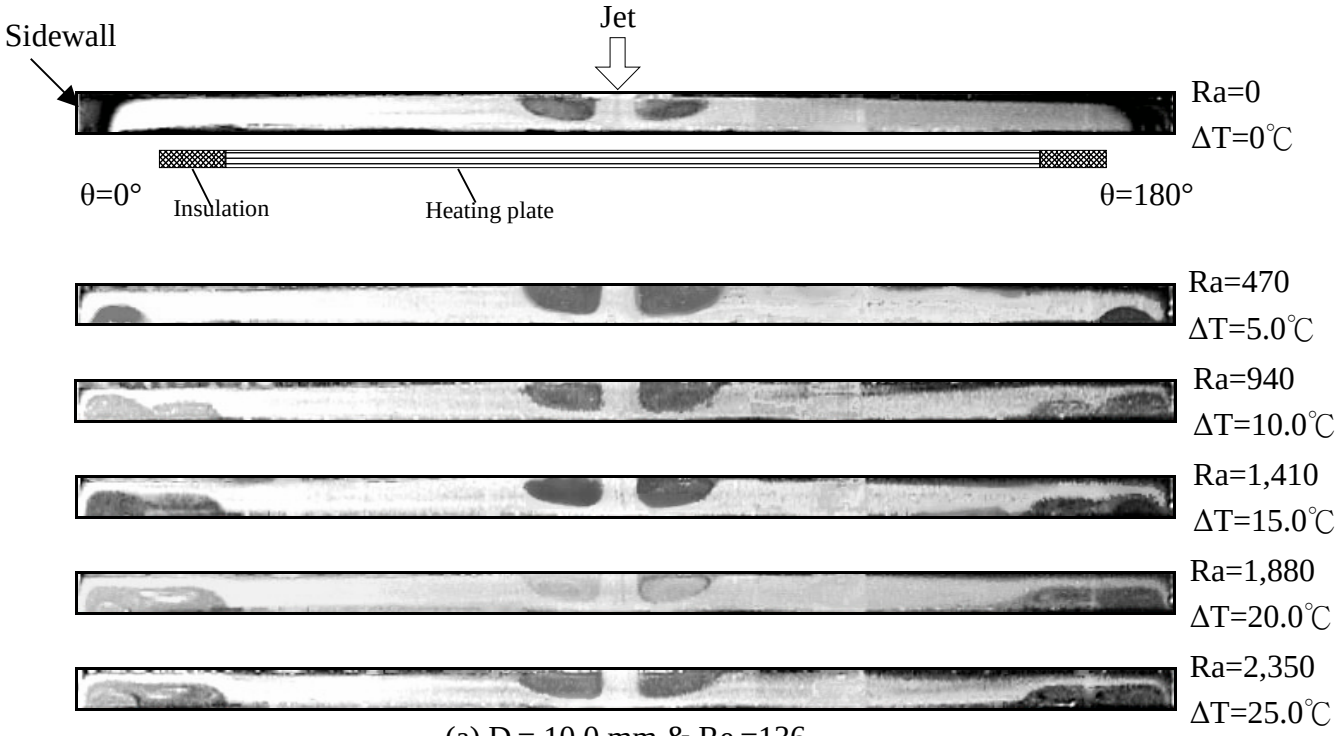

(a) D_j= 10.0 mm & Re_j=136

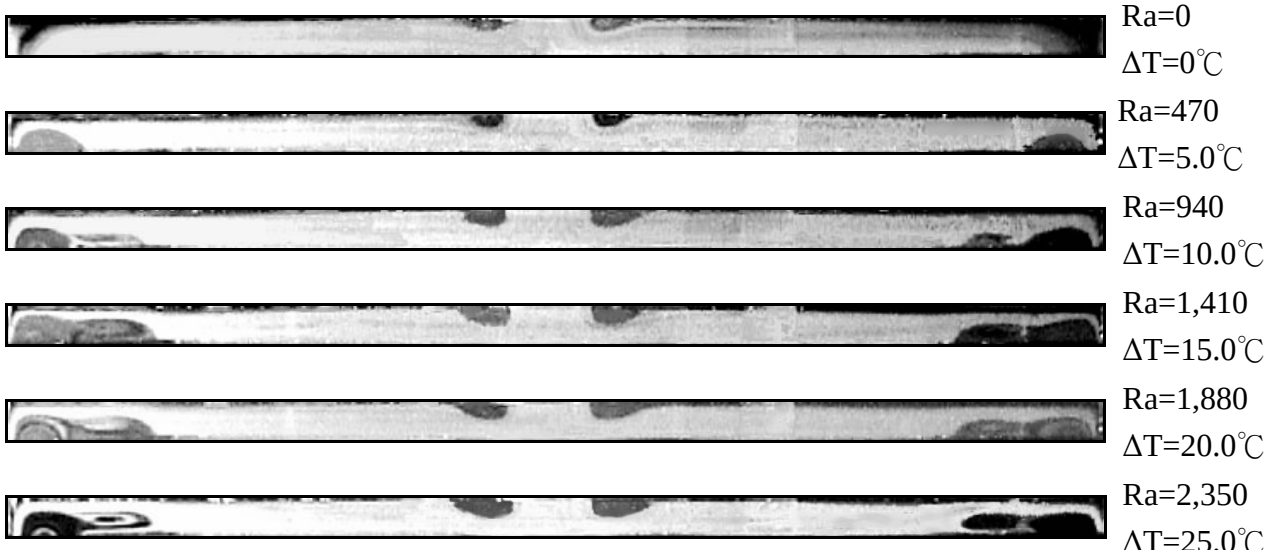

(b) D_j= 22.1 mm & Re_j=61

Fig. 3.40 Steady side view flow photos taken at the cross plane θ=0° & 180° for various Rayleigh numbers at H=10.0 mm & Q_j=1.0 slpm for D_j= (a) 10.0 mm and (b) 22.1 mm.

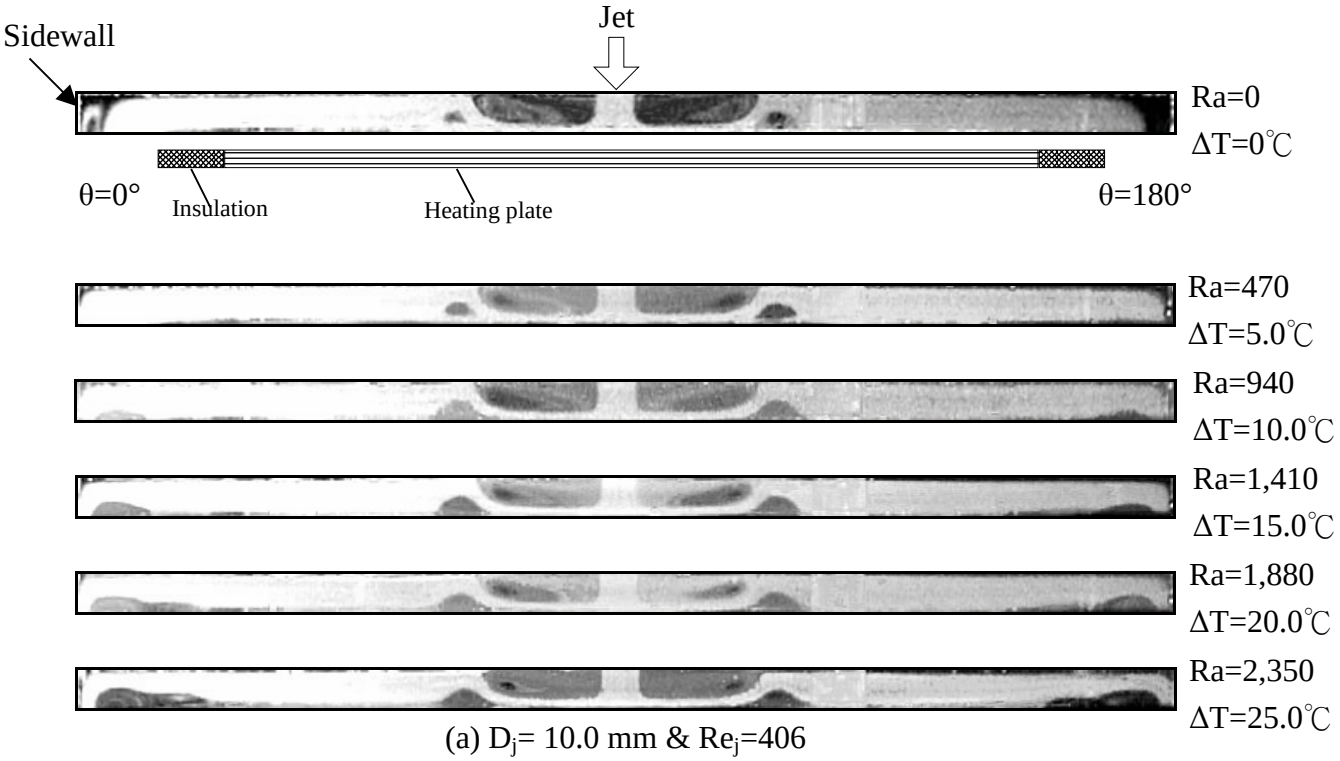

(a) D_j= 10.0 mm & Re_j=406

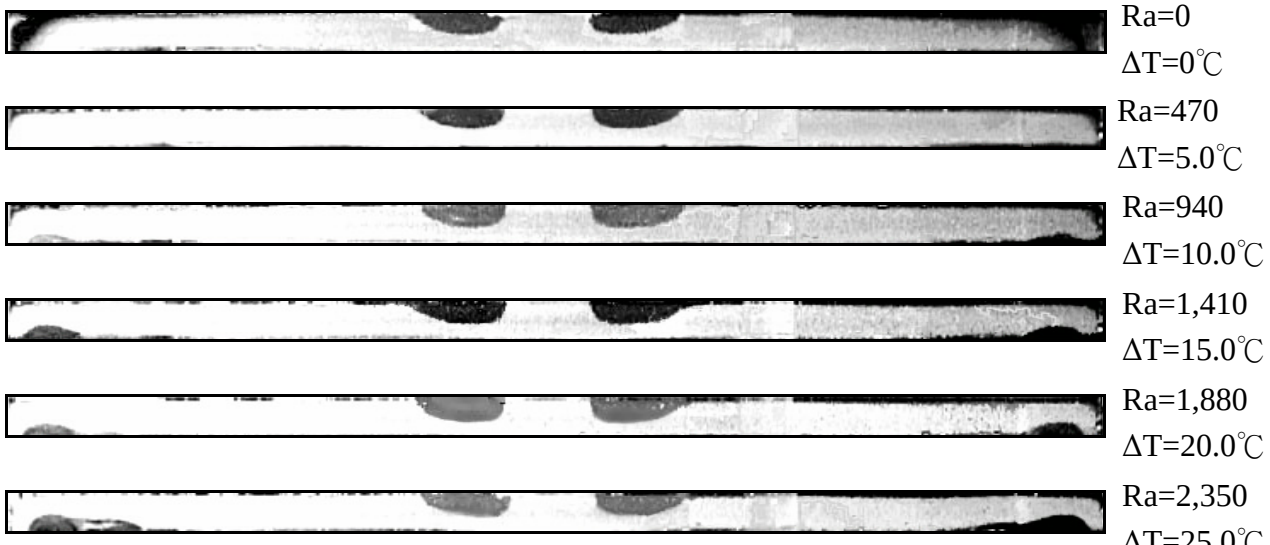

(b) D_j= 22.1 mm & Re_j=184

Fig. 3.41 Steady side view flow photos taken at the cross plane θ=0° & 180° for various Rayleigh numbers at H=10.0 mm & Q_j=3.0 slpm for D_j= (a) 10.0 mm and (b) 22.1 mm.

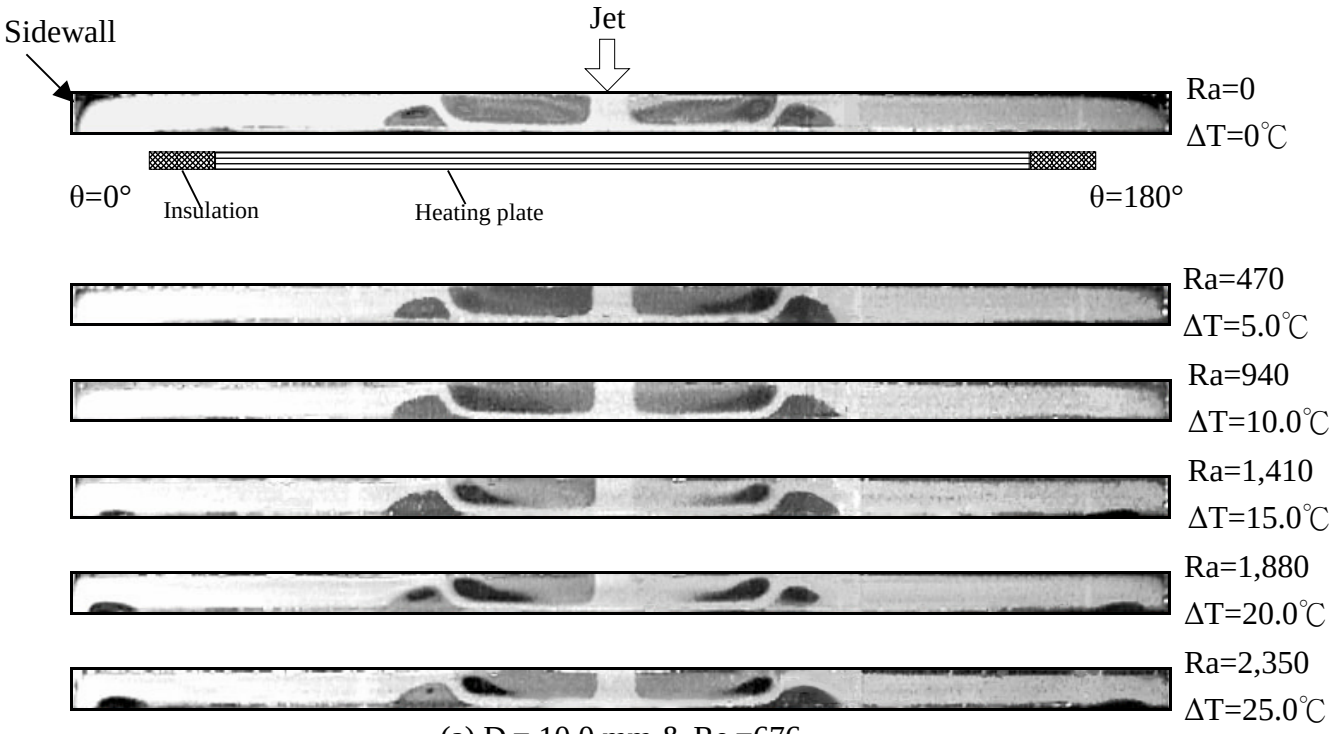

(a) D_j= 10.0 mm & Re_j=676

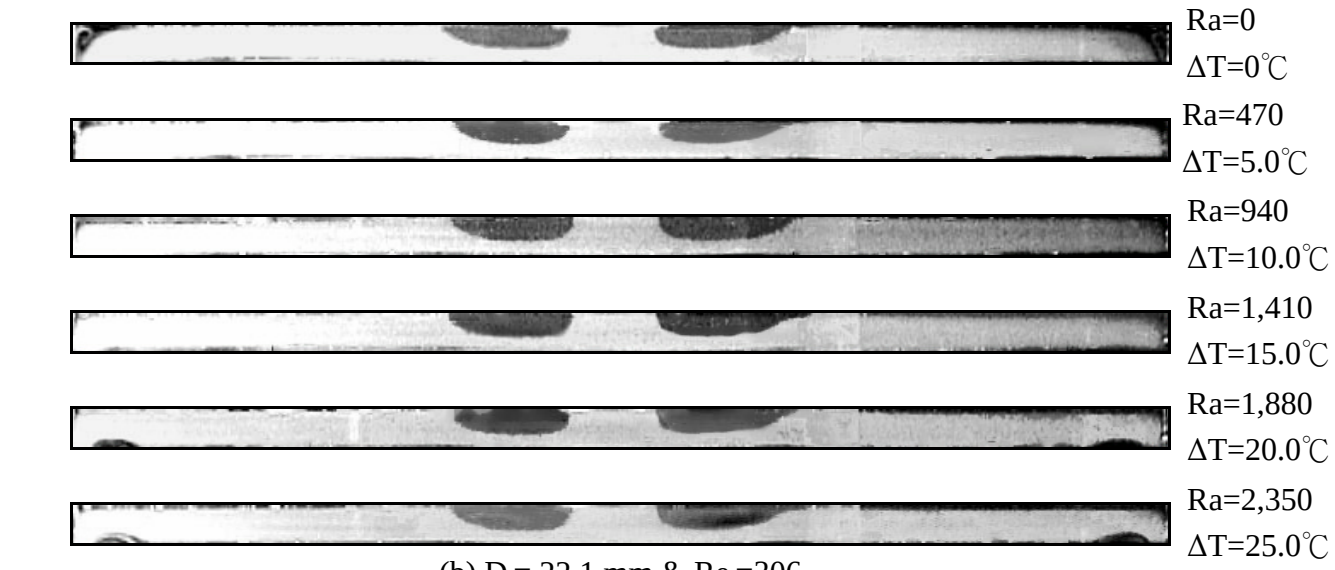

(b) D_j= 22.1 mm & Re_j=306

Fig. 3.42 Steady side view flow photos taken at the cross plane θ=0° & 180° for various Rayleigh numbers at H=10.0 mm & Q_j=5.0 slpm for D_j= (a) 10.0 mm and (b) 22.1 mm.

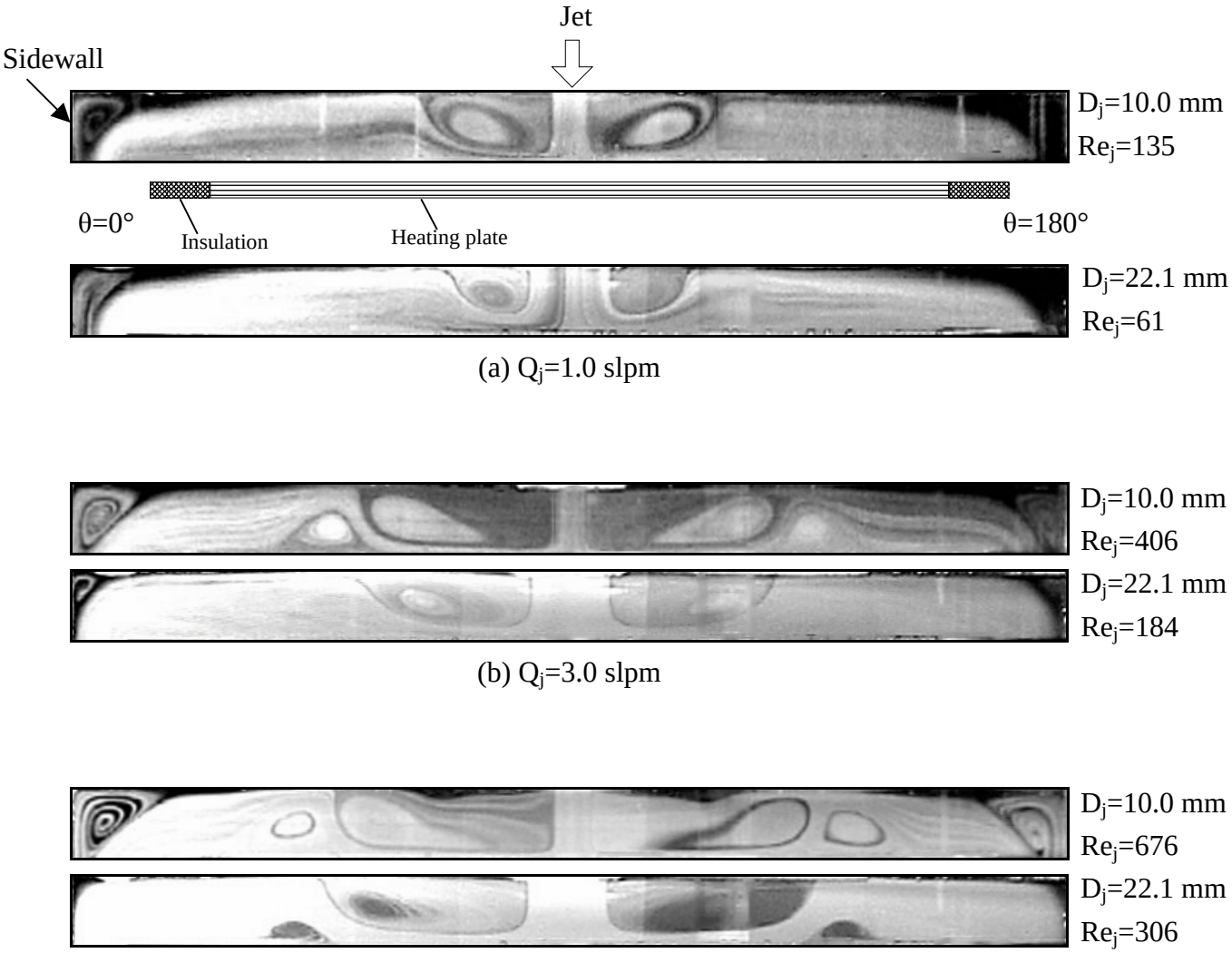

Fig. 3.43 Steady side view flow photos taken at the cross plane θ =0° & 180° at Q_j=3.0 slpm & H=20.0 mm with Ra=0.

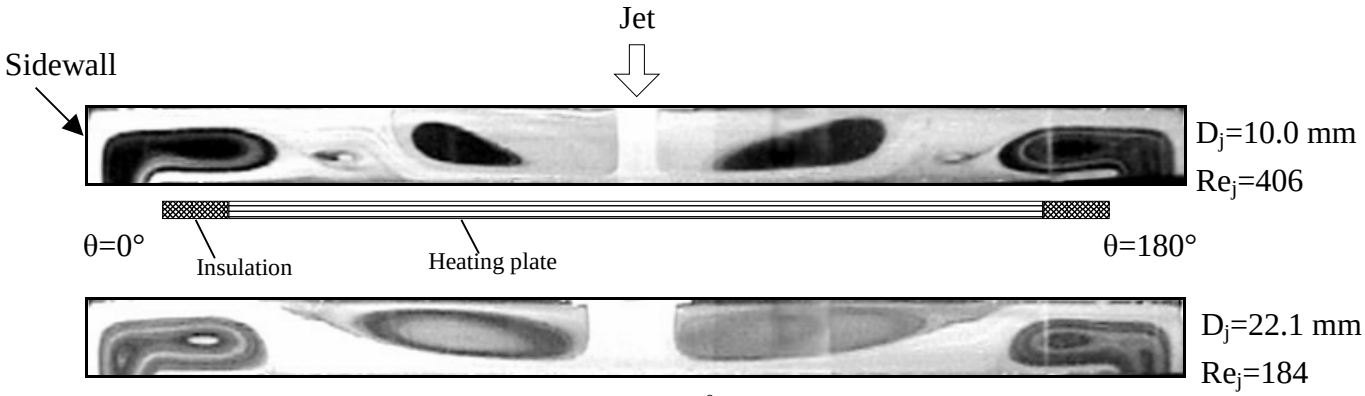

(a) Q_j=3.0 slpm & ΔT=15.0℃ (Ra=11,270)

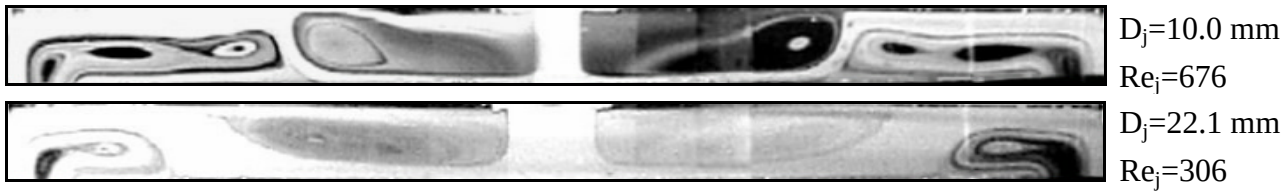

(b) Q_j=5.0 slpm & ΔT=15.0℃ (Ra=11,270)

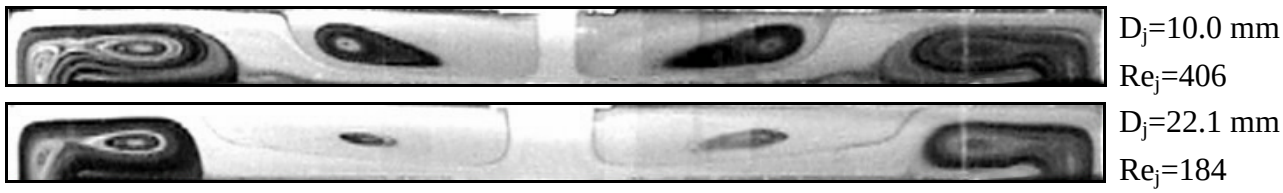

(c) Q_j=3.0 slpm & ΔT=25.0℃ (Ra=18,790)

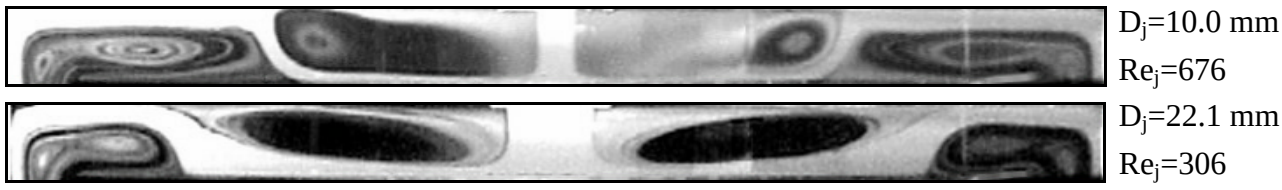

(d) Q_j=5.0 slpm & ΔT=25.0℃ (Ra=18,790)

Fig. 3.44 Steady side view flow photos taken at the cross plane θ =0° & 180° at H=20.0 mm.

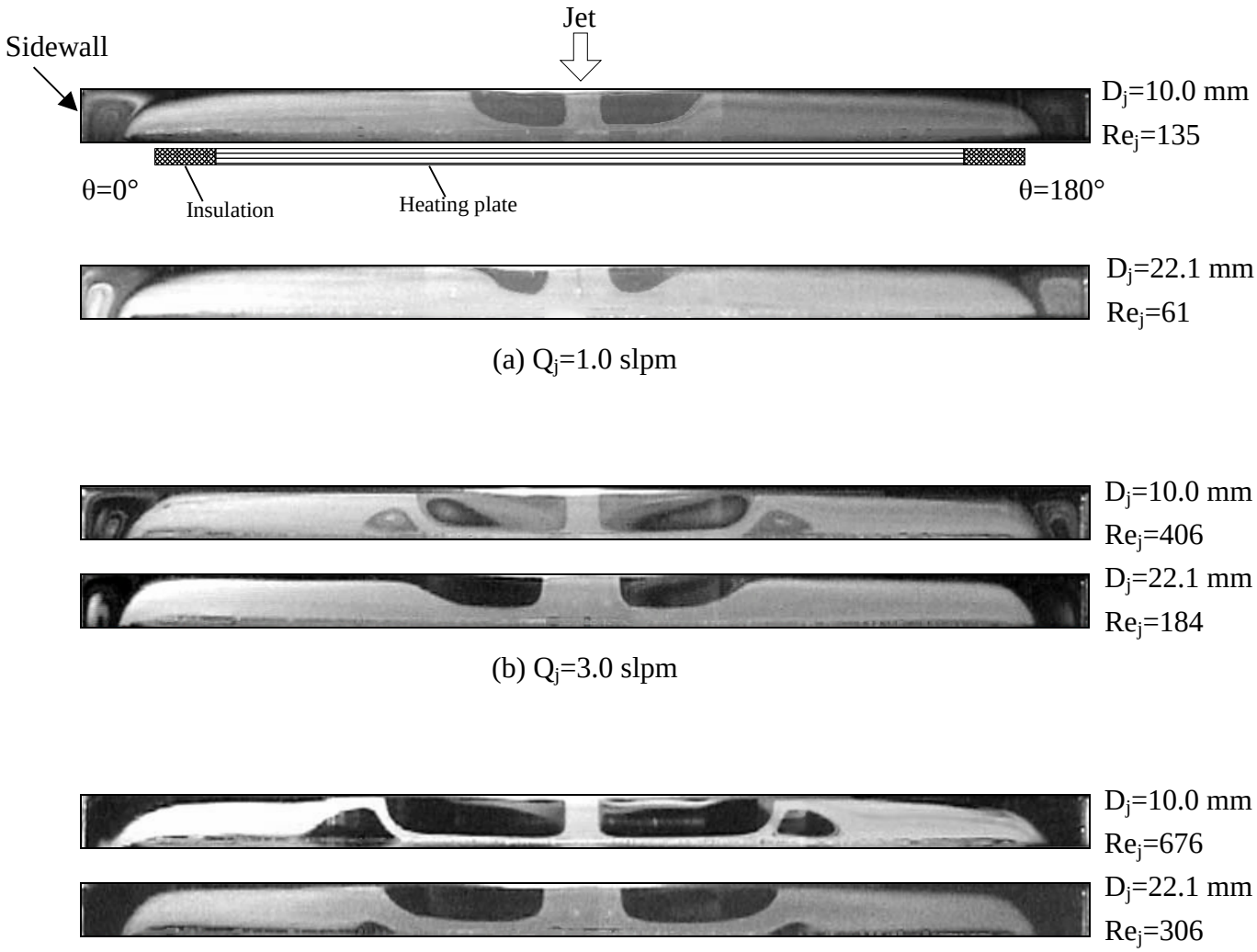

Fig. 3.45 Steady side view flow photos taken at the cross plane θ =0° & 180° at H=15.0 mm with Ra=0.

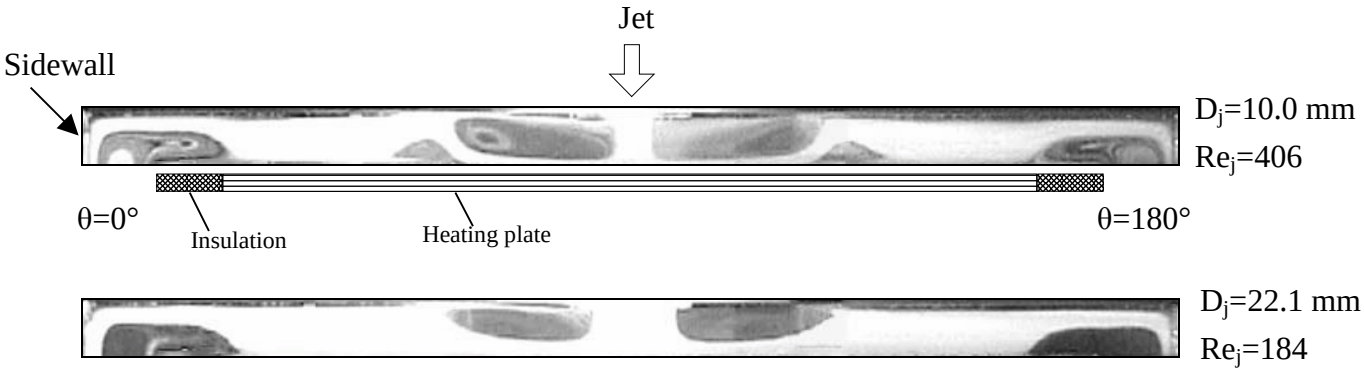

(a) Q_j=3.0 slpm & ΔT=15.0℃ (Ra=4,760)

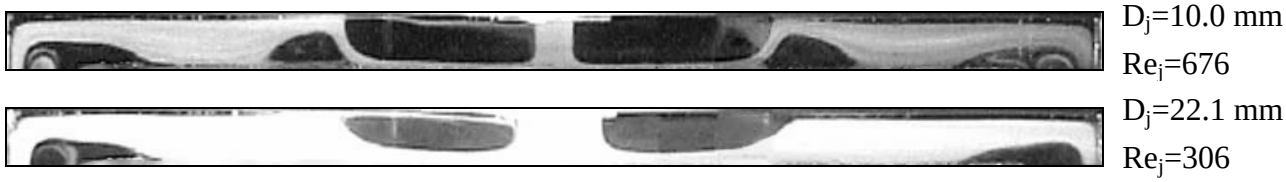

(b) Q_j=5.0 slpm & ΔT=15.0℃ (Ra=4,760)

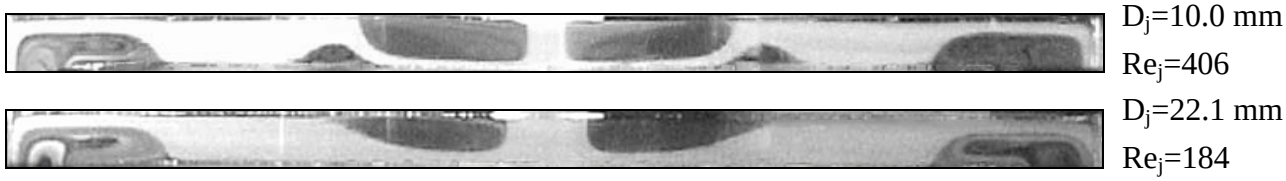

(c) Q_j=3.0 slpm & ΔT=25.0℃ (Ra=7,930)

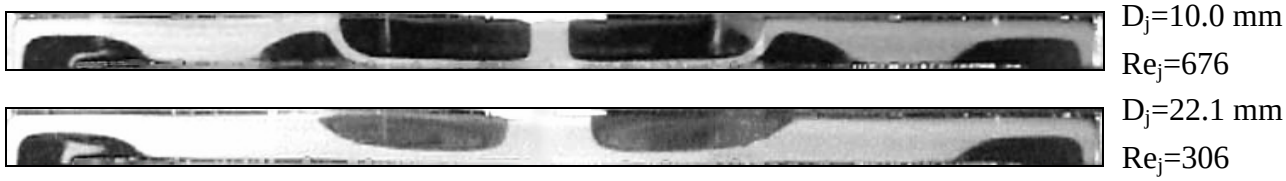

(d) Q_j=5.0 slpm & ΔT=25.0℃ (Ra=7,930)

Fig. 3.46 Steady side view flow photos taken at the cross plane θ =0° & 180° at H=15.0 mm.

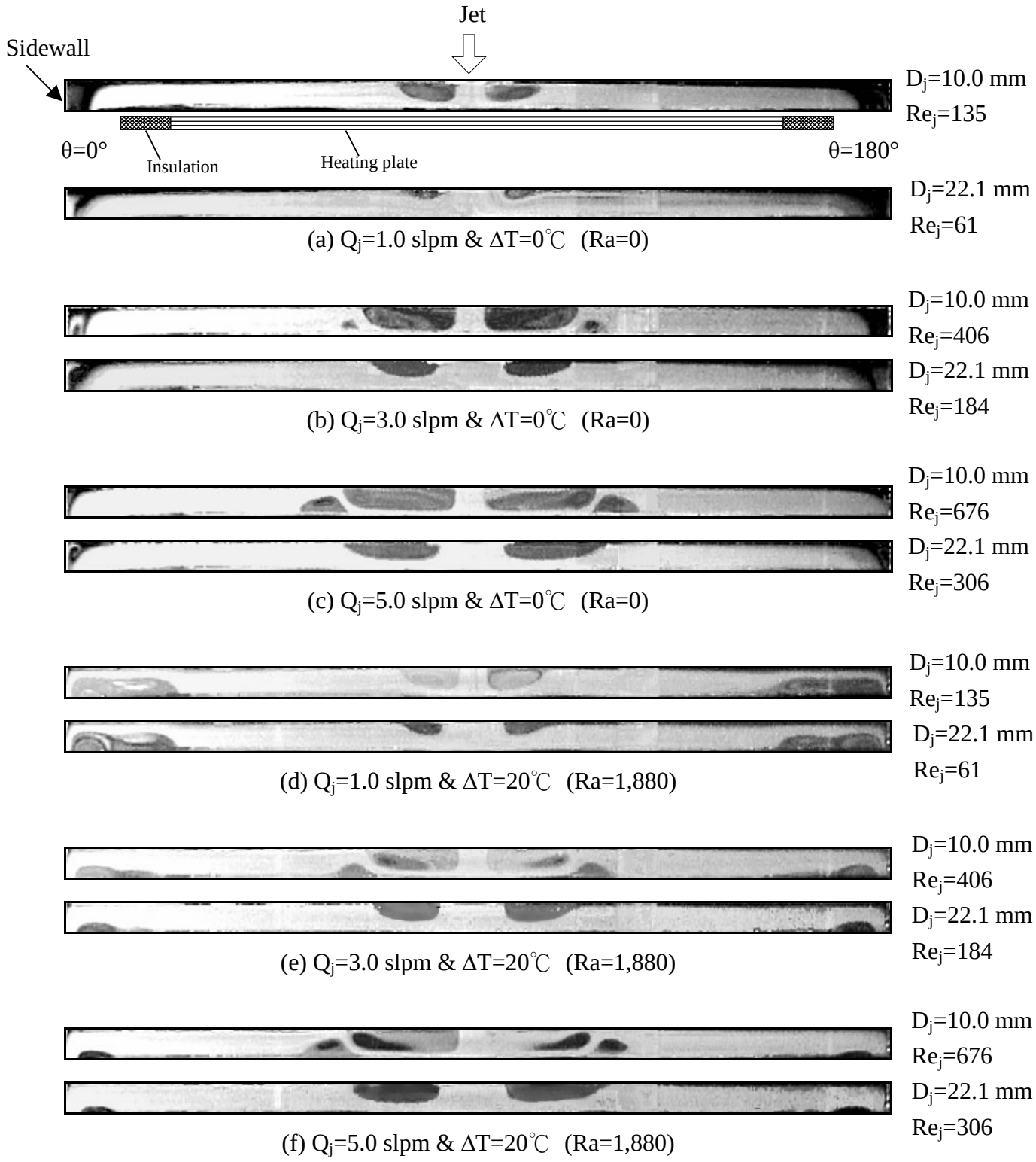

Fig. 3.47 Steady side view flow photos taken at the cross plane θ=0° & 180° at H=10.0 mm.

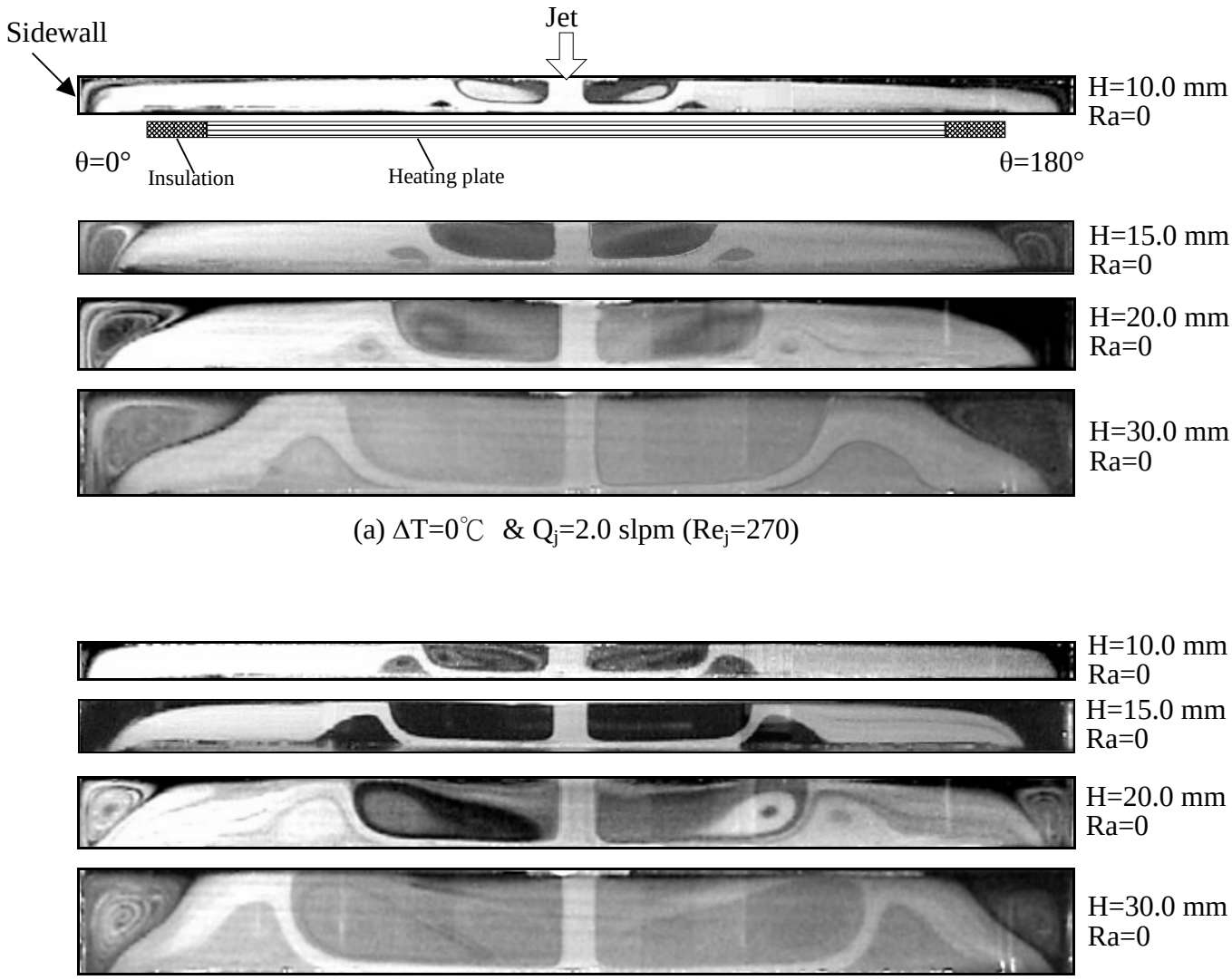

(a) $\Delta T=0℃$ & $Q_j=2.0$ slpm ($Re_j=270$)

(b) $\Delta T=0℃$ & $Q_j=4.0$ slpm ($Re_j=541$)

Fig. 3.48 Steady side view flow photos taken at the cross plane $\theta=0°$ & 180° for $D_j=10.0$ mm at given $\Delta T=0℃$ for various H.

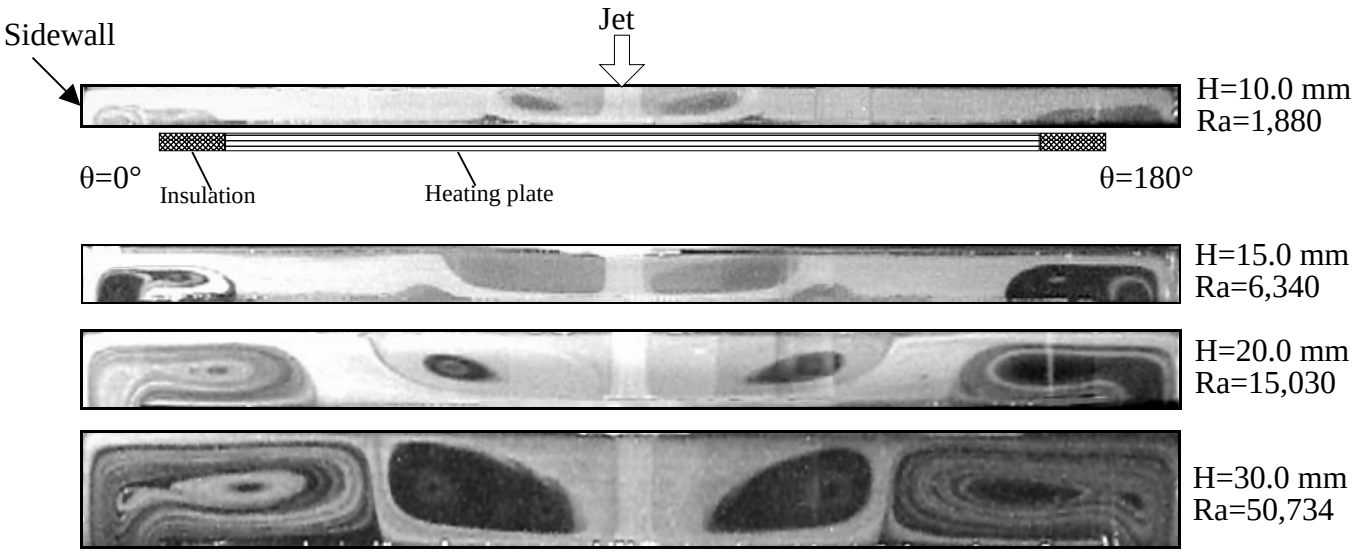

(a) ΔT=20.0℃ & Q_j=2.0 slpm (Re_j=270)

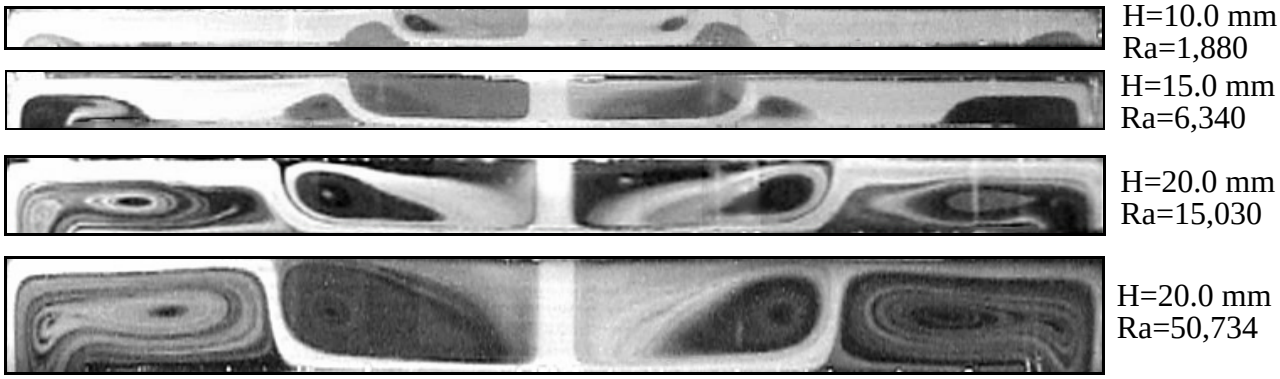

(b) ΔT=20.0℃ & Q_j=5.0 slpm (Re_j=676)

Fig. 3.49 Steady side view flow photos taken at the cross plane θ=0° & 180° for D_j=10.0 mm at given ΔT=20.0℃ for various H.

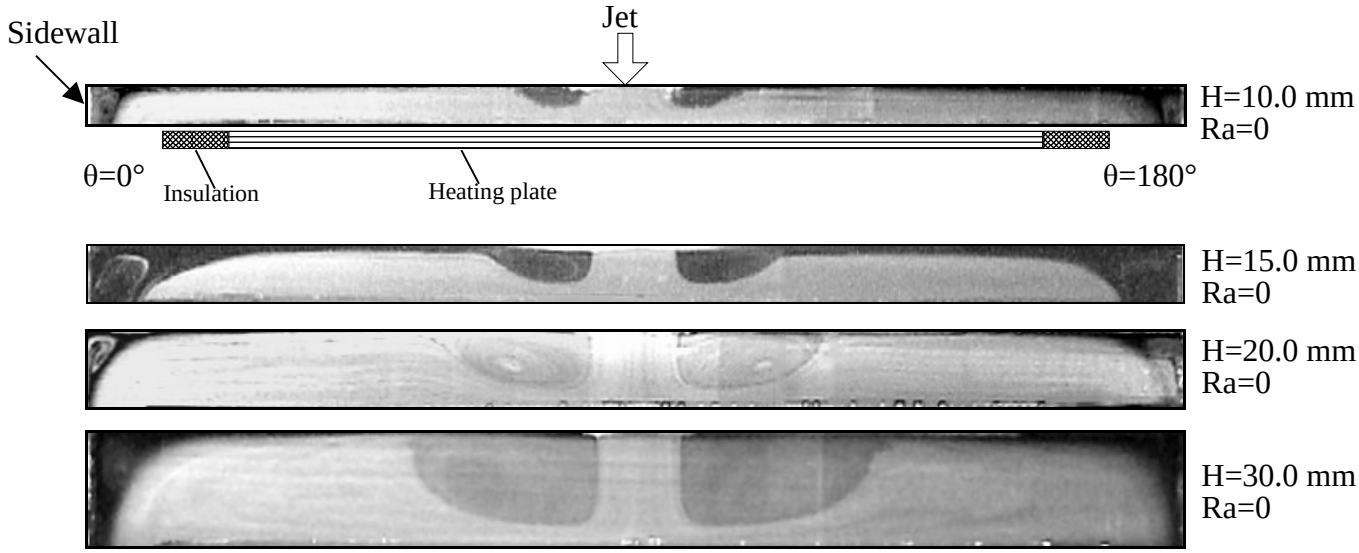

(a) $\Delta T=0℃$ & $Q_j=2.0$ slpm ($Re_j=122$)

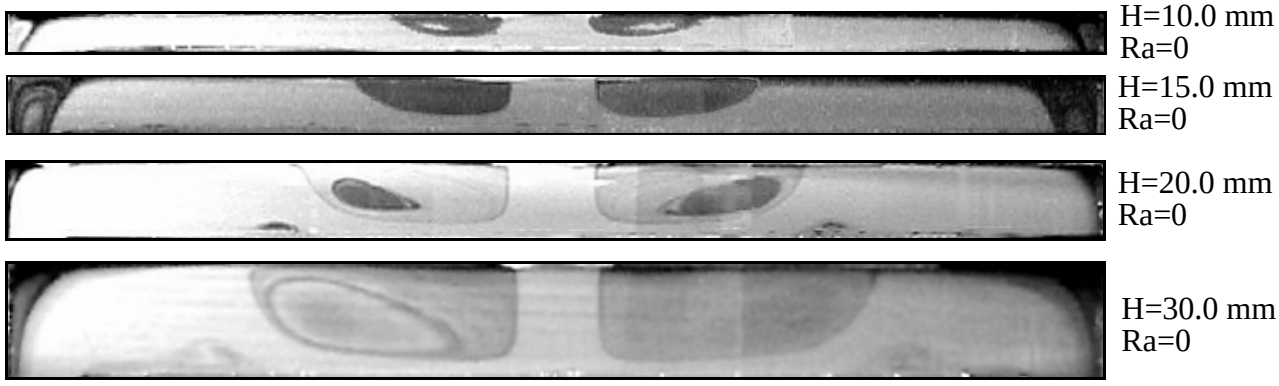

(b) $\Delta T=0℃$ & $Q_j=4.0$ slpm ($Re_j=245$)

Fig. 3.50 Steady side view flow photos taken at the cross plane $\theta=0°$ & 180° for $D_j=22.1$ mm at given $\Delta T=0℃$ for various H.

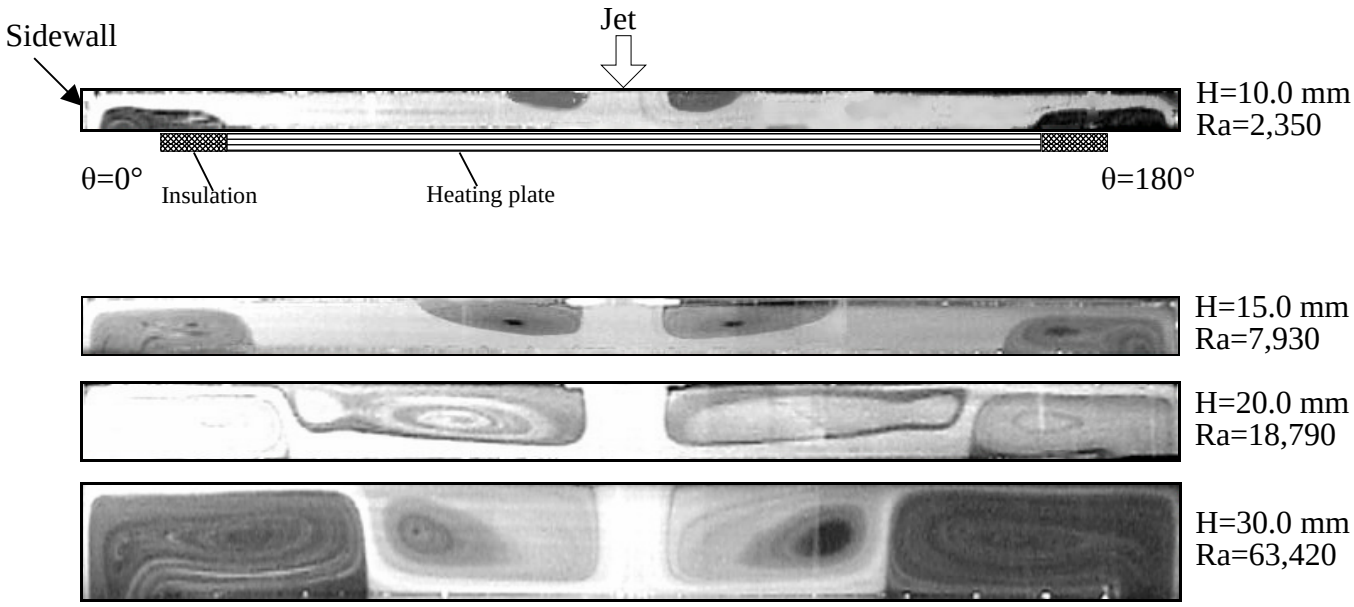

(a) ΔT=25.0℃ & Q_j=2.0 slpm (Re_j=122)

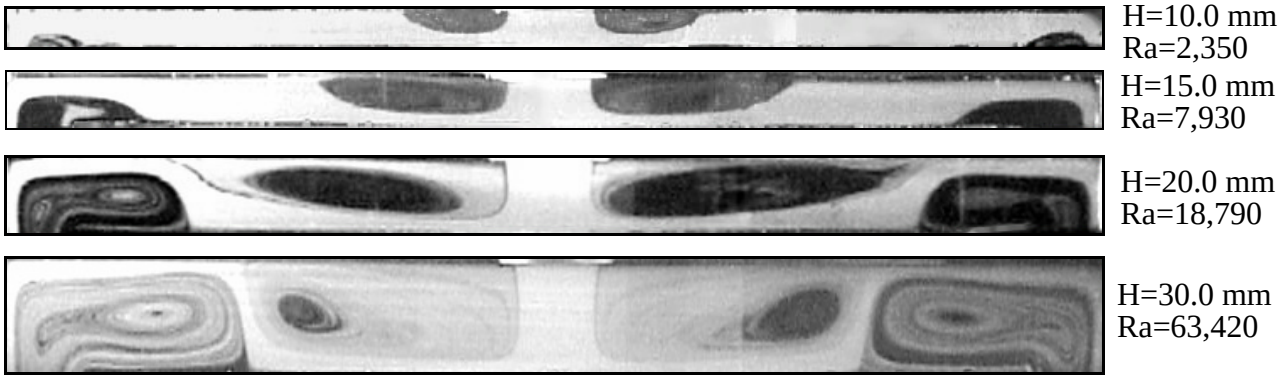

(b) ΔT=25.0℃ & Q_j=5.0 slpm (Re_j=306)

Fig. 3.51 Steady side view flow photos taken at the cross plane θ=0° & 180° for D_j=22.1 mm at given ΔT=25.0℃ for various H.

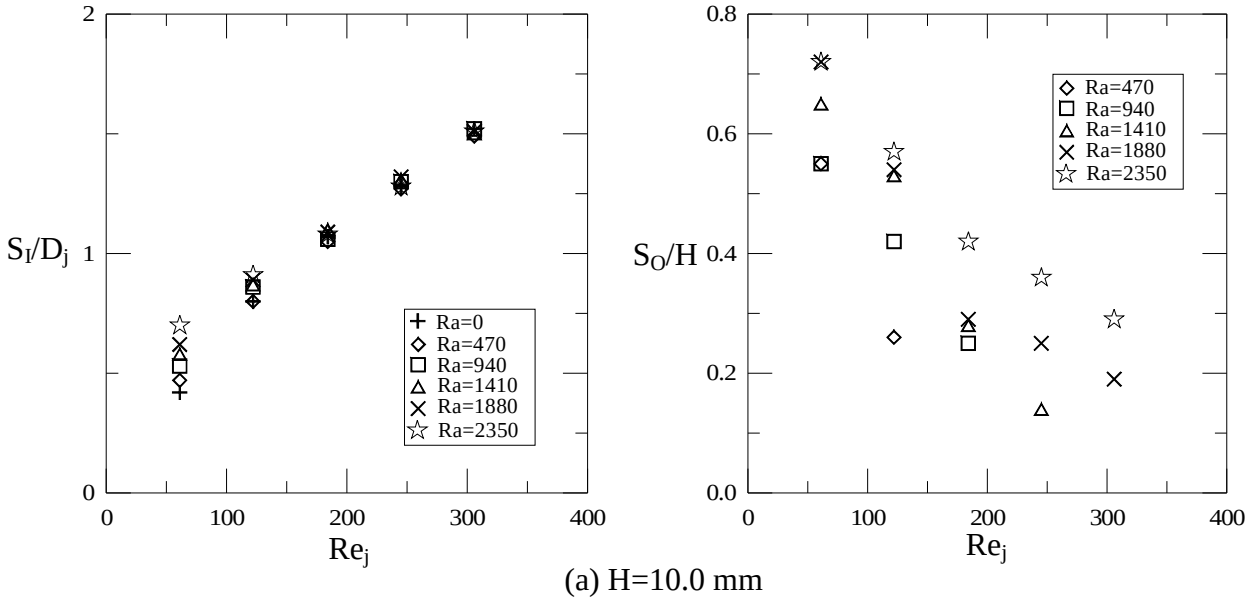

(a) H=10.0 mm

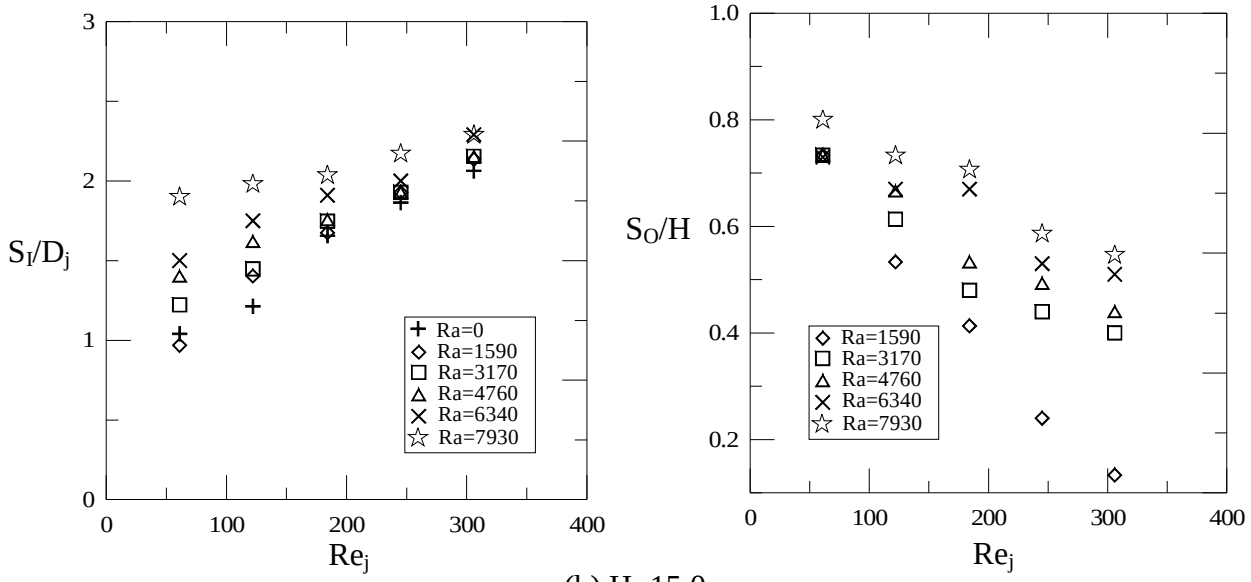

(b) H=15.0 mm

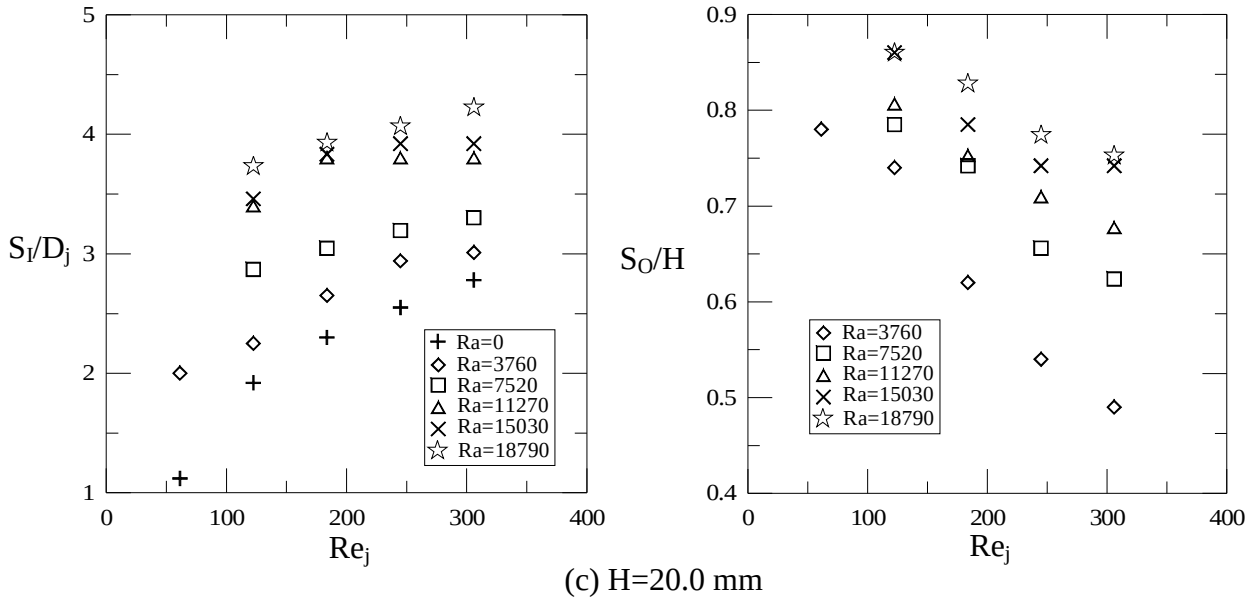

(c) H=20.0 mm

Fig. 3.52 Radial extent of the primary inertia-driven rolls with D_j=22.1 mm for H= (a) 10.0 mm, (b) 15.0 mm, and (c) 20.0 mm.

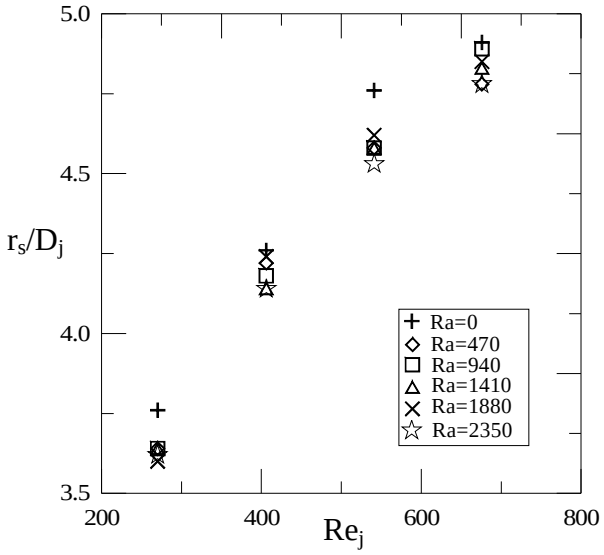

(a) H=10.0 mm

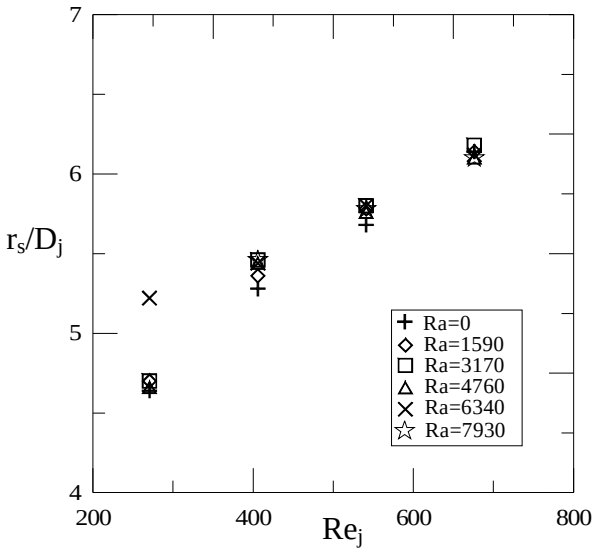

(b) H=15.0 mm

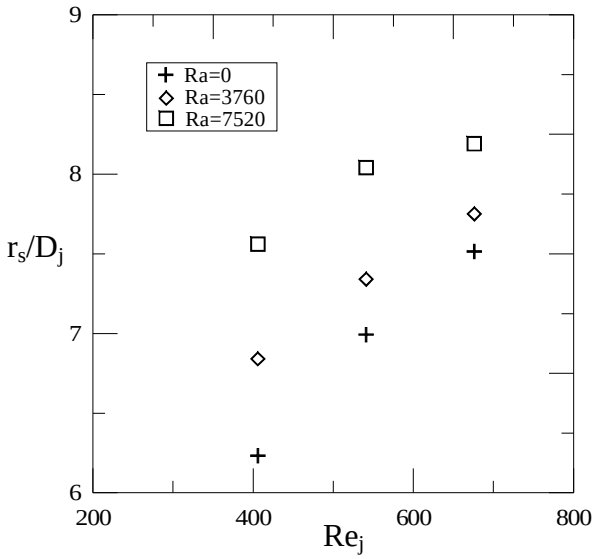

(c) H=20.0 mm

Fig. 3.53 Radial location of the secondary inertia-driven rolls with D_j=10 mm for H= (a) 10.0 mm, (b) 15.0 mm, and (c) 20.0 mm.

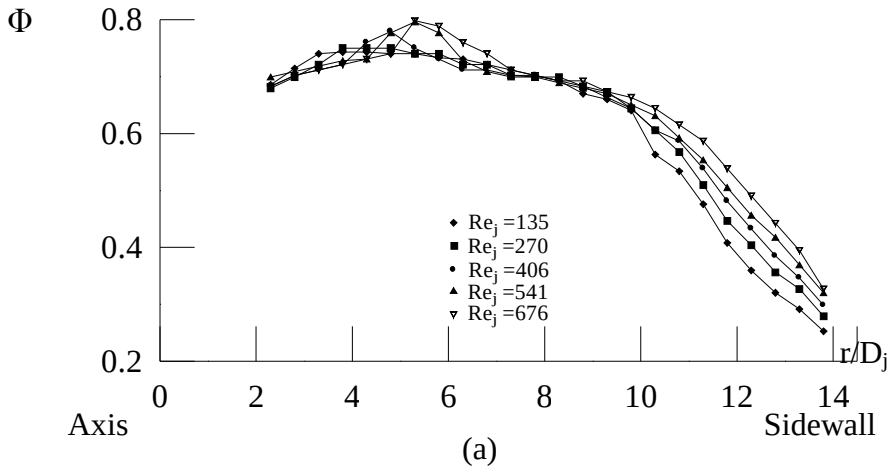

(a)

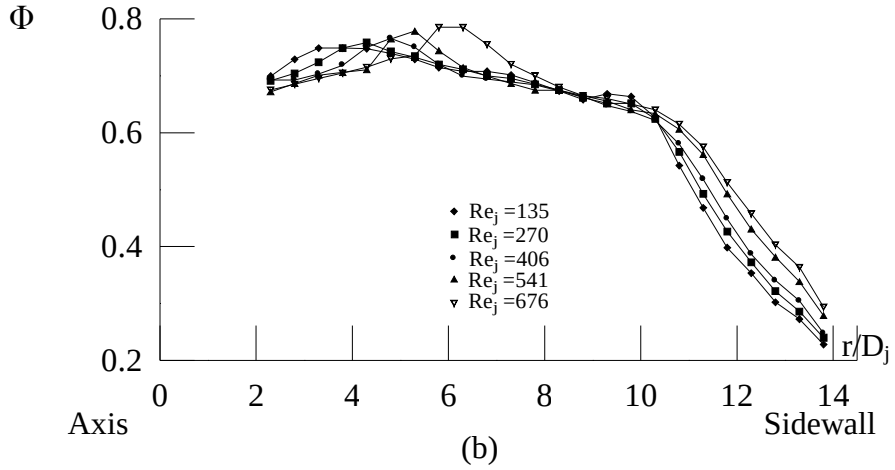

(b)

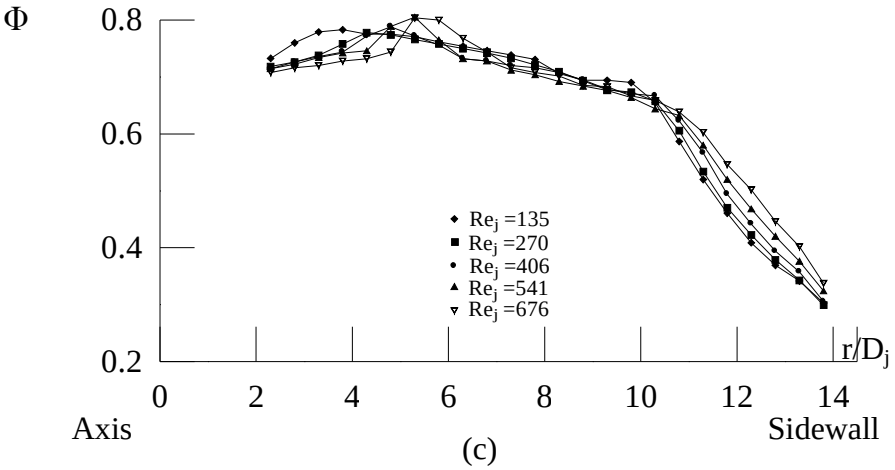

(c)

Fig. 3.54 Radial variation in non-dimensional steady air temperature with various Re_j for H=15.0 mm & D_j=10.0 mm at Z=0.5 for Ra= (a) 3,170, (b) 6,340, and (c) 7,930.

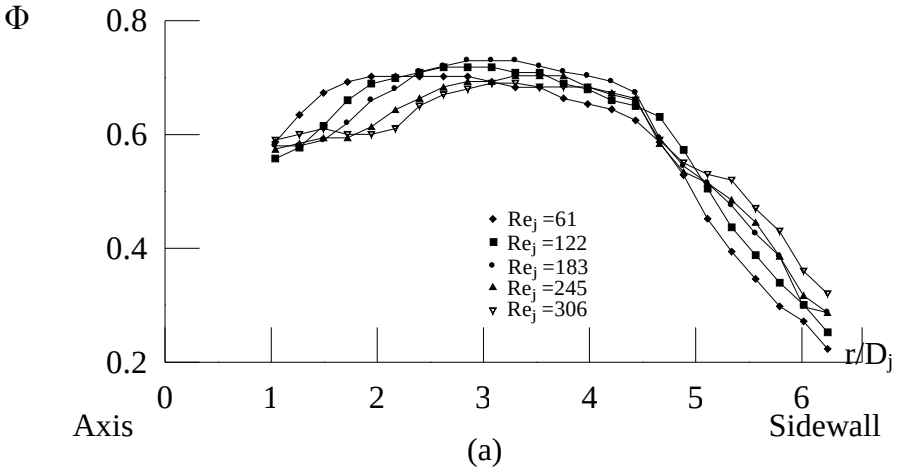

(a)

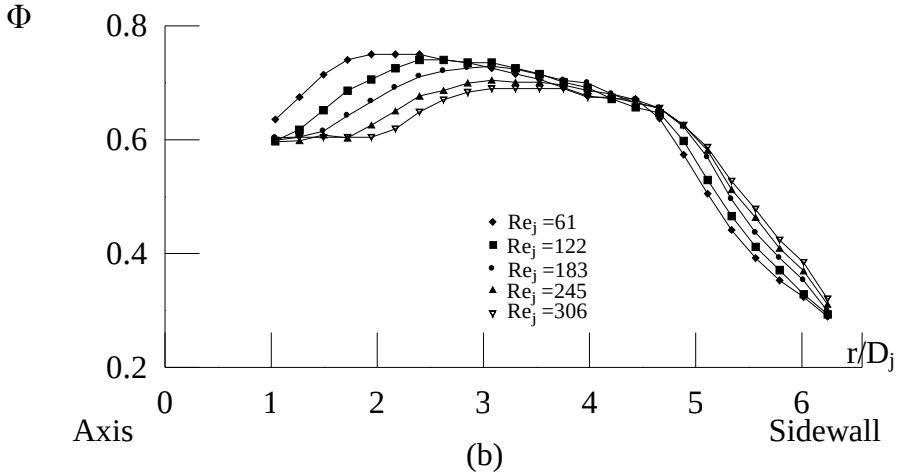

(b)

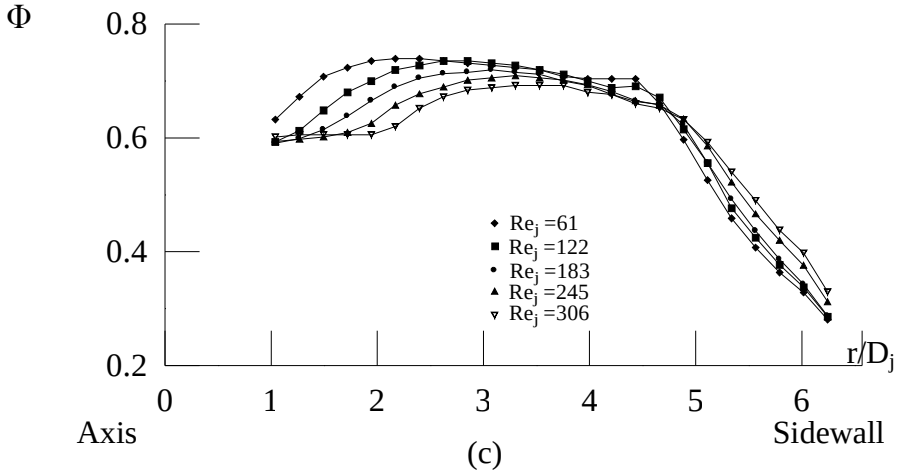

(c)

Fig. 3.55 Radial variation in non-dimensional steady air temperature with various Re_j for H=15.0 mm & D_j=22.1 mm at Z=0.5 for Ra= (a) 3,170, (b) 6,340, and (c) 7,930.

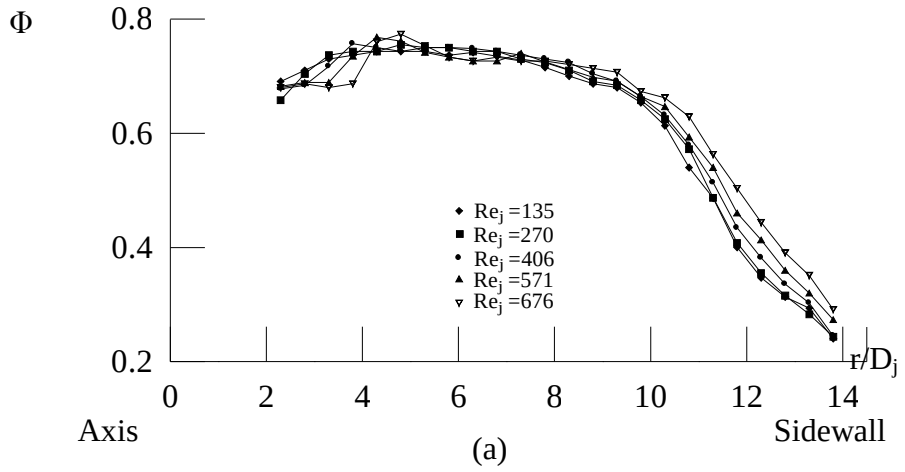

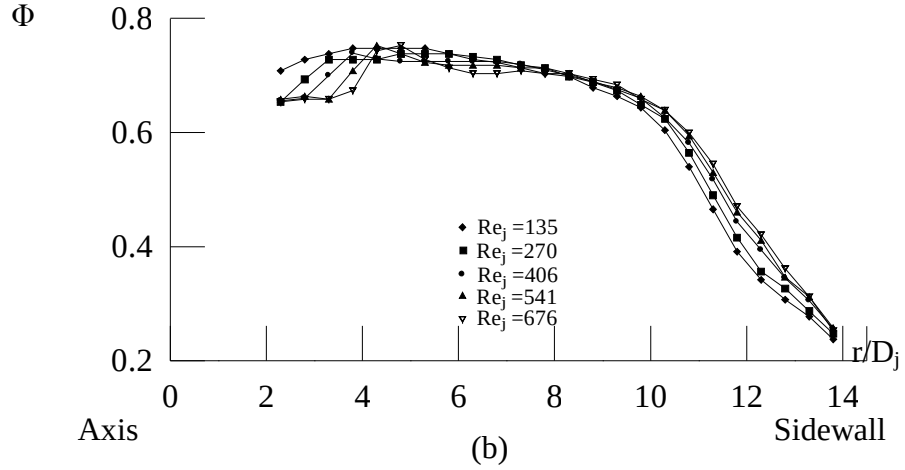

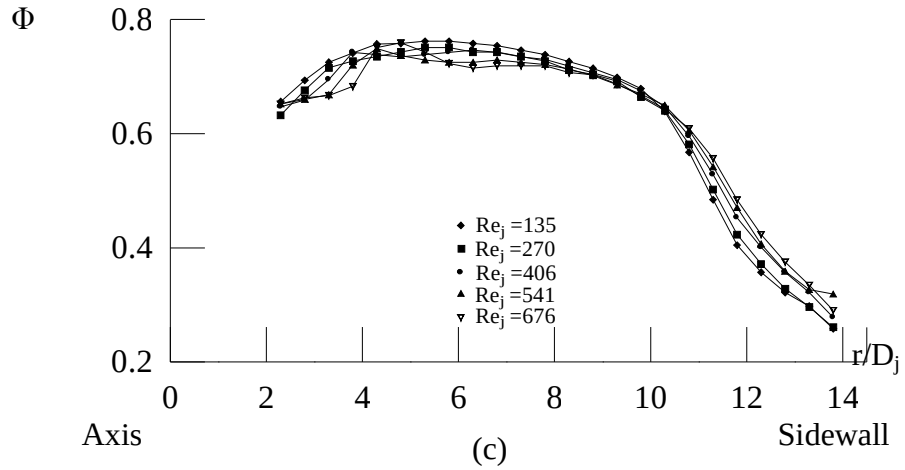

Fig. 3.56 Radial variation in non-dimensional steady air temperature with various Re_j for H=10.0 mm & D_j=10.0 mm at Z=0.5 for Ra= (a) 1,410, (b) 1,880, and (c) 2,350.

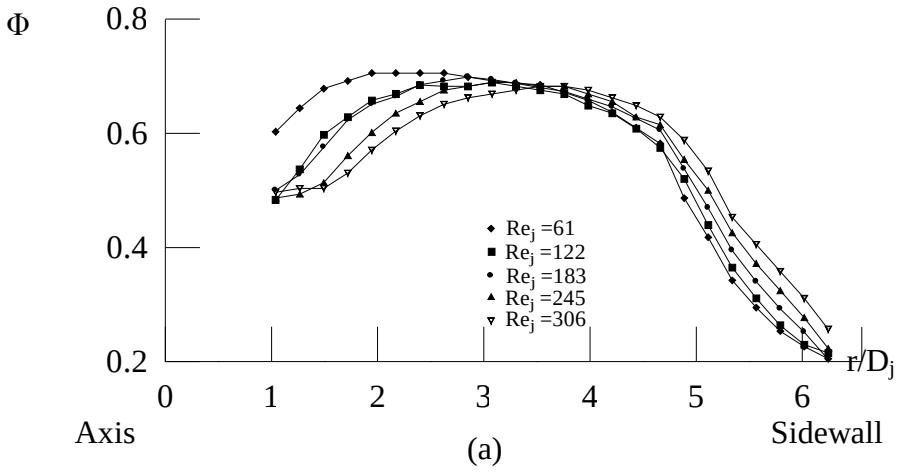

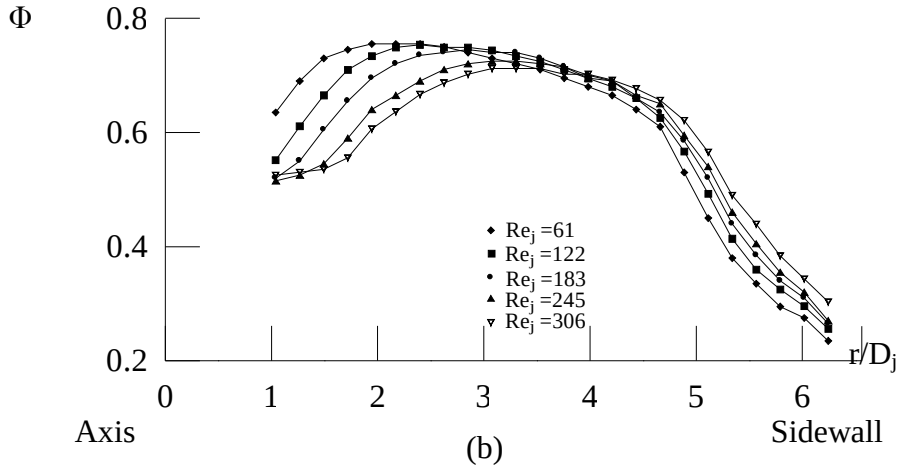

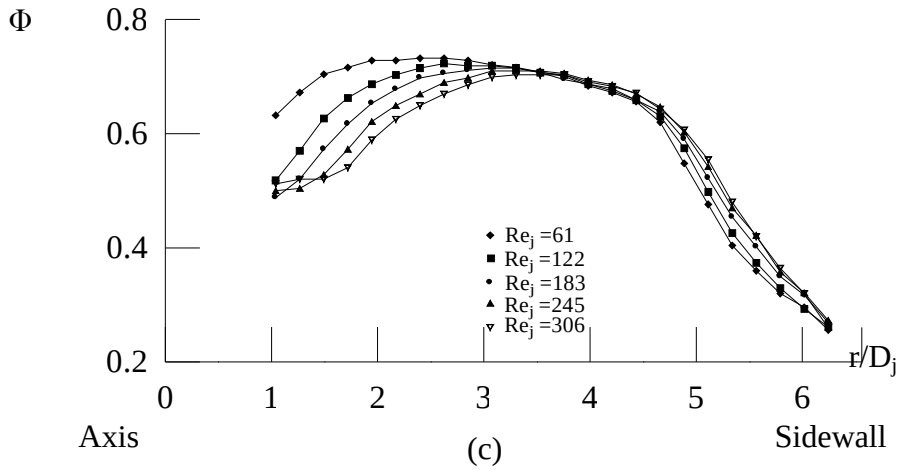

Fig. 3.57 Radial variation in non-dimensional steady air temperature with various Re_j for H=10.0 mm & D_j=22.1 mm at Z=0.5 for Ra= (a) 1,410, (b) 1,880, and (c) 2,350.

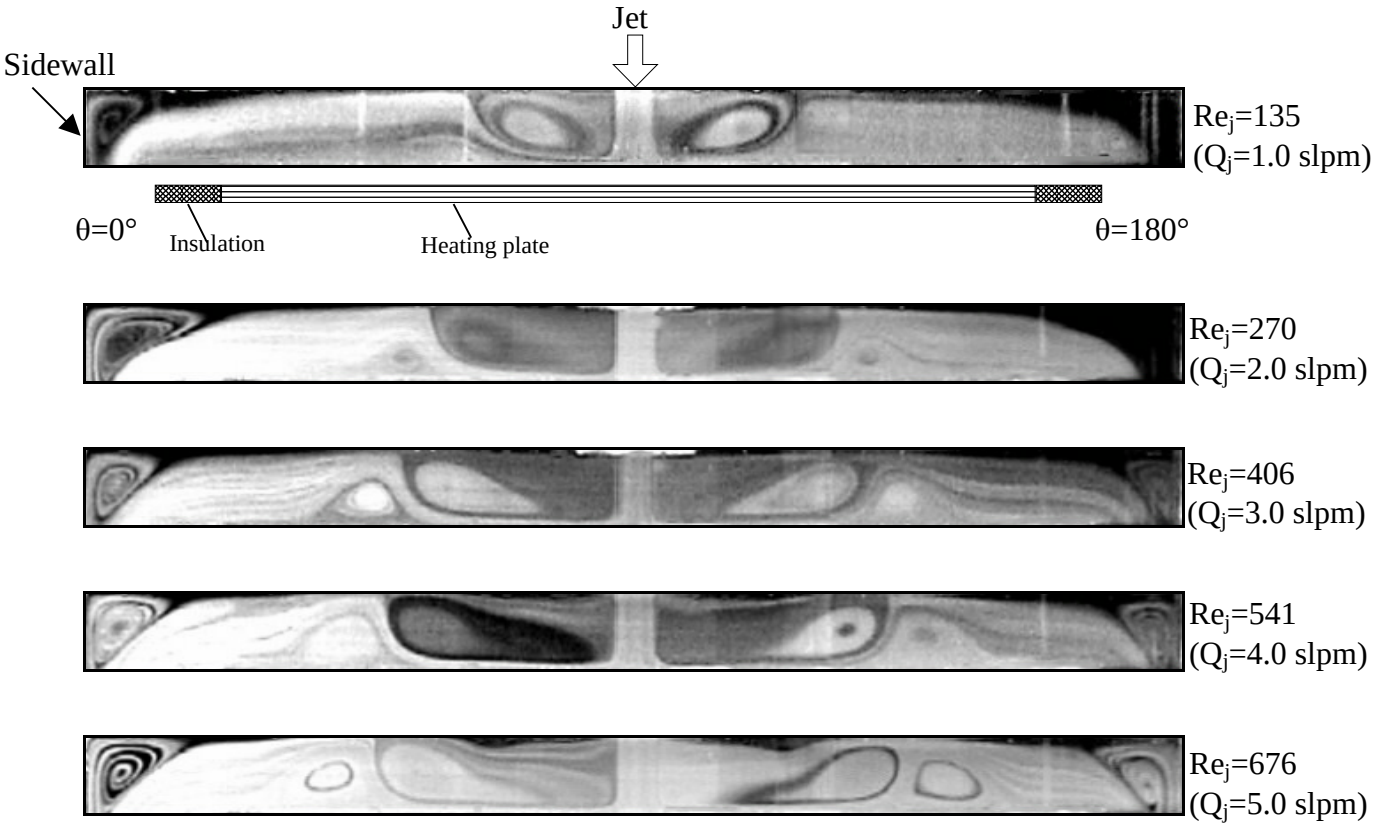

(a) ω=0 rpm

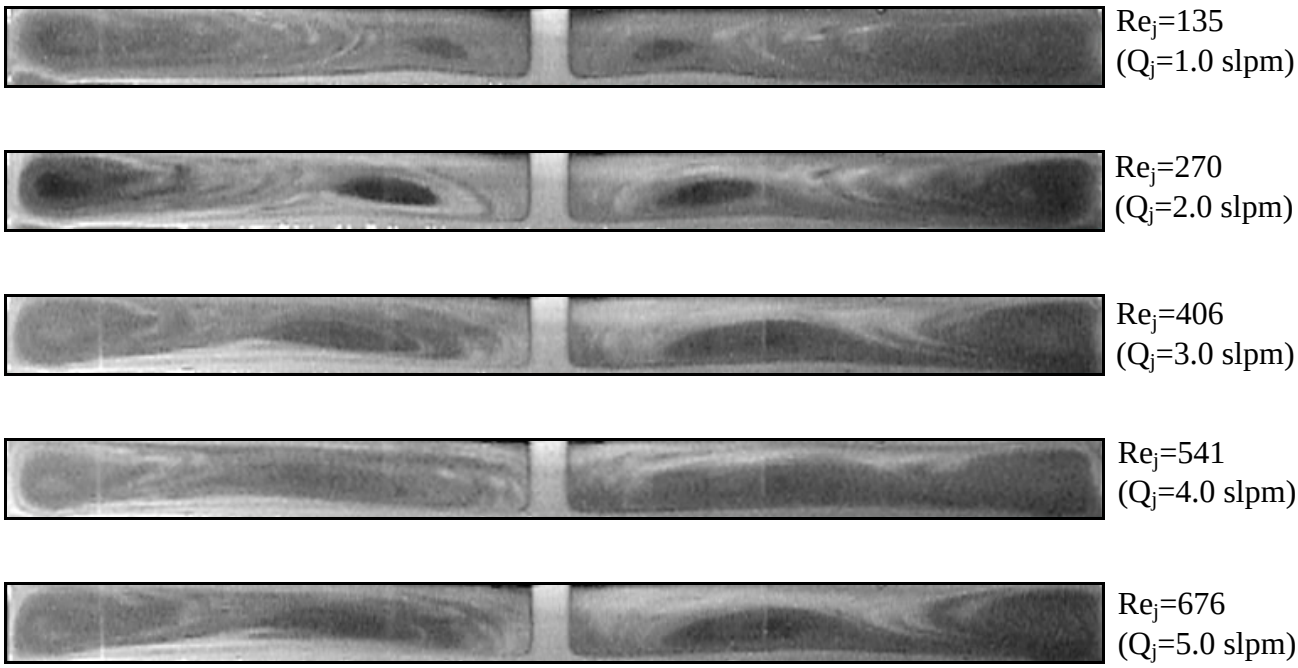

(b) ω=30.0 rpm

Fig. 3.58 Steady side view flow photos taken at the cross plane θ=0° & 180° for various jet Reynolds numbers at Ra=0 (ΔT=0℃) and D$_j$=10.0 mm for (a)ω=0 and (b) ω=30 rpm (Re$_\omega$=2,335).

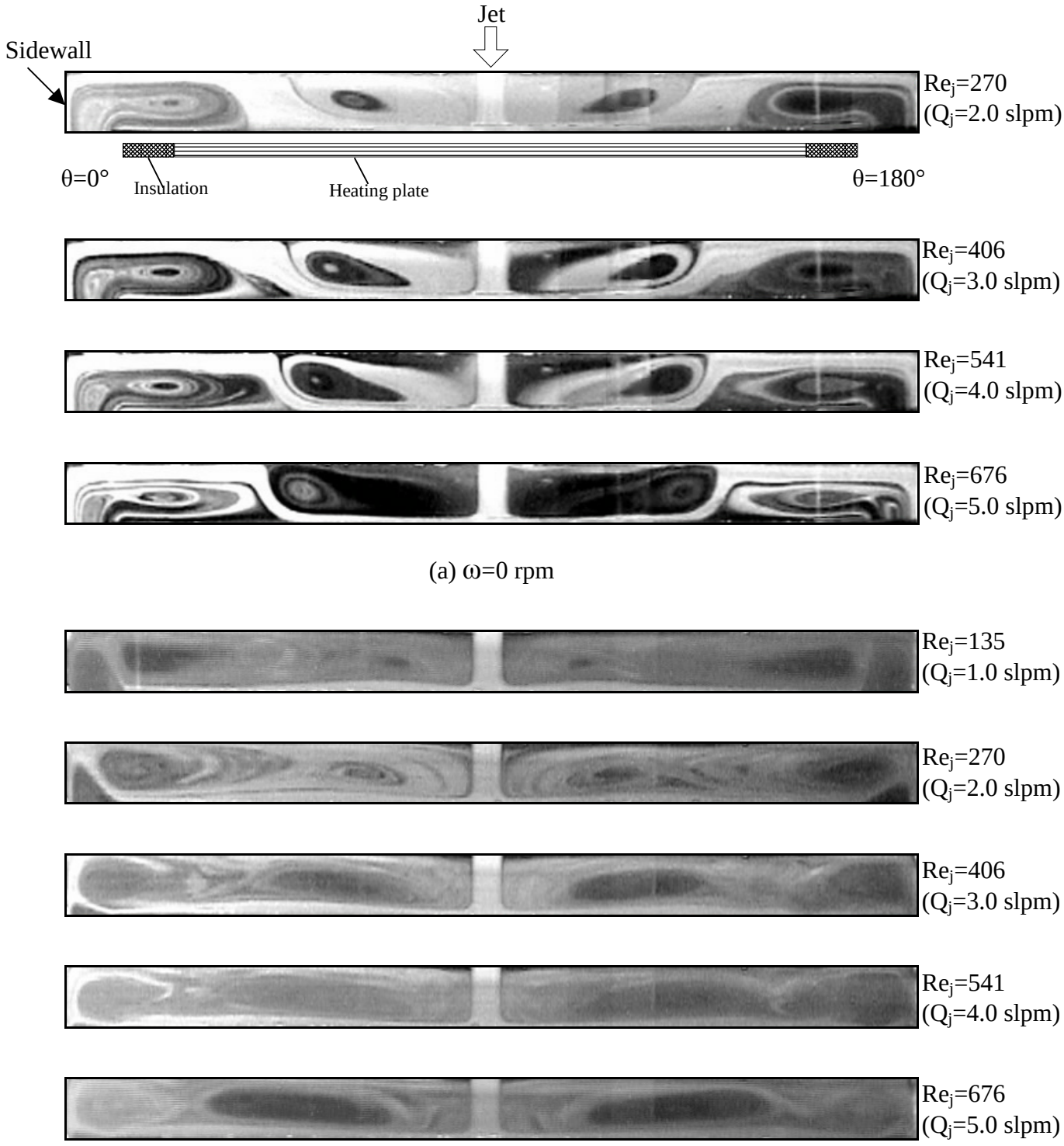

Fig. 3.59 Steady side view flow photos taken at the cross plane θ =0° & 180° for various jet Reynolds numbers at Ra=15,030 (ΔT=20.0℃) and D$_j$=10.0 mm for (a) ω=0 and (b) ω=30 rpm (Re$_\omega$=2,335).

Chapter 4

Characteristics of Time Dependent Vortex Flow

It is observed in the present experiment for a nonrotating disk ($\omega = 0$) that the vortex flow in the processing chamber does not reach steady state at long time when the buoyancy-to-inertia ratio Gr/Re_j^2 is raised to certain high level and the vortex flow gradually becomes time dependent. This normally occurs at low jet Reynolds numbers for the range of the Rayleigh number covered here. Besides, the transient stages during the formation of the inertia-driven vortex rolls are of interest in the fundamental fluid mechanics and heat transfer study. In this chapter these two different time dependent vortex flows will be examined in detail.

4.1 Time periodic vortex flows

The characteristics of a typical buoyancy-driven time periodic vortex flow are exemplified first in Fig. 4.1 for two cases with D_j=10.0 and 22.1 mm by showing selected cross plane flow photos at certain time instants and time records of air temperature at selected locations in the processing chamber in the statistical state for H=20.0 mm. We should first recall that at low Re_j only the primary inertia-driven inner and buoyancy-driven outer vortex rolls exist in the chamber. The secondary inertia-driven middle roll does not appear. Now the results in Fig. 4.1 clearly show that two additional circular rolls are induced in the time periodic vortex flow. These two new rolls are smaller and appear in the middle portion of the chamber right between the inner and outer rolls. Besides, the time periodic vortex flow is asymmetric. The data for the time records given in Fig. 4.1 indicate that only in the region dominated by the new rolls the air temperature oscillates significantly with time. Elsewhere the temperature oscillation is small. It is recognized that for the

smaller H of 10.0 and 15.0 mm the Rayleigh number of the flow subject to the ΔT investigated here is not high enough to cause the vortex flow to become time dependent at long time. Therefore at H=10.0 and 15.0 mm the vortex flow for various cases all evolves to steady state.

To further reveal the temporal characteristics of the time periodic vortex flow, the time records of the air temperature at a selected location and the corresponding power spectrum densities (PSD) are presented next in Fig. 4.2 for various Re_j for D_j=22.1 mm at Ra=15,030. The PSD are evaluated from the Fourier analysis of the measured data. The results clearly manifest that the flow oscillates at a large amplitude and a slightly lower frequency for a lower Re_j at the fixed Ra. This trend is apparently owing to the accompanying rise in the buoyancy-to-inertia ratio at reducing Re_j. Note that the time periodic flow prevails over a finite noticeable range of the jet Reynolds number (Figs. 4.2(b)-(d)) and the flow oscillation is characterized by a single fundamental frequency. At certain low Re_j (high Gr/Re_j^2) the flow oscillation becomes quasi-periodic in time and second fundamental frequency sets in (Fig. 4.2(a)).

Then, the effects of the Rayleigh number on the temporal characteristics of the time periodic vortex flow are illustrated in Fig. 4.3 by showing the time histories of the air temperature at a selected location for various Ra at Re_j=61 for the large injection pipe. Note that the oscillation amplitude of the air temperature is only slightly affected by the variation in the Rayleigh number. The corresponding power spectrum densities also shown in Fig. 4.3 suggest that the flow oscillates at a slightly lower frequency for a higher Rayleigh number.

Based on the data from the present temperature measurement for H=20.0 mm, the oscillation frequency of the buoyancy-driven time periodic vortex flow in the processing chamber with the large injection pipe can be correlated as

$$F = \frac{f}{(\alpha / H^2)} = -0.231 + 0.0183\,Re + 5{,}450\,Ra^{-1} \qquad (4.1)$$

While for the small injection pipe

$$F = \frac{f}{(\alpha / H^2)} = 0.0203 + 0.0105\,Re - 6{,}050\,Ra^{-1} \qquad (4.2)$$

Both equations can predict our data with a standard deviation less than 5%.

It is of interest to explore the temporal evolution of the time periodic vortex flow. This is illustrated in Fig. 4.4 by showing the side view flow photos and the corresponding schematically sketched vortex flow patterns at the cross plane θ =0° at selected time instants in a typical periodic cycle for the case with Re_j=61 and Ra=11,350 for D_j=22.1 mm. Note that in the beginning of the cycle designated as time t=0s we only have two big vortex rolls in the processing chamber, namely, the primary inertia-driven roll in the core region of the chamber and the buoyancy-driven roll near the chamber side. Shortly later at t=1s a weak and small thermal plume rises from the heated copper disk in the region below the outer portion of the primary inertia-driven roll, causing this portion of the roll to become elongated in the radial direction. The thermal plume then grows quickly with time and a slender neck is formed between the outer and main portions of the primary inertia-driven roll. As this process continues, it is observed that at t=3s the outer portion of the roll splits from the main portion of the roll and a new circular vortex roll is generated in the region between the two big rolls. For a further increase in time the new roll strengthens gradually. Meanwhile the thermal plume grows slowly and evolves into another new circular vortex roll, as evident from the flow photos at t=7 & 9s. Thus, two additional rolls appear and there are four circular rolls in the processing chamber in this period of time. It is important to note that as the process

keeps going, the roll resulting from the splitting of the inertia-driven roll begins to decay. Later the new roll evolving from the thermal plume decays quickly and at t=11s it becomes very small. At t=13s it is already very weak and nearly disappears. Finally at the end of the cycle at $t=t_p$=13.3s, the two new rolls disappear completely and we only have two big rolls in the chamber.

To reveal the complete picture of the complex time periodic vortex flow structure, the top view flow photos taken at the middle horizontal plane Z=0.5 along with the side view flow photos taken at the cross plane θ=0° for the typical case examined above are presented in Fig. 4.5 at selected time instants in a typical periodic cycle. The results clearly show that the vortex flow does not possess axisymmetry and exhibits significant circumferential variation. In fact, the cross sections of the two new rolls vary circumferentially to such a large degree that each roll is in the form of large connecting blobs. The blobs are essentially the flow recirculations and they connect with the adjacent blobs through narrow necks. Besides, the blobs in the same roll do not have the same size and circulation strength.

4.2 Vortex flow suppression

Next, the effects of the chamber top inclination on the buoyancy-driven vortex flow are exemplified in Fig. 4.6 by showing the steady side view flow photos for ΔT=20.0℃ and Q_j=1.0~5.0 slpm for the chambers with the horizontal and inclined tops for two injection pipes. The results in Fig. 4.6(a) for the chamber with the horizontal top indicate that at the low jet flow rate of 1.0 slpm, the buoyancy-driven vortex roll is big and strong. In fact, the buoyancy-induced roll dominates in the outer zone of the chamber. Now as the chamber top is inclined, the buoyancy-driven roll is suppressed significantly and becomes relatively small (Fig. 4.6(b)). This

vortex roll elimination by the chamber top inclination results apparently from the radial flow acceleration and the reduction in the local buoyancy force accompanied with the reducing chamber height in the radial direction. Moreover, it is noted from Fig. 4.6 that the primary inertia-driven roll is slightly weaker for the inclined chamber top than that for the horizontal chamber top at the same given Ra_o and Re_j. Even for the much higher ΔT of 20℃ the buoyancy-driven roll is suppressed significantly and the inertia-driven rolls are weakened to some degree by the chamber top inclination. Note that at the low Q_j of 1.0 slpm the unstable buoyancy-driven vortex rolls (Figs. 4.6(a) & 4.6(c)) in the chamber with the horizontal top are completely stabilized to become steady and they are significantly suppressed by the chamber top inclination (Figs. 4.6(b) & 4.6(d)). The corresponding top view flow photos indicate that the vortex flow is axisymmetric in the chamber with the inclined top. In the chamber with the horizontal top there is a significant change in the vortex flow pattern with time and the transient temperature data given in Fig. 4.7(a) suggest that the vortex flow is in a large amplitude time-periodic oscillation. But in the chamber with the inclined top the vortex flow is steady. The above results clearly indicate that the chamber top inclination is very effective in stabilizing the temporal oscillation of the flow. The same trend can be seen for the cases with Q_j=1.0 slpm and an even higher ΔT. Note that at the higher ΔT of 30.0℃ and 35.0℃ the vortex flow in the chamber with the inclined top is still steady (Figs. 4.7(b) & 4.7(c)).

4.3 Flow regime map

Based on the present data, a flow regime map for the cases with H=20.0 mm delineating the temporal state of the inertia- and buoyancy-driven vortex flow in the processing chamber is shown in Fig. 4.8 in terms of the parameters chosen as

$Ra(D_j/H)^{-0.3}$ vs. $Re_j(D_j/H)$. The results in this plot manifest that when the jet Reynolds number Re_j and/or the aspect ratio of the processing chamber D_j/H are high so that $Re_j(D_j/H) \geqq 200$, the buoyancy-to-inertia ratio in the flow is low for the range of the Rayleigh number considered here and we have stable vortex flow. But when $Re_j(D_j/H)$ is below 200, the vortex flow becomes time periodic as $Ra(D_j/H)^{-0.3}$ exceeds certain level. For a further raise in Ra the flow can evolve to a quasi-periodic state. Finally, for a high buoyancy-to-inertia ratio the vortex flow shows a chaotic variation with time. More specifically, the boundary between the quasi-periodic and chaotic unstable vortex flow can be correlated as

$$Ra \times \left(\frac{D_j}{H}\right)^{-0.3} = 10700 + 10\left[Re_j \times \left(\frac{D_j}{H}\right)\right]^{1.5} \tag{4.3}$$

In addition, the transitions from steady to time-periodic vortex flow occurs when

$$Ra \times \left(\frac{D_j}{H}\right)^{-0.3} = 2390 + 0.57\left[Re_j \times \left(\frac{D_j}{H}\right)\right]^{2} \tag{4.4}$$

These two correlations are also shown in Fig. 4.6.

4.4 Formation of vortex flow

It is of interest to understand how the inertia-driven vortex rolls form during the transient stage following the jet impinging onto the heated disk. To investigate the formation of the inertia-driven rolls, the experiment is carried out by visualizing the vortex flow immediately after we start to inject the air into the processing chamber for an unheated disk (Ra=0). The instant we begin to inject the air is designated as time t=0. The side view flow photos at selected time instants for a few selected cases from this experiment are shown in Figs. 4.9 and 4.10. The results in Fig. 4.9(a) for a low jet Reynolds number for the small injection pipe indicate that shortly after the jet impingement at t=1s a small circular vortex roll forms around the

jet axis in the inner zone of the processing chamber. The roll then gradually grows in size and strength at increasing time. Finally, at $t \geq 40s$ the flow arrives at steady state. During the entire flow formation processes, only the primary inertia-driven roll is induced at this low Re_j of 136.

Next, the results shown in Fig. 4.9(b) for a much higher jet Reynolds number of 676 indicate that the vortex flow evolves at a much faster pace and at t=3s an additional circular roll appears adjacent to the existing inner roll. The additional roll is known as "the secondary inertia-driven roll". In a short period of time the two rolls reach steady state at $t \geq 9s$.

Then, the flow formation in the chamber with the jet issued from the large injection pipe shown in Fig. 4.10 qualitatively resembles that in Fig. 4.9 for the small injection pipe. A close inspection of the results in Figs. 4.9 and 4.10, however, reveals that for the large injection pipe the jet Reynolds number is lower at the same Q_j, as evident from Equ. (3.1). Thus, the boundary layer in the wall-jet region over the disk is thicker and the induced rolls appear in the slightly upper region of the chamber. Finally, the time variations of the maximum radial extent of the primary inertia-driven roll and the location of the geometric center of the secondary inertia-driven roll are given in Figs. 4.11 and 4.12. The quick evolution of the rolls during the initial transient is noted.

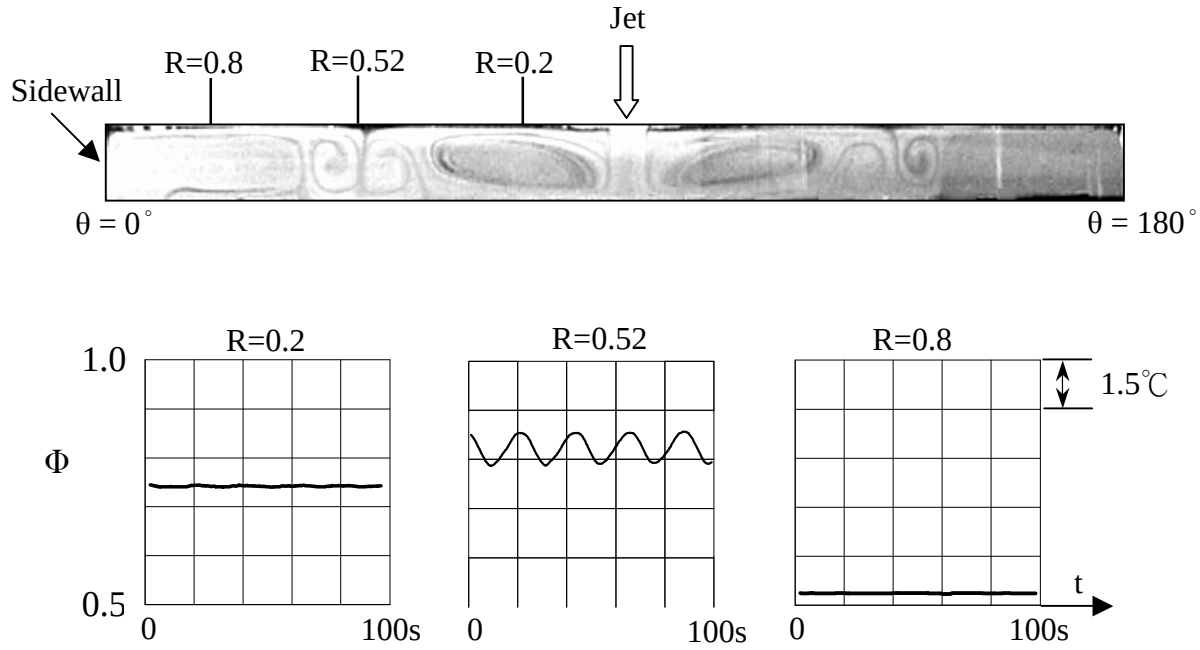

(a) Re_j=136, Ra=11,270 & D_j=10.0 mm (Gr/Re_j^2=0.61)

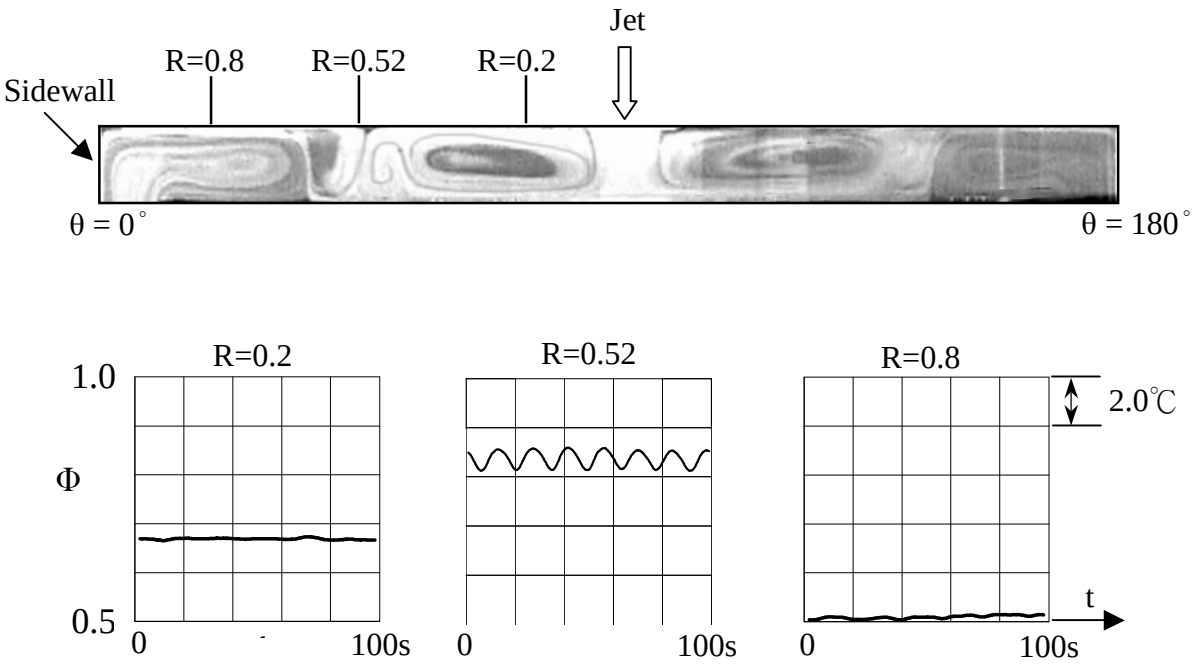

(b) Re_j=61, Ra=15,030 & D_j=22.1 mm (Gr/Re_j^2=4.03)

Fig. 4.1 Side view flow photos at the cross plane θ=0° & 180° at certain time instant in a typical periodic cycle and time records of air temperature at selected locations in the middle horizontal plane Z=0.5 with H=20.0 mm for (a) Re_j=136, Ra=11,270 & D_j=10.0 mm (t_p=21.1 sec) and (b) Re_j=61, Ra=15,030 & D_j=22.1 mm (t_p=13.8 sec).

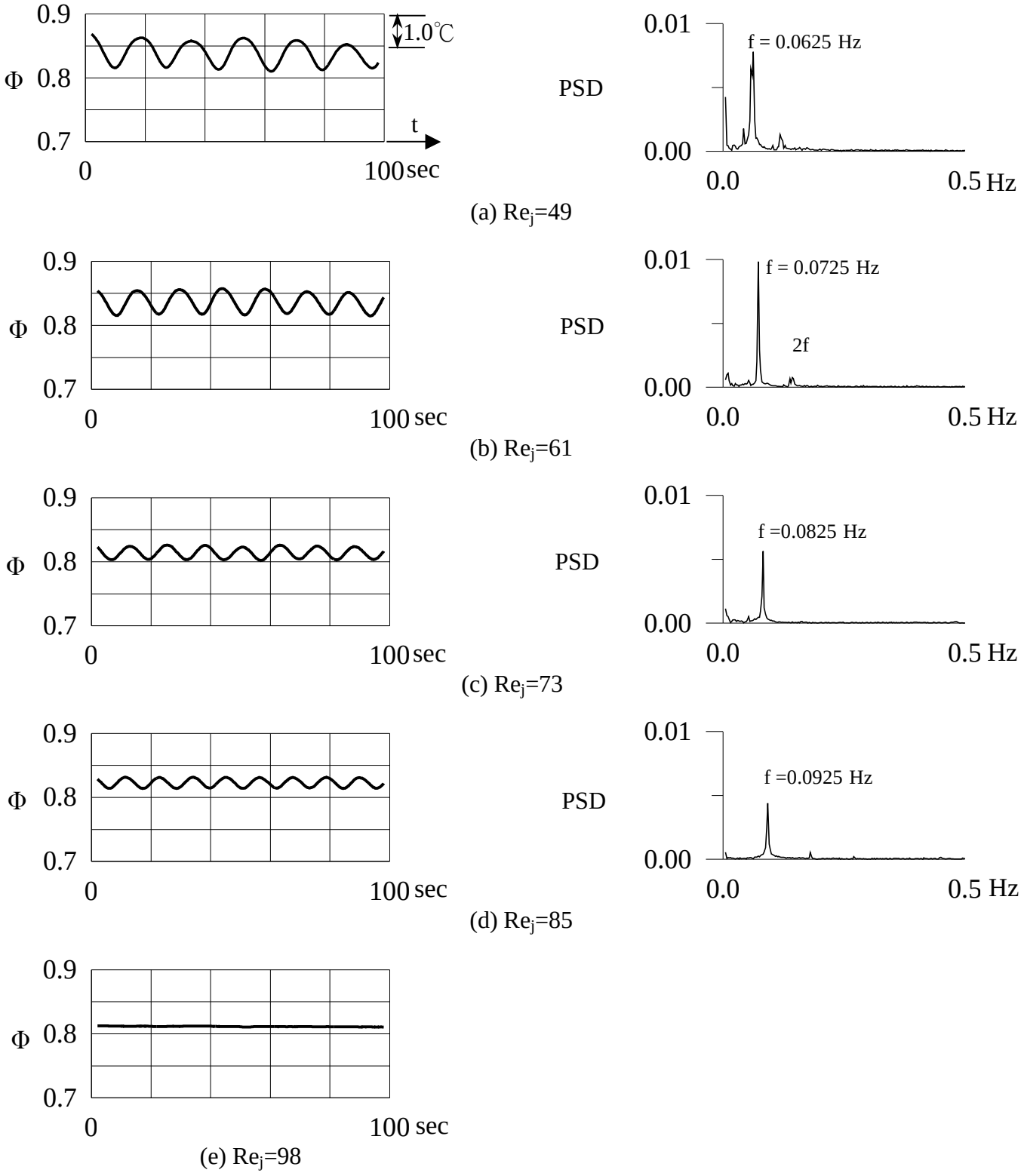

Fig. 4.2 The time records of non-dimensional air temperature and the corresponding power spectrum densities for Ra=15,030 and D_j=22.1 mm at location (R, Z) =(0.52, 0.5) for θ=0º with H=20.0 mm for various Reynolds numbers Re_j= (a)49, (b)61, (c)73, (d)85 and (e)98.

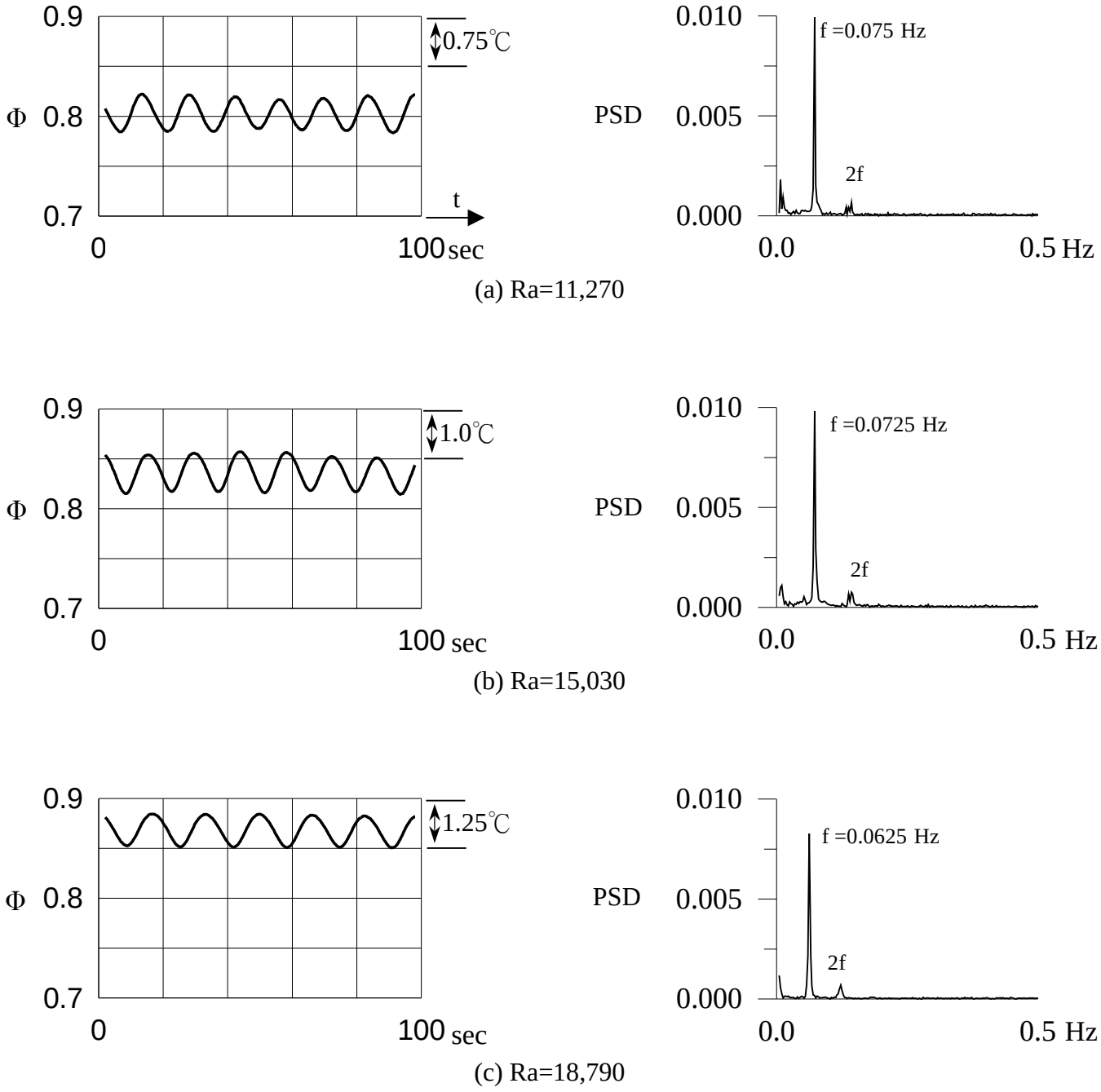

Fig. 4.3 The time records of non-dimensional air temperature and corresponding power spectrum densities for Re_j=61 and D_j=22.1 mm at location (R, Z) =(0.52, 0.5) for θ=0º with H=20.0 mm for various Rayleigh numbers Ra= (a) 11,270, (b) 15,030 and (c) 18,790.

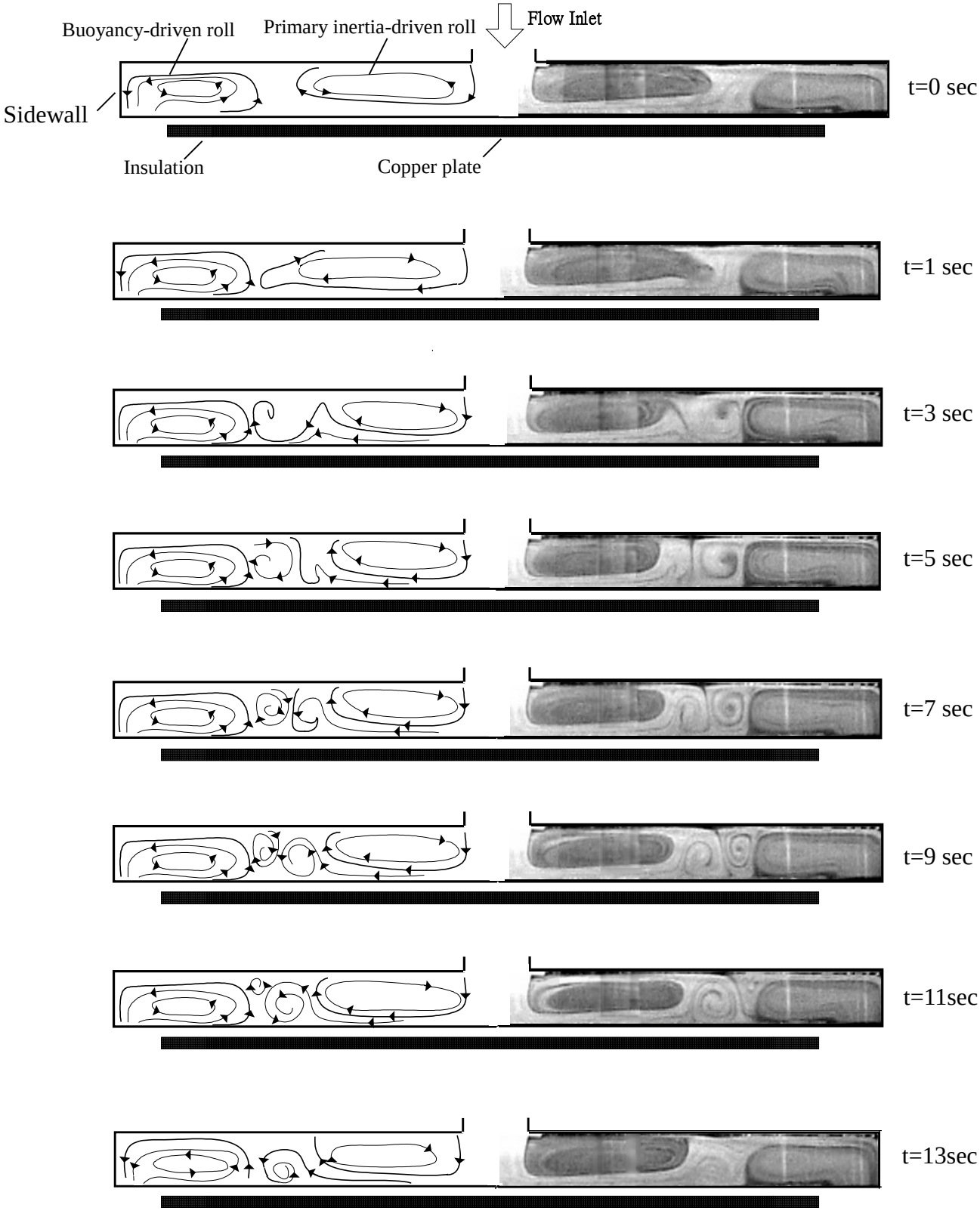

Fig. 4.4 Side view flow photos taken at the cross plane θ =0° for Re_j=61, Ra=11,270 and D_j=22.1 mm with H=20.0 mm at selected time instants (right) and the corresponding schematically sketched cross plane flow (left) in a typical periodic cycle (t_p=13.3sec).

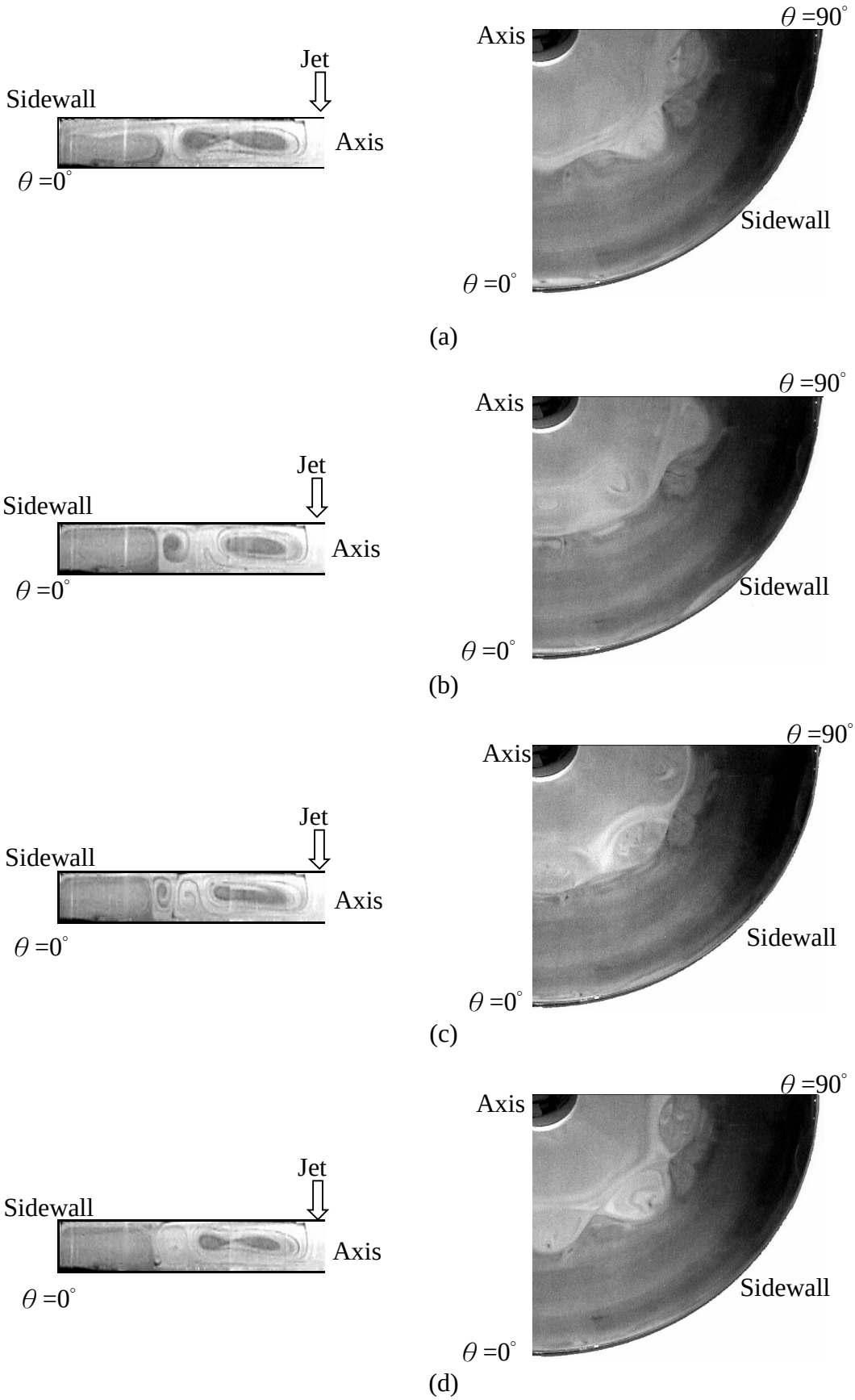

Fig. 4.5 Half side view flow photos taken at θ =0° (left) and quarter of top view flow photos (right) taken at midheight of the chamber with Re_j= 61, Ra=11,270 and D_j=22.1 mm for H=20.0 mm at selected time instants in statistical state for (a) t=0 sec, (b) t=5 sec, (c) t=9 sec and (d) t=13 sec.

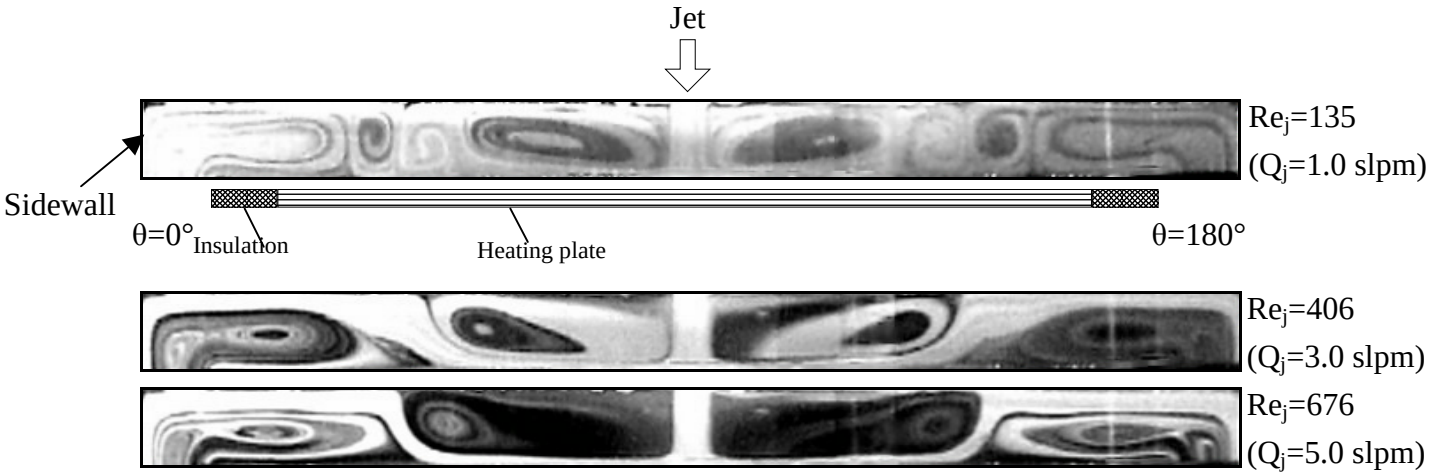

(a) Flow in the chamber with a horizontal top (D$_j$=10.0 mm)

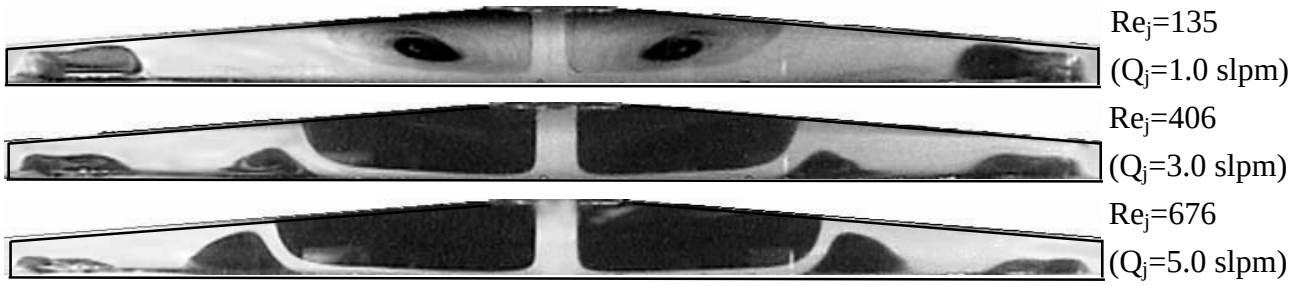

(b) Flow in the chamber with an inclined top (D$_j$=10.0 mm)

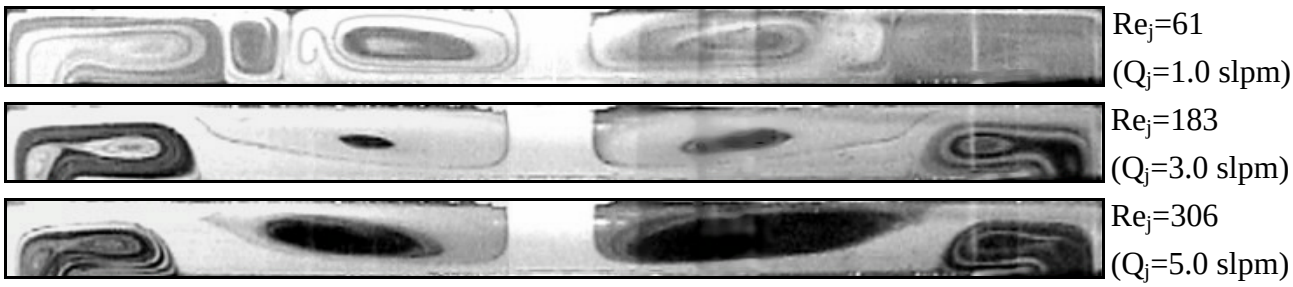

(c) Flow in the chamber with a horizontal top (D$_j$=22.1 mm)

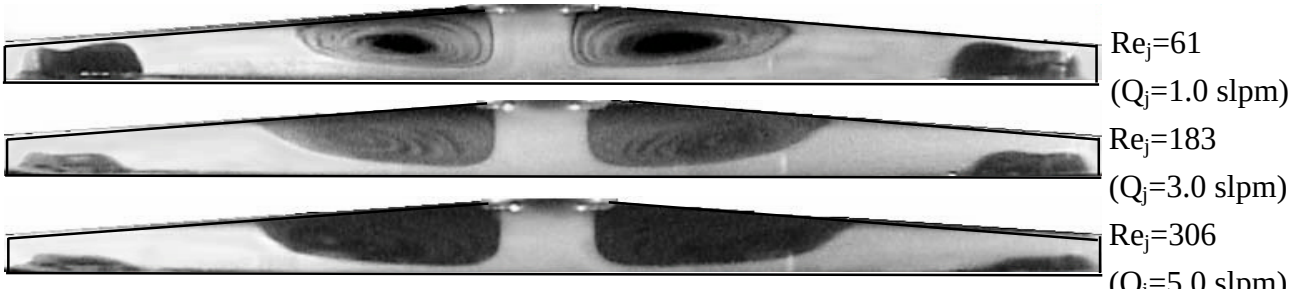

(d) Flow in the chamber with an inclined top (D$_j$=22.1 mm)

Fig. 4.6 Side view flow photos at long time taken from the chambers at the cross plane θ=0º & 180? for ΔT=20.0℃ (Ra$_o$=15,030) for various jet flow rates with (a) D$_j$=10.0 mm & horizontal top, (b) D$_j$=10.0 mm & inclined top, (c) D$_j$=22.1 mm & horizontal top and (d) D$_j$=22.1 mm & inclined top.

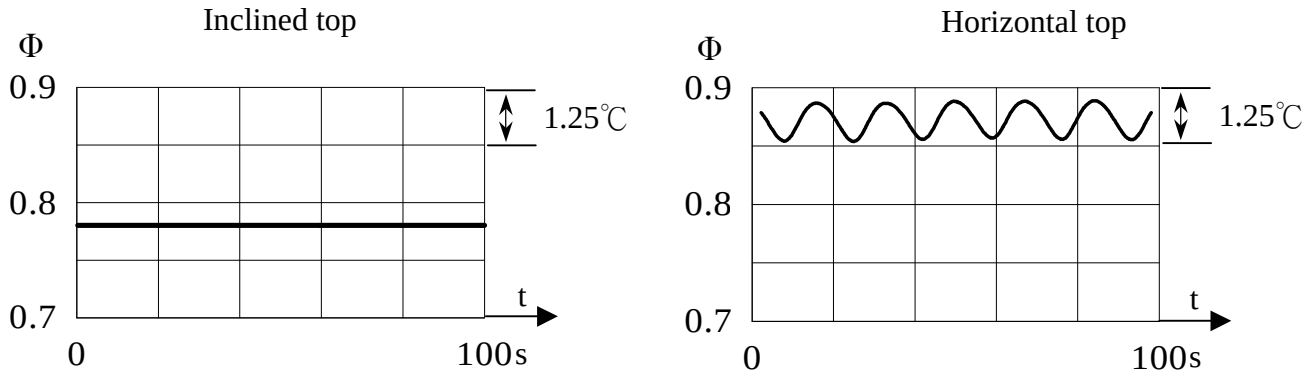

(a) Ra_o= 18,790 (ΔT=25.0℃)

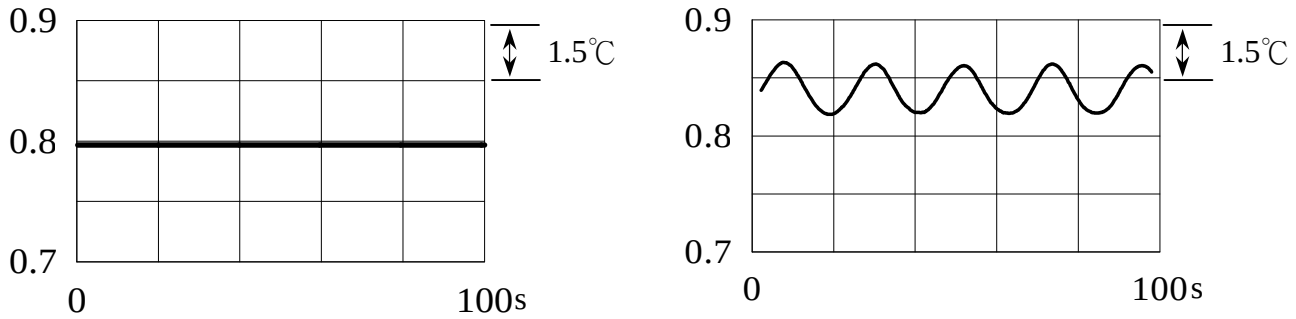

(b) Ra_o= 22,550 (ΔT=30.0℃)

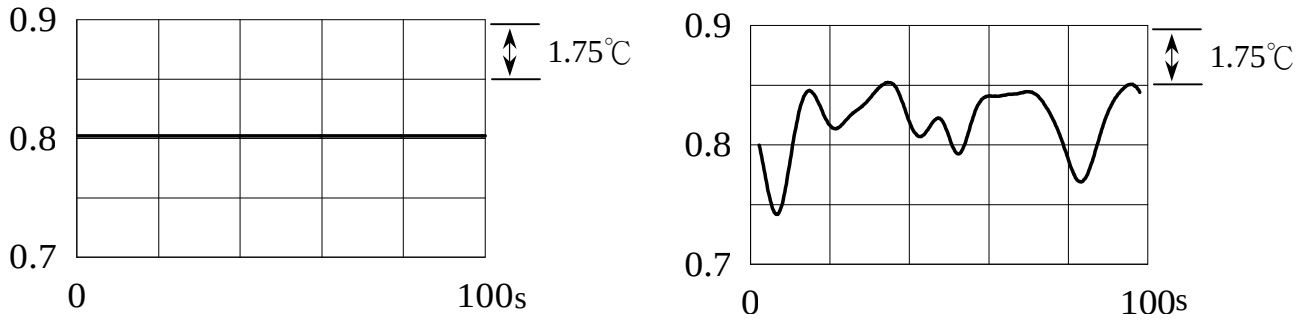

(c) Ra_o=26,300 (ΔT=35.0℃)

Fig. 4.7 Time records of non-dimensional air temperature in the chambers with the inclined and horizontal tops for D_j=22.1 mm and Re_j=61 at location (R, Z) = (0.52, 0.5) for horizontal top and (0.52, 0.25) for inclined top for θ=0º for various Rayleigh numbers: (a) Ra_o=18,790, (b) Ra_o=22,550 and (c) Ra_o=26,300.

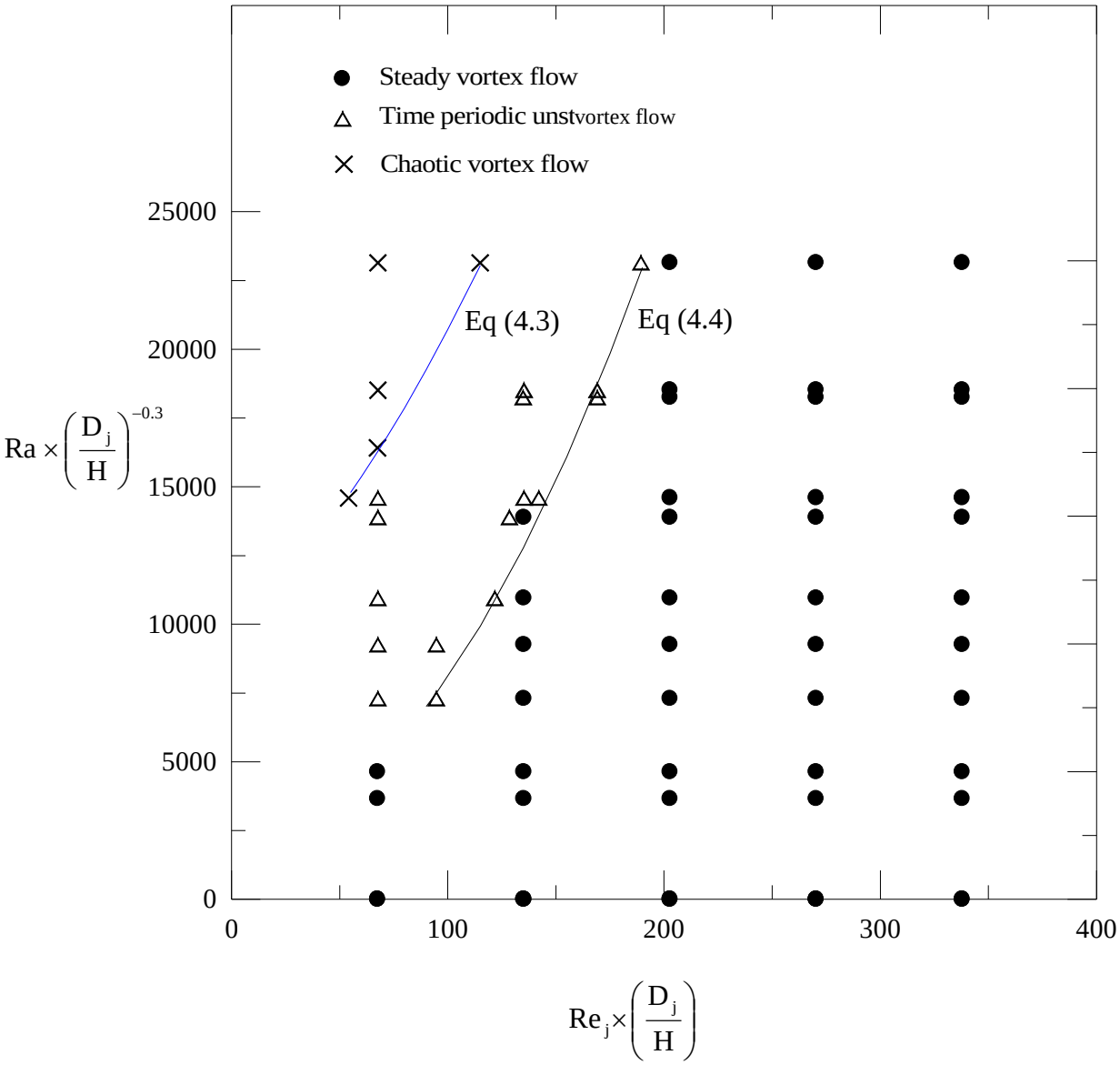

Fig. 4.8 Flow region map delineating the temporal state of the vortex flow for H=20.0 mm.

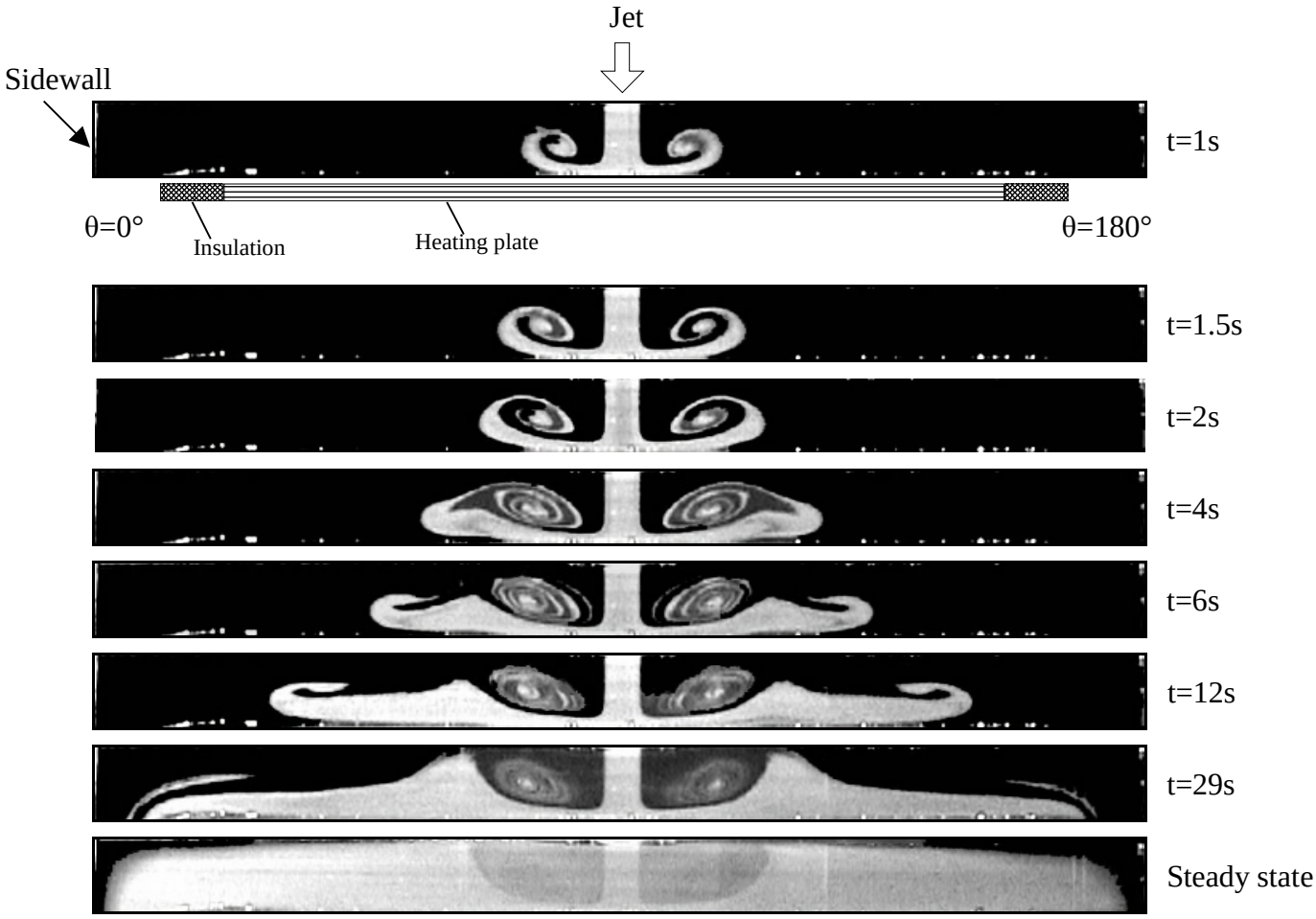

(a)

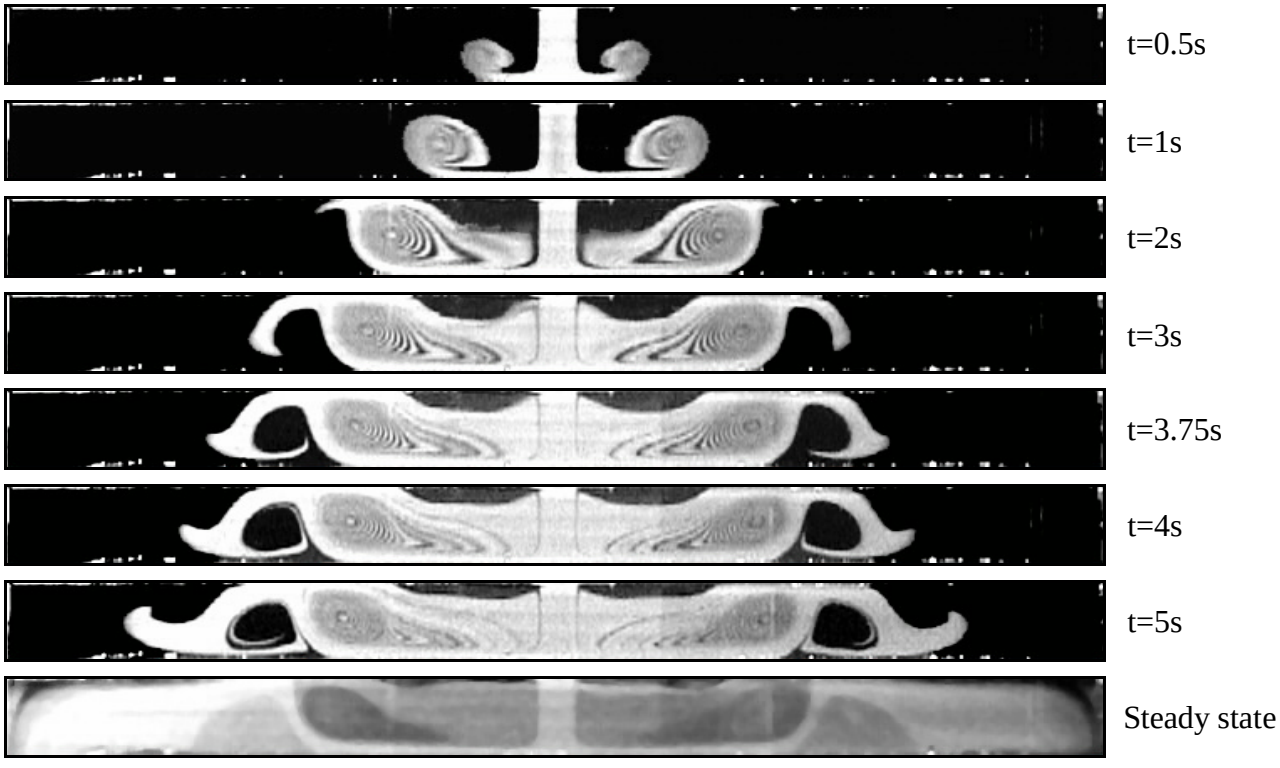

(b)

Fig. 4.9 The side view flow photos at selected time instants during flow formation at the cross plane θ =0° & 180° for Ra=0 at H=20.0 mm & D_j=10.0 mm for Re_j= (a) 136 and (b) 676.

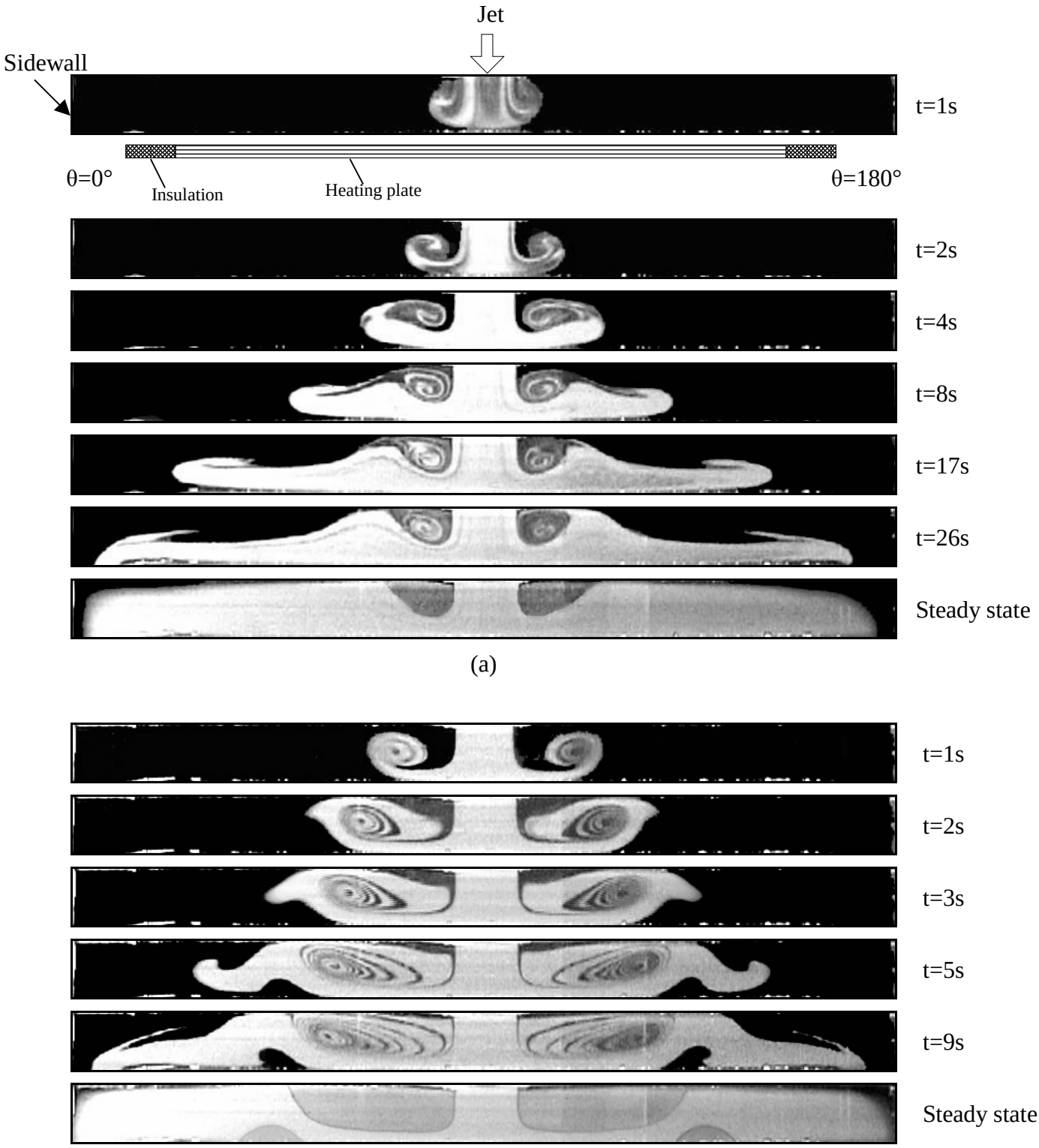

Fig. 4.10 The side view flow photos at selected time instants during flow formation at the cross plane θ =0° & 180° for Ra=0 at H=20.0 mm & D_j=22.1 mm for Re_j= (a) 61 and (b) 306.

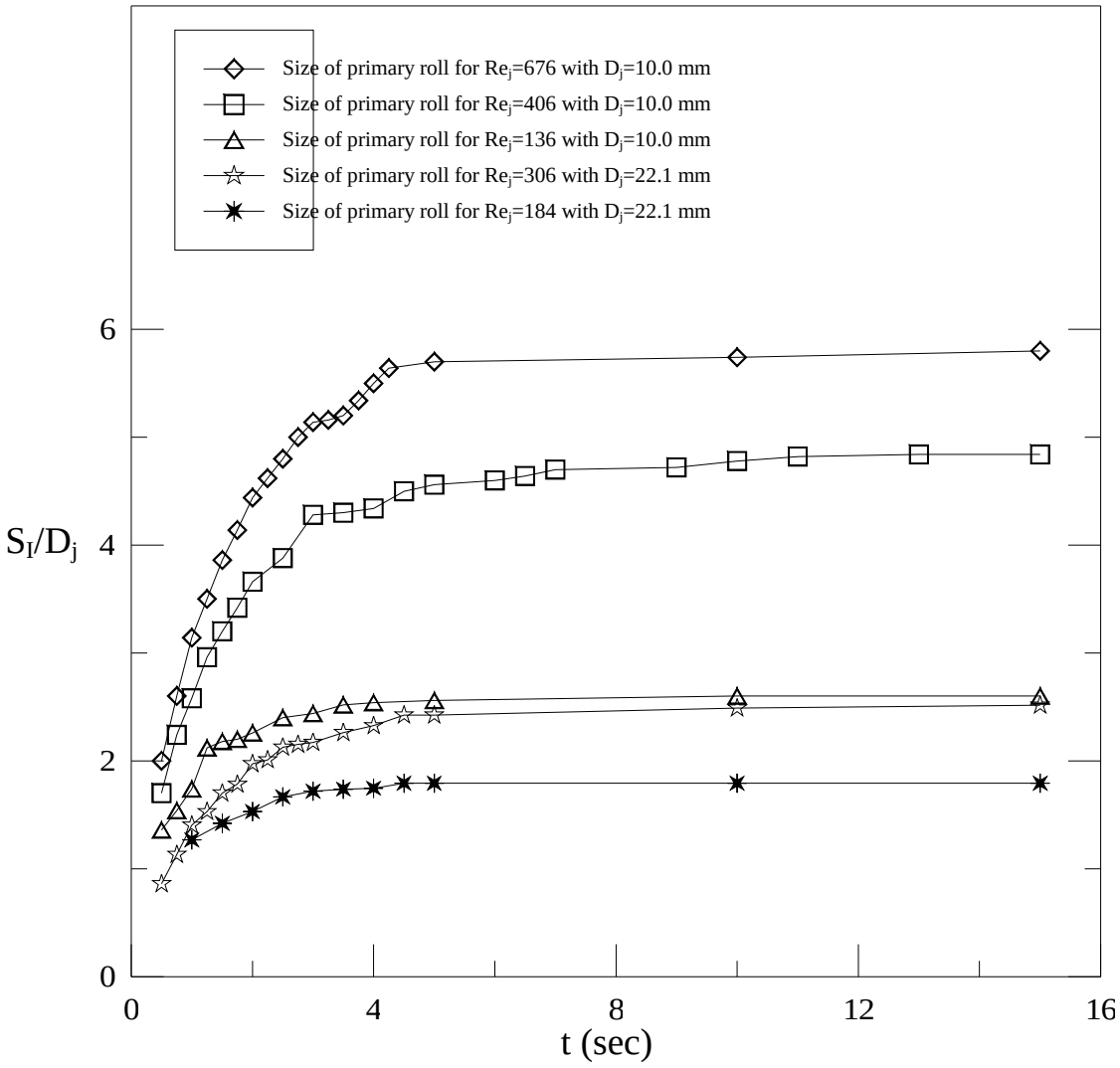

Fig. 4.11 Time variation of the size of the primary inertia-driven roll for various Re_j at Ra=0.

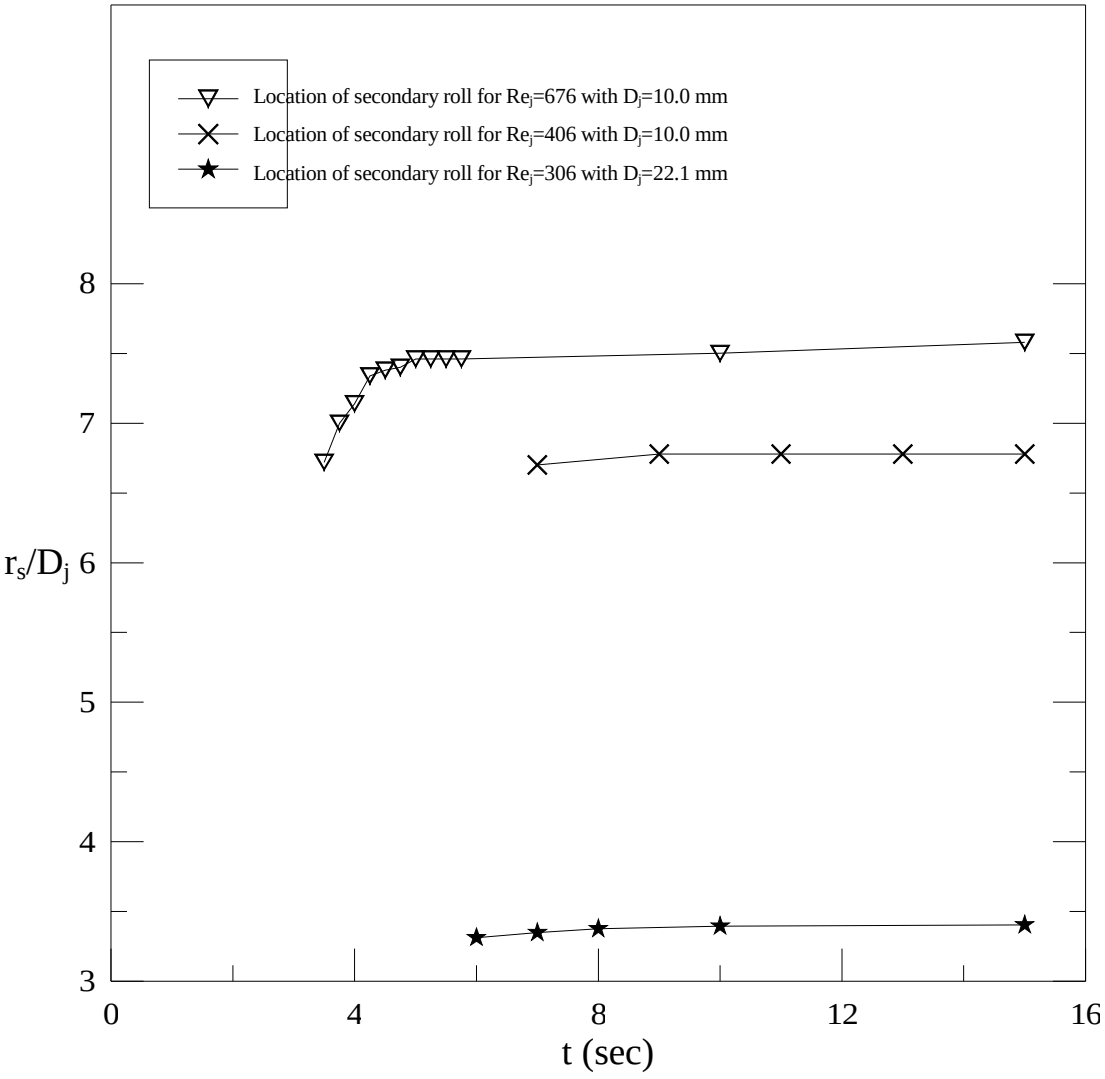

Fig. 4.12 Time variation of the location of the secondary inertia-driven roll for various Re_j at Ra=0.

Chapter 5

Concluding Remarks and Recommendations for Future Work

5.1 Concluding remarks

Combined experimental flow visualization, transient and steady temperature measurement have been conducted in the present study to explore the onset, steady and time dependent vortex flow characteristics associated with a low speed air jet impinging onto a horizontal circular heated disk confined in a vertical cylindrical chamber. Effects of the jet flow rate, temperature difference between the heated disk and cold air jet, and geometry of the chamber including diameter of the injection pipe and jet-to-disk separation distance on the vortex flow structures were inspected in detail. The formation of the inertia-driven vortex flow in the chamber during the transient stage is also examined. The major results obtained can be briefly summarized in the following:

1. The typical steady vortex flow in the processing chamber consists of the inertia-driven and buoyancy-driven circular rolls.
2. The critical jet Reynolds numbers for the onset of the primary, secondary and tertiary inertia-driven rolls increase noticeably when H is reduced from 20.0 to 10.0 mm. But the corresponding critical jet Reynolds numbers for the primary and tertiary inertia-driven rolls do not change for a reduction of H from 30.0 to 20.0 mm.
3. The secondary inertia-driven roll appears in the chamber with the jet issued from the small injection pipe as Re_j approximately exceeds 180 at H=20.0 mm and 240 at H=10.0 mm. For the large injection pipe the secondary inertia-driven roll is induced for Re_j above 220 at H=20.0 mm, for Re_j above 306 at H=15.0 mm and for Re_j above 427 at H=10.0 mm.

4. A tertiary inertia-driven circular vortex roll is first identified in the confined impinging air jet as the jet Reynolds number is sufficiently high. The tertiary roll is relatively small compared with the primary inertia-driven roll and becomes smaller at increasing Ra. Beyond the critical Re_j for onset of the tertiary roll the high jet inertia causes the vortex flow to become time dependent at $H \leqq 20.0$ mm.
5. A reduction in H results in a significant decrease in the Rayleigh number since $Ra \propto H^3$ and can substantially reduce the size and strength of the buoyancy-driven roll. The present data of the critical condition for the onset of the buoyancy-driven roll can be approximately expressed as the local buoyancy-to-inertia ratio at the edge of the disk $Gr/Re_{we}^2 \approx 33.0$ at $H \leqq 20.0$ mm.
6. At increasing jet Reynolds number the primary and the secondary inertia-driven rolls grow in size and strength with the accompanying decay of the buoyancy-driven roll. For H=20.0 mm, the radial extent of the buoyancy-driven roll is much larger than that for the largest jet-to-disk separation distance with H=30.0 mm because the buoyancy-driven roll can merge with the secondary inertia-driven roll as Re_j and Ra exceed certain level. At H=30.0 mm the primary inertia-driven and the buoyancy-driven rolls both become so large and they contact with each other. Thus no space is left for the secondary inertia-driven to appear.
7. The inertia-driven rolls become smaller with decreasing jet-to-disk separation distance at Ra=0. Moreover, the inertia-driven rolls are insignificantly affected by ΔT at the shorter jet-to-disk separation distance with H=10.0 mm.
8. At the same ΔT and Q_j the small injection pipe results in a larger and stronger primary inertia-driven roll and a secondary inertia-driven roll is prone to appear. However, the size of the buoyancy-driven roll is almost unaffected by the injection pipe diameter at $H \leqq 15.0$ mm.

9. The existence of a peak in the radial temperature distribution is noted to result from the presence of the counter-rotating primary inertia-driven and buoyancy-driven rolls in the chamber, and hence the nonmonotonic radial air temperature distribution prevails in the flow.
10. The flow is pumped outward by the rotating disk and encountered the chamber sidewall to form a long recirculation cell. The longer recirculation cell is caused by the inertia force combined with the centrifugal force. Meantime, the buoyancy-driven roll can be suppressed by centrifugal force.
11. Empirical equations are proposed to correlate the size and position of the steady vortex rolls and the oscillation frequency of the time periodic vortex flow.
12. At a high buoyancy-to-inertia ratio the vortex flow becomes time dependent and two new vortex rolls are induced due to an additional thermal plume rising from the heated disk and the splitting of the primary inertia-driven roll. In the region occupied by the two new rolls, the vortex flow oscillates significantly with time. Besides, the oscillation frequency and amplitude of the time periodic vortex flow respectively increases and decreases noticeably with the jet Reynolds number.
13. A flow regime map is given to delineate the temporal state of the vortex flow for H=20.0 mm.
14. The flow acceleration and local buoyancy reduction associated with the chamber top inclination can effectively suppress the buoyancy-driven roll to become smaller and weaker. At low and intermediate buoyancy-to-inertia ratios the buoyancy-driven roll can be completely wiped out. Moreover, at high buoyancy-to-inertia ratios the unsteady vortex flow oscillation can be completely stabilized and the flow becomes steady.
15. During the flow formation for the limiting case of an unheated disk the primary inertia-driven roll appears immediately after the jet is injected into the chamber

and it grows at a quicker speed for a high Re_j and reaches steady state in a shorter period of time. For the large injection pipe the rolls are induced in the slightly upper region of the chamber during the entire transient.

5.2 計劃成果自評

In the previous three-year research project (August 2001 to July 2004) we have carried out an experimental study on the mixed convective flow associated with vertical CVD reactors and revealed various characteristics of the circular vortex roll structure; including the onset and steady and time-dependent features of the rolls. Besides, a tertiary inertia driven roll was first identified. These results can provide a useful reference about designing gas flow in the thin film reactor in the future.

REFERENCES

1. S. Polat, B. Huang, A.S. Mujumdar, and W.J.M. Douglas, Numerical flow and heat transfer under impinging jets: a review, in C. L. Tien and T. C. Chawla(eds.), Annular Review of Numerical Fluid Mechanics and Heat Transfer 2, pp.157-197, Hemisphere, Washington, D. C. (1989).

2. G.B. Stringfellow, Organometallic Vapor Phase Epitaxy: Theory and Practice, Academic Press, San Diego, chapter 5 (1989).

3. S.A. Campbell, The Science and Engineering of Microelectronic Fabrication, Oxford University Press, New York, chapter 6 (1996).

4. M.L. Hitchamn and K.F. Jensen, Chemical vapor deposition (Principle and Application), Academic Press, San Diego, chapter 2 (1993).

5. T.C. Cheng, P.H. Chiou and T.F. Lin, Visualization of mixed convective vortex rolls in an impinging jet flow of air through a cylindrical chamber, International Journal of Heat and Mass Transfer 45 (2002) 3357-3368.

6. R. Gardon and J.C. Akfirat, The role of turbulence in determining the heat-transfer characteristics of impinging jets, International Journal of Heat and Mass Transfer 8 (1965) 1261-1272.

7. R. Gardon and J.C. Akfirat, Heat transfer characteristics of impinging two-dimensional air jets, ASME Transac. C, Journal of Heat Transfer (1966) 101-108.

8. M.T. Scholtz and O. Trass, Mass transfer in a nonuniform impinging jet, AIChE J. 16 (1970) 90-96.

9. E.M. Sparrow and T.C. Wong, Impingement transfer coefficients due to initially laminar slot jets, International Journal of Heat and Mass Transfer 18 (1975) 597-605.

10. J.H. Masliyah and T.T. Nguyen, Mass transfer due to an impinging slot jet, International Journal of Heat and Mass Transfer 22 (1979) 237-244.

11. P. Hrycak, Heat transfer from round impinging jets to a flat plate, International Journal of Heat and Mass Transfer 26 (1981) 1857-1865.

12. Ì.B. Özdermir and J.H. Whitelaw, Impingement of an axisymmetric jet on unheated and heated flat plates, J. Fluid Mech. 240 (1992) 503-532.

13. T. Liu and J.P. Sullivan, Heat transfer and flow structures in an excited circular impinging jet, International Journal of Heat and Mass Transfer 39 (1996) 3695-3706.

14. A.R.P. van Heiningen, A.S. Mujumdar and W.J.M. Douglas, Numerical prediction of the flow field and impingement heat transfer caused by a laminar slot jet, ASME Transac. C, J. Heat Transfer 98 (1976) 654-658.

15. N.R. Saad, W.J.M. Douglas and A.S. Mujumdar, Prediction of heat transfer under an axisymmetric laminar impinging jet, Int. Eng. Chem. Fundam. 16 (1977) 148-154.

16. H.S. Law and J.H. Masliyah, Mass transfer due to a confined laminar impinging axisymmetric jet, Int. Eng. Chem. Fundam. 23 (1984) 446-454.

17. S.M. Hosseinalipour and A.S. Mujumdar, Comparative evaluation of different turbulence models for confined impinging and opposing jet flows, Num. Heat Transfer, Part A 28 (1995) 647-666.

18. G.K. Morris and S.V. Garimella, Orifice and impingement flow fields in confined jet impingement, J. Electronic Packaging 120 (1998) 68-72.

19. Z.H. Lin, Y.J. Chou, and Y.H. Hung, Heat transfer behaviors of a confined slot jet impingement, International Journal of Heat and Mass Transfer 40 (1997) 1095-1107.

20. D.L. Besserman, F.P. Incropera and S. Ramadhyani, Experimental study of heat transfer from a discrete source to a circular liquid jet with annular collection of the spent fluid, Exper. Heat Transfer 4 (1991) 41-57.

21. D.L. Besserman, S. Ramadhyani and F.P. Incropera, Numerical simulation of laminar flow and heat transfer for liquid jet impingement cooling of a circular heat source with annular collection of the spent fluid, Numerical Heat Transfer, Part A 20 (1991) 263-278.

22. M. Behnia, S. Parneix, Y. Shabany. P.A. Durbin, Numerical study of turbulent heat transfer in confined and unconfined impinging jets, International Journal of Heat and Fluid Flow 20 (1999) 1-9.

23. L.P. Chua, S.C.M. Yu, H-S. Li, Flow visualization and preliminary measurements of a confined jet with and without target, International Communications in Heat

and Mass Transfer 27 (2000) 191-200.

24. P.R. Voke, S. Gao, Numerical study of heat transfer from an impinging jet, International Journal of Heat and Mass Transfer 41 (1998) 671-680.

25. J.A. Fitzgerald, S.V. Garimella, A study of the flow field of a confined and submerged impinging jet, International Journal of Heat and Mass Transfer 41 (1998) 1025-1034.

26. V.A. Marple, B.Y.H. Liu, K.T. Whitby, On the flow fields of inertial impactors, Transactions of the ASME, Journal of Fluids Engineering (1974) 394-400.

27. S.V. Garimella, R.A. Rice, Confined and submerged liquid jet impingement heat transfer, Journal of Heat Transfer 117 (1995) 871-877.

28. S. Ashforth-Forst, K. Jambunathan, C.F. Whitney, Velocity and turbulence characteristics of a semi-confined orthogonally impinging slot jet, Experimental Thermal and Fluid Science 14 (1997) 60-67.

29. S. Ashforth-Frost, K. Jambunathan, Effect of nozzle geometry and semi-confinement on the potential core of a turbulent axisymmetric free jet, International Communications in Heat and Mass Transfer 23 (1996) 155-162.

30 E. Baydar, Confined impinging air jet at low Reynolds numbers, Experimental Thermal and Science 19 (1993) 27-33.

31. J. Lee and S-J. Lee, The effect of nozzle aspect ratio on stagnation region heat transfer characteristics of elliptic impinging jet, International Journal of Heat and Mass Transfer 43 (2000) 555-575.

32. B.N. Pamadi, I.A. Belov, A note on the heat transfer characteristics of circular impinging jet, International Journal of Heat and Mass Transfer 23 (1980) 783-787.

33. D. Lytle, B.W. Webb, Air jet impingement heat transfer at low nozzle-plate spacings, International Journal of Heat and Mass Transfer 37 (1994) 1687-1697.

34. C.Y. Li, S.V. Garimella, Prandtl number effects and generalized correlations for confined and submerged jet impingement, International Journal of Heat and Mass Transfer 44 (2001) 3471-3480.

35. H.S. Law, J.H. Masliyah, Numerical prediction of the flow field due to a confined laminar two-dimensional submerged jet, Computers & Fluids 12 (1984) 199-215.

36. D. Schafer, F. P. Incropera, S. Ramadhyani, Planar liquid jet impingement cooling of multiple discrete heat sources, J. Electronic Packaging 113 (1991) 359-366.

37. D.W. Colucci, R. Viskanta, Effect of nozzle geometry on local convective heat transfer to a confined impinging air jet, Experimental Thermal and Fluid Science 13 (1996) 71-80.

38. M.D. Deshpande, R.N. Vaishnav, Submerged laminar jet impingement on a plane, Journal of Fluid Mechanics 114 (1982) 213-236.

39. L. Huang, M.S. El-Genk, Heat transfer and flow visualization experiments of swirling, multi-channel, and conventional impinging jets, International Journal Hate and Mass Transfer 41 (1998) 583-600.

40. V.A. Chiriac and A. Ortega, A numerical study of the unsteady flow and heat transfer in a transitional confined slot jet impinging on an isothermal surface, International Journal of Heat and Mass Transfer 45 (2002) 1237-1248.

41. R. Viskanta, Heat transfer to impinging isothermal gas and flame jets, Experimental Thermal and Fluid Science 6 (1993) 111-134.

42. K. Jambunathan, E. Lai, M.A. Moss, B.L. Button, A review of heat transfer data for single circular jet impingement, International Journal of Heat and Fluid Flow 13 (1992) 106-115.

43. K. Ichimiya, S. Takema, S. Morimoto, T. Kunugi, N. Akino, Movement of impingement heat transfer by single circular jet with a confined wall, International Journal of Heat and Mass Transfer 44 (2001) 3095-3102.

44. H.V. Stanten, C.R. Kleijn, H.E.A. Van Den Akker, Mixed convention in radial flow between horizontal plates— I. Numerical simulations, International Journal of Heat and Mass Transfer 43 (2000) 1523-1535.

45. H.V. Stanten, C.R. Kleijn, H.E.A. Van Den Akker, Mixed convention in radial flow between horizontal plates— II. Experiments, International Journal of Heat and Mass Transfer 43 (2000) 1537-1546.

46. B. Elison, B.W. Webb, Local heat transfer to impinging liquid jets in the initially laminar, transitional, and turbulent regimes, International Journal of Heat and Mass Transfer 37 (1994) 1207-1216.

47. K.J. McNaughton, C.G. Sinclair, Submerged jets in short cylindrical flow vessels,

Journal of Fluid Mechanics 25 (1966) 367-375.

48. G. Wahl, Hydrodynamic description of CVD processes, Thin Solid Films 40 (1977) 13-26.

49. D.I. Fotiads and S. Kieda, Transport phenomena in vertical reactors for metalorganic vapor phase epitaxy, J. Crystal Growth 102 (1990) 441-470.

50. A.H. Dilawari, and J. Szekely, A mathematical representation of a modified stagnation flow reactor for MOCVD application, J. Crystal Growth 108 (1991) 491-498.

51. C.R. Biber, C.A. Wang, and S. Motakef, Flow regime map and deposition rate in vertical rotating-disk OMVPE reactor, J. Crystal Growth 123 (1992) 545-554.

52. P.N. Gadgil, Optimization of a stagnation point flow reactor design for metalorganic chemical vapor deposition by flow visualization, J. Crystal Growth 134 (1993) 302-312.

53. H.V. Santen, C.R. Kleijn, H.E.A. Van Den Akker, Symmetry breaking in a stagnation-flow CVD reactor, J. Crystal Growth 212 (2000) 311-323.

54. S. Chatterjee, I. Trachtenberg, and T.F. Edgar, Mathematical modeling of a single-wafer RTP thermal reactor, J. Electrochem. Soc 139 (1992) 3682-3689.

55. P.N. Gadgil, Single wafer processing in stagnation point flow CVD reactor: prospects, constrains and reactor design, J. Electronic Materials 22 (1993) 171-177.

56. Y. Kusumoto, T. Hayashi, S. Komiya, Numerical analysis of the transport phenomena in MOCVD process, Japanese Journal of Applied Physics 24 (1985) 620-625.

57. H.V. Santen, C.R. Kleijn, H.E.A. Van Den Akker, On turbulent flows in cold-wall CVD reactors, J. Crystal Growth 212 (2000) 299-310.

58. S.J. Kline, F.A. McClintock, Describing uncertainties in single-sample experiment, Mech. Eng. 75 (1953) 3-8.